

**JOINT INSTITUTE FOR AERONAUTICS AND ACOUSTICS**

12-24-97  
001187

National Aeronautics and  
Space Administration

Ames Research Center



Stanford University

**JIAA TR 118**

**DIRECT NUMERICAL SIMULATION  
OF A TEMPORALLY EVOLVING  
INCOMPRESSIBLE PLANE WAKE:  
EFFECT OF INITIAL CONDITIONS ON  
EVOLUTION AND TOPOLOGY**

**R. Sondergaard, B. Cantwell and N. Mansour**

*Department of Aeronautics and Astronautics  
Stanford University  
Stanford, CA 94305*

**February 1997**



# Abstract

Direct numerical simulations have been used to examine the effect of the initial disturbance field on the development of three-dimensionality and the transition to turbulence in the incompressible plane wake. The simulations were performed using a new numerical method for solving the time-dependent, three-dimensional, incompressible Navier-Stokes equations in flows with one infinite and two periodic directions. The method uses standard Fast Fourier Transforms and is applicable to cases where the vorticity field is compact in the infinite direction. Initial disturbances fields examined were combinations of two-dimensional waves and symmetric pairs of  $60^\circ$  oblique waves at the fundamental, subharmonic, and sub-subharmonic wavelengths.

The results of these simulations indicate that the presence of  $60^\circ$  disturbances at the subharmonic streamwise wavelength results in the development of strong coherent three-dimensional structures. The resulting strong three-dimensional rate-of-strain triggers the growth of intense fine scale motions. Wakes initiated with  $60^\circ$  disturbances at the fundamental streamwise wavelength develop weak coherent streamwise structures, and do not develop significant fine scale motions, even at high Reynolds numbers. The wakes which develop strong three-dimensional structures exhibit growth rates on par with experimentally observed turbulent plane wakes. Wakes which develop only weak three-dimensional structures exhibit significantly lower late time growth rates.

Preliminary studies of wakes initiated with an oblique fundamental and a two-dimensional subharmonic, which develop asymmetric coherent oblique structures at the subharmonic wavelength, indicate that significant fine scale motions only develop if the resulting oblique structures are above an angle of approximately  $45^\circ$ .





# Acknowledgements

This work was supported by the Joint Institute for Aeronautics and Acoustics, grant NASA NCC 2-55 , Office of Naval Research , grant N00014-90-J-1976, and the National Aerodynamic Simulation program, which provided supercomputer resources.

Ralph Sondergaard was supported by The National Science Foundation Graduate Fellowship Program and the United States Air Force Palace Knight Program.



# Contents

<b>Abstract</b>	<b>iii</b>
<b>Acknowledgements</b>	<b>iv</b>
<b>List of Tables</b>	<b>x</b>
<b>List of Figures</b>	<b>xi</b>
<b>Nomenclature</b>	<b>xviii</b>
<b>1 Introduction</b>	<b>1</b>
1.1 Background . . . . .	1
1.1.1 The Incompressible Wake . . . . .	1
1.1.2 Topology of Fine Scale Motions . . . . .	7
1.1.3 Goals of This Study . . . . .	9
1.1.4 Direct Numerical Simulation of Free Shear Flows . . . . .	9
1.2 Outline of Present Work . . . . .	13
1.3 Summary of Results . . . . .	14
1.3.1 The Two-dimensional Plane Wake . . . . .	14
1.3.2 The Three-dimensional Plane Wake . . . . .	15
<b>2 Numerical Methodology</b>	<b>18</b>
2.1 Introduction . . . . .	18
2.2 Approach . . . . .	20
2.3 Governing Equations . . . . .	22



2.3.1	Vorticity Form of the Navier-Stokes Equations . . . . .	22
2.3.2	Stretching Grid . . . . .	24
2.4	Numerical Method . . . . .	25
2.4.1	Transformed Equations . . . . .	25
2.4.2	Asymptotic Matching of Velocities . . . . .	27
2.4.3	Time Advance . . . . .	29
2.4.4	Accuracy and Stability . . . . .	30
2.4.5	Alias Control . . . . .	32
2.5	Code Implementation and Data Management . . . . .	33
2.6	Boundary Conditions . . . . .	35
2.7	Initial Conditions . . . . .	36
2.7.1	Vorticity Field . . . . .	36
2.7.2	Passive Scalar Field . . . . .	39
2.7.3	Grid Stretching Rate . . . . .	40
2.7.4	Flow Reference Convention . . . . .	41
2.8	Code Validation . . . . .	42
2.8.1	One Dimensional Diffusion . . . . .	42
2.8.2	Linear Growth Rate . . . . .	45
2.8.3	Comparison with Accepted Jacobi Polynomial Code . . . . .	46
2.8.4	Behavior Near the Matching Boundaries . . . . .	49
<b>3</b>	<b>Two-dimensional Simulations</b>	<b>52</b>
3.1	Motivation . . . . .	52
3.2	Simulation Parameters . . . . .	52
3.3	Evolution of the Two Dimensional Wake . . . . .	53
3.3.1	Initial Development . . . . .	53
3.3.2	Effect of Disturbance Wavelength and Phase . . . . .	56
3.3.3	Effect of Reynolds Number . . . . .	73
3.3.4	Scalar Field . . . . .	78
3.4	Growth of the Mean Flow . . . . .	81
3.4.1	Effect of Disturbance Wavelength . . . . .	81



3.4.2	Effect of Disturbance Phase . . . . .	84
3.4.3	Effect of Reynolds Number . . . . .	86
<b>4</b>	<b>Three-dimensional Simulations</b>	<b>93</b>
4.1	Motivation . . . . .	93
4.2	Simulation Parameters . . . . .	93
4.2.1	Three-dimensional Forcing . . . . .	93
4.3	Structural Development of the Three-dimensional Wake . . . . .	94
4.3.1	Effect of Disturbance Wavelength . . . . .	98
4.3.2	Effect of Disturbance Phase . . . . .	105
4.3.3	Effect of Reynolds Number . . . . .	106
4.4	Growth of the Mean Flow . . . . .	115
4.4.1	Effect of Disturbance Wavelength . . . . .	115
4.4.2	Effect of Disturbance Phasing . . . . .	117
4.4.3	Effect of Reynolds Number . . . . .	128
4.5	Comparison with Experiment . . . . .	131
4.6	Selected Spectra, Mean Profiles, and Turbulence Statistics . . . . .	132
<b>5</b>	<b>Three-dimensional Topological Description</b>	<b>153</b>
5.1	Topological Method . . . . .	153
5.2	Effect of Initial Conditions . . . . .	158
5.3	Effect of Reynolds Number . . . . .	173
5.4	Time Evolution in Invariant Space . . . . .	173
5.5	Rate-of-Strain Distribution and Vorticity-Strain Alignment . . . . .	180
<b>6</b>	<b>Conclusions</b>	<b>182</b>
6.1	Numerical Method . . . . .	182
6.2	The Incompressible Plane Wake . . . . .	183
6.2.1	Physical Development . . . . .	183
6.2.2	Topological Development . . . . .	184
6.3	Future Work . . . . .	185
<b>A</b>	<b>Classical Similarity Theory</b>	<b>187</b>





A.1	Preliminaries . . . . .	187
A.1.1	Energy Transport Equation . . . . .	187
A.2	Scales of Motion . . . . .	190
A.2.1	The Taylor Microscale . . . . .	191
A.2.2	The Kolmogorov Microscale . . . . .	192
A.3	Evolution of the Spatially Evolving Incompressible Plane Wake . . . .	192
A.3.1	Momentum Balance . . . . .	192
A.3.2	Mean Kinetic Energy . . . . .	195
A.4	Evolution of the Temporally Evolving Incompressible Plane Wake . .	197
A.4.1	Momentum Balance . . . . .	197
A.4.2	Mean Kinetic Energy . . . . .	198
<b>B</b>	<b>Linear Stability Theory</b>	<b>200</b>
B.1	Mean Flow . . . . .	200
B.2	Linearized Disturbance Equations . . . . .	201
B.3	Solution of the Linear Equations . . . . .	203
<b>C</b>	<b>Aliasing and Alias Control</b>	<b>206</b>
C.1	Discrete Fourier Transforms and Aliasing . . . . .	206
C.2	Dealiasing using Truncation . . . . .	208
C.3	Dealiasing using Phase Shifts . . . . .	209
C.4	Multidimensional Dealiasing . . . . .	210
<b>D</b>	<b>Topological Classification</b>	<b>213</b>
D.1	Local Flow Trajectories . . . . .	214
D.2	Eigenvalues . . . . .	215
D.3	Incompressible Flows . . . . .	217
D.4	Joint Pdf's of Invariants . . . . .	219
D.5	Enstrophy Density, Dissipation, and Vortex Stretching . . . . .	219
<b>E</b>	<b>Invariant Space Pdf's for Selected Datasets</b>	<b>221</b>
<b>F</b>	<b>Turbulence Statistics for Selected Datasets</b>	<b>258</b>



<b>G Wakes with an Oblique Fundamental</b>	<b>268</b>
<b>H Summary of Simulations</b>	<b>278</b>
<b>Bibliography</b>	<b>287</b>



# List of Tables

2.1	Code Structure . . . . .	34
H.1	Summary of Two-dimensional Simulations . . . . .	278
H.2	Summary of Three-dimensional Simulations . . . . .	281



# List of Figures

2.1	Numerical domains . . . . .	20
2.2	Mean flow parameters . . . . .	22
2.3	Stability neutral curve. . . . .	31
2.4	Two-dimensional disturbance phasing . . . . .	38
2.5	Disturbance phase for three-dimensional fundamental. . . . .	39
2.6	Disturbance phase for three-dimensional subharmonic. . . . .	40
2.7	Halfwidth vs. time for $Re_b = 35$ diffusing parallel wake. . . . .	43
2.8	Vorticity thickness vs. time for $Re_\theta = 50$ diffusing parallel mixing layer. . . . .	43
2.9	Centerline velocity defect and total $x_2$ momentum vs. time for $Re_b =$ 35 diffusing parallel wake. . . . .	44
2.10	Magnitude of two-dimensional fundamental disturbance vs. time for parallel wake. . . . .	46
2.11	Comparison of direct numerical simulations of $346(60)_{0xx}^{x0x}$ wakes using the SMR code and the present code. . . . .	47
2.12	Comparison of wake halfwidth versus time for direct numerical simu- lation of $346(60)_{0xx}^{x0x}$ wakes using present code and SMR code . . . . .	48
2.13	Behavior of relative vorticity magnitude near the matching boundaries. $Re_b = 35$ wake. . . . .	50
2.14	Behavior of vorticity magnitude near the matching boundaries. $Re_b =$ 346 wake. . . . .	50
3.1	Two-dimensional disturbance phasing . . . . .	53
3.2	Iso-vorticity contours for $346(0)_{0xx}^{xxx}$ wake at various times. . . . .	54
3.3	Mean and fundamental mode energies versus time for $346(0)_{0xx}^{xxx}$ wake. . . . .	55





3.4	Iso-vorticity contours for $346(0)_{00x}^{xxx}$ wake at various times. . . . .	59
3.5	Iso-vorticity contours for $346(0)_{0\frac{\pi}{4}x}^{xx}$ wake at various times. . . . .	62
3.6	Iso-vorticity contours for $346(0)_{0\frac{\pi}{2}x}^{xx}$ wake at various times. . . . .	65
3.7	Mean, fundamental, and subharmonic mode energies versus time for $346(0)_{00x}^{xxx}$ wake. . . . .	66
3.8	Mean, fundamental, and subharmonic mode energies versus time for $346(0)_{0\frac{\pi}{4}x}^{xx}$ wake. . . . .	66
3.9	Mean, fundamental, and subharmonic mode energies versus time for $346(0)_{0\frac{\pi}{2}x}^{xx}$ wake. . . . .	67
3.10	Iso-vorticity contours for $346(0)_{000}^{xxx}$ wake at various times. . . . .	71
3.11	Mean, fundamental, subharmonic, and sub-subharmonic mode energies versus time for $346(0)_{000}^{xxx}$ wake. . . . .	72
3.12	Iso-vorticity contours for $\langle ? \rangle (0)_{0xx}^{xxx}$ wakes. . . . .	74
3.13	Iso-vorticity contours for $\langle ? \rangle (0)_{00x}^{xxx}$ wakes. . . . .	75
3.14	Iso-vorticity contours for $\langle ? \rangle (0)_{0\frac{\pi}{4}x}^{xx}$ wakes. . . . .	76
3.15	Iso-vorticity contours for $\langle ? \rangle (0)_{0\frac{\pi}{2}x}^{xx}$ wakes. . . . .	77
3.16	Comparison of iso-ensrophy density and iso-scalar contours for $1384(0)_{0(?)x}^{xxx}$ wakes. . . . .	80
3.17	Square of wake halfwidth versus time for $Re = 346$ wakes with various disturbance wavelengths. . . . .	82
3.18	Square of wake halfwidth versus time for $346(0)_{0(?)x}^{xxx}$ wakes. . . . .	85
3.19	Square of wake halfwidth versus time for $\langle ? \rangle (0)_{0xx}^{xxx}$ wakes. . . . .	87
3.20	Square of wake halfwidth versus time for $\langle ? \rangle (0)_{00x}^{xx}$ wakes. . . . .	88
3.21	Square of wake halfwidth versus time for $\langle ? \rangle (0)_{0\frac{\pi}{4}x}^{xx}$ wakes. . . . .	89
3.22	Square of wake halfwidth versus time for $\langle ? \rangle (0)_{0\frac{\pi}{2}x}^{xx}$ wakes. . . . .	90
3.23	Comparison of mean velocity profiles for $(692)(0)_{00x}^{xxx}$ and $\langle 1384 \rangle (0)_{00x}^{xxx}$ wakes. . . . .	91
4.1	Iso-ensrophy density contour for $346(60)_{0xx}^{x0x}$ wake at various times. . . . .	97
4.2	Iso-ensrophy density contour for $346(60)_{0xx}^{0xx}$ wake. . . . .	98
4.3	Iso-ensrophy density contour for $346(60)_{00x}^{0xx}$ wake. . . . .	100



4.4	Comparison of mean, two-dimensional fundamental, and two-dimensional subharmonic mode energies versus time for $346(0)_{00x}^{xxx}$ and $346(0)_{00x}^{0xx}$ wakes. . . . .	101
4.5	Iso-entrophy density contour for $346(60)_{00x}^{x0x}$ wake. . . . .	102
4.6	Comparison of mean, two-dimensional fundamental, and two-dimensional subharmonic mode energies versus time for $346(0)_{00x}^{xxx}$ and $346(0)_{00x}^{x0x}$ wakes. . . . .	103
4.7	Iso-entrophy density contour for $346(60)_{000}^{x00}$ wake. . . . .	103
4.8	Mean, two-dimensional fundamental, two-dimensional subharmonic, and two-dimensional sub-subharmonic mode energies versus time for $346(0)_{000}^{x00}$ wake. . . . .	104
4.9	Iso-entrophy density contour for $346(60)_{0xx}^{x\frac{\pi}{2}x}$ wake. . . . .	105
4.10	Iso-entrophy density contour for $346(60)_{0xx}^{\frac{\pi}{2}xx}$ wake. . . . .	106
4.11	Iso-entrophy density contour for $346(60)_{00x}^{\frac{\pi}{2}xx}$ wake. . . . .	107
4.12	Iso-entrophy density contour for $346(60)_{00x}^{x\frac{\pi}{2}x}$ wake. . . . .	108
4.13	Iso-entrophy density contours for $(?)(60)_{0xx}^{x0x}$ wakes at various Reynolds numbers. . . . .	111
4.14	Iso-entrophy density contour for $1384(60)_{00x}^{0xx}$ wake. . . . .	112
4.15	Streamwise energy spectra for $346(60)_{0xx}^{x0x}$ and $2768(60)_{0xx}^{x0x}$ wakes. . . . .	114
4.16	Square of wake halfwidth versus time for $Re = 346$ wakes with various combinations of initial disturbance wavelengths. . . . .	116
4.17	Square of wake halfwidth versus time for $346(60)_{0xx}^{(?)xx}$ wakes. . . . .	118
4.18	Square of wake halfwidth versus time for $346(60)_{00x}^{(?)xx}$ wakes. . . . .	119
4.19	Square of wake halfwidth versus time for $346(60)_{0\frac{\pi}{2}x}^{(?)xx}$ wakes. . . . .	120
4.20	Square of wake halfwidth versus time for $346(60)_{0\frac{\pi}{2}x}^{(?)xx}$ wakes. . . . .	121
4.21	Square of wake halfwidth versus time for $346(60)_{0xx}^{x(?)x}$ wakes. . . . .	123
4.22	Mean velocity profiles for $346(60)_{0xx}^{x0x}$ and $346(60)_{0xx}^{x\frac{\pi}{4}x}$ wakes. . . . .	124
4.23	Square of wake halfwidth versus time for $346(60)_{00x}^{x(?)x}$ wakes. . . . .	125
4.24	Square of wake halfwidth versus time for $346(60)_{0\frac{\pi}{2}x}^{x(?)x}$ wakes. . . . .	126
4.25	Square of wake halfwidth versus time for $346(60)_{0\frac{\pi}{2}x}^{x(?)x}$ wakes. . . . .	127



4.26	Square of normalized direct wake halfwidth versus normalized time for $\langle ? \rangle (60)_{0xx}^{x0x}$ wakes. . . . .	129
4.27	Square of normalized wake integral halfwidth versus normalized time for $\langle ? \rangle (60)_{0xx}^{x0x}$ wakes. . . . .	130
4.28	Comparison of halfwidth versus downstream distance for 119(60) $_{0xx}^{x0x}$ wake and experiments of Corke, Krull, & Ghassemi [14] . . . . .	131
4.29	Rescaled streamwise energy spectra for 346(60) $_{0xx}^{x0x}$ and 2768(60) $_{0xx}^{x0x}$ wakes. . . . .	133
4.30	Mean streamwise velocity profiles for $\langle ? \rangle (60)_{0xx}^{x0x}$ wakes. $t \sim 100.0$ . . . . .	135
4.31	Second order velocity correlations for $\langle ? \rangle (60)_{0xx}^{x0x}$ wakes. $t \sim 100.0$ . . . . .	137
4.32	Normalized long time mean streamwise velocity defect profiles for $\langle ? \rangle (60)_{0xx}^{x0x}$ wakes. $t \sim 100.0$ . . . . .	139
4.33	Normalized long time second order velocity correlations for $\langle ? \rangle (60)_{0xx}^{x0x}$ wakes. $t \sim 100.0$ . . . . .	141
4.34	Mean streamwise velocity profiles for $\langle ? \rangle (60)_{0xx}^{x0x}$ wakes. $t \sim 200.0$ . . . . .	143
4.35	Second order velocity correlations for $\langle ? \rangle (60)_{0xx}^{x0x}$ wakes. $t \sim 200.0$ . . . . .	145
4.36	Normalized long time mean streamwise velocity defect profiles for $\langle ? \rangle (60)_{0xx}^{x0x}$ wakes. $t \sim 200.0$ . . . . .	147
4.37	Normalized long time second order velocity correlations for $\langle ? \rangle (60)_{0xx}^{x0x}$ wakes. $t \sim 200.0$ . . . . .	149
5.1	Invariant Space for Incompressible Flows . . . . .	155
5.2	Contour plots of joint pdf of $Q$ vs. $R$ for $Re_b = 346$ wakes with various initial disturbance wavelengths . . . . .	161
5.3	Contour plots of joint pdf of $Q_s$ vs. $R_s$ for $Re_b = 346$ wakes with various initial disturbance wavelengths . . . . .	165
5.4	Enlarged plot of pdf of $Q_s$ vs. $R_s$ for 346(60) $_{0xx}^{x0x}$ . . . . .	166
5.5	Contour plots of joint pdf of $-Q_s$ vs. $Q_w$ for $Re_b = 346$ wakes with various initial disturbance wavelengths . . . . .	169
5.6	Contour plots of joint pdf of $Q_w$ vs. $R_s - R$ for 346(60) $_{000}^{x00}$ . . . . .	170
5.7	Contour plots of joint pdf of $Q$ vs. $R$ for $\langle ? \rangle (60)_{0xx}^{x0x}$ wakes. . . . .	172



5.8	Time evolution of contour plots of joint pdf of $Q$ , vs. $R$ , for $346(60)_{0xx}^{x0x}$ wake. . . . .	175
5.9	Pdf of normalized rates-of-strain for $346(60)_{0xx}^{x0x}$ wake. . . . .	176
5.10	Pdf of normalized rates-of-strain for $1384(60)_{0xx}^{x0x}$ wake. . . . .	177
5.11	Pdf of cosine of angle between vorticity vector and principal strain rate directions for $346(60)_{0xx}^{x0x}$ wake. . . . .	178
5.12	Pdf of cosine of angle between vorticity vector and principal strain rate directions for $1384(60)_{0xx}^{x0x}$ wake. . . . .	179
A.1	Schematic of spatially evolving wake. Control volume for momentum balance. . . . .	193
A.2	Schematic of spatially evolving wake. Control volume for energy balance. . . . .	194
C.1	Example of aliasing . . . . .	208
D.1	Invariant Space for Incompressible Flows . . . . .	218
E.1	Contour plots of joint pdf of $Q$ vs. $R$ for $Re_b = 346$ wakes with various initial disturbance wavelengths . . . . .	224
E.2	Contour plots of joint pdf of $Q$ , vs. $R$ , for $Re_b = 346$ wakes with various initial disturbance wavelengths . . . . .	227
E.3	Contour plots of joint pdf of $-Q$ , vs. $Q_w$ for $Re_b = 346$ wakes with various initial disturbance wavelengths . . . . .	230
E.4	Contour plots of joint pdf of $Q_w$ vs. $R$ , $-R$ for $Re_b = 346$ wakes with various initial disturbance wavelengths . . . . .	233
E.5	Contour plots of joint pdf of $Q$ vs. $R$ for $\langle ? \rangle (60)_{0xx}^{x0x}$ wakes. . . . .	235
E.6	Contour plots of joint pdf of $Q$ , vs. $R$ , for $\langle ? \rangle (60)_{0xx}^{x0x}$ wakes . . . . .	237
E.7	Contour plots of joint pdf of $-Q$ , vs. $Q_w$ for $\langle ? \rangle (60)_{0xx}^{x0x}$ wakes . . . . .	239
E.8	Contour plots of joint pdf of $Q_w$ vs. $R$ , $-R$ for $\langle ? \rangle (60)_{0xx}^{x0x}$ wakes . . . . .	241
E.9	Time evolution of contour plots of joint pdf of $Q$ vs. $R$ for $346(60)_{0xx}^{x0x}$ wake. . . . .	243
E.10	Time evolution of contour plots of joint pdf of $Q$ , vs. $R$ , for $346(60)_{0xx}^{x0x}$ wake. . . . .	245





E.11	Time evolution of contour plots of joint pdf of $-Q$ , vs. $Q_w$ for $346(60)_{0xx}^{x0x}$ wake. . . . .	247
E.12	Time evolution of contour plots of joint pdf of $Q_w$ vs. $R_s - R$ for $346(60)_{0xx}^{x0x}$ wake. . . . .	249
E.13	Time evolution of contour plots of joint pdf of $Q$ vs. $R$ for $1384(60)_{0xx}^{x0x}$ wake. . . . .	251
E.14	Time evolution of contour plots of joint pdf of $Q$ , vs. $R_s$ for $1384(60)_{0xx}^{x0x}$ wake. . . . .	253
E.15	Time evolution of contour plots of joint pdf of $-Q$ , vs. $Q_w$ for $1384(60)_{0xx}^{x0x}$ wake. . . . .	255
E.16	Time evolution of contour plots of joint pdf of $Q_w$ vs. $R_s - R$ for $1384(60)_{0xx}^{x0x}$ wake. . . . .	257
F.1	Mean velocity profiles and second order turbulence profiles for for $Re_b = 346$ wakes with various initial disturbance wavelengths . . . . .	261
F.2	Mean velocity profiles and second order turbulence profiles for $(?)(60)_{0xx}^{x0x}$ wakes. . . . .	263
F.3	Mean velocity profiles and second order turbulence profiles for $346(60)_{0xx}^{x0x}$ wake. . . . .	265
F.4	Mean velocity profiles and second order turbulence profiles for $1384(60)_{0xx}^{x0x}$ wake. . . . .	267
G.1	Iso-entrrophy density contour for $5^\circ$ oblique fundamental plus two-dimensional subharmonic. $Re_b = 180$ . . . . .	270
G.2	Iso-entrrophy density contour for $15^\circ$ oblique fundamental plus two-dimensional subharmonic. $Re_b = 180$ . . . . .	271
G.3	Iso-entrrophy density contour for $30^\circ$ oblique fundamental plus two-dimensional subharmonic. $Re_b = 180$ . . . . .	272
G.4	Spanwise vorticity at various spanwise locations for $5^\circ$ oblique fundamental plus two-dimensional subharmonic. $Re_b = 180$ . . . . .	273
G.5	Top view of iso-entrrophy density contour for $30^\circ$ oblique fundamental plus two-dimensional subharmonic. $Re_b = 180$ . . . . .	274



G.6	Iso-ensrophy density contour for $5^\circ$ oblique fundamental plus two-dimensional subharmonic. $Re_b = 1800$ . . . . .	275
G.7	Iso-ensrophy density contour for $30^\circ$ oblique fundamental plus two-dimensional subharmonic. $Re_b = 1800$ . . . . .	276



# Chapter 1

## Introduction

### 1.1 Background

This section presents a review of results from previous theoretical, experimental, and computational studies of incompressible plane wakes. A brief review of numerical simulations of free shear flows is also presented.

#### 1.1.1 The Incompressible Wake

Significant progress has been made in understanding the primary stages of transition in incompressible wakes behind slender bodies. There exists substantial theoretical, experimental, and computational work describing the initial development of the initial wake instability: the growth of two-dimensional Kelvin-Helmholtz waves into the well known Kármán vortex street.

Sato & Kuriki [39] performed a now classic set of experiments on both natural and forced wakes behind a thin flat plate. They identified three distinct developmental regions in the wake: the linear region (also known as the Kelvin-Helmholtz instability region), where small amplitude disturbances grow exponentially; the nonlinear growth region, where the fundamental two-dimensional mode saturates and the wake rolls up into the Kármán vortex street; and the three-dimensional region, where strong three-dimensional motions appear. They found that growth rates and mode shapes of the

disturbances in the linear region were well predicted by linear stability analysis of a Gaussian mean base flow. Past the short linear region, however, they observed that the evolution of the wake deviates substantially from the predictions of linear theory. The amplitude of the two-dimensional fundamental disturbance saturated, and then decreased, higher harmonics of the two-dimensional fundamental appeared in the wake, and the mean velocity and wake width changed at a rate which was far more rapid than could be accounted for by linear theory.

Ko, Kubota, & Lees [22] performed a two-dimensional finite amplitude, single frequency disturbance analysis of the plane wake to explain the results reported by Sato & Kuriki for the nonlinear region. By applying an integral method to a boundary layer approximation of the Navier-Stokes equations, they were able to study the energy balance between the mean flow and the finite amplitude disturbances. They related the observed behavior of the wake disturbance amplitude and the rapid variations in the mean flow to energy transfer between the disturbance and the mean flow via the Reynolds stresses. Their analysis also emphasized the importance of binary interactions between disturbance modes, which are the source of higher harmonics in the wake.

These studies, plus others such as those by Sato & Saito [40], who extended the work of Sato & Kuriki [39] by examining the effect of multiple frequency forcing, and Mattingly & Criminale [26], who developed a disturbance theory which included the effects of the non-parallel nature of the near-field wake, give a fairly comprehensive picture of the early stages of wake instability. Understanding of two-dimensional near wakes behind bluff bodies much more difficult since the initial instability is dominated by a complex mixture of large amplitude motions including flow separation dynamics, rollup of the shed shear layers, and reversed flow in the near wake (c.f. the studies of Karniadakis & Triantafyllou [20, 21]). It is reasonable to assume, however, that far downstream, away from the vicinity of the body, the dynamics of the fully developed blunt body wake should be similar to those for the wakes of slender bodies. Only the initial conditions should differ.

In contrast to the fairly complete understanding of the initial stability characteristics and early development of the plane wake, there still remain significant unresolved

issues related to the stability characteristics of the two-dimensional non-linear wake. It is these secondary stages of instability that lead to the appearance of strong three-dimensional motions in the wake.

Early experiments on the three-dimensional structure of the far wake were performed by Townsend [45]. These experiments were later extended by Grant [17], who took long-time-averaged velocity correlations in the far wake of a cylinder. Coherent three-dimensional structures, later referred to as “double-roller eddies” by Townsend [46], were inferred from these measurements. These structures were described as pairs of curved, counter-rotating vortices oriented perpendicular to the plane of the wake. Roshko [37] suggested that the time-averaged data was actually due to a superposition of vortex loops, formed by the distortion of spanwise vortices from opposite sides of the wake. Mumford [29] later used a pattern recognition technique to study the double-roller eddies, and concluded that they were often confined to one side of the wake or the other, and that they tended to appear in groups.

A set of experiments by Cimbala, Nagib, & Roshko [13] were among the first in which the existence of spanwise periodic streamwise structures in the planar far wake of a bluff body was documented. They identified the structures as hairpin vortices produced by a parametric resonance between the two-dimensional and oblique subharmonic disturbances. They regarded this secondary instability as similar to one studied by Pierrehumbert & Widnall [32] in plane mixing layers.

Flemming [16] performed an analysis of the secondary instability of the plane wake. Taking as a base flow a Gaussian mean velocity field with a two-dimensional fundamental Orr-Sommerfeld mode superimposed, Flemming obtained a Hill-type system of equations for the stability of the far wake. Numerical studies of the stability equations indicated that, for sufficiently high fundamental (Orr-Sommerfeld) mode amplitudes, pairs of oblique waves at the subharmonic streamwise wavelength were unstable. The angle of the most unstable disturbance was found to depend on the wake Reynolds number, but unstable disturbances were found to exist at angles of between  $45^\circ$  and  $70^\circ$  with respect to the spanwise direction.

Corke, Krull, & Ghassemi [14], using the results of Flemming, performed a study of the mechanisms for the secondary growth of three dimensional modes in the far

wake of an airfoil. They focused on a parametric resonance mechanism between the fundamental two dimensional Kármán instability mode and pairs of phase locked oblique disturbances at the subharmonic wavelength that were oriented  $60^\circ$  and  $73^\circ$  with respect to the spanwise direction. These resonances were expected from the form of the stability equations developed by Flemming. They found that, at least under certain conditions, a resonance develops where the two dimensional fundamental mode and the subharmonic oblique modes exchange energy over several long period cycles.

Williamson [52] and Williamson & Prasad [53, 54, 55] suggest an alternate mechanism for the development of strong three-dimensional motions. Recent experiments they performed indicate that the oblique waves observed in the far wake of a cylinder by Cimbala *et al.* are due to an interaction between oblique shedding waves produced by the wake generator and two-dimensional subharmonic waves which arise from the inherent hydrodynamic instability of the mean flow in the far wake.

These differing theories on the source of three-dimensional motions — one which ascribes the three-dimensional motions in the far wake to the growth of pairs of highly oblique subharmonic waves which exist from early in the flow, and one which ascribes the three-dimensional motions in the far wake as being composed of oblique waves generated from an interaction between asymmetric fundamental vortex shedding and long wavelength two-dimensional motions — reinforce the need to examine the effect of initial conditions on the development of the wake. Both theories suggest the importance of studying the dynamics of highly oblique disturbances in plane wakes.

Wynanski, Champagne, & Marasli [58] conducted an experimental study of small deficit turbulent wakes created using a variety of wake generators. The generators were carefully chosen to have the same drag, and therefore to create wakes with the same momentum thickness and momentum thickness Reynolds number. They found that the normalized characteristic velocity and length scales as well as the normalized longitudinal turbulence intensity depended on the generator used, and hence depended on the initial conditions created by that generator. The shape of the mean velocity profile, however, was found to be independent of initial conditions. They attributed the lack of universality in part to the interaction between the sinuous (cross-stream component of velocity antisymmetric about the wake centerline) and



varicose (cross-stream component of velocity symmetric about the wake centerline) instability modes in the far wake. A common interpretation of classical similarity theory, which characterizes the turbulent wake through a single parameter — the momentum deficit (see appendix A) — holds that the turbulent wake should have a universal growth rate, independent of initial conditions. In fact, classical theory addresses only the late time growth laws for the turbulent wake, not the actual rates. The implication of the results of Wygnanski *et al.* is that the rate of development of the turbulent far field of the plane wake is indeed dependent on parameters related to the initial conditions, and therefore not universal.

In addition to the primarily experimental and theoretical studies discussed above, there have been a large number of computational studies of free shear flows.

Mixing layer simulations by Riley, Mourad, Moser & Rogers [33] indicates that the large scale structures that develop in an incompressible mixing layer are strongly dependent on the phase angle between a two-dimensional fundamental disturbance and a pair of oblique disturbances. They found that the existence of strong vorticity in the region between spanwise rollers at late times required the presence of streamwise vorticity in the same region from early on in the development of the layer. They determined that the intense streamwise vorticity was produced by stretching of the early vorticity by the strain field induced by the large structures.

Moser & Rogers [27] and Rogers & Moser [35, 36] conducted a comprehensive numerical study of a temporally evolving incompressible plane mixing layer started from “clean” initial conditions (the initial conditions consisted of a mean flow plus a small number of low wavenumber disturbances). They found that most of the sets of initial conditions they studied led to the development of very intense streamwise vortical structures. Those mixing layers that did not develop these strong streamwise structures during the initial period of growth took much longer to develop any significant three-dimensionality. Because of this they concluded that the development of the strong streamwise structures were a key step in the development of three-dimensionality and the eventual transition to turbulence.

Chen, Cantwell, & Mansour [9, 10] carried out a direct numerical simulation of a temporally evolving compressible plane wake. They found that linear theory accurately predicted the early growth of the plane wake for freestream Mach numbers between  $M = 0.01$  and  $M = 3.0$ . They also found that the development of three-dimensionality in the compressible wake was significantly affected by the relative phase of the initial disturbance.

Maekawa, Mansour, & Buell [24] performed direct numerical simulations of a set of two-dimensional spatially evolving incompressible plane wakes. They found that wakes initiated with a two-dimensional fundamental and a two-dimensional subharmonic disturbance initially form a Kármán vortex street at the fundamental wavelength. Once the fundamental has saturated, the subharmonic disturbance begins to become significant and the vortices in the vortex street combine, forming pairs of both like and opposite signed vortices. A wake forced with a combination of a fundamental and random noise showed similar behavior.

Moser & Rogers [28] performed a direct numerical simulation of a pair of temporally evolving incompressible plane wakes started from pairs of temporally evolving turbulent boundary layers which had been previously computed by Spalart [43]. The first wake was initiated with only the computed boundary layers. The second was initiated with modified boundary layers which had all the two-dimensional modes increased by a factor of 20 in an attempt to simulate the receptivity of the plane wake to two-dimensional disturbances which normally would occur at the wake generator. The high amplification of the two-dimensional modes, which amounted to a 13 fold increase in total disturbance energy, was found to be necessary to spur the development of the large scale two-dimensional structures that were expected to appear.

The first turbulent wake case computed by Moser & Rogers showed eventual self-similar ( $t^{1/2}$ ) growth and energy spectra with a short region of  $k^{-5/3}$  slope. However, the late time growth rate was found to be well below the range of rates measured by Wygnanski *et al.* [58]. The second wake, with the enhanced two-dimensional disturbance field, also showed a region of  $k^{-5/3}$  spectra, but never developed the expected self-similar  $t^{1/2}$  growth pattern for any extended period of time. The forced wake also had a growth rate well above the Wygnanski range.

### 1.1.2 Topology of Fine Scale Motions

One of the major unsolved problems of fluid mechanics is how to model turbulent flows. Model development has been hindered by the fact that different types of flows require different models since the large scale features of the turbulence are highly flow dependent. An attempt to get around this problem is the technique of large eddy simulation, which splits the flow into the mean flow and large scale turbulence, which is simulated numerically, and the fine scale turbulence, which is modeled. The basic premise of the technique is that the fine scale turbulence has features which are flow independent and therefore more amenable to modeling than the larger scales.

The typical approach to developing a model for the fine scale turbulence is to assume statistical isotropy of the turbulent motions at high wavenumbers — therefore relying on the assumption that the spectral characteristics of the turbulence are universal. A number of recent studies of the topology of the fine scale velocity fields of a variety of turbulent flows have revealed another potential path to developing a turbulence model for use in large eddy simulations. They have found what appear to be universal features in the geometric properties of fine scale turbulence in physical space. The existence of such universal features could potentially lead to models for fine scale turbulence based on the physical (local) rather than the spectral (global) properties of the turbulence.

Ashurst, Kerstein, Kerr & Gibson [2] studied direct numerical simulations of incompressible forced isotropic turbulence and homogeneous sheared turbulence. They found that the intermediate principal strain-rate tended to be positive throughout the flow. Furthermore, data conditioned on high levels of local dissipation of kinetic energy had a uniformly positive intermediate strain-rate, with strain rates in the ratio of approximately  $3 : 1 : -4$ . They also found that the highly dissipating motions tended to have the vorticity vector aligned with the intermediate principal strain-rate direction.

More recent studies of incompressible forced isotropic turbulence by Vincent & Meneguzzi [50, 51] and Ruetsch & Maxey [38] indicate that the small scale structures take the form of vortex tubes. The highest rates-of-strain, and therefore highest rates of dissipation, were found to occur in the vicinity of, but outside the cores of, these

vortex tubes. Vincent & Meneguzzi again found that the vorticity in these high dissipation regions was aligned with the intermediate principal strain-rate. Furthermore they found that this result held before the vortex tubes had developed.

Chen *et al.* [11] studied a set of direct numerical simulations of transitional compressible and incompressible mixing layers. They used a new data display method based on the classification of local flow topologies using the techniques outlined by Chong, Perry & Cantwell [12] (see appendix D). The method allows for simple and straightforward study of global trends in the topology of the fine scales and correlations between physical and topological features. As in the other studies, they found that the intermediate principal rate-of-strain tended to be positive, and that the trend became stronger as the data was conditioned on higher rate of dissipation. They also found that regions of high dissipation tended to be associated with similarly high enstrophy density. Sondergaard *et al.* [41], Soria, Sondergaard & Cantwell [42] and Blackburn, Mansour & Cantwell [3] extended the study of Chen *et al.* to include data from simulations of compressible and incompressible wakes, a turbulent incompressible mixing layer, and incompressible channel flow respectively. Again the same general topological features were observed.

Finally, Tsinober, Kit & Dracos [47] performed an experimental study of the alignment of strain and vorticity in both grid-generated and boundary layer turbulence. They observed a tendency for the vorticity vector to align with the intermediate principal rate-of-strain in agreement with the previous studies of numerical simulations.

Attempts have been made to explain these observations. Jiménez [19] suggested a kinematic model for the alignment of the vorticity and strain using the stretched Burgers' vortex as an example. Though the model described a vortical flow in which the observed alignment occurred, there was no attempt to explain the evolution of such structures in a real flow. Cantwell [5] studied a restricted Euler equation, first studied by Vieillefosse [48, 49], in which viscous terms and mixed second derivatives of the pressure had been dropped. The resulting closed-form solution for the evolution of the velocity gradients reproduced the tendency for the strain-rates to evolve to a state with a positive intermediate principal rate-of-strain. Cantwell [6] later developed an intermediate asymptotic model for the case where the viscous terms and mixed

derivatives of the pressure were non-zero. This model helped to explain the structure of the invariant pdfs in the mixing layer data examined by Soria *et al.*

### 1.1.3 Goals of This Study

In light of the studies discussed above, the following questions arise:

- Is the parametric resonance model proposed by Flemming and Corke *et al.* for the development of three-dimensionality in the far wake an appropriate one? If so:
- How do the initial conditions affect the development of three-dimensionality in the incompressible plane wake?
- How do the initial conditions affect the mean flow and structure of the turbulence in the far wake?
- How do the initial conditions affect the growth rate and mean properties of the turbulence in the far wake?

The intent of this study is to begin to address these questions.

### 1.1.4 Direct Numerical Simulation of Free Shear Flows

The basic tool used in this study is direct numerical simulation. Here the term “direct” indicates that there is no attempt to model unresolved scales in the simulation. All of the scales in the flow which contain significant amounts of energy are numerically resolved and evolve as solutions to the full Navier-Stokes equations.

The major shortcoming of numerical simulation is the limitation on resolution. A numerical simulation is restricted by the size and speed of the computational hardware used. For a given simulation on a given machine, there is a fixed range of scales which can be reasonably computed. For the time being at least, this means that flows studied by numerical methods in general, and direct numerical methods in particular, are either limited to relatively small flow domains or to Reynolds numbers that are quite low compared to those obtainable in laboratory experiments.

The size of the flow domain which can be represented numerically is also limited by the computational resources available. This limitation can have an impact on the development of the computed flow. While this constraint also appears in laboratory experiments (where walls, boundary layers, and limited facility length can affect the flow), it is typically less severe in experiments. Because of these facts, care must be taken when attempting to generalize the results of numerical studies.

To maximize the range of computed flow scales, a temporal formulation has been used in the simulations performed for this study. A temporal simulation may be thought of as approximating the evolution of a representative set of structures in the physically realizable spatially evolving flow as they convect downstream. In the case of the wake, a temporal formulation approximates the view an observer that was convecting downstream with the freestream (or alternately a fixed observer that has been passed by the wake generator) would have of the evolution of the flow structures. In a temporal formulation, the roles of time and the downstream coordinate direction are swapped with respect to the corresponding spatial formulation. Time in the temporal formulations becomes the measure of the level of development of the flow, in place of downstream distance for the spatial formulation. Variations in the flow at different streamwise coordinates at a fixed time in the temporal formulation are analogous to variations with time at a fixed point in the spatial formulation.

Using a temporal rather than a spatial formulation has the advantage of allowing the resolution of smaller scales for a given set of computational resources. A spatial formulation requires the resolution of both a large flow domain and the fine scale motions. This represents a potentially very wide range of scales, with correspondingly large computational requirements. Using a temporal formulation allows the range of resolved scales to be reduced by restricting the largest resolved scales in the flow to at most a few representative large structures instead of the full domain. By reducing the computational requirements associated with the large scales, more of the available resources may be focused on resolving the small scales.

One assumption inherent in any temporal formulation is that the streamwise rate of change of a spatially evolving flow is small at the scale of the structures being studied. When this assumption holds, the mean flow may be approximated as being

locally parallel without significantly affecting the development of the structures of interest. This assumption is generally a very poor one very near the origin in any spatially developing free shear flow. It can, however, be quite reasonable away from that region if the growth of the far field flow is sufficiently slow. For wakes, in which the far downstream flow grows as  $x^{\frac{1}{2}}$  (where  $x$  is the downstream distance) the assumption of parallel mean flow is quite good. For mixing layers, in which the far downstream flow grows like  $x$ , the assumption of parallel mean flow is less valid. Under the proper conditions, however, the change in width of the mixing layer over the length of the structures being studied can be relatively small, making the temporal approximation useful.

Temporal formulations also inherently ignore the details of how disturbances are initially created in the flow. Since here we are interested in how specific disturbance modes (disturbances with specific wavelengths, angles, and phases) affect the development of the far wake, the exact details of how those specific modes are generated in a spatially evolving wake are not addressed. All of the geometric details of the wake generator are subsumed in the choice of disturbance modes and disturbance phases.

Finally, temporal formulations (and to a lesser extent spatial formulations), by limiting the computational domain to a few large structures in the flow, can confine the development of the flow in the streamwise and cross-stream directions, possibly quite severely. This artificial confinement can inhibit or prohibit the development large scale motions which might normally exist, and become dynamically significant, in a physical flow. The effects of the finite computational domain must be taken into account when interpreting the computational results, particularly in the late stages of development of the flow..

Numerical simulations in general have some special advantages in answering the type of questions asked at the end of section 1.1.1 above. The initial conditions can be very precisely controlled and the results present a complete description of the entire flow field, including physical variables that would normally be very hard to measure. This allows for unambiguous connections to be made between initial conditions and developed structures. In addition, direct numerical simulations give access to all the

physical quantities in the flow at a given instant. This allows study of quantities which are not normally available from a laboratory experiment.

The numerical technique used here to perform the simulations is known as a “pseudo-spectral” method. In a “spectral” method, the dependent variables are expanded as a sum of (usually orthogonal) basis functions. This allows the governing partial differential equations for the physical variables in the problem to be converted into a set of ordinary differential equations for the time evolution of the coefficients of the basis functions in the approximating sums. The primary benefit of such an approach is that, by expressing spatial derivatives of the basis functions in terms of the basis functions, calculation of spatial derivatives is greatly simplified. It also allows derivatives to be calculated with “spectral” accuracy. This means that the error in the representation of derivatives goes to zero exponentially as the number of functions in the basis set goes to infinity. Other approaches, such as finite difference schemes, typically have errors that go to zero algebraically.

Another benefit of spectral methods is that they lead to algorithms that are simple to implement on parallel processing computers (machines that are designed to use multiple interconnected microprocessors to work different parts of the same problem simultaneously). Larger and more complex simulations can be carried out on these parallel machines.

In what is known as a “fully” spectral method, any nonlinear terms in the governing equations are computed using convolution integrals involving the coefficients of the expansions. This is a computationally intensive process. A “pseudo”-spectral method makes use of fast transforms to convert between the physical representation of the dependent variables and the basis function expansions. This allows any nonlinear terms to be calculated in physical space using simple multiplication then re-expanded in terms of the basis functions. For large problems, the use of fast Fourier transforms makes pseudo-spectral methods significantly more efficient than fully spectral methods.



## 1.2 Outline of Present Work

The intent of the present work is to examine the effect of the choice of initial conditions on the development of the incompressible plane wake. Of particular interest is how the initial conditions relate to the development of three-dimensionality and eventual transition to turbulence in the wake. Also of interest is whether the structure of the turbulence which develops is independent of initial conditions as predicted by the usual one parameter similarity analysis of the far wake.

All of the flows that will be described here were started from a laminar base flow upon which was superimposed a small number of disturbance modes at very specific wavelengths. The disturbance modes were the most unstable eigenfunctions as predicted by linear stability theory. Understanding these very simple, “clean”, wake flows should allow for a better understanding of wakes started with more realistic initial conditions, which will contain uncontrolled disturbances.

Chapter 2 describes the numerical methodology used to perform the direct numerical simulations used in this study. A new pseudo-spectral algorithm for simulating planar shear flows with periodic freestream boundary conditions is described and tested. The method uses Fourier transforms in all three spatial directions to solve for the flow in a finite, time-varying, computational domain using velocities which are matched at the domain boundaries to known analytic solutions.

Chapter 3 presents results from a series of two-dimensional direct numerical simulations. The effect of the choice and phasing of two-dimensional disturbance modes is described. The effect of flow Reynolds number on the development is also examined.

Chapter 4 presents results from a wide series of three-dimensional direct numerical simulations of the plane incompressible wake. The effects of disturbance mode, relative disturbance phasing, and flow Reynolds number on the wake development are discussed.

Chapter 5 examines the evolution of the topology of the small scale motions for a selected subset of the three-dimensional simulations discussed in chapter 4.

Chapter 6 presents the major conclusions of this work and outlines some recommendations for future work.

Appendix A presents a brief outline of classical similarity theory as applied to incompressible plane wakes, as well a definitions of some of the turbulence measures used.

Appendix B presents a review of basic linear stability theory and the method used to generate the disturbance eigenfunctions for the computed flows.

Appendix C presents an overview of numerical aliasing and a description of the dealiasing algorithm used.

Appendix D describes in greater detail the topological methods used in chapter 5 to study the structure of the fine scale motions in the computed flows.

Appendix E presents a full set of invariant space pdfs for selected wake simulations.

Appendix F presents mean turbulence statistics for selected wake simulations.

Appendix G presents preliminary results from a set of wake simulations initiated with combinations of oblique fundamentals at various angles and two-dimensional subharmonic disturbances. This approximates the initial conditions in the experiments of Williamson and Williamson & Prasad.

Appendix H gives a listing of all the computations performed for this study along with the values of the relevant flow parameters for each simulation.

## 1.3 Summary of Results

### 1.3.1 The Two-dimensional Plane Wake

Two-dimensional simulations of the temporally evolving plane wake initiated with combinations of disturbance eigenfunctions at the fundamental, subharmonic, and sub-subharmonic wavelength indicate the following:

- The presence of a subharmonic disturbance causes the initial Kármán rollers to amalgamate and/or pair, depending on the phase relative to the fundamental. The presence of a sub-subharmonic disturbance has minimal effect on the structure or growth of the wake.
- Increasing the Reynolds number increases the intensity of the large scale structures in the flow at a given development time without having a major effect

on their overall shape. Increasing Reynolds number significantly increases the number, intensity, and duration of small scale features.

- The passive scalar and enstrophy density fields track each other well. Major differences between the enstrophy density and scalar fields only appear in regions of the flow where there has been significant cancellation of vorticity of opposite sign.

### 1.3.2 The Three-dimensional Plane Wake

#### Physical Space

Temporal simulations of the three-dimensional plane wake at various Reynolds numbers, initiated with combinations of two-dimensional and three-dimensional disturbance eigenfunctions at the fundamental, subharmonic, and sub-subharmonic wavelength at various phases indicate the following:

- The mechanism proposed by Flemming and Corke *et al.* is a legitimate route for the development of three-dimensional motions in the far wake.
- Wakes with two-dimensional and oblique disturbances at only the fundamental wavelength do not produce any significant three-dimensionality in the far wake. The addition of a two-dimensional subharmonic disturbance produces coherent three-dimensional structures of only moderate strength.
- The presence of an oblique disturbance at the subharmonic wavelength results in the development of very strong three-dimensional structures, independent of the presence or absence of disturbances other than the two-dimensional fundamental.
- The primary effect of the phase of the oblique disturbances is to determine which side of the wake develops the dominant three-dimensional structures. The phase of the two-dimensional subharmonic disturbances has a significant effect on the development of streamwise structures in the wake only in the absence

of subharmonic oblique disturbances (when the wake dynamics are primarily two-dimensional).

- As the wake Reynolds number is increased, the strength of the three-dimensional structures increases. At the highest Reynolds numbers simulated, where there is a significant volume of intense vorticity spread through the wake, the highest enstrophy density regions appear as coherent three-dimensional structures. These structures take the form of elongated vortex tubes with lengths on the order of the wake width and diameters on the order of the turbulent scales.
- Preliminary studies indicate that the mechanism proposed by Williamson & Prasad for the development of three-dimensional motions in the far wake is also legitimate so long as the shedding angle of the oblique fundamental is sufficiently high. Weakly oblique shedding does not appear to result in the strong streamwise structures that are necessary for the development of fine scales.

### Invariant Space

The simulation results have been used to study the invariants of the velocity gradient tensor. Topological analysis of the fine scale, high gradient, motions in the incompressible wakes revealed the following:

- The wakes with a three-dimensional subharmonic have both a greater quantity of and more intense high gradient motions.
- The characteristic shapes of the joint probability density functions for invariants of the incompressible plane wake are similar to those observed in the other three-dimensional flows discussed in section 1.1.2:
  - Joint pdfs of the second and third invariants of the velocity gradient tensor have a characteristic “skewed teardrop” shape, with high gradient motions tending to be of topological types stable vortex/stretching and unstable node/saddle/saddle.

- Joint pdfs of the second and third invariants of the rate-of-strain tensor indicate that the most dissipative motions are associated exclusively with an unstable node/saddle/saddle type strain topology. More moderately dissipating motions, which account for the majority of the integrated dissipation in the flow, are also very strongly associated that strain topology.
- Joint pdfs of the enstrophy density and vortex stretching indicate that highly rotational motions occur in regions where the vortex stretching is positive, even at late times when the intensity of all gradients are decreasing in the wake. In addition, regions with moderate to high rates of dissipation tend to have the vorticity vector aligned with the intermediate principal rate-of-strain direction.
- Increasing the wake Reynolds number increased the intensity of the gradients while preserving the shape of the pdfs in invariant space. In effect, the shape of the pdfs are Reynolds number invariant. In addition, changes in the phases of the initial disturbances have minimal effect on the shape of the invariant space pdfs.

# Chapter 2

## Numerical Methodology

### 2.1 Introduction

The challenge of calculating free shear flows using spectral methods has been approached using a variety of numerical schemes. The problems of interest are turbulent flows which are periodic in two directions and have vorticity which is “compact” (of finite extent) in the third direction. An early computation of such a case was performed by Orszag & Pao [30] who simulated a temporally developing momentumless wake using a pseudo-spectral method. They approximated the infinite direction in the flow by truncating to a finite domain and using sine and cosine transforms in the inhomogeneous direction, effectively imposing free slip conditions at the non-periodic boundaries of the finite computational box. A similar approach using a three-dimensional vorticity stream function formulation was taken by Mansour, Ferziger, & Reynolds [25] to compute a time-developing turbulent mixing layer using a large eddy simulation technique. The disadvantage of approaches such as these is that they fail to accurately treat the irrotational field in the infinite direction by forcing the flow to be parallel some finite distance into the freestream regions.

Cain, Reynolds, & Ferziger [4] analyzed the method of Orszag & Pao [30] and found that the size of the domain in the inhomogeneous direction can influence the computational results. To circumvent the restriction of a finite size domain, they introduced a cotangent mapping in the infinite direction which allowed the use of

Fourier spectral methods in the doubly infinite domain. This effectively moved the no-stress boundaries out to a very large distance from the rotational region, minimizing the error inherent in such an artificial boundary condition. This sort of approach has become the mainstay of numerical simulations of flows with infinite domains (i.e. Chen, Cantwell & Mansour [10], Laurien & Kleiser [23]). The disadvantage of this scheme is that it sacrifices some of the simplicities of using the Fourier transform (such as differentiation in physical space being represented by simple multiplication by a wave vector in Fourier space), resulting in greater coding complexity. Computational resolution is also wasted on regions of the flow which are free of vorticity.

Spalart, Moser, & Rogers [44] approached the problem by using a set of basis functions for their expansions that are defined on the semi-infinite interval. They used a set of Jacobi polynomials in a mapped variable to represent the vortical region, and slowly decaying exponential “extra” functions to accurately represent the potential flow far from the vortical region. This combination of quickly decaying and slowly decaying basis functions allowed them to achieve good accuracy and good (though not spectral) convergence. The drawback is that the use of Jacobi polynomials is numerically expensive as each Jacobi transform must be accomplished by quadrature. In addition, this approach, as well as the Cain mapping approach, tends to concentrate resolution very near the centerline, at the expense of resolution a small but finite distance away. This approach is well suited to mixing layers, but is inconvenient for flows for which high gradients and small scales develop away from the centerline as occurs in the wake.

The goal of the method described here is to avoid the drawbacks of the previous methods. It is based on an algorithm similar to one presented by Corral & Jiménez [15]. Fourier transform techniques, for which fast numerical transforms exist, are used to solve problems which have one infinite and two periodic directions without having to resort to nonlinear mapping of the infinite direction to a finite domain. This preserves all of the benefits of using Fourier transforms (differentiation accomplished by multiplication by a wave number, integration accomplished by division by a wave number, interpolation accomplished by multiplication by a phase factor, resolution

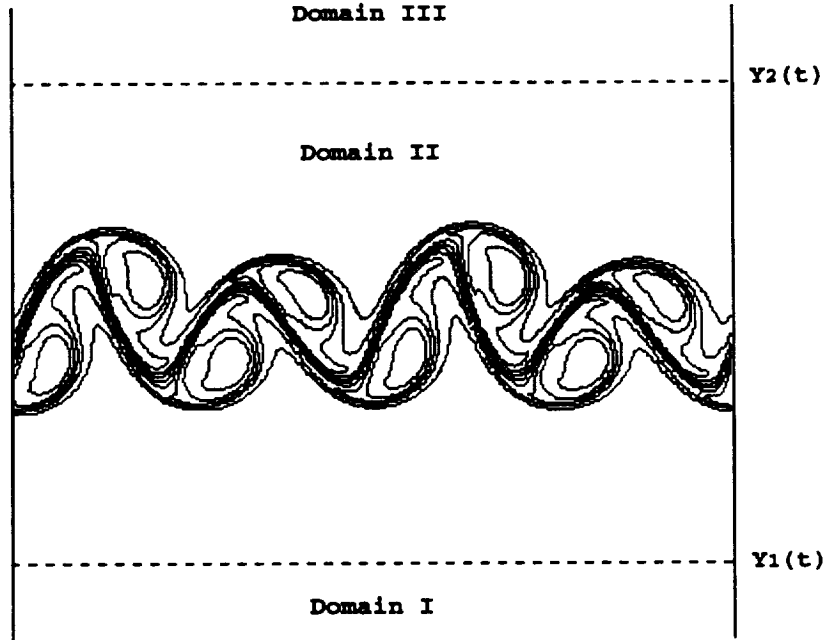


Figure 2.1: Numerical domains

changes accomplished by adding or truncating zeros in wave space) while still accurately representing the boundary conditions. It also allows for uniform resolution of the domain of interest.

## 2.2 Approach

The basic approach is to divide the flow into three domains in the non-periodic direction as shown in Figure 2.1. Domain I extends from  $-\infty$  to  $Y_1(t)$ , domain II from  $Y_1(t)$  to  $Y_2(t)$ , and domain III from  $Y_2(t)$  to  $+\infty$ . The boundaries  $Y_1(t)$  and  $Y_2(t)$  are chosen such that domain II contains all the vorticity in the flow, and domains I and III are vorticity free. This choice of  $Y_1(t)$  and  $Y_2(t)$  requires that the vorticity magnitude and vorticity gradient at the top and bottom of domain II be zero (or in practice very small). This is the case for many flows of interest, particularly at



moderate to high Reynolds number where the interface between rotational fluid and irrotational fluid is sharp. Choosing  $Y_1(t)$  and  $Y_2(t)$  in this way allows the vorticity in domain II to be treated as fully periodic. The vorticity equations governing the flow may then be solved with a pseudo-spectral technique which uses standard complex Fourier transforms in all three directions.

The inherent non-periodic nature of the flow in the cross stream direction only enters into the equations of motion through the nonlinear term of the momentum equation, which involve the velocity. The vorticity,  $\omega_j$ , is not directly affected by the images of the flow created by artificially introducing periodicity in the non-periodic direction. The vorticity is effectively zero at the nonperiodic edges of the box and can accurately be expanded using periodic functions. The velocity,  $u_j$ , which is a solution of a Poisson equation involving the vorticity as a source term, is affected by the vorticity images and must be corrected to remove the effect of the artificial periodicity. This is accomplished by adding an incompressible, irrotational component to the velocity field in domain II which matches it to analytic asymptotic solutions for the velocity in domains I and III.

**Note:** In the following discussion, all quantities have been normalized by the initial flow halfwidth  $b_0$  and the freestream velocity  $U_0$  as follows:

$$\begin{aligned} x_j &= \frac{x_j^\circ}{b_0} & u_j &= \frac{u_j^\circ}{U_0} & t &= \frac{U_0 t^\circ}{b_0} & \frac{p}{\rho} &= \frac{1}{U_0^2} \left( \frac{p}{\rho} \right)^\circ \\ \nu &= \frac{\nu^\circ}{b_0 U_0} & \kappa &= \frac{\kappa^\circ}{b_0 U_0} \equiv \frac{\nu}{Pr} \end{aligned} \quad (2.1)$$

where  $()^\circ$  are the unnormalized quantities. The initial halfwidth,  $b_0$  is defined as half the width of the initial mean velocity profile at half the maximum mean defect velocity (see figure 2.2). The mean profile is generated by averaging over  $x_1$ - $x_3$  planes.

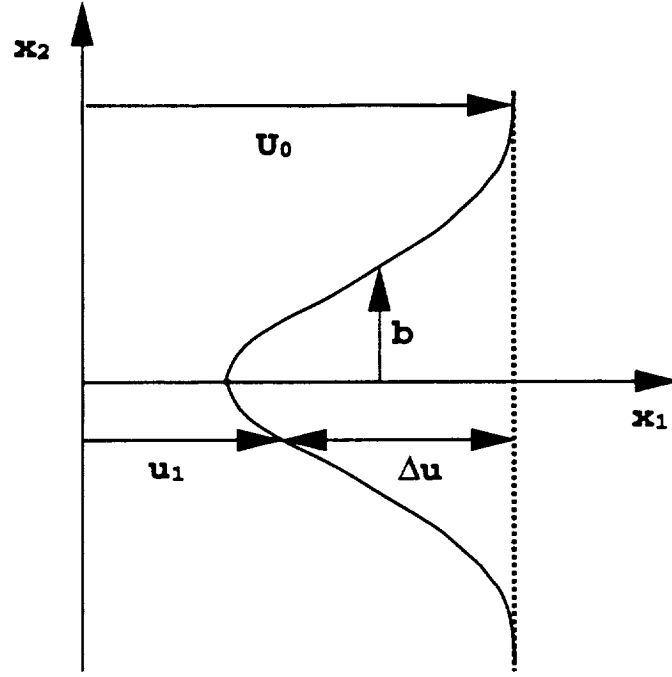


Figure 2.2: Mean flow parameters

## 2.3 Governing Equations

### 2.3.1 Vorticity Form of the Navier-Stokes Equations

The incompressible, uniform density, Navier-Stokes equations are

$$u_{j,j} = 0 \quad (2.2)$$

$$u_{j,t} + u_k u_{j,k} + \frac{p_{,j}}{\rho} = \nu u_{j,kk} \quad (2.3)$$

where  $u_j$  is the velocity in the  $x_j$  direction,  $p$  is the pressure, and  $\rho$  is the (constant) density. Here, and throughout the remainder of this dissertation, the Einstein convention

$$a_j b_j \equiv \sum_{j=1}^N a_j b_j \quad (2.4)$$

will be used to simplify the form of the equations. Here  $N$  is the number of physical dimensions in the problem.

Rewriting the nonlinear term in equation 2.3 using the identity

$$u_k u_{j,k} = \epsilon_{jkl} u_l \omega_k + \frac{(u_k u_k)_{,j}}{2} \quad (2.5)$$

$$\omega_j \equiv \epsilon_{jkl} u_{l,k} \quad (2.6)$$

yields

$$u_{j,j} = 0 \quad (2.7)$$

$$u_{j,t} + \epsilon_{jkl} u_l \omega_k + \left( \frac{p}{\rho} + \frac{u_k u_k}{2} \right)_{,j} = \nu u_{j,kk} \quad (2.8)$$

where  $\omega_j$  is the vorticity component in the  $x_j$  direction, and  $\epsilon_{jkl}$  is the alternating unit tensor

$$\epsilon_{jkl} \equiv \begin{cases} 1, & \text{if } (j, k, l) = (1, 2, 3), (3, 1, 2), \text{ or } (2, 3, 1) \\ -1, & \text{if } (j, k, l) = (3, 2, 1), (1, 3, 2), \text{ or } (2, 1, 3) \\ 0, & \text{if } j = k, j = l, \text{ or } k = l. \end{cases} \quad (2.9)$$

Taking the curl of equation 2.8 and using the identity

$$\epsilon_{jkl} \phi_{,lk} = 0 \quad (2.10)$$

where  $\phi$  is any scalar, yields the vorticity form of the Navier-Stokes equations.

$$\boxed{\omega_{j,t} + \epsilon_{jkl} \epsilon_{lmn} (u_n \omega_m)_{,k} = \nu \omega_{j,kk}} \quad (2.11)$$

$$\boxed{\omega_j = \epsilon_{jkl} u_{l,k}} \quad (2.12)$$

These equations will be solved along with the set of passive scalar equations

$$\boxed{C_{j,t} + u_k C_{j,k} = \kappa C_{j,kk}} \quad (2.13)$$

where  $C_j$  is a scalar concentration and  $\kappa$  is the scalar diffusion coefficient. Since equation 2.13 is linear and homogeneous in  $C_j$  the magnitude of  $C_j$  is arbitrary, hence normalization is irrelevant. In addition, because of the form of equation 2.13

$C_j$  may be offset by any arbitrary constant. This affords wide latitude in the choice of initial conditions for the scalar field.

### 2.3.2 Stretching Grid

In order to maximize the available resolution for a given number of grid points while at the same time keeping the vorticity at the edges of the resolved box small to satisfy the asymptotic matching condition, a growing uniform grid is used in the non-periodic  $x_2$  direction. To implement this, the coordinates in each direction are rescaled to an interval of length  $2\pi$ , the “natural” interval for Fast Fourier Transforms.

$$\xi_1 = \frac{2\pi x_1}{L_1} \quad \xi_2(t) = \frac{2\pi x_2}{L_2(t)} \quad \xi_3 = \frac{2\pi x_3}{L_3} \quad (2.14)$$

where  $L_1$  and  $L_3$  are the fixed box lengths in the periodic  $x_1$  and  $x_3$  directions respectively, and  $L_2(t) = Y_2(t) - Y_1(t)$  is the time varying box size in the aperiodic  $x_2$  direction. For convenience it will be assumed that  $Y_2(t) = -Y_1(t)$ .

Applying these coordinate transforms to equations 2.11, 2.12, and 2.13 yields

$$\omega_{j,t} - \frac{\xi_2 L_{2,t}}{L_2} \omega_{j,2} + \epsilon_{jkl} (\epsilon_{lnq} u_q \omega_n)_{,m} \Lambda_{mk} = \nu \omega_{j,kl} \Lambda_{lm} \Lambda_{mk} \quad (2.15)$$

$$\omega_j = \epsilon_{jkl} u_{l,m} \Lambda_{mk} \quad (2.16)$$

$$C_{j,t} - \frac{\xi_2 L_{2,t}}{L_2} C_{j,2} + u_k C_{j,m} \Lambda_{mk} = \kappa C_{j,kl} \Lambda_{lm} \Lambda_{mk} \quad (2.17)$$

$$\Lambda_{jk} \equiv \begin{cases} 2\pi/L_j, & \text{if } j=k; \\ 0, & \text{otherwise.} \end{cases} \quad (2.18)$$

The second term on the left hand side of equation 2.15 and the similar term on the left hand side of equation 2.17 are due to grid stretching. They may be absorbed into the nonlinear terms by defining a grid-relative velocity  $u_j^* = u_j - L_{2,t}(t)\xi_2\delta_{2j}/2\pi$ . In terms of this modified velocity the equations of motion become

$$\omega_{j,t} + \epsilon_{jkl} (\epsilon_{lnq} u_q^* \omega_n)_{,m} \Lambda_{mk} + \gamma \omega_j L_{2,t}/L_2 = \nu \omega_{j,kl} \Lambda_{lm} \Lambda_{mk} \quad (2.19)$$

$$\omega_j = \epsilon_{jkl} u_{l,m}^* \Lambda_{mk} = \epsilon_{jkl} u_{l,m} \Lambda_{mk} \quad (2.20)$$

$$C_{j,t} + u_k^* C_{j,m} \Lambda_{km} = \kappa C_{j,kl} \Lambda_{lm} \Lambda_{mk} \quad (2.21)$$

$$\Lambda_{jk} \equiv \begin{cases} 2\pi/L_j, & \text{if } j=k; \\ 0, & \text{otherwise.} \end{cases} \quad (2.22)$$

$$\gamma \equiv \begin{cases} 1, & \text{if } j=1,3; \\ 0, & \text{otherwise.} \end{cases} \quad (2.23)$$

The remaining grid stretching terms in equation 2.19 are in a form that may be readily Fourier transformed.

In domains I and III, the terms in equation 2.19 are identically zero, and the left hand side of equation 2.20 goes to zero. Equation 2.20 will be solved to obtain asymptotic solutions for the velocity in domains I and III and total velocity in domain II.

## 2.4 Numerical Method

### 2.4.1 Transformed Equations

The governing equations 2.19 through 2.21 are solved in domain II using a standard Fourier pseudo-spectral technique treating the vorticity as periodic in the aperiodic direction  $\xi_2$ . Note that all of the terms in equation 2.19 can be treated as periodic since by construction  $\omega_j \rightarrow 0$  at the top and bottom of the computational box. The same holds true for the scalar convection equation 2.21. The governing equations are advanced in wave space with nonlinear terms which are calculated in physical space at each timestep.

Equations 2.19, 2.20, and 2.21 Fourier transformed in all three directions become

$$\hat{\omega}_{j,t} + \left( \frac{\gamma L_{2,t}}{L_2} + \nu \hat{\omega}_j k_k k_l \Lambda_{lm} \Lambda_{mk} \right) + i k_m \mathcal{F}(\epsilon_{jkl} (\epsilon_{lnq} u_q^* \omega_n) \Lambda_{km}) = 0 \quad (2.24)$$

$$\hat{\omega}_j = i \epsilon_{jkl} \hat{u}_l^* k_m \Lambda_{mk} = i \epsilon_{jkl} \hat{u}_l k_m \Lambda_{mk} \quad (2.25)$$

$$\hat{C}_{j,t} + \kappa \hat{C}_j k_k k_l \Lambda_{lm} \Lambda_{mk} + \mathcal{F}(C_{j,k} u_m^* \Lambda_{mk}) = 0 \quad (2.26)$$

$$\Lambda_{jk} \equiv \begin{cases} 2\pi/L_j, & \text{if } j=k; \\ 0, & \text{otherwise.} \end{cases} \quad (2.27)$$

$$\gamma \equiv \begin{cases} 1, & \text{if } j=1,3; \\ 0, & \text{otherwise.} \end{cases} \quad (2.28)$$

where  $k_j$  is the wavenumber in the  $\xi_j$  direction, hatted quantities are Fourier transforms of the corresponding physical vector, and  $\mathcal{F}()$  is the Fourier transform operator.

The diffusion term in equation 2.26 as well as both the diffusion term and the grid stretching term which appear in equation 2.24 are absorbed into the time derivative terms by use of integrating factors, yielding the basic set of equations in wavespace.

$$\frac{1}{G(t)}(G(t)\hat{\omega}_j)_{,t} + ik_m \mathcal{F}(\epsilon_{jkl}(\epsilon_{lnq}u_q^* \omega_n) \Lambda_{mk}) = 0 \quad (2.29)$$

$$\hat{\omega}_j = i\epsilon_{jkl}\hat{u}_l^* k_m \Lambda_{mk} = i\epsilon_{jkl}\hat{u}_l k_m \Lambda_{mk} \quad (2.30)$$

$$\frac{1}{H(t)}(H(t)\hat{C}_j)_{,t} + \mathcal{F}(u_k^* \Lambda_{mk} C_{j,m}) = 0 \quad (2.31)$$

$$G(t) = L_2^\gamma(t) \exp(\nu k_l k_k \int_{t_0}^t \Lambda_{lm} \Lambda_{mk} d\tau) \quad (2.32)$$

$$H(t) = \exp(\kappa k_l k_k \int_{t_0}^t \Lambda_{lm} \Lambda_{mk} d\tau) \quad (2.33)$$

$$\Lambda_{jk} \equiv \begin{cases} 2\pi/L_j, & \text{if } j=k; \\ 0, & \text{otherwise.} \end{cases} \quad (2.34)$$

$$\gamma \equiv \begin{cases} 1, & \text{if } j=1,3; \\ 0, & \text{otherwise.} \end{cases} \quad (2.35)$$

The solution procedure for this set of equations is as follows.

- The periodic part of the velocity field is calculated from the periodic vorticity in wave space for domain II.
- The velocity and vorticity fields are transformed into physical space in the aperiodic direction.

- An aperiodic field is added to the periodic velocity field to form the total, aperiodic, velocity.
- The velocity and vorticity fields are transformed into physical space in the remaining two directions and the nonlinear terms are formed.
- The nonlinear terms, which are periodic by virtue of the vorticity going to zero at the edges of the box, are then transformed in all directions back into wave space.
- The nonlinear terms are dealiased.
- The nonlinear terms are used to advance the vorticity field in time.

### 2.4.2 Asymptotic Matching of Velocities

The crux of the procedure outlined above is the calculation of the aperiodic component of the velocity field. This is calculated from the curl of 2.20 which is

$$u_{j,kl}\Lambda_{lm}\Lambda_{mk} = -\epsilon_{jkl}\omega_{l,m}\Lambda_{mk}. \quad (2.36)$$

Only one component of  $u_j$  need be solved for, since the remaining two components can be constructed from continuity and the definition of vorticity. It is convenient to solve for the cross-stream velocity  $u_2$ . The equation for  $u_2$  is transformed in the two periodic ( $\xi_1$  and  $\xi_3$ ) directions, but not in the non-periodic ( $\xi_2$ ) direction giving the second order ordinary differential equation

$$\frac{1}{L_2^2}\tilde{u}_{2,22} + \left(\frac{k_1^2}{L_1^2} + \frac{k_3^2}{L_3^2}\right)\tilde{u}_2 = -\frac{1}{4\pi^2}k_k\Lambda_{kl}\epsilon_{2lm}\tilde{\omega}_m. \quad (2.37)$$

For  $K^2 \equiv L_2^2(k_1^2/L_1^2 + k_3^2/L_3^2) > 0$ , the general solution to equation 2.37 is

$$\tilde{u}_2 = \tilde{u}_2^P + \tilde{A}\exp(L_2(\frac{k_1^2}{L_1^2} + \frac{k_3^2}{L_3^2})^{\frac{1}{2}}\xi_2) + \tilde{B}\exp(-L_2(\frac{k_1^2}{L_1^2} + \frac{k_3^2}{L_3^2})^{\frac{1}{2}}\xi_2) \quad (2.38)$$

where  $\tilde{u}_2^P$  is the particular solution of equation 2.37 (zero in domains I and III where the vorticity is zero, calculated numerically from the vorticity field in domain II), and  $\tilde{A}$  and  $\tilde{B}$  are functions of  $K$  which are determined by asymptotic matching of the velocity and velocity gradient.

The solution for the velocity must be bounded at  $\xi_2 = \pm\infty$ , hence in the three domains

$$\tilde{u}_2 = \begin{cases} \tilde{A}_I e^{K\xi_2} & \text{domain I} \\ \tilde{u}_2^P + \tilde{A}_{II} e^{K\xi_2} + \tilde{B}_{II} e^{-K\xi_2} & \text{domain II} \\ \tilde{B}_{III} e^{-K\xi_2} & \text{domain III.} \end{cases} \quad (2.39)$$

Matching the velocities and velocity gradients at the domain boundaries  $\xi_2 = \pm\pi$  yields four algebraic equations in four unknowns

$$\tilde{A}_I e^{-\pi K} = \tilde{u}_2^P(-\pi) + \tilde{A}_{II} e^{-\pi K} + \tilde{B}_{II} e^{\pi K} \quad (2.40)$$

$$K \tilde{A}_I e^{-\pi K} = \tilde{u}_{2,2}^P(-\pi) + K \tilde{A}_{II} e^{-\pi K} - K \tilde{B}_{II} e^{\pi K} \quad (2.41)$$

$$\tilde{B}_{III} e^{-\pi K} = \tilde{u}_2^P(\pi) + \tilde{A}_{II} e^{\pi K} + \tilde{B}_{II} e^{-\pi K} \quad (2.42)$$

$$-K \tilde{B}_{III} e^{-\pi K} = \tilde{u}_{2,2}^P(\pi) + K \tilde{A}_{II} e^{\pi K} - K \tilde{B}_{II} e^{-\pi K}. \quad (2.43)$$

Solving for  $\tilde{A}_{II}$  and  $\tilde{B}_{II}$  gives

$$\tilde{u}_2 = \tilde{u}_2^P + \frac{1}{2} \left( \left( \frac{\tilde{u}_{2,2}^P(-\pi)}{K} - \tilde{u}_2^P(-\pi) \right) \exp(-K\xi_2) - \left( \frac{\tilde{u}_{2,2}^P(\pi)}{K} + \tilde{u}_2^P(\pi) \right) \exp(K\xi_2) \right) \quad (2.44)$$

$$K \equiv L_2 \left( \frac{k_1^2}{L_1^2} + \frac{k_3^2}{L_3^2} \right). \quad (2.45)$$

Solutions for  $u_1$  and  $u_3$  are constructed from the incompressibility condition and the definition of vorticity.

If  $K = 0$ , equation 2.37 is replaced by the two-direction transform of 2.20 with  $k_1 = k_3 = 0$

$$\tilde{\omega}_j = \epsilon_{j2l} \tilde{u}_{l,2} \Lambda_{22}. \quad (2.46)$$



Integrating in the  $\xi_2$  direction yields

$$\tilde{u}_j = \frac{-2\pi\xi_2}{L_2}\epsilon_{j2l}\tilde{\omega}_l + \tilde{D}_j \quad (2.47)$$

where  $\tilde{D}_j$  are constants which are determined by the mean velocity in each direction.

Solutions for  $\tilde{u}_1$  and  $\tilde{u}_3$  are constructed from the resulting solution for  $\tilde{u}_2$  in domain II for each  $(k_1, k_3)$  pair and the total solution for the velocity is transformed to physical space in the periodic directions. The cross product of the velocity and the vorticity is taken to form the periodic nonlinear term. The nonlinear term is then transformed back into wave space to advance the vorticity and scalar fields in time.

### 2.4.3 Time Advance

The time advancement method used for all dependent variables is the second order Runge-Kutta scheme

$$\Phi_{,t} = f(\Phi; t) \quad (2.48)$$

$$\Phi_{\dagger}^{n+1} = \Phi^n + \Delta t f(\Phi^n; t^n) \quad (2.49)$$

$$\Phi^{n+1} = \Phi^n + \frac{\Delta t}{2}(f(\Phi^n; t^n) + f(\Phi_{\dagger}^{n+1}; t^{n+1})) \quad (2.50)$$

where  $n$  is the time index.

This particular scheme was chosen because it minimizes memory requirements for a given simulation size. It requires only two copies of the three vorticities and each scalar (one field at  $t = t^n$  and one at  $t = t_{\dagger}^{n+1}$ ) to be stored at any given time. It also allows for the use of the random-shift dealiasing scheme described in section 2.4.5 and appendix C, which helps make maximum use of the available computational power.

Applying this scheme to the governing equations 2.29 and 2.31 yields

$$\begin{aligned} \hat{\omega}_j^{n+1} = & \frac{G^n}{G^{n+1}}\hat{\omega}_j^n + \frac{\Delta t}{2}\left(\frac{G^n}{G^{n+1}}ik_m^n\mathcal{F}^n((\omega_q u_r^* \epsilon_{lqr})\Lambda_{mk}\epsilon_{jkl}) \right. \\ & \left. + ik_m^{n+1}\mathcal{F}^{n+1}((\omega_q u_r^* \epsilon_{lqr})\Lambda_{mk}\epsilon_{jkl})\right) \end{aligned} \quad (2.51)$$

$$\hat{C}_j^{n+1} = \frac{H^n}{H^{n+1}} \hat{C}_j^n + \frac{\Delta t}{2} \left( \frac{H^n}{H^{n+1}} \mathcal{F}^n(u_k^* \Lambda_{mk} C_{j,m}) + \mathcal{F}^{n+1}(u_k^* \Lambda_{mk} C_{j,m}) \right). \quad (2.52)$$

The precise forms of  $G^n$  and  $H^n$  depend on the way in which the grid is stretched. In the present code, grid stretching was taken to be piecewise linear, hence

$$\frac{G^n}{G^{n+1}} = \left( \frac{L_2^n}{L_2^{n+1}} \right)^\gamma \exp \left( -4\pi^2 \nu \left( \frac{k_1^2}{L_1^2} \Delta t + \frac{k_2^2}{L_{2,t}^n} \left( \frac{1}{L_2^n} - \frac{1}{L_2^{n+1}} \right) + \frac{k_3^2}{L_3^2} \Delta t \right) \right) \quad (2.53)$$

and

$$\frac{H^n}{H^{n+1}} = \exp \left( -4\pi^2 \kappa \left( \frac{k_1^2}{L_1^2} \Delta t + \frac{k_2^2}{L_{2,t}^n} \left( \frac{1}{L_2^n} - \frac{1}{L_2^{n+1}} \right) + \frac{k_3^2}{L_3^2} \Delta t \right) \right). \quad (2.54)$$

This is the form of the equations implemented.

#### 2.4.4 Accuracy and Stability

As implemented, the code has standard Fourier spectral accuracy in all three spatial directions and is second order accurate in time. The second order Runge-Kutta timestepping scheme used is “weakly” unstable (it is unstable in the absence of viscosity, though only mildly so for small  $\Delta t$ ). However in the presence of even a small viscosity the method is stable for a range of  $\Delta t$ .

This can be quantified by applying the method to the one dimensional linear convection-diffusion equation

$$u_t + cu_x = \nu u_{xx} \quad (2.55)$$

for a single Fourier component

$$u = C(t) \exp \left( \frac{2\pi i k x}{N \Delta x} \right). \quad (2.56)$$

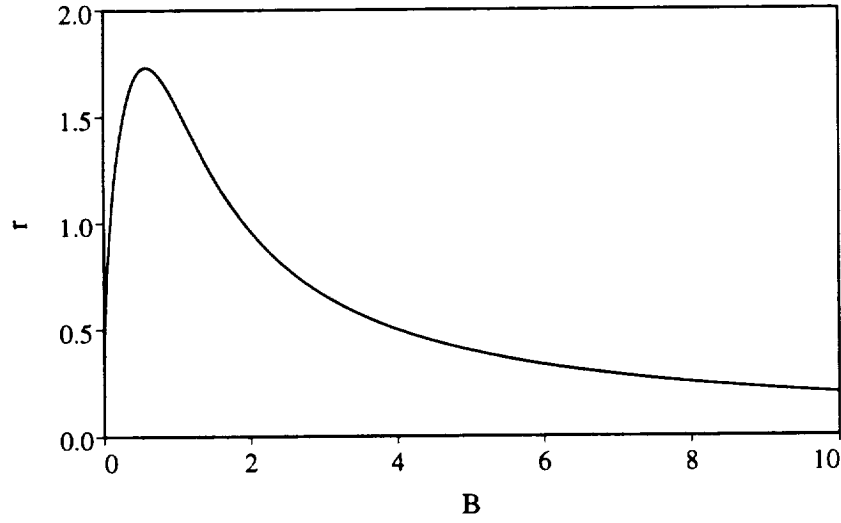


Figure 2.3: Neutral stability curve for second order Runge-Kutta timestepping algorithm applied to linear con-vec-tion-diffusion equation  $u_t + cu_x = \nu u_{xx}$ . Coordinates are  $B \equiv \frac{2\pi\nu k}{cN\Delta x}$  and  $r \equiv \frac{2\pi kc\Delta t}{N\Delta x}$ .

Substituting equation 2.56 into equation 2.55 yields

$$\begin{aligned} u_t &= -\left(\frac{2\pi i k c}{N\Delta x} + \frac{4\pi^2 k^2 \nu}{N^2 \Delta x^2}\right) u \\ &\equiv Lu. \end{aligned} \quad (2.57)$$

Applying the timestepping algorithm from equations 2.48 through 2.50 to equation 2.57 gives

$$u^{n+1} = \left(1 + L\Delta t + \frac{L^2 \Delta t^2}{2}\right) u^n. \quad (2.58)$$

The timestepping method is considered stable if  $u^n$  remains finite as  $n \rightarrow \infty$ . This will be true if

$$\left|\frac{u^{n+1}}{u^n}\right|^2 = \left|1 + L\Delta t + \frac{L^2 \Delta t^2}{2}\right|^2 \leq 1. \quad (2.59)$$

It is convenient to define the dimensionless variable

$$r \equiv \frac{2\pi k c \Delta t}{N\Delta x} = \frac{2\pi k}{N} CFL \quad (2.60)$$

and the dimensionless parameter

$$B \equiv \frac{2\pi\nu k}{cN\Delta x} \quad (2.61)$$

where  $CFL$  is the Courant-Friedrichs-Lewy number. In terms of these dimensionless quantities

$$L\Delta t = -(B + i)r \quad (2.62)$$

and the stability condition from equation 2.59 expands to

$$\frac{(B^2 + 1)^2}{4}r^3 - B(B^2 + 1)r^2 + 2B^2r - 2B \leq 0. \quad (2.63)$$

The neutral curve for equation 2.63 is shown in figure 2.3. The equation is third order in  $r$  (hence third order in  $\Delta t$ ) and no simple analytic stability criterion exists. In order to choose a  $\Delta t$ , therefore, a simple Newton method solver was used to solve equation 2.63 numerically for  $r(B)$  at each timestep. Note that for a given timestep the parameter  $B$  is a quantity with known limits (at  $k = 1$  and  $k = N/2$ ). At each timestep  $r(B)$  was evaluated twice, once for  $k = 1$  and once for  $k = N/2$ . The minimum of the two resulting values for  $\Delta t$ , multiplied by a factor of  $C = 0.8$ , was used for the next timestep size.

The factor  $C < 1.0$  was necessary to ensure time accuracy in addition to stability of the method. Several test runs with identical initial conditions (the same as the test case discussed in section 2.8.3) but with  $C$  varying from 0.4 to 1.0 were performed. The value  $C = 0.8$  was found to be sufficiently small for the solution to converge to a solution independent of  $C$ .

### 2.4.5 Alias Control

Following the approach of Rogallo [34], aliasing was controlled with a combination of high wavenumber masking and phase shifting. All modes with wavenumbers such that

$$\frac{k_1^2}{N_1^2} + \frac{k_1^2}{N_1^2} + \frac{k_1^2}{N_1^2} > \frac{2}{9} \quad (2.64)$$

are set to zero. This eliminates all two- and three-dimensional aliasing, leaving only the one-dimensional aliasing term in each direction. The one-dimensional alias errors are dealt with by phase shifting the data a random fraction of a grid cell width in each direction at every other time substep followed by a further shift of exactly one half a grid cell width in each direction at the subsequent time substep. This random shifting cancels the aliasing error to second order in time, the same order as the time advancement algorithm. Using this dealiasing technique instead of a perfect (2/3 rule or multiple phase shift) technique reduces both memory requirements and operations per timestep. See Appendix C for a more complete discussion of aliasing and dealiasing for Discrete Fourier Transforms.

## 2.5 Code Implementation and Data Management

The code described above has been implemented on an Intel iPSC/860 supercomputer. Also known as the “Hypercube”, the iPSC/860 used is a massively parallel computer which has 128 computational nodes each consisting of a 40 megahertz Intel i860 processor with 8 megabytes of random access memory (RAM). The code is written in *VECTORAL*, a high level programming language developed by Wray [57] which facilitates the handling of large data sets.

The architecture of the machine dictated the implementation of the code. The whole simulation, executable and data, had to fit in the distributed RAM on the machine. This requires careful division of the data into useful subsets which reside separately on each processing node. The method described is natural to implement on a machine with such an architecture since nearly all of the operations at any given point in the algorithm are performed independently on separate parts of the data set. This leads to a simple division of tasks among the multiple processors, making for a fast and efficient code.

In order to perform a transform on a line of data, a given processor must have all the data in the transform direction for that line. To achieve this, the data was structured for a two pass method, with each of the  $N$  computational nodes storing

Table 2.1: Code Structure

**Pass 1**

1. Transform nonlinear terms into wave  $\xi_2$  space, shifted mesh.
2. Unshift nonlinear terms.
3. Advance governing equations for substep.
4. Save data and/or stop if necessary.
5. If first R-K substep, calculate  $\Delta t$ , dealiasing shifts, integrating factors, etc. for timestep.
6. Zero “oddball” ( $k_j = N_j/2$ ) wavenumber contributions.
7. Zero high wavenumber modes to eliminate multi-dimensional aliasing.
8. Shift data for one-dimensional alias control.
9. Form needed  $\xi_2$  derivatives of data.
10. Transform data into physical  $\xi_2$  space, shifted mesh.
11. Execute Pass 2.

**Pass 2**

1. Transpose data to  $(\xi_1, \xi_3)$  planes.
2. Calculate additional velocity and form corrected velocity terms.
3. Form needed  $\xi_1$  and  $\xi_3$  derivatives of data.
4. Transform data into physical  $\xi_1$  and  $\xi_3$  space, shifted mesh.
5. If second R-K substep, calculate  $\max\left(\frac{u}{\Delta x}\right)_j$  for *CFL* stability requirements.
6. Form nonlinear terms in physical space, shifted mesh.
7. Transform data into wave  $\xi_1$  and  $\xi_3$  space, shifted mesh.
8. Transpose data to  $(\xi_1, \xi_2)$  planes.
9. Execute Pass 1.

and manipulating  $1/N$  of the total data set during each pass, and swapping data between passes.

For the first pass, each computational node holds all the  $\xi_1$  and  $\xi_2$  data for  $1/N$  of the  $\xi_3$  planes. All  $\xi_2$  derivatives and transforms are evaluated during this pass. For the second pass, the data is swapped between computational nodes so that each node now holds all of the  $\xi_1$  and  $\xi_3$  data for  $1/N$  of the  $\xi_2$  planes. All  $\xi_1$  and  $\xi_3$  derivatives and transforms are evaluated during this second pass. The data is then swapped back to its original configuration and the governing equations are advanced in time. Table 2.1 lists the operations executed during each time substep.

## 2.6 Boundary Conditions

Periodic boundary conditions are imposed in the streamwise  $\xi_1$  and spanwise  $\xi_3$  directions

$$\Phi(\xi_1 + 2\pi, \xi_2, \xi_3; t) = \Phi(\xi_1, \xi_2, \xi_3; t) \quad (2.65)$$

$$\Phi(\xi_1, \xi_2, \xi_3 + 2\pi; t) = \Phi(\xi_1, \xi_2, \xi_3; t) \quad (2.66)$$

where  $\Phi$  is any dependent variable.

The boundary conditions imposed on the vorticity field in the cross-stream direction  $\xi_2$  are that the vorticity is zero outside the resolved box

$$\omega_j = 0 \quad \text{for } \xi_2 < 0 \quad \text{or} \quad \xi_2 > 2\pi \quad (2.67)$$

and that the velocity perturbations go to zero at infinity

$$u_j(\xi_1, \xi_2, \xi_3; t) \xrightarrow{\xi_2 \rightarrow \pm\infty} 1. \quad (2.68)$$

The boundary conditions imposed on the scalar field in the cross-stream direction are that each scalar concentration be the same at the top and bottom of the resolved box

$$C_j(\xi_1, 0, \xi_3) = C_j(\xi_1, 2\pi, \xi_3). \quad (2.69)$$

This is most easily satisfied by picking initial scalar concentration distributions that go to zero in the freestream.

## 2.7 Initial Conditions

### 2.7.1 Vorticity Field

The initial conditions for the vorticity field of the time developing wake consist of a Gaussian mean streamwise velocity profile

$$\bar{u}_1 = 1 - \Delta u_{\mathbb{Q}0} e^{-c_1 x_2^2} \quad (2.70)$$

$$\bar{u}_2 = \bar{u}_3 = 0 \quad (2.71)$$

which gives the mean vorticity profile

$$\bar{\omega}_1 = \bar{\omega}_2 = 0. \quad (2.72)$$

$$\bar{\omega}_3 = -2c_1 \Delta u_{\mathbb{Q}0} x_2 e^{-c_1 x_2^2} \quad (2.73)$$

The centerline velocity defect,  $\Delta u_{\mathbb{Q}0}$ , was chosen to be 0.692 and  $c_1$  was chosen to be 0.69315. This particular profile was used in the experiments of Sato & Kuriki [39] and Corke, Krull, & Ghassemi [14], and in the computations of Chen, Cantwell, & Mansour [10]. It gives an initial wake halfwidth of  $b_0 = 1.0$  and an initial Reynolds number based on halfwidth of  $Re_b = 0.692/\nu$ .

For this mean velocity profile, the relationship between the various possible wake width length scales is as follows:

$$b_0 = 1 \quad (2.74)$$

$$\delta_0^* \equiv \int_{-\infty}^{\infty} (1 - \bar{u}_1) dx_2 = \left(\frac{\pi}{c_1}\right)^{\frac{1}{2}} \Delta u_{\mathbb{Q}0} b_0 = 1.473 b_0 \quad (2.75)$$

$$\delta_{\theta 0} \equiv \int_{-\infty}^{\infty} \bar{u}_1 (1 - \bar{u}_1) dx_2 = \left(\frac{\pi}{c_1}\right)^{\frac{1}{2}} \left(1 - \frac{\Delta u_{\mathbb{Q}0}}{\sqrt{2}}\right) \Delta u_{\mathbb{Q}0} b_0 = 0.7524 b_0. \quad (2.76)$$



Though the wake halfwidth,  $b_0$ , is used here as the reference scale (see figure 2.2 on page 22), the other scales given above will be used later when comparing results to data from other studies.

Small disturbances which were periodic in the streamwise and spanwise directions were added to the mean flow.

$$\begin{aligned}
\Omega(\xi_1, \xi_2, \xi_3; 0) = & \bar{\Omega} \\
& + \text{Real}[\varepsilon_{100}\hat{\Omega}_{100}\exp(i\alpha\xi_1) \\
& + \varepsilon_{010}\hat{\Omega}_{010}\exp(i\frac{\alpha\xi_1 + \phi_{010}}{2}) \\
& + \varepsilon_{001}\hat{\Omega}_{001}\exp(i\frac{\alpha\xi_1 + \phi_{001}}{4}) \\
& + \varepsilon^{100}\hat{\Omega}^{100}(\exp(i(\alpha\xi_1 - \beta\xi_3 + \phi^{100})) - \exp(i(\alpha\xi_1 + \beta\xi_3 + \phi^{100}))) \\
& + \varepsilon^{010}\hat{\Omega}^{010}(\exp(i\frac{\alpha\xi_1 - \beta\xi_3 + \phi^{010}}{2}) - \exp(i\frac{\alpha\xi_1 + \beta\xi_3 + \phi^{010}}{2})) \\
& + \varepsilon^{001}\hat{\Omega}^{001}(\exp(i\frac{\alpha\xi_1 - \beta\xi_3 + \phi^{001}}{4}) - \exp(i\frac{\alpha\xi_1 + \beta\xi_3 + \phi^{001}}{4})) \\
& + \dots]
\end{aligned} \tag{2.77}$$

where  $\Omega$  is any of the three vorticities,  $\bar{\Omega} = \bar{\Omega}(\xi_2)$  is the mean flow, and  $\hat{\Omega} = \hat{\Omega}(\xi_2)$  is a disturbance eigenfunction determined from linear theory as described in appendix B. The quantities  $\alpha$  and  $\beta$  are the streamwise and spanwise wavenumbers of the fundamental mode respectively, and  $\phi$  is a disturbance phase angle. Subscripts indicate a two-dimensional disturbance, superscripts indicate a three-dimensional disturbance, and the positions of the “1”s indicate the streamwise wavelength of the mode. As an example,  $\varepsilon^{001}$  is the disturbance amplitude of the three-dimensional disturbance at the sub-subharmonic streamwise wavelength.

The disturbance phases,  $\phi$ , are all defined with respect to the two-dimensional fundamental disturbance, with  $\phi = 2\pi$  corresponding to a physical shift of one fundamental wavelength. For the two-dimensional disturbances, the phase is measured from the first zero ( $\xi_1 = 0$ ) of the fundamental velocity disturbance to the first zero of the longer wavelength velocity disturbance as shown in figure 2.4. Figures 2.5 and 2.6 show the phase for the three-dimensional fundamental and three-dimensional

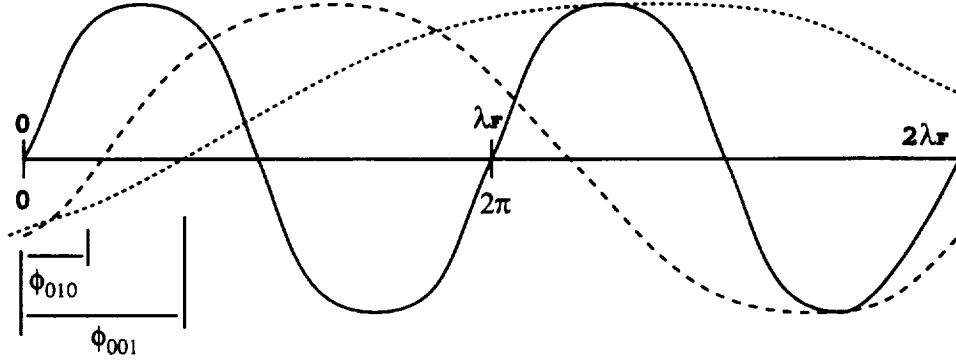


Figure 2.4: Two-dimensional disturbance phasing

subharmonic disturbances respectively. In each case, the phase is measured from the first maximum of the two-dimensional vorticity fundamental disturbance to the first crossing of the maxima of the pair of oblique vorticity disturbances.

Hence  $\phi^{010} = 0$  represents the phase of a three-dimensional subharmonic of the vorticity with its first crossing points aligned with the maximum of the two-dimensional fundamental. Similarly,  $\phi^{010} = \pi/4$  represents a three-dimensional subharmonic with its crossing points aligned with zeros of the two-dimensional fundamental.

All of the flows simulated had two-dimensional disturbances at a wavelength equal to the fundamental (Kármán) mode superimposed on the mean ( $\varepsilon_{100} > 0$ ). The three dimensional disturbances were pairs of oblique waves with equal and opposite spanwise wavenumbers oriented  $60^\circ$  to the spanwise direction ( $\beta/\alpha = \tan(60^\circ)$ ). This choice of three-dimensional modes was motivated by the stability analysis of Fleming [16] which suggested that the most unstable three dimensional modes should be wave pairs at angles near  $60^\circ$  at the subharmonic wavelength. The experimental observations of Corke, Krull, & Ghassemi [14] supported this analysis.

The amplitude for each disturbance eigenfunction was chosen such that the integral over  $x_2$  of the magnitude of the disturbance velocity eigenfunction for the given mode was equal to  $0.02U_0b_0$ . This initial magnitude was found to be small enough for the initial wake growth to be within the linear regime. At the same time it was large enough to allow the wake to enter the non-linear growth regime without undue expenditure of computational time.

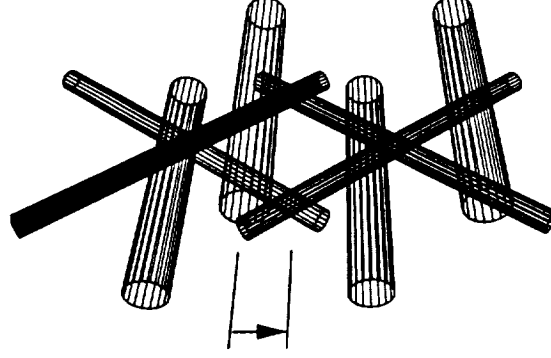


Figure 2.5: Disturbance phase for three-dimensional fundamental.

### 2.7.2 Passive Scalar Field

Though the method allows for carrying an arbitrary number of passive scalars, in practice only one scalar was carried in the simulations. The initial passive scalar concentration at each point was taken to be the magnitude of the vorticity (the enstrophy density)

$$C_1 = (\omega_k \omega_k)^{\frac{1}{2}}. \quad (2.78)$$

Since the vorticity perturbations were small, the initial scalar field is very nearly the square of the mean vorticity field

$$C_1 \approx 2c_1 \Delta u_{\mathbb{Q}0} |x_2| e^{-c_1 x_2^2}. \quad (2.79)$$

After the simulation was initiated, the vorticity and scalar fields were allowed to evolve independently.

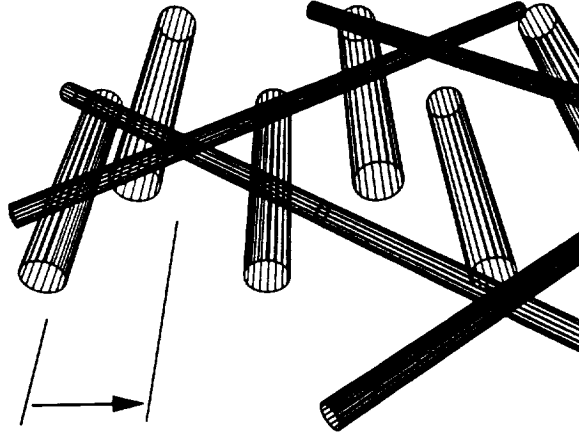


Figure 2.6: Disturbance phase for three-dimensional subharmonic.

### 2.7.3 Grid Stretching Rate

The grid stretching rate,  $L_{2,t}$ , was initially set to follow a  $L_2 \sim (t - t_0)^{1/2}$  growth curve to match the expected long-time growth of the wake. This gives

$$L_{2,t}(t) = \frac{L_2^2(t = t_0)}{2t_0 L_2(t)} \quad (2.80)$$

where  $t_0$  is a virtual time origin which depends on the initial Reynolds number.

The growth rate was periodically adjusted manually as the simulations progressed to keep the magnitude of the mean vorticity at the boundaries of the resolved box below a fixed percentage of the maximum mean vorticity magnitude. This manual adjustment was primarily necessary during the initial stages in the development of the wakes when the growth was significantly different than the asymptotic  $t^{1/2}$  curve.

### 2.7.4 Flow Reference Convention

In order to facilitate references to the various wake flows discussed throughout the remainder of this document, it is useful to introduce a standard naming convention which will present all the relevant information about a given flow in a compact form. From this point forward, the simulations presented here will be referenced with a tag of the form

$$\langle R \rangle (\langle A \rangle)_{\langle 2D \rangle}^{(3D)} \quad (2.81)$$

where  $\langle R \rangle$  is the initial wake halfwidth Reynolds number,  $Re_b$ ,  $\langle A \rangle$  is the angle of the three-dimensional disturbances with respect to the spanwise direction (zero if the flow is two-dimensional), and  $\langle 2D \rangle$  and  $\langle 3D \rangle$  are three-element strings which indicate which disturbance modes are present and gives their phases with respect to the two-dimensional fundamental disturbance.

The possible elements in the strings  $\langle 2D \rangle$  and  $\langle 3D \rangle$  are  $x$ , which indicates the given mode is not present, and  $0$ ,  $\pi/4$ , or  $\pi/2$  which indicate that the given mode is present and is at the corresponding phase with respect to the fundamental. The location of the element in the string gives the wavelength of the disturbance as outlined above for  $\varepsilon$  and  $\phi$ . The first slot indicates a disturbance at the fundamental streamwise wavelength, the second indicates a disturbance at the subharmonic streamwise wavelength, and the third indicates a disturbance at the sub-subharmonic streamwise wavelength.

As an example, the tag  $346(60)_{0\frac{\pi}{2}x}^{x\frac{\pi}{4}x}$  refers to a wake with a Reynolds number of  $Re_b = 346$ , and disturbances corresponding to a two-dimensional fundamental (which must be at a phase of 0 to itself), a two-dimensional subharmonic with  $\phi_{010} = \pi/2$ , and a pair of  $60^\circ$  oblique disturbances with  $\phi^{010} = \pi/4$ .

In addition, the wildcard character ' $\langle ? \rangle$ ' will be used to indicate that the given parameter can take on any appropriate value. For example, the tag  $346(60)_{0\frac{\pi}{4}x}^{x\langle ? \rangle x}$  refers to all  $Re_b = 346$  wakes with a two-dimensional fundamental, a two-dimensional subharmonic with  $\phi_{010} = \pi/4$ , and a pair of  $60^\circ$  oblique disturbances at any of the calculated phases. The tag  $\langle ? \rangle(60)_{0xx}^{x0x}$  refers to all wakes with a two-dimensional

fundamental, a pair of  $60^\circ$  oblique disturbances with  $\phi^{010} = 0$ , and any of the initial Reynolds numbers simulated.

## 2.8 Code Validation

The code has been validated with three sets of test cases. The first two tests, pure diffusion and linear disturbance cases, compare results from the code to linear flow solutions. The third is a comparison of results for identical initial conditions between the present code and the well tested and generally accepted code of Spalart, Moser, & Rogers [44] The results of these test cases are outlined below.

### 2.8.1 One Dimensional Diffusion

For two-dimensional parallel flow in the  $x_1$  direction, the Navier-Stokes equations reduce to the one-dimensional diffusion equation

$$u_{1,t} = \nu u_{1,22}. \quad (2.82)$$

This equation admits analytic solutions for the diffusing parallel wake

$$u_1 = 1 - \Delta u_{\mathbb{E}0} \left( \frac{t_0}{t - t_0} \right)^{\frac{1}{2}} \exp\left(-\frac{x_2^2}{4\nu(t - t_0)}\right) \quad (2.83)$$

and for the diffusing parallel mixing layer

$$u_1 = 2\text{erf}\left(\frac{x_2}{(4\nu(t - t_0))^{\frac{1}{2}}}\right) - 1. \quad (2.84)$$

To check agreement with the analytic solutions, four two-dimensional test cases were run: two parallel wakes started from a Gaussian velocity profile, one with grid stretching turned off and one with grid stretching turned on; and two parallel mixing layers started from an error function profile, again with grid stretching off in the first and on in the second. Each case was run on a  $4 \times 128 \times 4$  grid on two computational

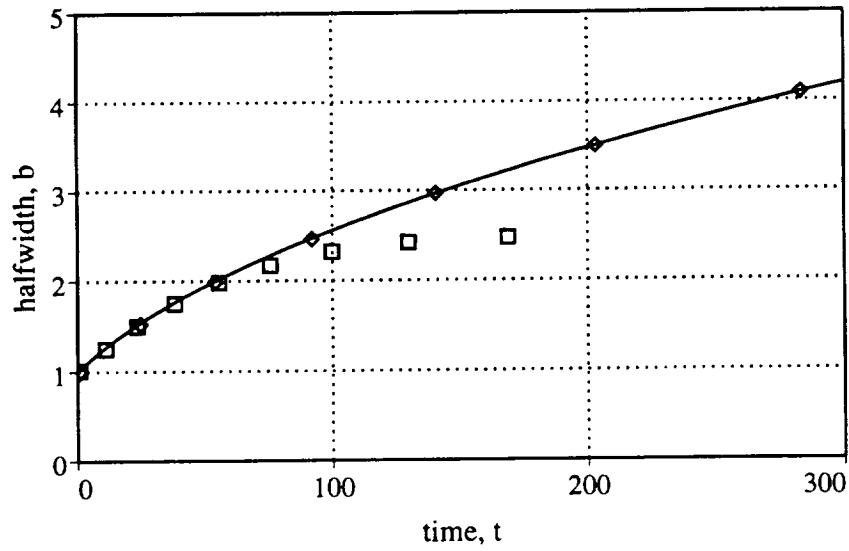


Figure 2.7: Halfwidth vs. time for  $Re_b = 35$  diffusing parallel wake.  $L_2(0) = 10.0$ .  $\square$ : Computed wake on fixed grid,  $L_{2,t}(t) = 0.0$ .  $\diamond$ : Computed wake on growing grid,  $L_{2,t}(t) = 0.125$ . — : Analytic solution.

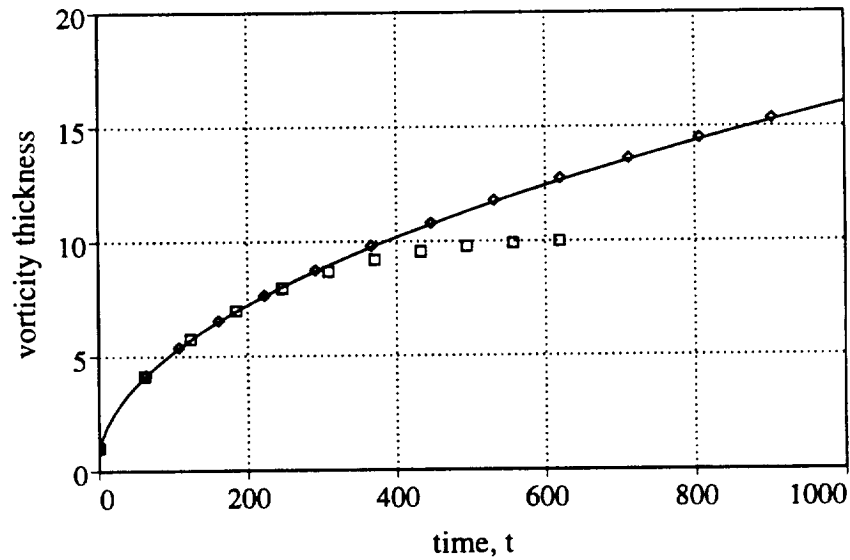


Figure 2.8: Vorticity thickness vs. time for  $Re_\theta = 50$  diffusing parallel mixing layer.  $L_2(0) = 10.0$ .  $\square$ : Computed mixing layer on fixed grid,  $L_{2,t}(t) = 0.0$ .  $\diamond$ : Computed mixing layer on growing grid,  $L_{2,t}(t) = 0.18$ . — : Analytic solution.

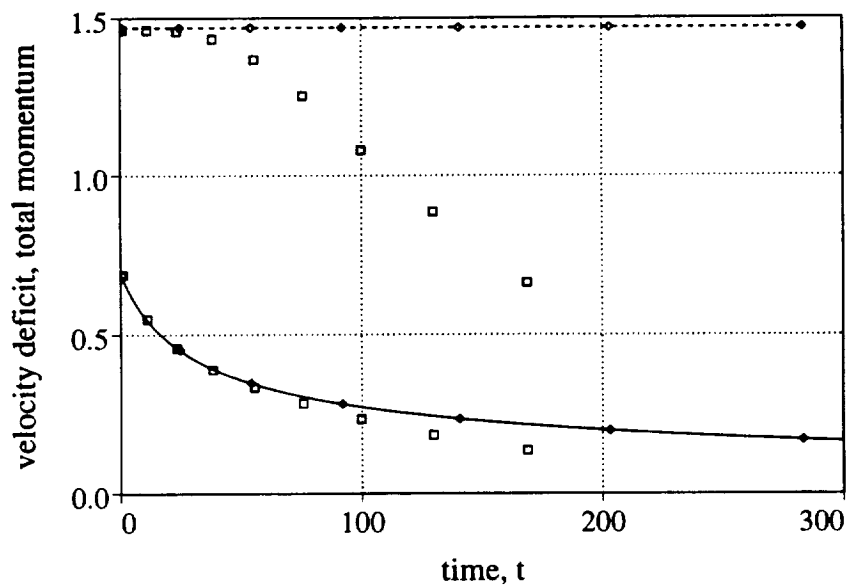


Figure 2.9: Centerline velocity defect and total  $x_2$  momentum vs. time for  $Re_b = 35$  diffusing parallel wake.  $L_2(0) = 10.0$ .  $\square$ : Computed wake on fixed grid,  $L_{2,t}(t) = 0.0$ .  $\diamond$ : Computed wake on growing grid,  $L_{2,t}(t) = 0.125$ . —: Analytic solution for centerline velocity defect. ----: Analytic solution for total  $x_2$  momentum.

nodes. Two computational nodes were not required by the problem size, but were used to verify internode message passing.

The numerical results and the analytic solutions are plotted in figures 2.7, 2.8, and 2.9. The wake flow halfwidth,  $b$ , is defined as half the width at half the centerline defect velocity. The mixing layer vorticity thickness is defined as the freestream velocity difference divided by the maximum mean vorticity (in this case the vorticity at the centerline).

The agreement between the numerical results and the analytic predictions for  $t \leq 50.0$  is excellent for both wake cases and for  $t \leq 225.0$  for both mixing layer cases. Past a time of  $t = 50.0$  for the wake and  $t = 225.0$  for the mixing layer the simulations with fixed grids begin to deviate significantly from the analytic solutions as the vorticity field outgrows the resolved domain. This violates, benignly, the requirements of the numerical scheme.

The excellent agreement for even very late times for the cases with the grid growing to keep pace with the spreading vorticity indicates that the diffusion portion of the



code, including the implementation of the growing grid, works properly. Over the course of the runs the wake simulation grid grew by a factor of nearly five and the mixing layer grid grew by a factor of over nineteen. These are rather stringent tests of the diffusion part of the implementation.

### 2.8.2 Linear Growth Rate

The second verification test for the code was a comparison between eigenmode growth rates for a computed solution of the Navier-Stokes equations using the present code and the eigenmode growth rates predicted by linear stability theory. The numerical simulation started from a Gaussian mean profile perturbed by a very low amplitude most-unstable eigenfunction (as predicted from linear theory). The eigenmode growth rate was calculated by assuming that each eigenmode can be represented by a wave having complex growth rate  $\alpha c$  and complex modeshape  $\hat{U}_i$ . In particular, for the  $u_1$  velocity component

$$\hat{u}_1(\alpha, x_2; t) = \hat{U}_1(\alpha, x_2)e^{-i\alpha c t}. \quad (2.85)$$

Taking the logarithm of equation 2.85 and solving for the real part of the result yields an equation for the growth of the disturbance

$$\alpha c_i t = \text{Real}[\ln \hat{u}_1(\alpha, x_2; t) - \ln \hat{U}_1(\alpha, x_2)]. \quad (2.86)$$

Hence, the growth rate,  $\alpha c_i$ , is the rate of change of the real part of the logarithm of the given dependent variable.

Figure 2.10 shows the calculated linear growth rate and the predicted linear growth rate for the test computation. The numerical simulation was performed on a  $128 \times 128 \times 4$  grid on 4 processor nodes. The flow Reynolds number was set at  $Re_b = 1384$  to reduce the effect of viscosity on the results as much as possible without requiring excessive resolution. Agreement between prediction and the computation is excellent. Deviations in growth rate near  $t = 0$  are due to small errors in the disturbance eigenfunction incurred while mapping the disturbance from the nonuniform numerical mesh used by the linear stability solver code to the uniform numerical mesh used in

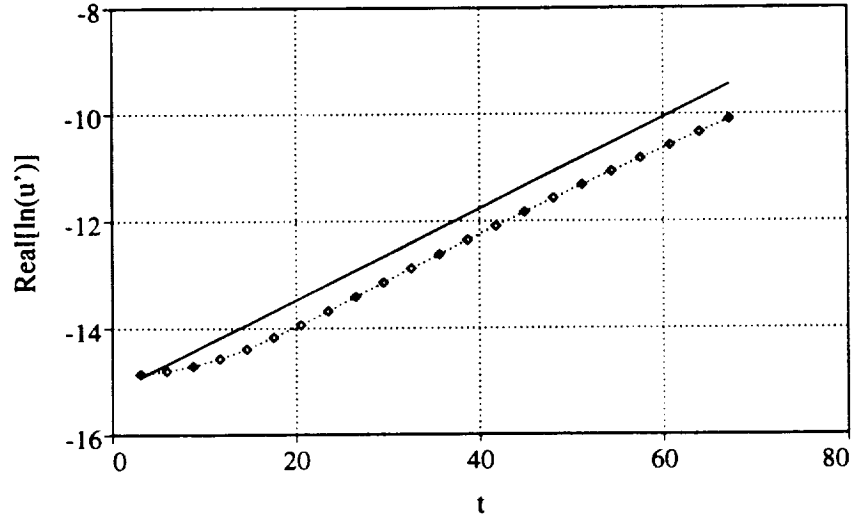


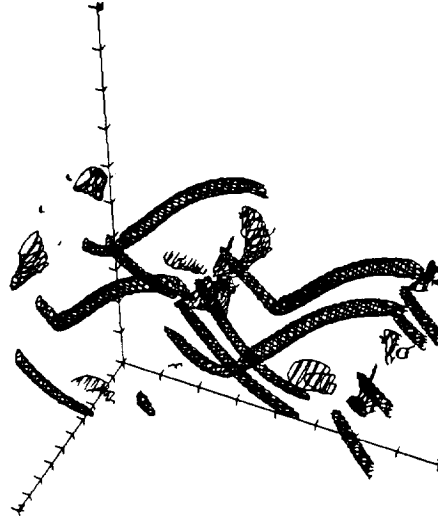
Figure 2.10: Magnitude of two-dimensional fundamental disturbance vs. time for parallel wake. — : Linear stability prediction.  $\diamond$ : Computed flow.

the simulation code. The slight dropoff in the growth rate at late times for the computed flow is due to viscous spreading of the mean flow, which is not accounted for in the linear theory.

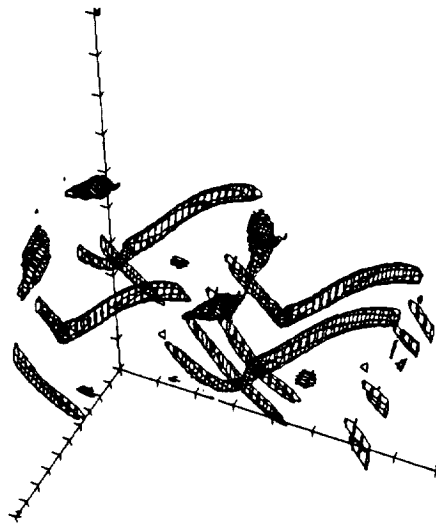
### 2.8.3 Comparison with Accepted Jacobi Polynomial Code

The final test consisted of a comparison between a numerical simulation using the present code and a numerical simulation started from identical initial conditions using the accepted code developed by Spalart, Moser, & Rogers [44] (hereafter referred to as the SMR code).

Figure 2.11a shows the three-dimensional vorticity magnitude for a  $Re_b = 346$  wake started from a Gaussian mean velocity profile with a two-dimensional disturbance at the most unstable (Kármán) wavelength and a three-dimensional disturbance at the subharmonic wavelength and sixty degrees from the spanwise direction. For this case grid growth was active with  $L_{2,t} = 0.1$ , which translates to a 50% increase in grid size from the initial grid to the grid at the time shown. This condition should provide the most stringent test of code performance.



(a)



(b)

Figure 2.11: Enstrophy Density isosurface from direct numerical simulations of  $346(60)_{0xx}^{x0x}$  wake.  $|\omega| = 0.7$ . (a) Present code.  $t = 103.3$ . (b) SMR code.  $t = 104.4$ .

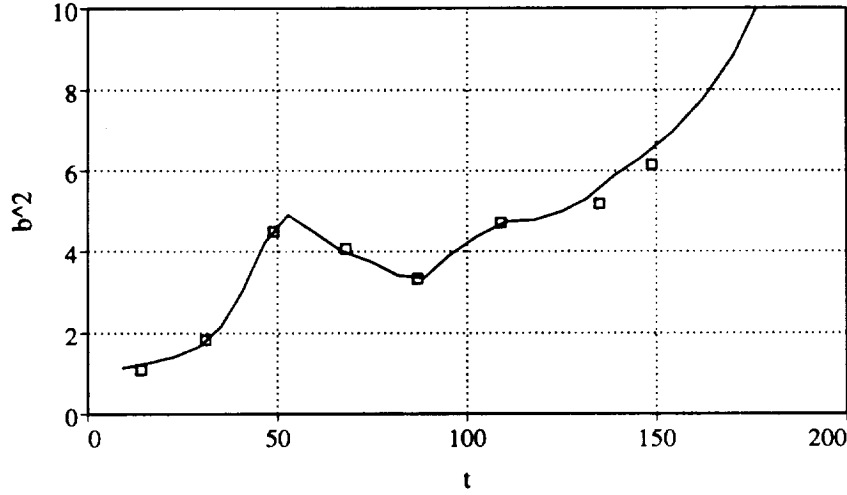


Figure 2.12: Wake halfwidth vs. time for direct numerical simulation of  $346(60)_{0xx}^{x0x}$  wakes. — : Present code.  $\square$  SMR code.

Figure 2.11b shows the identical flow calculated using the Rogers and Moser code. Some differences between the two calculations are expected due to differences in the computational grid and time advance algorithms. Despite this, the magnitude and shape of the structures in both codes are very similar even at the advanced time shown. Such excellent agreement is a strong indicator that the code functions properly.

As a check of the resolution of the test simulation, two variants of the Taylor microscale,  $\lambda_T$  (calculated from all three velocity components) and  $\lambda_{T1}$  (the traditional microscale calculated from only the streamwise velocity) were computed as functions of  $\xi_2$  (see appendix A for definitions of the microscales used). Both measures gave a minimum nondimensional microscale length of approximately 0.9 ( $\lambda_T = 0.83$ ,  $\lambda_{T1} = 0.87$ ) at the time shown in figure 2.11a. That length corresponds to a minimum of approximately 5 grid points in any direction, thus it is reasonable to conclude that the flow is sufficiently resolved.

Figure 2.12 is a plot of the square of the flow halfwidth versus time for the same two simulations. This represents a good measure of how well the codes match mean flow characteristics. There is no significant difference between the results obtained from the two codes. The small deviations at late time are due to small difference in

flow time and the fact that the vorticity field is beginning to outgrow the well resolved portion of the fixed mesh in the SMR code.

This test also gives a rough comparison of performance between the two codes. The iPSC/860 run required 5 hours on 16 of the available 128 nodes to run to the time shown. The Cray simulation took approximately 15 cpu hours spread out over 2 weeks of run time on a single processor of an 8 processor Cray-YMP.

### 2.8.4 Behavior Near the Matching Boundaries

The fundamental assumption of this method is that the vorticity remains confined to the resolved domain (it is compact) and therefore the vorticity magnitude at the matching boundaries remains negligible. It is important to know if this assumption is valid in cases of interest, and what consequences arise when these assumptions are violated.

Figures 2.13 and 2.14 show the behavior of the vorticity magnitude, normalized by the maximum vorticity magnitude in the flow, near the matching boundaries for two wake simulations. Figure 2.13 is data from the low Reynolds number two-dimensional diffusing wake discussed in section 2.8.1. Figure 2.14 is data from the higher Reynolds number strongly three-dimensional wake discussed in section 2.8.3. The sample line for the data in this figure was chosen to be the one on which the high enstrophy density regions of the wake pass closest to the edge of the box at late times. This line of data represents the worst case condition.

At early times in each flow, the behavior of the vorticity magnitude near the matching boundaries fit very well with the assumptions of the numerical method ( $\max |\omega_j|_{edge} \ll \max |\omega_j|_{flow}$ ). Even at late times the flow near the boundary remains well behaved. The small amplitude ripples near the matching boundary for the late time of the  $Re_b = 346$  wake are due to the slight mismatch in the vorticity magnitude between the top and bottom edges of the resolved domain. Attempting to resolve this small jump using a finite set of basis functions results in Gibbs phenomenon waves near the jump point.

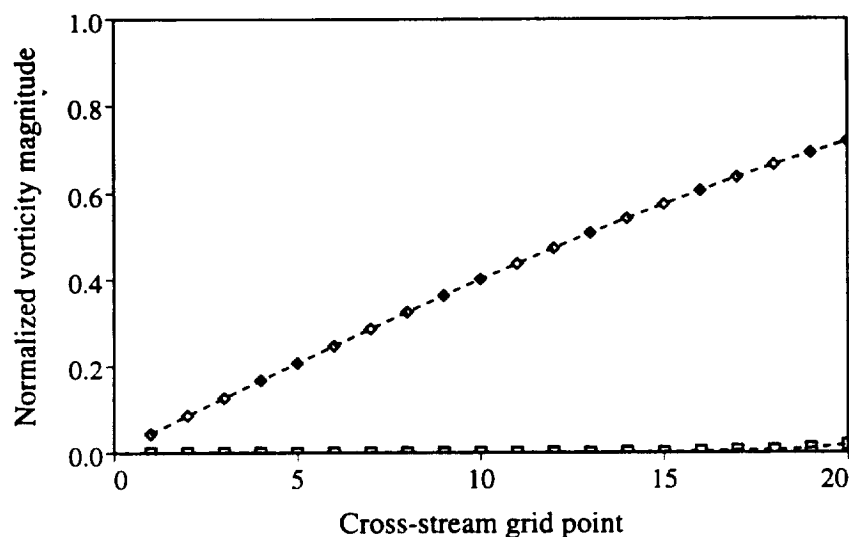


Figure 2.13: Behavior of relative vorticity magnitude  $\frac{|\omega|}{\max|\bar{\omega}|}$  near the matching boundaries for parallel diffusing wake,  $Re_b = 35$ .  $\square$ :  $t = 1.9$ .  $\diamond$ :  $t = 168.9$ . Matching boundary occurs between grid point 0 and 1 (left edge of plot).

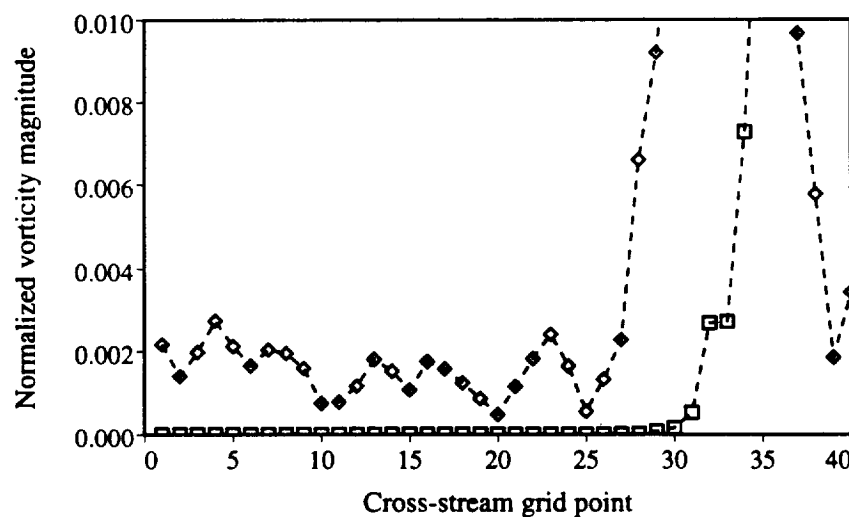


Figure 2.14: Behavior of relative vorticity magnitude  $\frac{|\omega|}{\max|\bar{\omega}|}$  near the matching boundaries for three-dimensional wake,  $Re_b = 346$ .  $\square$ :  $t = 2.8$ .  $\diamond$ :  $t = 103.3$ . Matching boundary occurs between grid point 0 and 1.

These small ripples are not a significant source of error in the simulations for a number of reasons. First, the magnitude of the Gibbs phenomena ripples are proportional to the magnitude of the vorticity mismatch across the edges of the resolved box. Thus so long as the vorticity mismatch is kept small, the magnitude of the ripples will be small. Second, the Gibbs phenomena ripples represent both positive and negative deviations in the vorticity field (note that figure 2.14 shows *magnitude*). Since the ripples are confined primarily to the edges of the resolved box, far from the vorticity containing region of the wake, the integrated (Biot-Savart) effect of the ripples is much smaller than the magnitude of the ripples would suggest. Finally, the Gibbs phenomena ripples occur at the highest wavenumbers, which are strongly damped in a well resolved viscous flow. Here the magnitude of the Gibbs waves are less than 0.2% of the maximum mean vorticity at their worst (cut through widest part of the wake). This magnitude is easily small enough to keep from having a significant influence on the flow.

# Chapter 3

## Two-dimensional Simulations

### 3.1 Motivation

In order to have a reference with which to compare the three-dimensional wake calculations presented in the next chapter (starting on page 93), a set of two-dimensional plane wakes was simulated with a variety of initial conditions and Reynolds numbers. The effect of these parameters on the evolution of two-dimensional structures in a wake and on the mean velocity profile is examined in this section.

### 3.2 Simulation Parameters

Two-dimensional simulations require a relatively small investment of computational resources, and are therefore ideal for parametric investigations. Simulations with a variety of combinations of disturbance wavelength and phases, and flow Reynolds numbers were run. All of the simulations were initiated from a Gaussian mean wake profile upon which a most unstable anti-symmetric (Kármán) disturbance is superimposed. Combinations of subharmonic and sub-subharmonic disturbances were added to the initial fields in some of the simulations. Wake Reynolds numbers based on initial wake halfwidth and centerline defect velocity were varied from  $Re_b = 69$  to  $Re_b = 2768$ . The initial passive scalar field in all the simulations was set equal to the



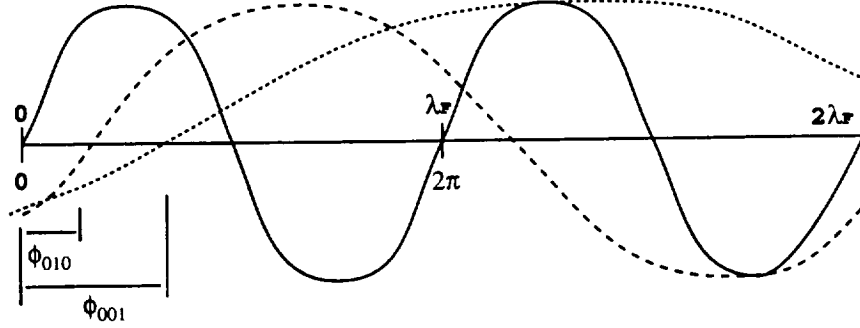


Figure 3.1: Two-dimensional disturbance phasing

initial enstrophy density at each point

$$C_j = (\omega_k \omega_k)^{\frac{1}{2}}. \quad (3.1)$$

and the Prandtl number

$$Pr \equiv \frac{\nu}{\kappa} \quad (3.2)$$

was set to a value of 0.7. Table H.1 in appendix H lists all the two-dimensional wakes simulated and their parameters.

Figure 3.1 gives a graphic summary of the disturbance wavelengths and the meaning of the disturbance phases used in the two-dimensional simulations. Initial disturbances were combinations of most-unstable eigenmodes at the fundamental, subharmonic, and sub-subharmonic wavelengths. Note that the phase is always in reference to the wavelength of the fundamental, so (for example) a phase of  $\pi/2$  results in a shift of one quarter of a fundamental wavelength. See section 2.7 for a more general description of the disturbance functions.

## 3.3 Evolution of the Two Dimensional Wake

### 3.3.1 Initial Development

For all of the two-dimensional wakes studied, the early evolution followed the same general pattern. This is typified by figure 3.2, which shows contour plots of vorticity

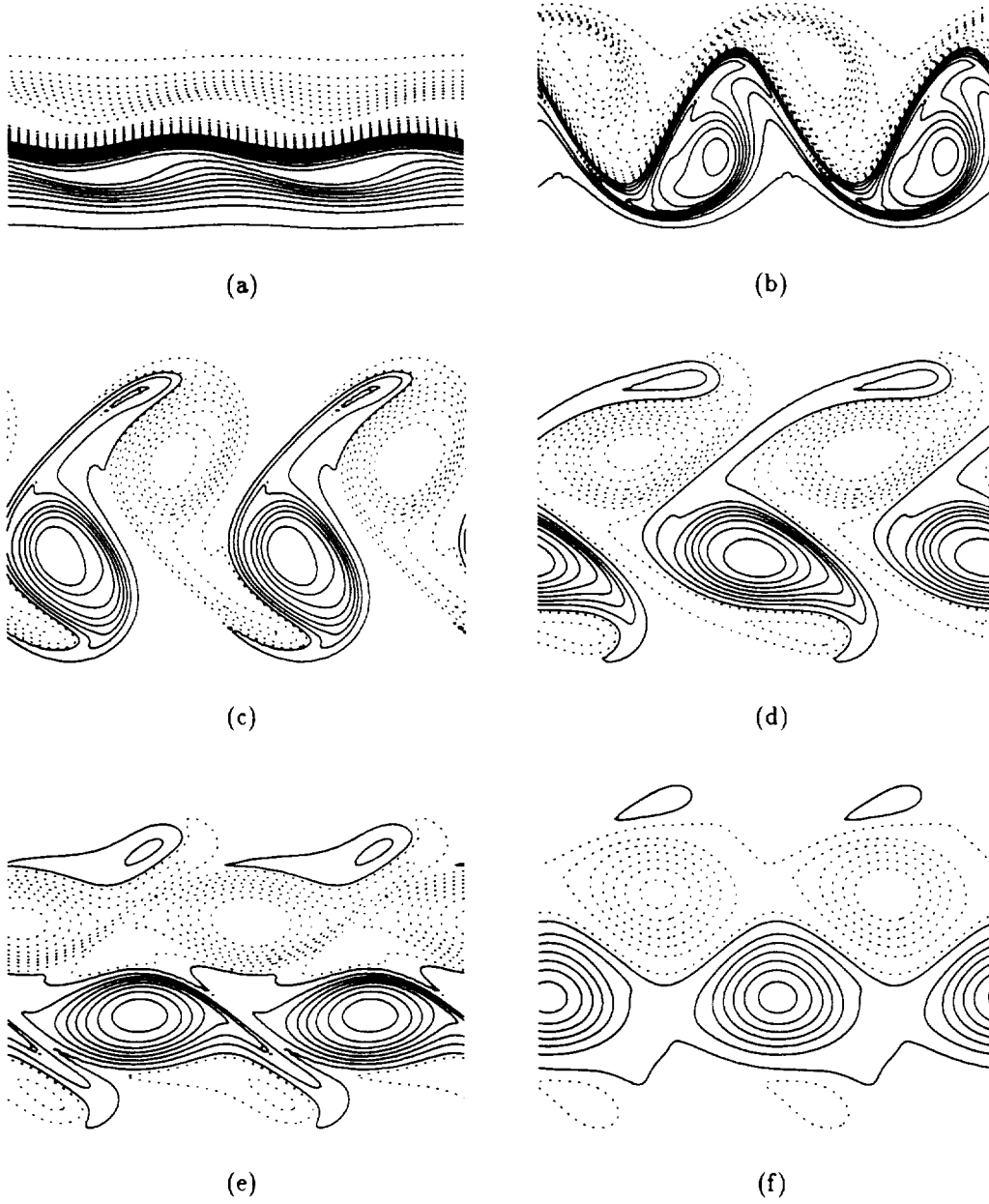


Figure 3.2: Iso-vorticity contours for  $346(0)_{0xx}^{xxx}$  wake (two-dimensional fundamental) at various times. (a)  $t = 22.6$ . (b)  $t = 49.7$ . (c)  $t = 70.1$ . (d)  $t = 83.6$ . (e)  $t = 97.1$ . (f)  $t = 198.6$ . Contours are  $0.01 \leq |\omega| \leq 0.4$  in increments of 0.05.

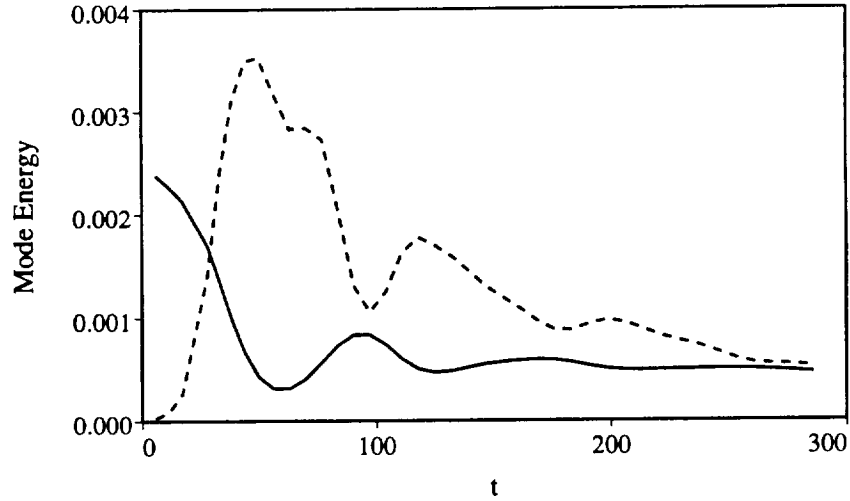


Figure 3.3: Mean and fundamental mode energies versus time for  $346(0)_{0xx}^{xxx}$  wake. — :  $0.1 \times$  mean flow energy. ---- : Fundamental disturbance energy.

at several times for the  $346(0)_{0xx}^{xxx}$  run (an  $Re_b = 346$  wake with a two-dimensional fundamental only). Note that these plots are in a frame of reference moving with the free stream (moving left to right at speed  $U_0 > \bar{u}_\infty$ ), hence the structures will appear to be convecting from right to left. The evolution starts with the linear growth of the disturbances, dominated by the growth of the most unstable (fundamental) wavelength perturbation (figure 3.2a). This is followed by nonlinear growth and rollup of the fundamental disturbance into a Kármán vortex street (figure 3.2b), which consists of a staggered double row of roughly circular regions of vorticity, known as “rollers”. These are positive signed on the bottom of the wake, negative signed on the top, and separated by regions of low enstrophy density (figure 3.2e). In the absence of longer wavelength disturbances, the rollers become roughly circular in cross section (figure 3.2f) and settle into a stable configuration. The wake then slowly diffuses under the influence of viscosity.

The process of linear growth, saturation, and decay described above is readily evident in figure 3.3 which shows the time evolution of the mode energy (the energy contained in motions with a given streamwise wavelength) of the mean flow and fundamental disturbance. Note that, in the figures, the mean energy line has

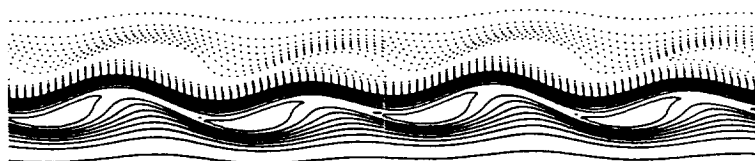
been rescaled to fit on the same plot as the fundamental mode energy. The fundamental mode energy grows exponentially (linear growth region) until approximately  $t = 30$ , the fundamental mode then enters a nonlinear growth regime, and saturates at approximately  $t = 50$  (at which time the vortex street has formed). Up to this time the fundamental mode has been drawing energy from the mean flow. The fundamental mode then begins to decay, releasing energy into both shorter wavelength disturbances and back into the mean flow. Oscillations in both the fundamental and mean mode energies past a time of 100 represent a long period exchange of energy between the mean flow and fundamental. These oscillations damp out as the wake slowly approaches an asymptotic state in which the wake is dominated by diffusion of the vortex street. These oscillations will appear again in plots of the evolution of the halfwidth of this wake presented later in this chapter (figures 3.17 and 3.19).

Returning to the enstrophy density plots, figure 3.2c and figure 3.2d show a pinching off event in the development of the  $346(0)_{0xx}^{xxx}$  wake. Fluid containing vorticity of the opposite sign is convected across the wake centerline to the opposite side of the wake during the rollup process. This sort of event is not unique to the temporal wake. A similar convection of fluid across the wake is evident in the flow visualizations of the wake behind a circular cylinder by Zdravkovitch [59] and direct numerical simulations of a spatially evolving two-dimensional wake by Maekawa & Mansour [24].

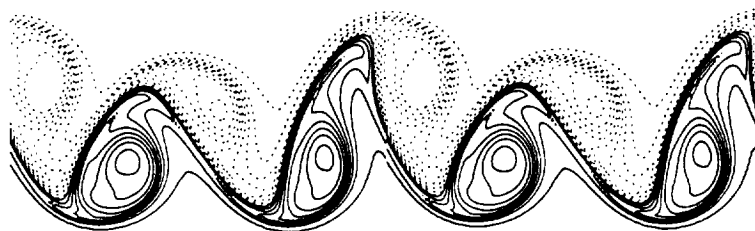
Note that there is a slight asymmetry across the wake at the latest time shown in this simulation. This asymmetry is due to the accumulation of small errors introduced by the approximate dealiasing scheme, which introduces a very small amplitude random forcing at the longest wavelengths. Such small numerical errors are sufficient to break the exact numerical symmetry over a very long calculation, but do not have a significant impact on the overall results at the times examined.

### 3.3.2 Effect of Disturbance Wavelength and Phase

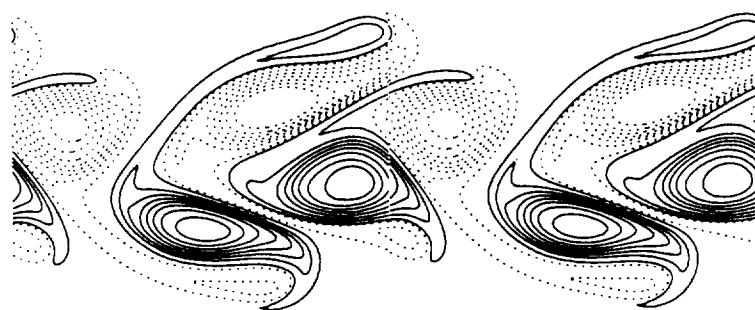
The presence of a fundamental wavelength disturbance causes the initially uniform wake to develop into the familiar double row of vortices that make up the Kármán vortex street. The rows of vortices are staggered, with the array of rollers on one side of the wake being  $180^\circ$  out of phase with the rollers on the other side. The



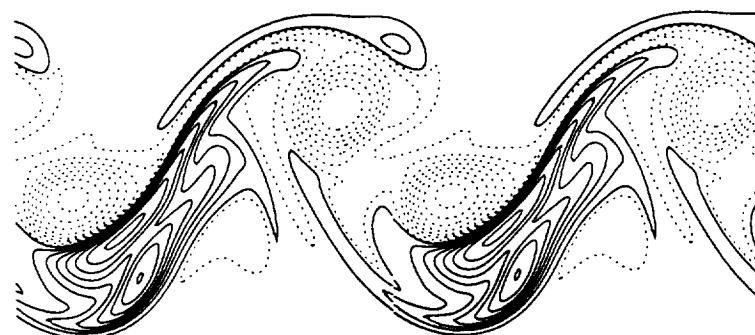
(a)



(b)



(c)



(d)

Figure 3.4: See caption page 59.

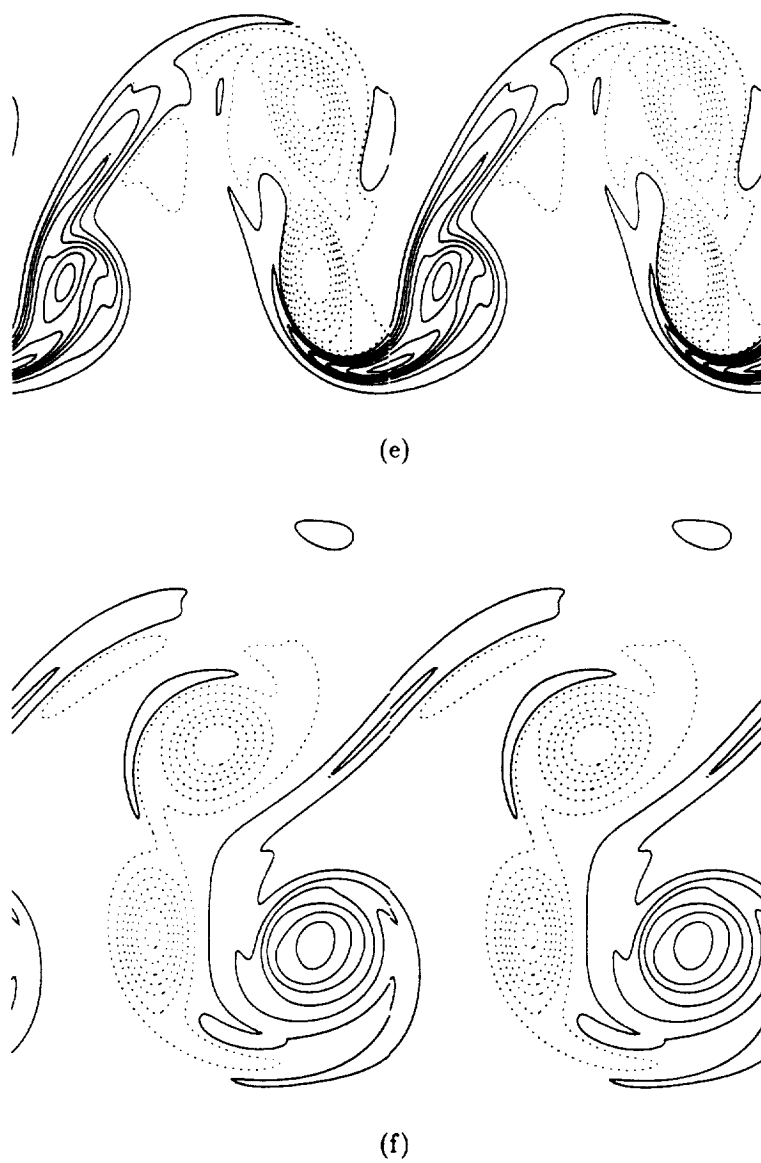


Figure 3.4: See caption page 59.

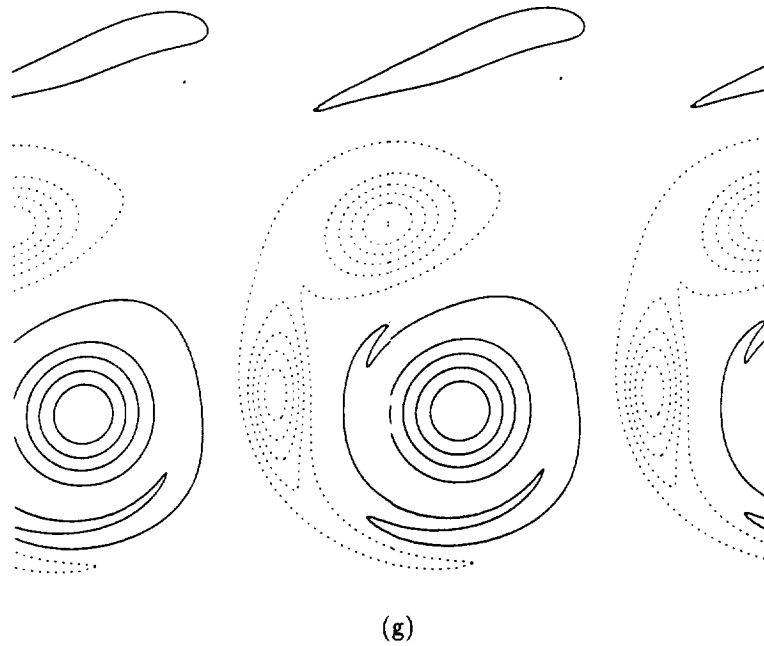
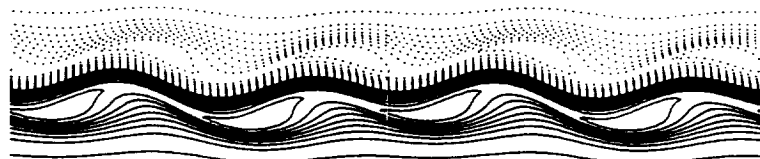
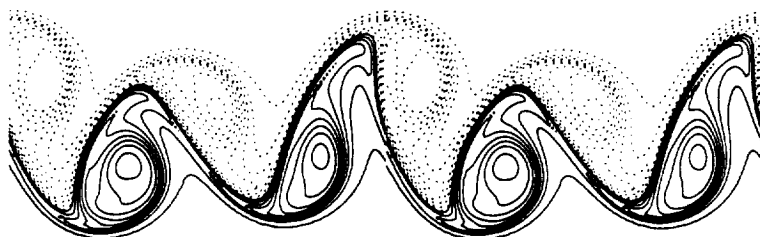


Figure 3.4: Iso-vorticity contours for  $346(0)_{00x}^{xxx}$  wake (two-dimensional fundamental and subharmonic) at various times. (a)  $t = 27.5$ . (b)  $t = 54.5$ . (c)  $t = 86.5$ . (d)  $t = 119.3$ . (e)  $t = 144.7$ . (f)  $t = 200.8$ . (g)  $t = 304.1$ . Contours are  $0.01 \leq |\omega| \leq 0.4$  in increments of 0.05.



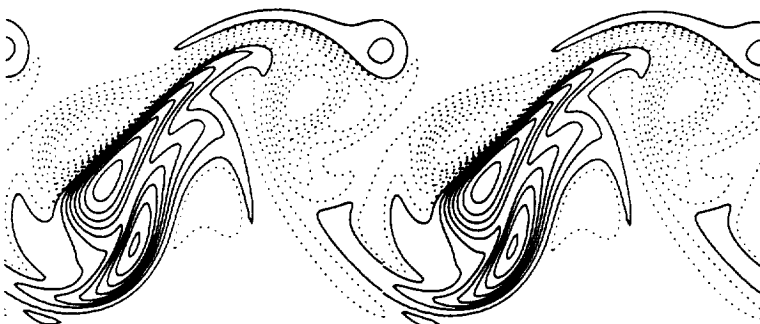
(a)



(b)



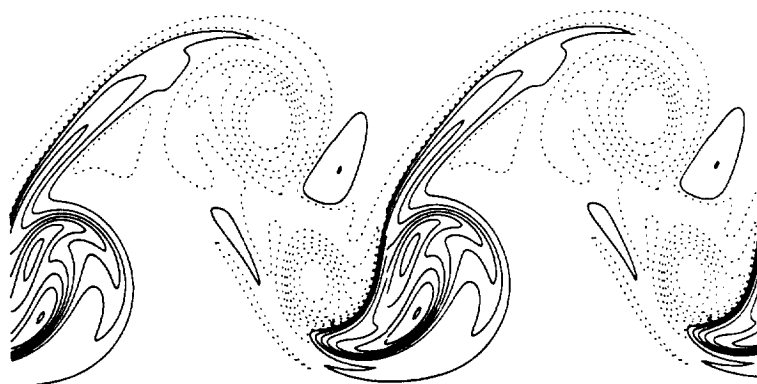
(c)



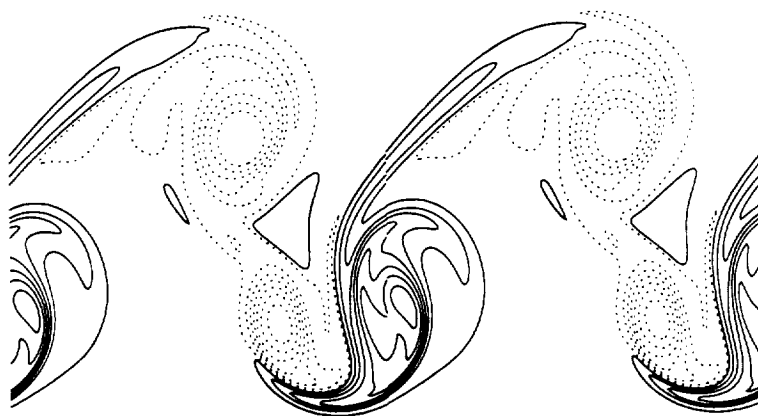
(d)

Figure 3.5: See caption page 62.





(e)



(f)

Figure 3.5: See caption page 62.

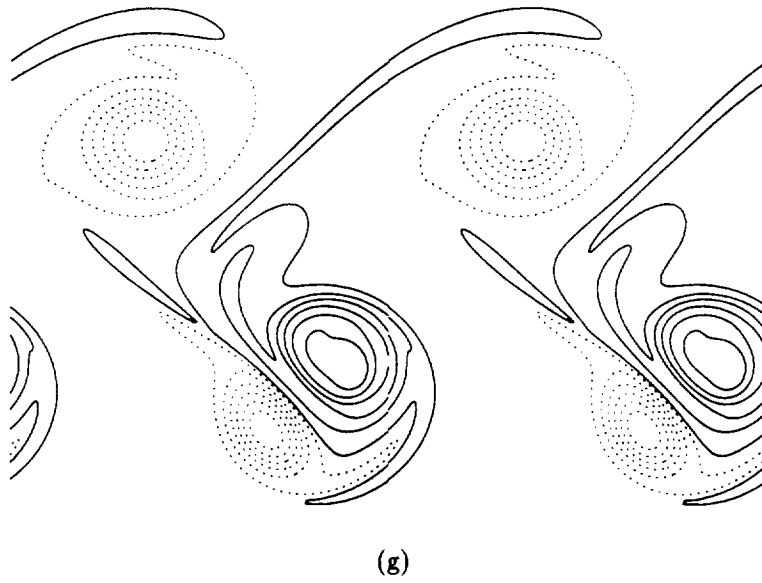


Figure 3.5: Iso-vorticity contours for  $346(0)_{0\frac{\pi}{4}x}^{\pi\pi\pi}$  wake (two-dimensional fundamental and subharmonic at  $\frac{\pi}{4}$ ) at various times. (a)  $t = 27.6$ . (b)  $t = 54.7$ . (c)  $t = 85.6$ . (d)  $t = 118.7$ . (e)  $t = 144.6$ . (f)  $t = 157.1$ . (g)  $t = 198.7$ . Contours are  $0.01 \leq |\omega| \leq 0.4$  in increments of 0.05.

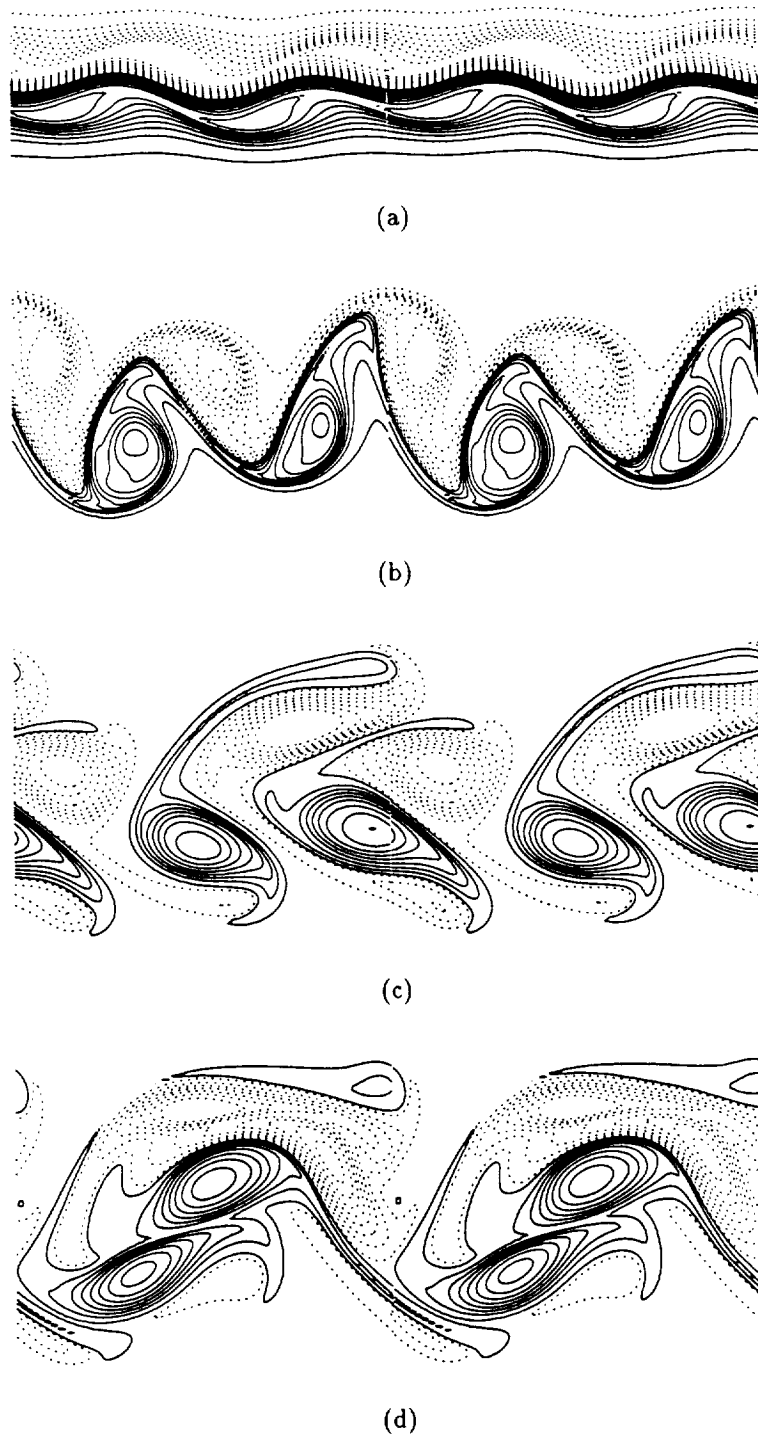
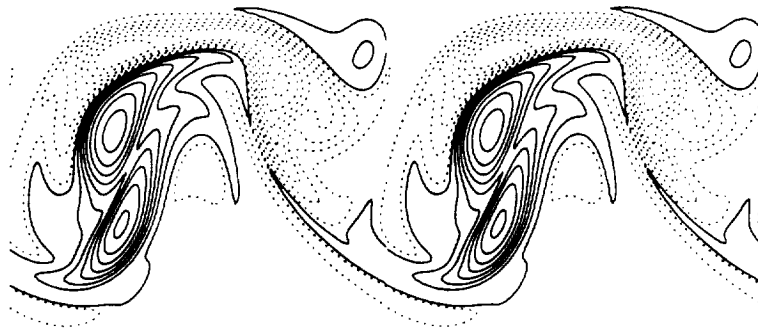
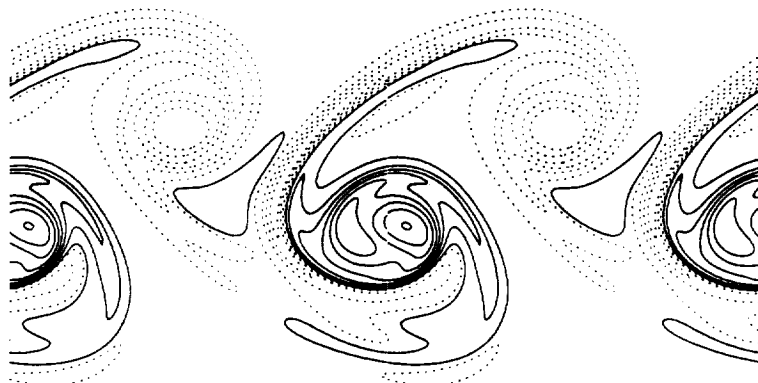


Figure 3.6: See caption page 65.



(e)



(f)

Figure 3.6: See caption page 65.

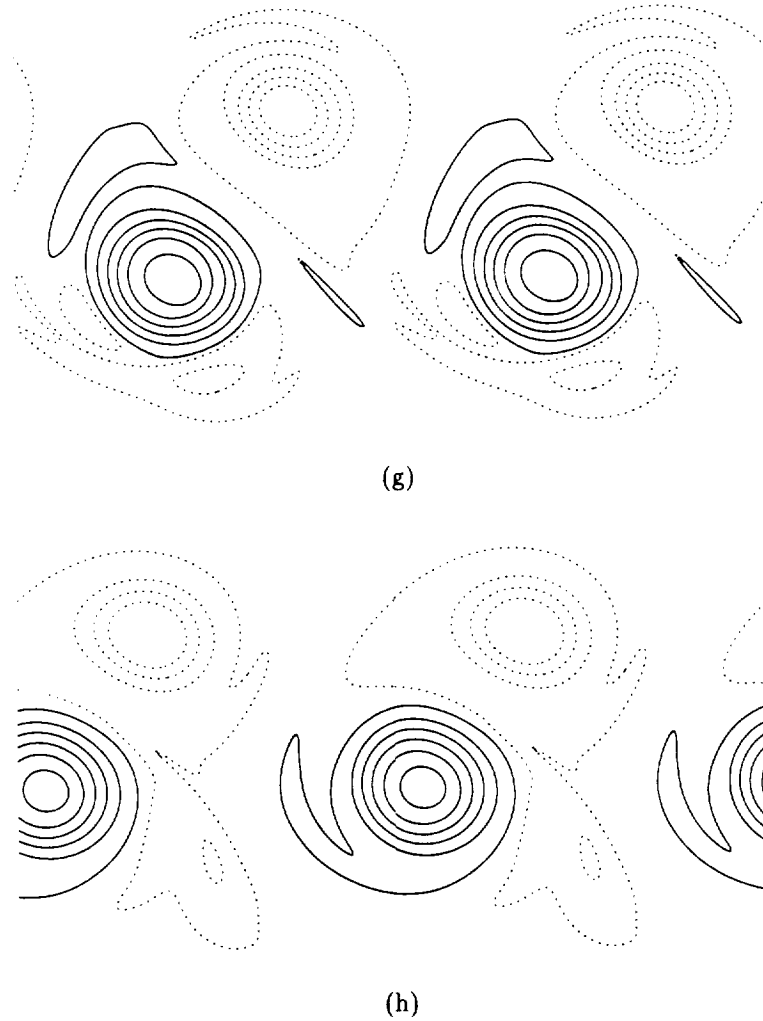


Figure 3.6: Iso-vorticity contours for  $346(0)_{0\frac{\pi}{2}x}$  wake (two-dimensional fundamental and subharmonic at  $\frac{\pi}{2}$ ) at various times. (a)  $t = 27.6$ . (b)  $t = 54.6$ . (c)  $t = 84.9$ . (d)  $t = 107.2$ . (e)  $t = 119.6$ . (f)  $t = 155.4$ . (g)  $t = 247.7$ . (h)  $t = 301.1$ . Contours are  $0.01 \leq |\omega| \leq 0.4$  in increments of 0.05.

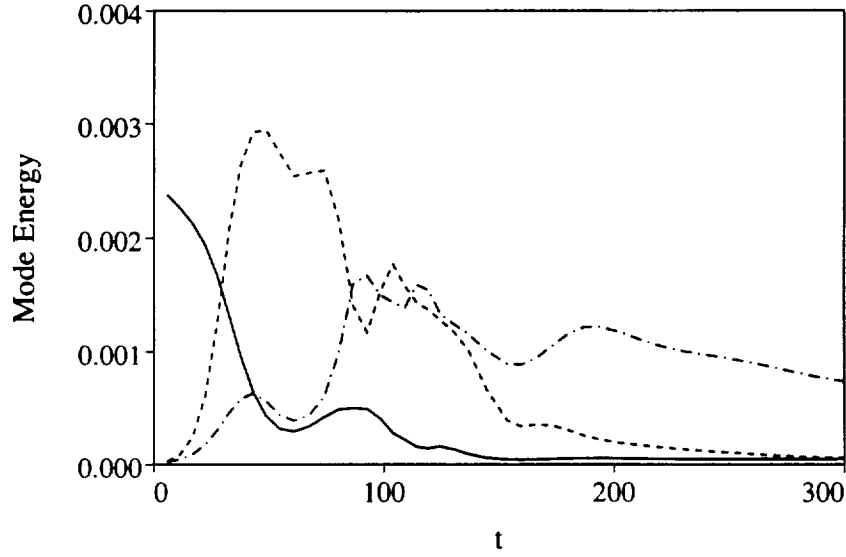


Figure 3.7: Mean, fundamental, and subharmonic mode energies versus time for  $346(0)_{00x}^{xxx}$  wake. —:  $0.1 \times$  mean flow energy. ----: Fundamental mode energy. - · - · -: Subharmonic mode energy.

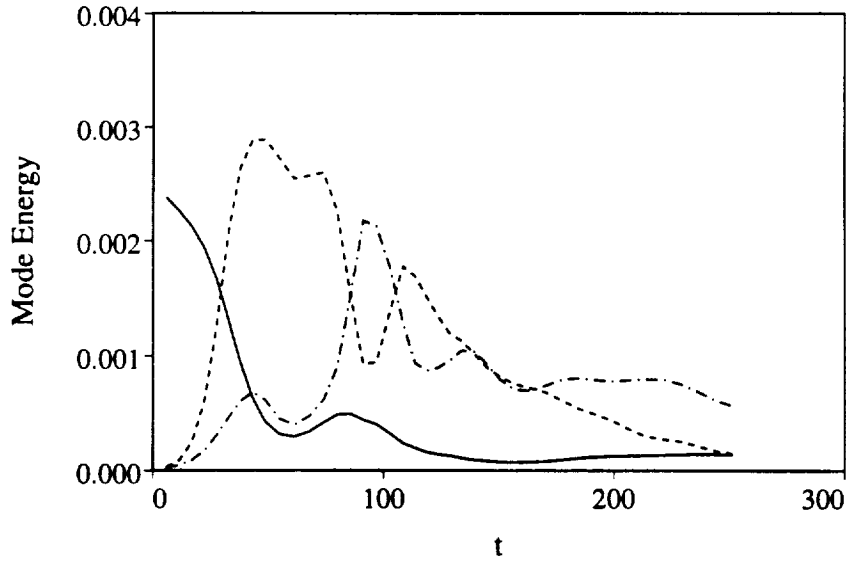


Figure 3.8: Mean, fundamental, and subharmonic mode energies versus time for  $346(0)_{0_{\frac{\pi}{4}}x}^{xxx}$  wake. —:  $0.1 \times$  mean flow energy. ----: Fundamental mode energy. - · - · -: Subharmonic mode energy.

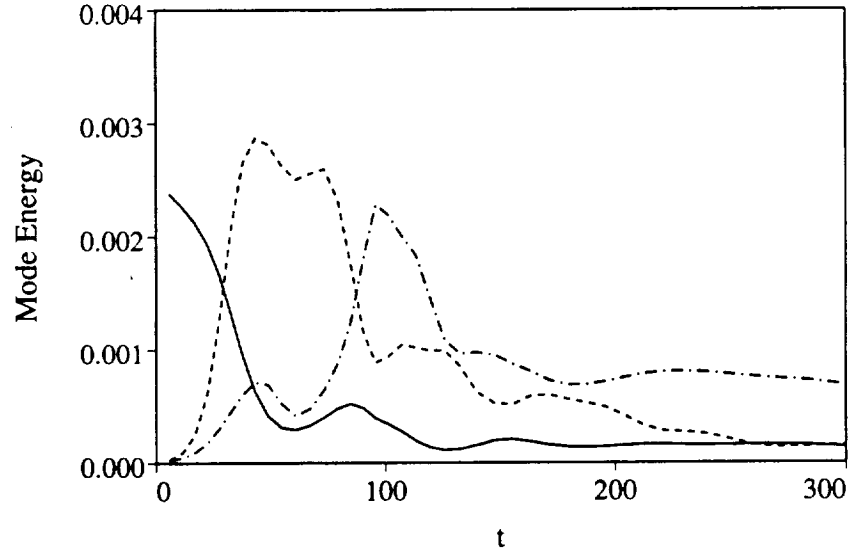


Figure 3.9: Mean, fundamental, and subharmonic mode energies versus time for  $346(0)_{0\frac{\pi}{2}x}^{xxx}$  wake. —:  $0.1 \times$  mean flow energy. ----: Fundamental mode energy. - · - · - : Subharmonic mode energy.

addition of longer wavelength disturbances has the effect of strengthening some of the rollers while simultaneously weakening others. This causes the rollers to merge, orbit one another, or shred as the wake evolves. The details of the evolution depend on which rollers are strengthened or weakened, and hence depends on the relative phasing of the fundamental and subharmonic disturbances. Figures 3.4, 3.5, and 3.6 show the evolution of the vorticity fields for the wakes  $346(0)_{00x}^{xxx}$ ,  $346(0)_{0\frac{\pi}{4}x}^{xx}$ , and  $346(0)_{0\frac{\pi}{2}x}^{xx}$ . As stated above, the initial development of all of these wakes parallels that of the flow in figure 3.2, which has only the fundamental wavelength disturbance, up through the development of the vortex street. Significant differences arise only after the fundamental disturbance begins to saturate during rollup.

In the wake in figure 3.4 ( $346(0)_{00x}^{xxx}$ ), the subharmonic, which is at zero phase with respect to the fundamental, acts to strengthen one of the rollers on the top of the wake while weakening the other (figure 3.4b). Because of the phasing, the two rollers on the bottom of the wake are initially of equal strength (the subharmonic disturbance has zero amplitude at the locations where the bottom rollers form). The strong top roller captures both of the bottom rollers (figure 3.4c), stretching them and forcing

them together (figure 3.4d). The elongated bottom rollers then agglomerate leaving a single new bottom roller and a pair of top rollers which are of roughly equal strength (figure 3.4e,f). One of the top rollers is then pulled to the bottom of the wake and sandwiched between the (periodic) bottom rollers. There it is stretched and slowly absorbed by the bottom roller (figure 3.4g)

The wake in figure 3.5 ( $(346(0)_{0\frac{\pi}{4}}^{\pi\pi\pi})$ ), which has a subharmonic at a phase of  $\pi/4$  with respect to the fundamental (shifted by one eighth of a fundamental wavelength), follows a similar evolution as the wake in figure 3.5. A dominant top roller forms which causes the bottom rollers, which in this case are of slightly different strengths, to agglomerate into a single large roller. This is followed by the bottom roller capturing one of the top rollers and forming a vortex pair. It is not clear whether this is a stable arrangement, but it persists well past  $t = 200$ .

Simulations by Aref & Siggia [1] of a two-dimensional inviscid wake using a discrete vortex method showed similar results. When they initiated their simulations with a random variation in the position of their vortices (which translates into a random initial disturbance field) they observed pairing of regions of vorticity of the same sign and the formation of vortex pairs (as seen here) and triplets. The vortex pairs were observed to persist through the length of the simulations.

Williamson & Roshko [56], in experiments on vortex formation in the wake of an oscillating cylinder, observed similar asymmetric pairing of vortices. By varying the frequency and amplitude of oscillation, they were able to produce repeatable wakes with various combinations of single vortices and pairs of opposite signed vortices. Under certain conditions the vortex pairs would self-convect away from the wake centerline (cf. their figure 17), much as is seen here in figures 3.4 and 3.5.

The wake in figure 3.6 ( $(346(0)_{0\frac{\pi}{2}}^{\pi\pi\pi})$ ), which has a subharmonic at a phase of  $\pi/2$  with respect to the fundamental (shifted by one quarter of a fundamental wavelength), undergoes a markedly different evolution. In this simulation, the phasing of the subharmonic disturbance creates a symmetry condition such that each side of the wake develops a strong roller and a weak roller, with the difference in strength between the rollers on each side of the wake the same. Instead of one side of the wake pairing and then absorbing a roller from the other side, the symmetry of the flow allows the



rollers on both sides of the wake to pair simultaneously. Note that this results in a much faster growth of the new vortex street than either of the other two wakes presented ( $t \approx 160.0$  as opposed to  $t > 200.0$  for both  $346(0)_{00x}^{\pi\pi\pi}$  and  $346(0)_{0\frac{\pi}{4}x}^{\pi\pi\pi}$ ). The resulting wake is nearly symmetric across the wake centerline (the small asymmetry is due to the fact that the value of  $\pi$  could only be represented to a finite accuracy), which is not the case for the wakes in figures 3.4 and 3.5.

Maekawa, Mansour, & Buell [24] performed direct numerical simulations of the two-dimensional *spatially* evolving incompressible wake forced with high amplitude random noise. Groups of structures very similar to those which appear in figures 3.4, 3.5, and 3.6 appear in those simulations (cf. their figure 11). At least for some structures in the spatially evolving wake, the random noise behaves dynamically like a fundamental plus a subharmonic at a random phase.

Figures 3.7, 3.8, and 3.9 show the evolution of the mean, fundamental, and subharmonic mode energies for the wakes shown in figures 3.4, 3.5, and 3.6. Up to a time of approximately  $t = 30$  the energies of the mean and fundamental mode develop as if there were no subharmonic disturbance present. This is consistent with the fact that up to that time the wake is in a linear growth regime, and therefore the main flow of energy should be from the mean to the fundamental.

After a time of  $t = 30$ , the subharmonic has gained enough energy to begin to affect the development of the fundamental mode. The presence of the subharmonic disturbance, which initially saps energy from the fundamental, lowers the saturation (peak) energy of the fundamental disturbance and causes it to saturate slightly earlier. The subharmonic experiences a “mini-saturation” slightly after the fundamental mode saturates, and begins to decay until a time of approximately  $t = 60$ . The subharmonic then begins to rapidly extract energy from the fundamental disturbance.

Up to a time of  $t = 90$  the energies in the flows with a subharmonic disturbance develop identically, independent of phase. The time  $t = 90$  corresponds to the time at which the rollers in the initial fundamental wavelength vortex street begin to pair (figures 3.4c/d, 3.5c/d, and 3.6c/d). After  $t = 90$  evolution of the mode energies begins to become phase dependent. Between  $t = 90$  and  $t = 150$  all of the subharmonic wakes show a periodic exchange of energy between the fundamental and subharmonic

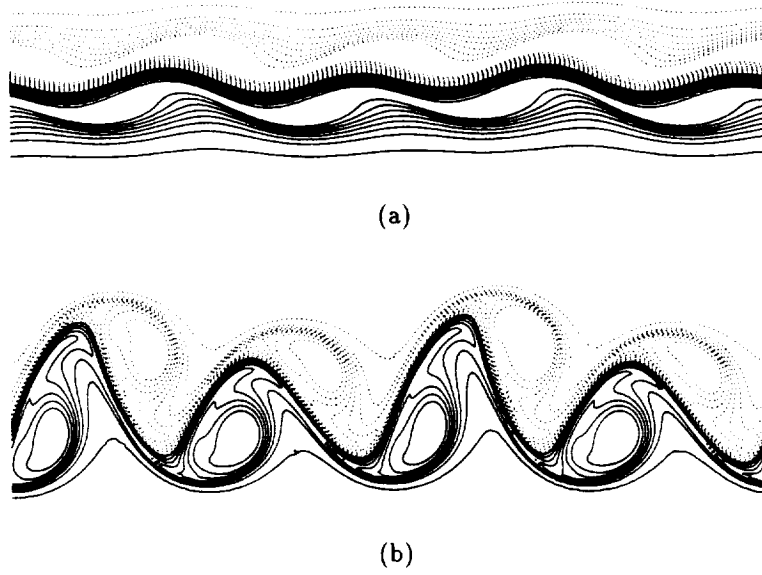
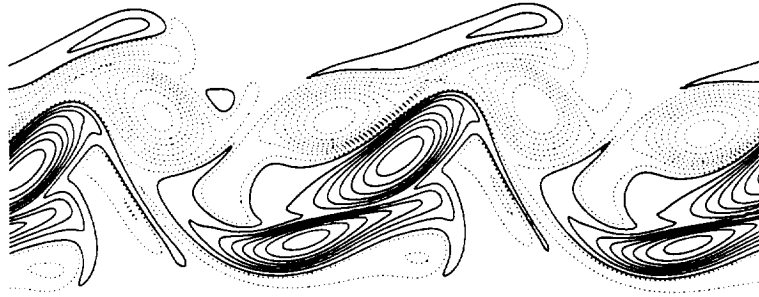
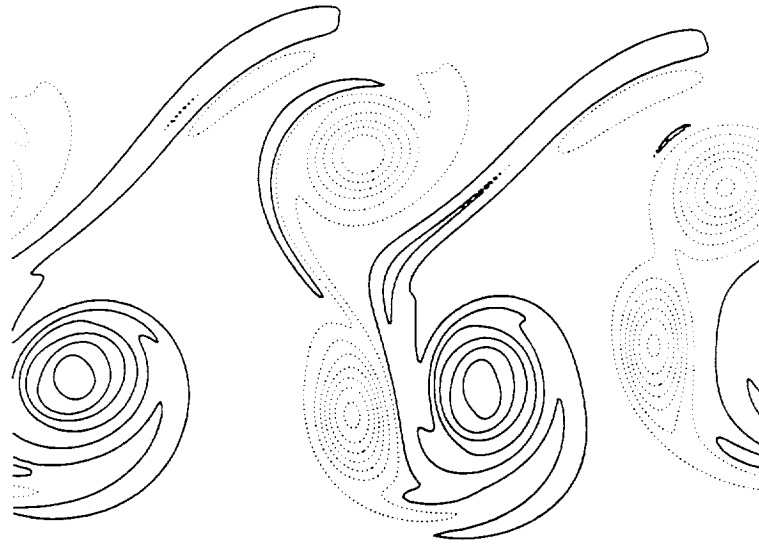


Figure 3.10: See caption page 71.



(c)



(d)

Figure 3.10: Iso-vorticity contours for  $346(0)_{000}^{xxx}$  wake (two-dimensional fundamental, subharmonic, and sub-subharmonic) at various times. (a)  $t = 25.5$ . (b)  $t = 48.6$ . (c)  $t = 102.5$ . (d)  $t = 204.4$ . Contours are  $0.01 \leq |\omega| \leq 0.4$  in increments of 0.05.

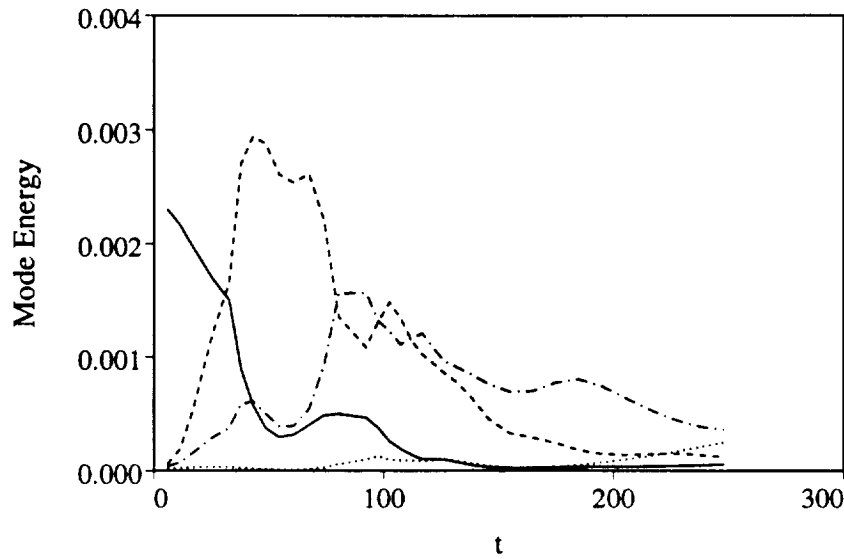


Figure 3.11: Mean, fundamental, subharmonic, and sub-subharmonic mode energies versus time for  $346(0)_{000}^{xxx}$  wake. —:  $0.1 \times$  mean flow energy. ----: Fundamental mode energy. - · - · -: Subharmonic mode energy. · · · · ·: Sub-subharmonic mode energy.

disturbances, as well as between the fundamental and the mean (this is most obvious in figure 3.9, but appears to a lesser degree in the other two figures). In each case, the fundamental eventually decays, dumping its energy into both the subharmonic and the mean, leaving the subharmonic as the dominant disturbance mode.

All of the wakes with subharmonic disturbances develop large structures that could potentially be constricted by the finite streamwise size of the box. To attempt to get a handle on the significance this constriction on the development of the wakes in figures 3.4 through 3.6, a wake with a sub-subharmonic disturbance was simulated. Figure 3.10 shows plots of iso-vorticity contours at four times in the development of the  $346(0)_{000}^{xxx}$  wake. Comparing figure 3.10 with the results for the  $346(0)_{00x}^{xxx}$  wake in figure 3.4, it is clear that at least up to a time of  $t = 200$ , the finite length of the computational box is not unduly affecting the wake structure. The sub-subharmonic disturbance has only a small noticeable effect on the development of the wake. Only at very late times is the presence of the sub-subharmonic disturbance likely to become

important, but for the moderate times studied here and in the three-dimensional simulations it is reasonable to assume that a subharmonic length box is sufficient.

Figure 3.11 shows the evolution of the mean, fundamental, subharmonic, and sub-subharmonic mode energies for the wake in figure 3.10. Comparing this figure to the corresponding figure for the  $346(0)_{00x}^{xxx}$  wake (figure 3.7 on page 66) it is clear that the sub-subharmonic disturbance remains at a very low energy late until in the simulation. The sub-subharmonic has no noticeable impact on the evolution of the energies of the shorter wavelength disturbances up until a time of approximately  $t = 150$ . After that time, the sub-subharmonic disturbance begins to slowly draw energy from the (dominant) subharmonic mode. Even at the latest time simulated the sub-subharmonic is beginning to grow rapidly at the expense of the subharmonic, but is still much weaker than the subharmonic mode.

### 3.3.3 Effect of Reynolds Number

Figures 3.12, 3.13, 3.14, and 3.15 show contour plots of vorticity for sets of wakes with the same initial disturbances at approximately the same time, but with different Reynolds numbers. In general, varying the Reynolds number has minimal effect on the large scale structure of the flow (given a high enough Reynolds number to allow the initial rollup). The major differences between flows with different Reynolds numbers has to do with the development of small scales.

At very low Reynolds numbers (figure 3.12a), viscosity dominates the wake to the point that it never enters the nonlinear growth regime. At slightly higher Reynolds numbers (figures 3.12b, 3.13a, 3.14a, and 3.15a), the wake rolls up and non-linear dynamics, including pairing of the rollers, are evident. The structures are still very diffuse, however, and adjacent regions of opposite signed vorticity annihilate each other quickly.

As the Reynolds number increases (figures 3.12c-f, 3.13b,c, 3.14b,c, and 3.15b,c), the decay of the intensity of the large vortical structures is significantly reduced and much smaller vorticity scales begin to appear. These small scales are the result of vortical regions being wrapped and folded around the rollers and vorticity being stretched in the high strain-rate regions between rollers. Without the strong diffusion

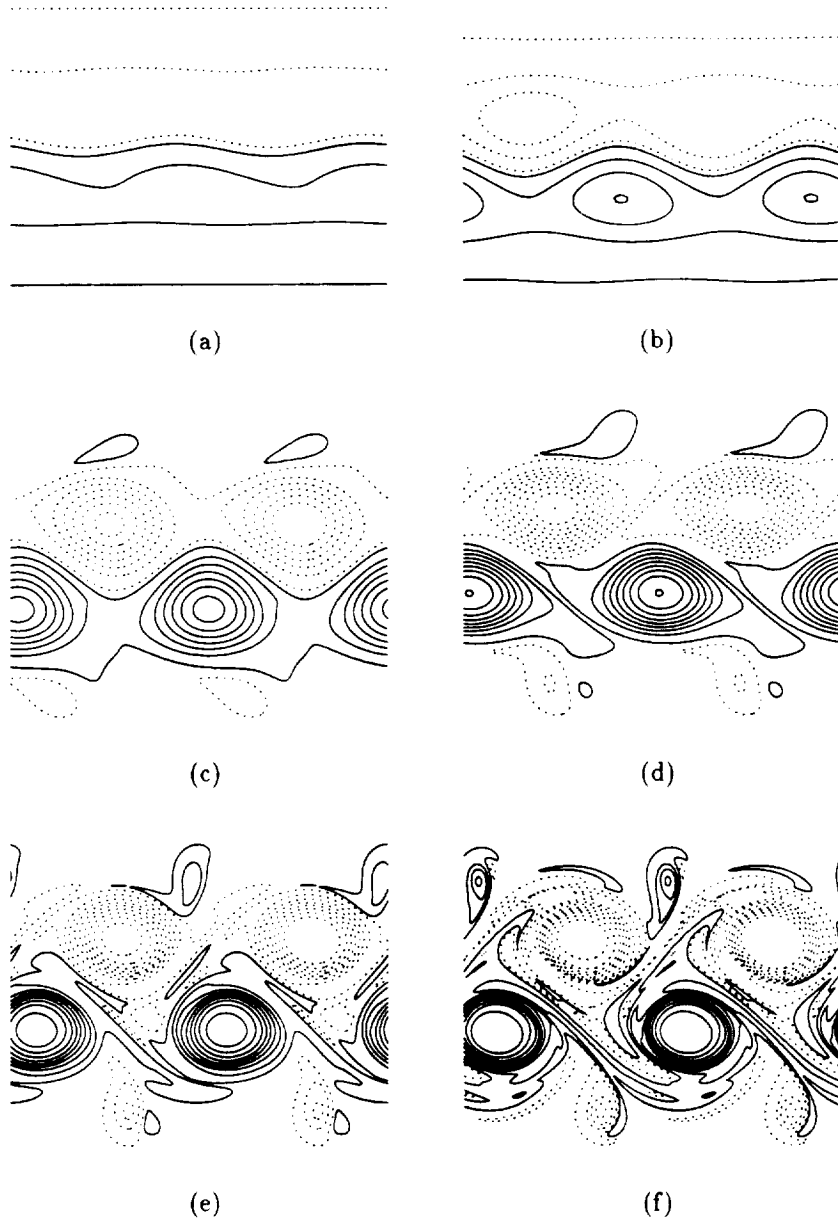


Figure 3.12: Iso-vorticity contours for  $\langle \tau \rangle(0)_{0xx}^{xxx}$  wakes (two-dimensional fundamental with various Reynolds numbers). (a)  $Re_b = 69, t = 200.7$ . (b)  $Re_b = 119, t = 201.8$ . (c)  $Re_b = 346, t = 198.6$ . (d)  $Re_b = 692, t = 201.3$ . (e)  $Re_b = 1384, t = 197.8$ . (f)  $Re_b = 2768, t = 196.3$ . Contours are  $0.01 \leq |\omega| \leq 0.4$  in increments of 0.05.

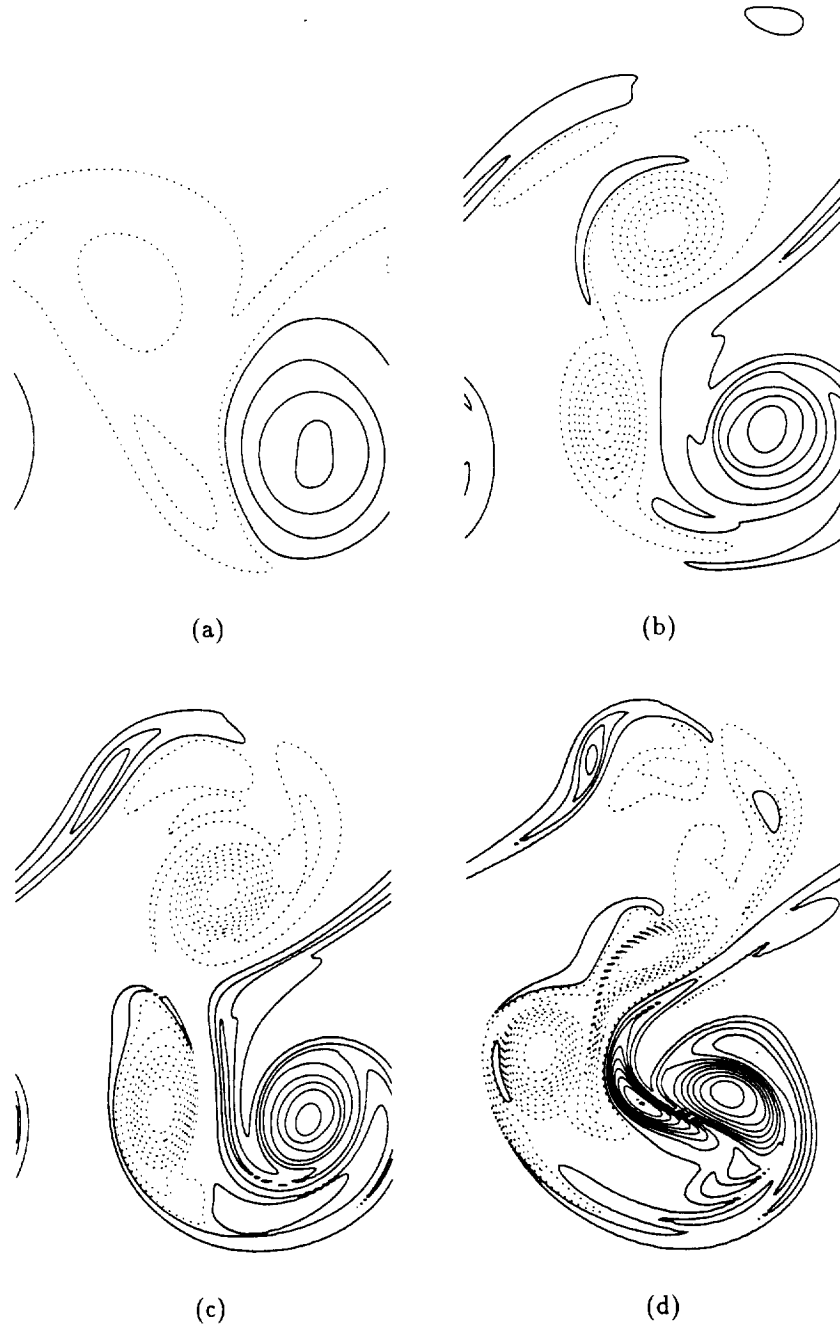


Figure 3.13: Iso-vorticity contours for  $\langle \omega \rangle(0)_{00x}^{xx}$  wakes (two-dimensional fundamental plus subharmonic with various Reynolds numbers). (a)  $Re_b = 119$ ,  $t = 194.6$ . (b)  $Re_b = 346$ ,  $t = 200.8$ . (c)  $Re_b = 692$ ,  $t = 199.1$ . (d)  $Re_b = 1384$ ,  $t = 208.1$ . Contours are  $0.01 \leq |\omega| \leq 0.4$  in increments of 0.05.

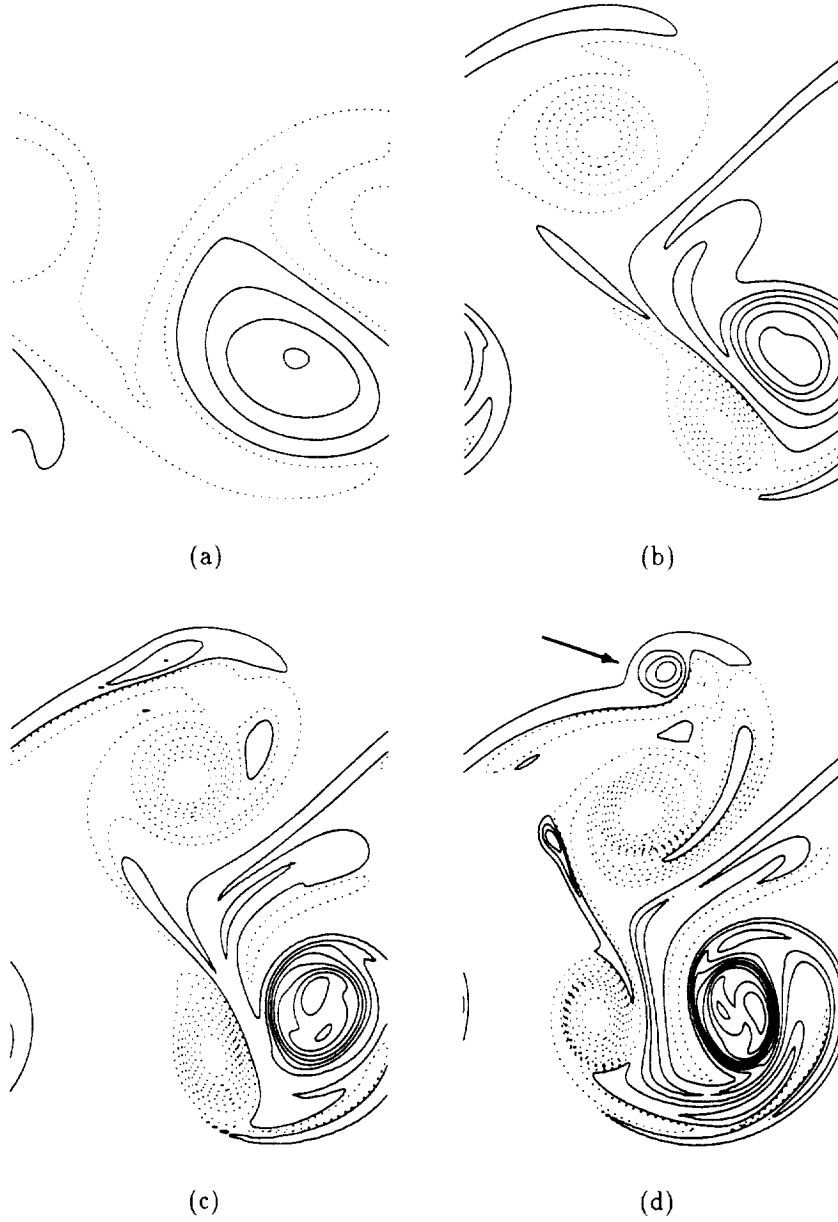


Figure 3.14: Iso-vorticity contours for  $(?) (0)_{0 \frac{\pi}{4} x}^{xxx}$  wakes (two-dimensional fundamental plus subharmonic at  $\frac{\pi}{4}$  with various Reynolds numbers). (a)  $Re_b = 119, t = 201.4$ . (b)  $Re_b = 346, t = 198.7$ . (c)  $Re_b = 692, t = 193.4$ . (d)  $Re_b = 1384, t = 195.2$ . Contours are  $0.01 \leq |\omega| \leq 0.4$  in increments of 0.05. Arrow indicates rollup of secondary shear layer.



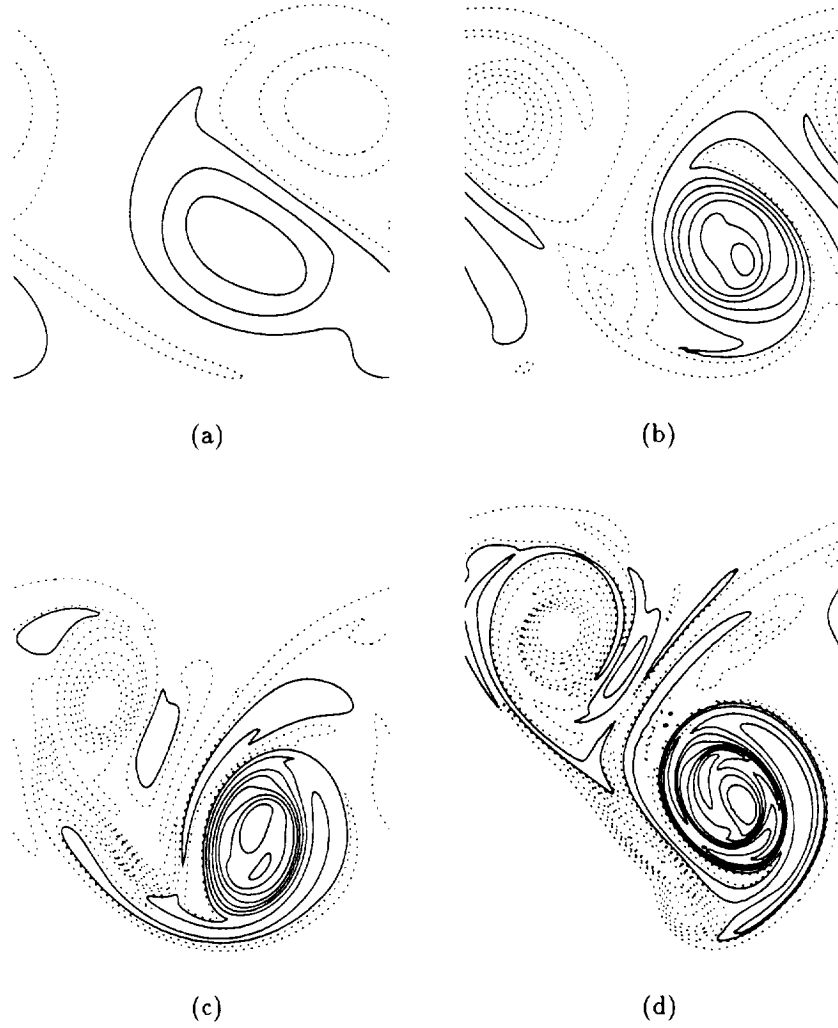


Figure 3.15: Iso-vorticity contours for  $(?) (0)_{0 \frac{\pi}{2} x}^{\pi x x}$  wakes (two-dimensional fundamental plus subharmonic at  $\frac{\pi}{2}$  with various Reynolds numbers). (a)  $Re_b = 119$ ,  $t = 205.3$ . (b)  $Re_b = 346$ ,  $t = 196.0$ . (c)  $Re_b = 692$ ,  $t = 197.3$ . (d)  $Re_b = 1384$ ,  $t = 200.2$ . Contours are  $0.01 \leq |\omega| \leq 0.4$  in increments of 0.05.

present in the wakes with lower Reynolds number, these fine structures do not get smeared out or absorbed by the larger structures.

As the Reynolds number increases there is also an increase in the strength and persistence of the vorticity in the fluid which has been convected across the wake in pinching off events during rollup and pairing. These pockets of pinched off fluid contain vorticity of the opposite sign as the rollers, adding significant complexity to the overall wake structure.

For the cases with pairing, at the higher Reynolds numbers (figures 3.13c,d 3.14c,d, and 3.15c,d) the post-pairing rollers show small scale internal structures (this is most evident in figure 3.13d, where the bottom “roller” still consists of two separate structures). There is also evidence of the onset of secondary rollup of the small scale shear layers which develop during the pairing process. The most obvious of these is in the long thin structure at the top of figure 3.14d (see arrow).

### 3.3.4 Scalar Field

Figure 3.16 shows contours of enstrophy density and scalar concentration for three of the wakes discussed above. Since the initial scalar field was set to the initial enstrophy density field, it is reasonable to assume that contour plots of these quantities should be similar in appearance. Any major differences are due to the fact that vorticity can be canceled out by vorticity of the opposite sign whereas the scalar is a positive quantity which is conserved.

It is clear from figure 3.16 that even at high Reynolds numbers where there is complex structure to the wake, the scalar field and the enstrophy density field are similar. Portions of the flow which have large enstrophy density tend to be regions where vorticity of opposite signs is not present. These regions have matching large values for the passive scalar. Regions of the flow with nonzero passive scalar concentrations but little enstrophy density correspond to once-vortical fluid which has undergone cancellation.

The scalar concentration plots in figure 3.16 give a good estimate for the level of entrainment of free-stream fluid by the various wakes. The wake in figure 3.16b (1384(0)<sub>00r</sub><sup>xxx</sup>) has entrained a large quantity of fluid from both the freestream above

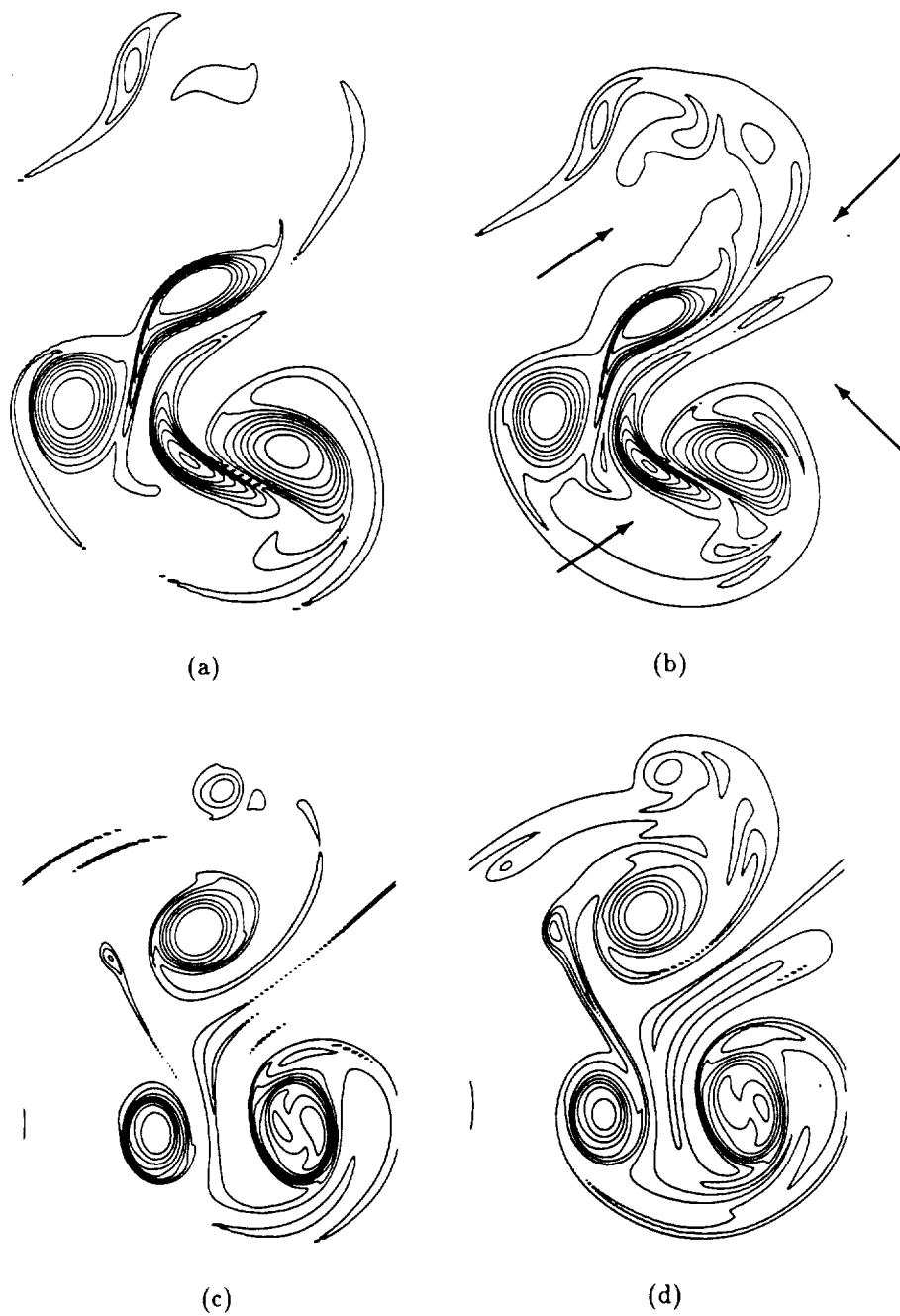


Figure 3.16: See caption page 80.

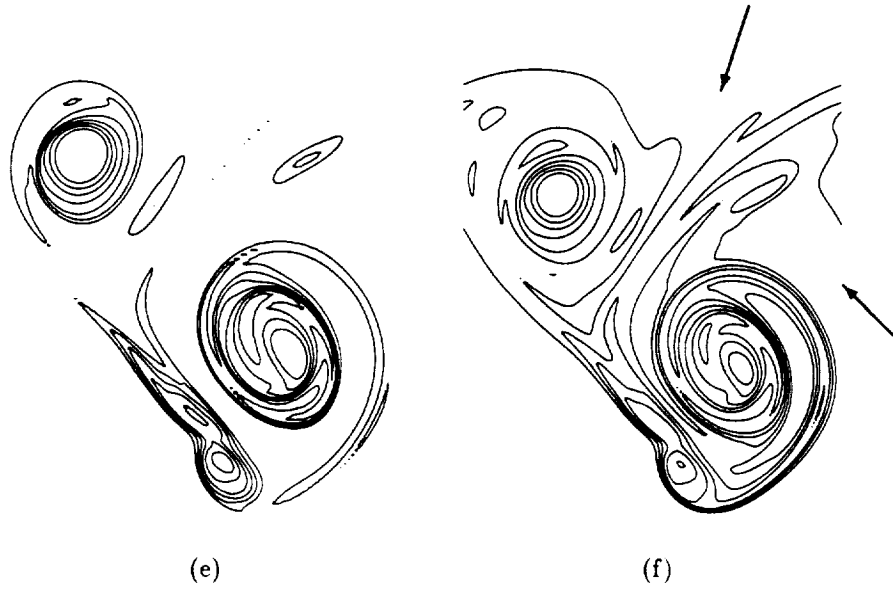


Figure 3.16: Comparison of iso-entrophy density and iso-scalar contours for  $1384(0)_{0(7)x}^{xxx}$  wakes (two-dimensional fundamental and subharmonic at various phases).  $1384(0)_{00x}^{xxx}$ ,  $t = 208.1$ . (a) Enstrophy Density. (b) Passive scalar.  $1384(0)_{0\frac{7}{4}x}^{xxx}$ ,  $t = 195.2$ . (c) Enstrophy Density. (d) Passive scalar.  $1384(0)_{0\frac{7}{2}x}^{xxx}$ ,  $t = 200.2$ . (e) Enstrophy Density. (f) Passive scalar. Contours are  $0.05 \leq |\omega|, C_1 \leq 0.4$  in increments of 0.05. Arrows indicate entrained fluid.

and below the wake (see arrows). In contrast, the wake in figure 3.16f (1384(0) $_{0\frac{x}{2}}^{xxx}$ ) has entrained very little freestream fluid (only what has been convected in between the periodic rollers on each side of the wake — see arrows). The differences in entrainment make a significant difference in the mixing which occurs in these wakes, and has a strong impact on their relative growth rates.

### 3.4 Growth of the Mean Flow

In all of the simulations, the mean velocity profile is defined to be the average velocity over the streamwise and spanwise directions for a given cross-stream position. The (“direct”) wake halfwidth,  $b$ , is then calculated by finding the maximum mean velocity for a given time in the simulation and taking half the width between outermost crossings of the mean velocity profile with the half maximum velocity point.

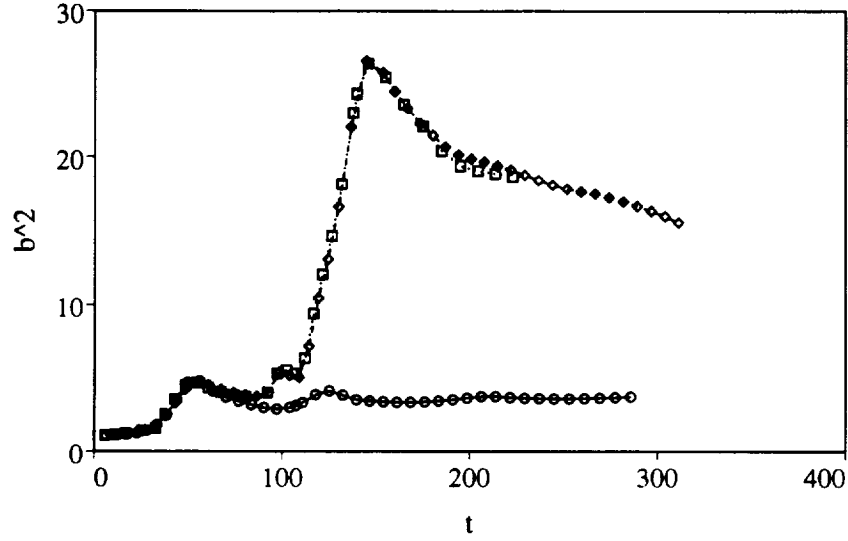
Since many of the flows to be presented develop non-Gaussian mean profiles, primarily due to the limited number of long wavelength modes available over which to average, a second, integral measure will also be presented. This integral halfwidth,  $b_i$ , is defined as

$$b_i = \sqrt{\frac{\ln 2}{2\pi}} \frac{\left( \int_{-\infty}^{+\infty} \Delta u dx_2 \right)^2}{\int_{-\infty}^{+\infty} \Delta u^2 dx_2} \quad (3.3)$$

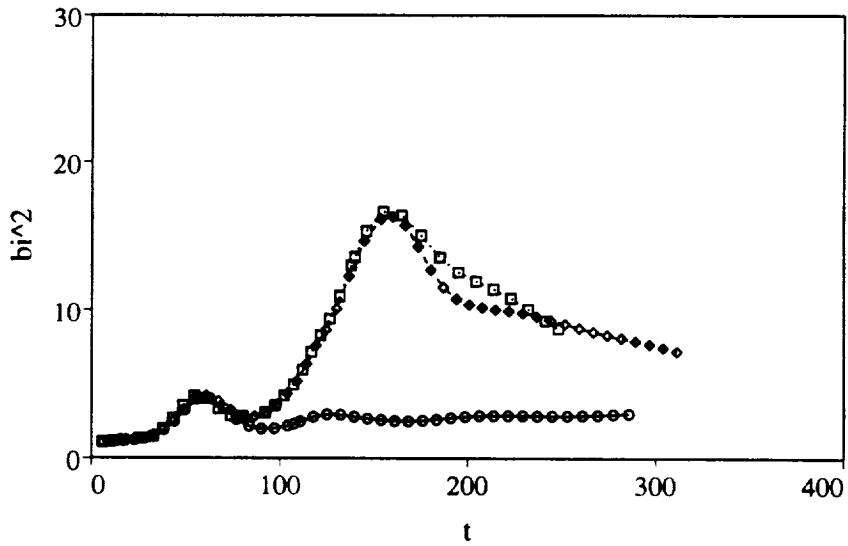
where  $\Delta u$  is the mean (streamwise) velocity defect profile. The integral halfwidth  $b_i$  has been formulated such that for a Gaussian velocity defect profile  $b_i = b$ . Since the initial velocity profiles are all Gaussian,  $b_i(t = 0) = b_0 = 1.0$ .

#### 3.4.1 Effect of Disturbance Wavelength

Similarity arguments applied to the temporally developing plane wake, where the momentum per unit streamwise length is assumed to be the only important governing parameter, lead to the conclusion that the far wake should grow asymptotically like  $t^{\frac{1}{2}}$ . Therefore it is convenient to use plots of the square of the wake halfwidth,  $b^2$  or  $b_i^2$ , versus time,  $t$ , to study the growth of the mean flow. In these coordinates,  $b \sim t^{\frac{1}{2}}$  or  $b_i \sim t^{\frac{1}{2}}$  growth will appear as a straight line.



(a)



(b)

Figure 3.17: Square of normalized wake halfwidth versus normalized time for  $Re = 346$  wakes with various disturbance wavelengths.  $\circ$ :  $346(0)_{0xx}^{xxx}$ .  $\diamond$ :  $346(0)_{00x}^{xxx}$ .  $\square$ :  $346(0)_{000}^{xxx}$ . (a) Direct halfwidth  $b$ . (b) Integral halfwidth  $b_i$ .

As a reference, the streamwise fundamental wavelength, as calculated from linear stability theory, is  $L_f = 7.85$ . The halfwidth  $b$  is therefore equal to the halflength of the computational domain when  $b^2 = 15.4$  for the fundamental only case,  $b^2 = 61.7$  for the cases with subharmonic disturbances, and  $b^2 = 246.7$  for the cases with sub-subharmonic disturbances. When  $b^2$  approaches these values it is likely that the streamwise confinement imposed by the computational box will become very significant. (Note: these values will also hold for the later three-dimensional computations).

Figure 3.17 shows plots of the square of the wake halfwidths versus time for three wakes with  $Re_b = 346$  started from initial fields containing a fundamental, a fundamental and a subharmonic, and a fundamental, a subharmonic, and a sub-subharmonic respectively. The circles correspond to the simulation that appears in figure 3.2 ( $346(0)_{0xx}^{xxx}$ ), the diamonds to the simulation in figure 3.4 ( $346(0)_{00x}^{xxx}$ ), and the squares to the simulation in figure 3.10 ( $346(0)_{000}^{xxx}$ ).

As discussed above, the wakes go through three distinct stages of evolution. Up to a time of approximately  $t = 30$ , which is the linear growth regime, the flow is laminar with exponentially growing sinusoidal disturbances. After a time of  $t = 30$ , the flow enters a nonlinear growth regime where the fundamental disturbance grows rapidly and the wake spreads quickly. At a time of approximately  $t = 50$  the wake width peaks as the fundamental begins to saturate and the vorticity field rolls up to form the Kármán vortex street. As the vortex street forms, the rollers relax slightly toward the wake centerline and the wake halfwidth drops.

Up to a time of  $t = 90$ , the growth of the wakes shown (and indeed all of the two-dimensional wakes studied) is clearly dominated by the evolution of the fundamental disturbance. After a time of  $t = 100$ , however, the longer wavelength disturbances become important. After  $t = 100$ , the simulation with only the fundamental disturbance ( $346(0)_{0xx}^{xxx}$ ) settles down to a uniform vortex street which spreads only slowly through viscous diffusion. The small oscillations in wake width at late time are due to the vortices positioning themselves into an asymptotically stable configuration, and are therefore less pronounced in the plot of the integral halfwidth.

The sharp increase in wake width at a time of  $t = 105$  for the simulations with the longer wavelength (subharmonic,  $346(0)_{00x}^{xxx}$ , and sub-subharmonic,  $346(0)_{000}^{xxx}$ ) disturbances corresponds to the growth of the subharmonic disturbance, which results in the initial pairing of the vortices on the bottom side of the wake (figures 3.4c,d). The wake width then peaks as the bottom rollers finish pairing and force one of the top rollers upwards (figures 3.4e). As the wake approaches a subharmonic vortex street configuration the rollers again settle back toward the centerline and the wake width decreases.

There is very little difference in the evolution of the wake with only the subharmonic and the wake with the addition of a sub-subharmonic disturbance. Up to the time simulated, the sub-subharmonic does not play a significant role. For a very long simulation, however, it is reasonable to expect that the sub-subharmonic would eventually lead to a second pairing of the vortex street. The effect of the sub-subharmonic are more evident in the plots of the integral halfwidth at late times, but the difference is still not significant.

### 3.4.2 Effect of Disturbance Phase

Figure 3.18 shows plots of the wake halfwidths versus time for the three simulations with  $Re_b = 346$  which were initiated with a fundamental and a subharmonic disturbance. These are the same wakes that appear in the vorticity contour plots in figures 3.4, 3.5, and 3.6. As one would expect after examining the vorticity contour plots, the phasing of the subharmonic has a very strong impact on the evolution of the mean width.

The two wakes with subharmonic phasing such that the rollers pair on one side and then capture a roller from the other side ( $346(0)_{00x}^{xxx}$  and  $346(0)_{0\frac{\pi}{4}x}^{xxx}$ ) have significantly greater maximum widths than the wake that pairs on both sides simultaneously. The point of maximum width for all of the wakes occurs in the middle of the pairing process, before the original rollers have fully combined. In the wakes that pair only on one side, the pairing process pushes one of the rollers on the other side of the wake away from the centerline. This serves to sharply increase the mean halfwidth of the wake. After the pairing rollers have completed their agglomeration, the roller that



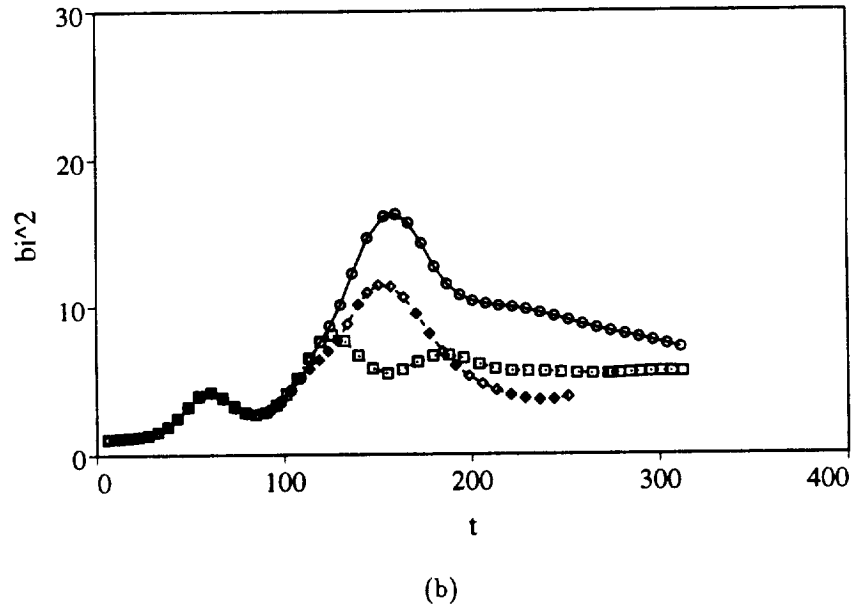
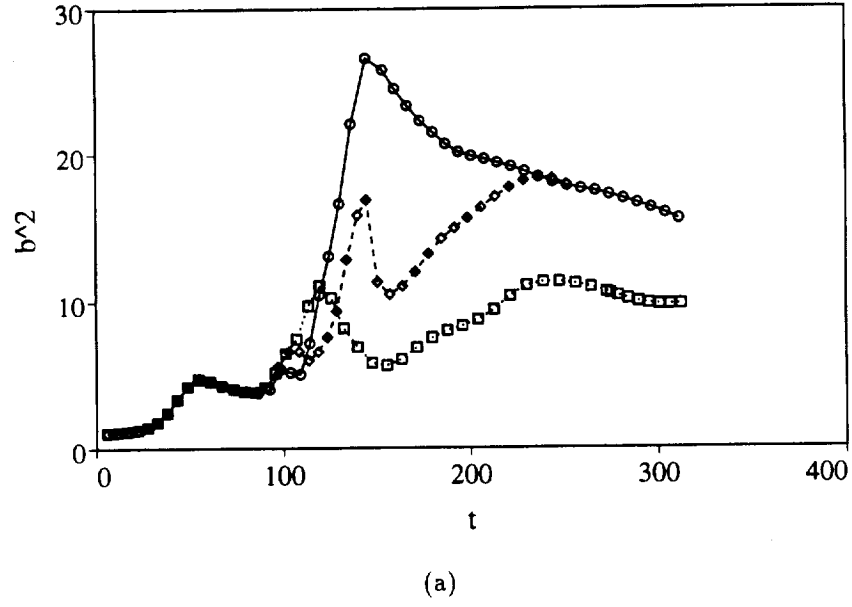


Figure 3.18: Square of normalized wake halfwidth versus normalized time for  $346(0)_{0(?)x}^{xxx}$  wakes (two-dimensional fundamental and subharmonic at various phases).  $\circ$ :  $346(0)_{00x}^{xxx}$ .  $\diamond$ :  $346(0)_{0\frac{\pi}{4}x}^{xxx}$ .  $\square$ :  $346(0)_{0\frac{\pi}{2}x}^{xxx}$ . (a) Direct halfwidth  $b$ . (b) Integral halfwidth  $b_i$ .

was pushed out is drawn back toward the centerline, decreasing the halfwidth again. In the wake which pairs on both sides simultaneously, the rollers on both sides of the wake stay close to the centerline, and the width peaks only slightly.

### 3.4.3 Effect of Reynolds Number

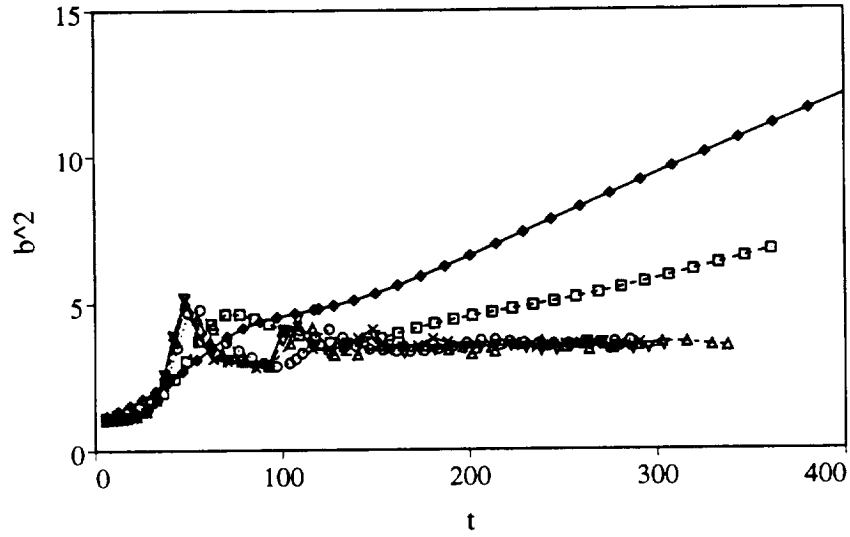
Figures 3.19, 3.20, 3.21, and 3.22 show plots of the square of the halfwidths versus time for wakes with identical initial disturbances but with different Reynolds numbers. The wake with the lowest Reynolds number shown is  $69(0)_{0xx}^{xxx}$  (open diamonds in figure 3.19). At this Reynolds number, the wake never rolls up. Although there is some nonlinear growth of the disturbances at early times (as evidenced by the small hump in the growth curves), the growth of this wake is due almost entirely to (rather rapid) viscous diffusion.

At a somewhat higher Reynolds number ( $119(0)_{0xx}^{xxx}$ ,  $119(0)_{00x}^{xxx}$ ,  $119(0)_{0\frac{x}{4}x}^{xxx}$ , and  $119(0)_{0\frac{x}{2}x}^{xxx}$ , all shown as open squares in figures 3.19, 3.20, 3.21, and 3.22), the wakes roll up to form vortex streets. Although pairing does occur where a subharmonic disturbance is present, the late time growth of all the wakes quickly become dominated by diffusion.

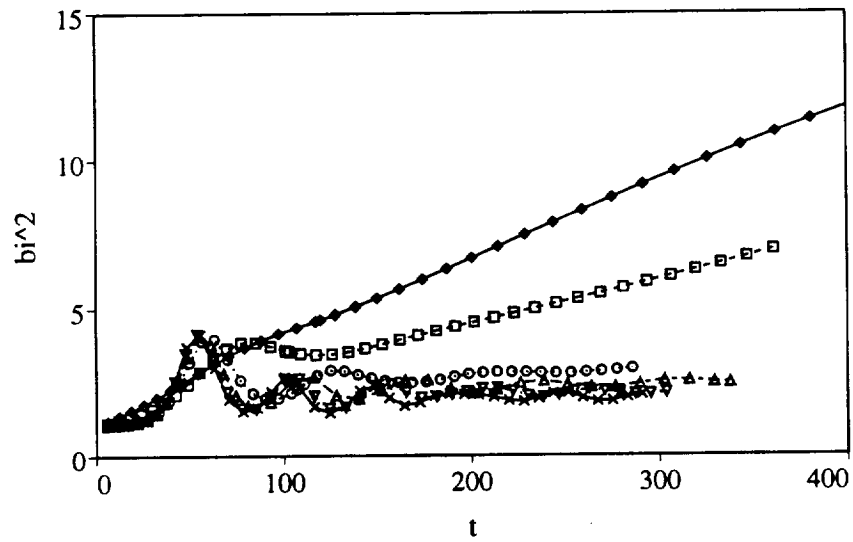
As the Reynolds number increases further, some measure of Reynolds number independence begins to appear in the growth of the mean flow. This is particularly true for the  $(?)_{0xx}^{xxx}$  wakes (figure 3.19). The growth curves for the  $Re_b = 346$ , 692, 1384, and 2768 wakes lie almost exactly atop one another. The only noticeable difference is that the initial wake rollup occurs slightly earlier at higher Reynolds numbers.

For the wakes that undergo pairing (figures 3.20, 3.21, and 3.22) the case for Reynolds number independence is somewhat weaker. The growth seems to be independent of Reynolds number up to approximately midway through the pairing of the rollers, at a point where the rollers are still recognizable as separate structures. Beyond this point the growth of the halfwidth appears to become dependent on viscosity again.

A large part of the variation in the “direct” halfwidth  $b$ , as compared to the integral halfwidth  $b_i$ , is due to the sensitivity of the measure to the shape of the mean velocity

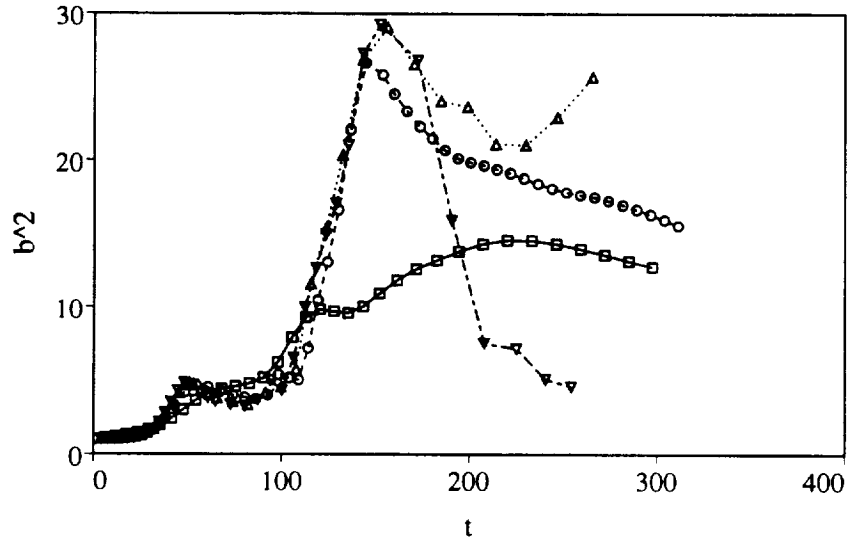


(a)

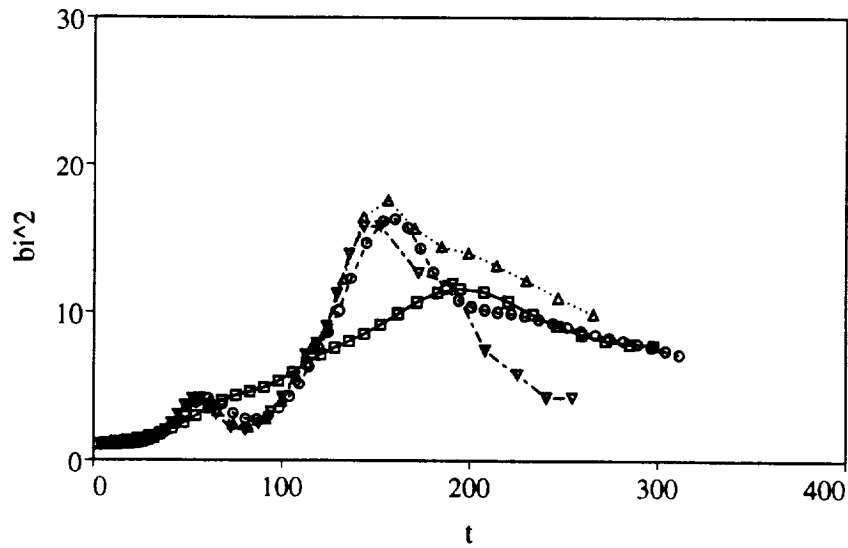


(b)

Figure 3.19: Square of normalized wake halfwidth versus normalized time for  $\langle ? \rangle(0)_{0xx}^{xxx}$  wakes (two-dimensional fundamental with various Reynolds numbers).  $\diamond$ :  $69(0)_{0xx}^{xxx}$ .  $\square$ :  $119(0)_{0xx}^{xxx}$ .  $\circ$ :  $346(0)_{0xx}^{xxx}$ .  $\triangle$ :  $692(0)_{0xx}^{xxx}$ .  $\nabla$ :  $1384(0)_{0xx}^{xxx}$ .  $\times$ :  $2768(0)_{0xx}^{xxx}$ . (a) Direct halfwidth  $b$ . (b) Integral halfwidth  $b_i$ .

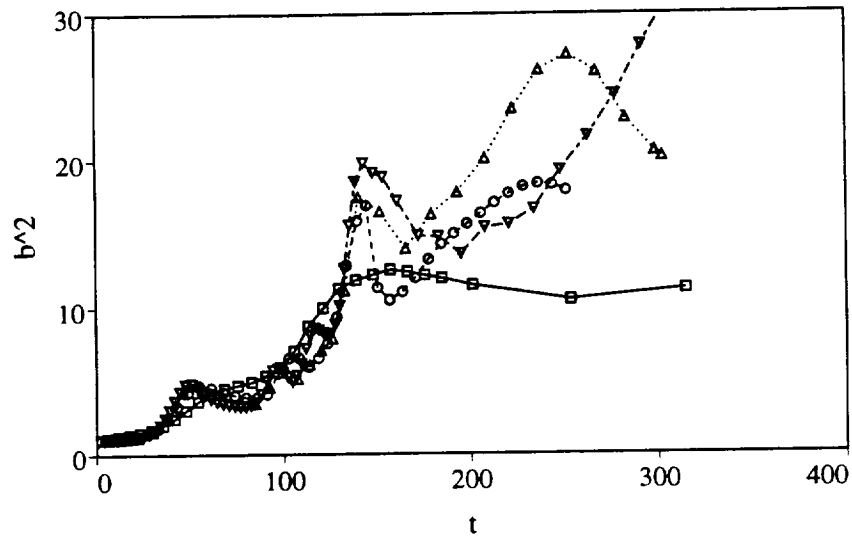


(a)

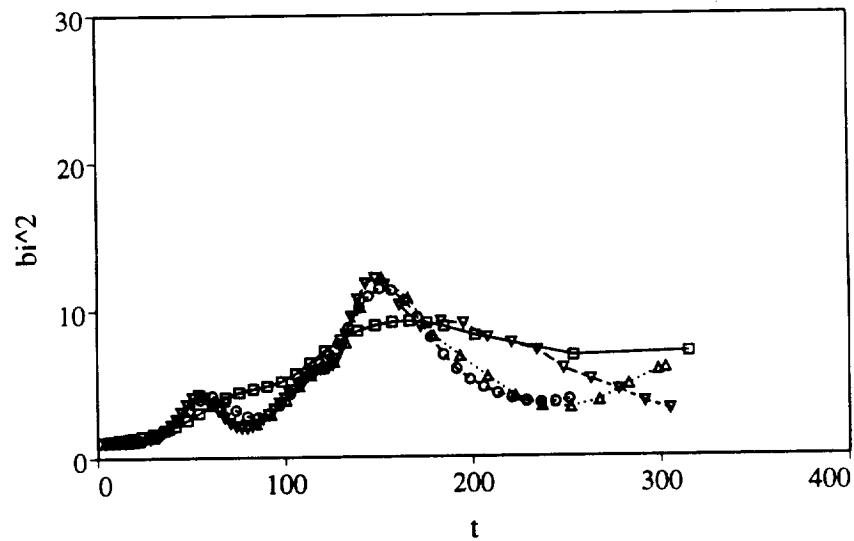


(b)

Figure 3.20: Square of normalized wake halfwidth versus normalized time for  $(?) (0)_{00x}^{xxx}$  wakes (two-dimensional fundamental and subharmonic with various Reynolds numbers).  $\square$ :  $119(0)_{00x}^{xxx}$ .  $\circ$ :  $346(0)_{00x}^{xxx}$ .  $\triangle$ :  $692(0)_{00x}^{xxx}$ .  $\nabla$ :  $1384(0)_{00x}^{xxx}$ . (a) Direct halfwidth  $b$ . (b) Integral halfwidth  $b_i$ .

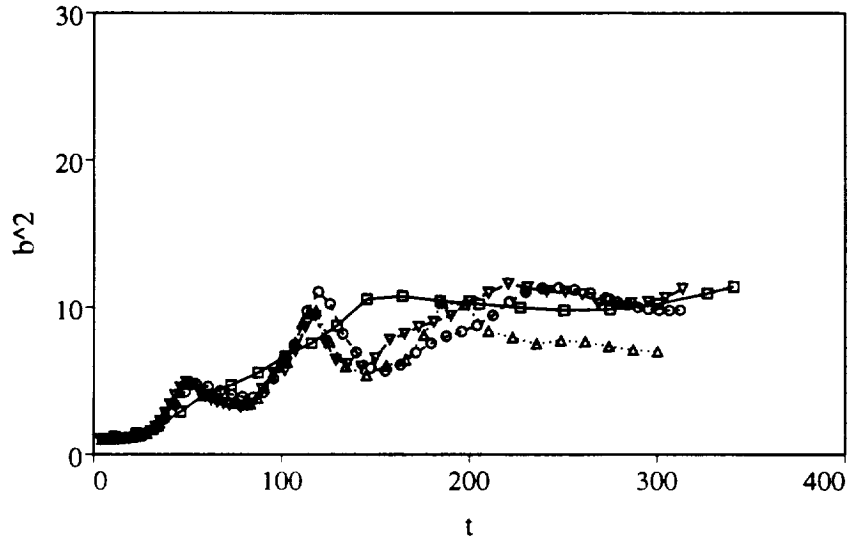


(a)

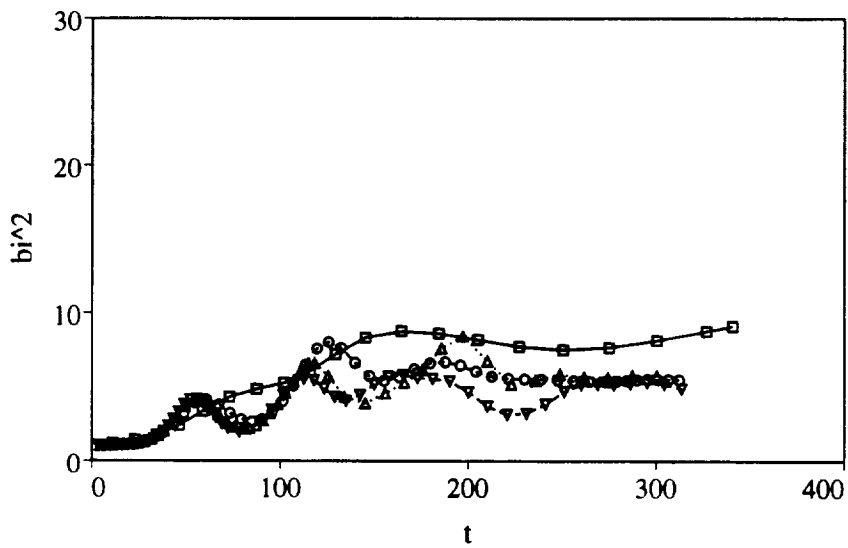


(b)

Figure 3.21: Square of normalized wake halfwidth versus normalized time for  $\langle ? \rangle(0)_{0 \frac{\pi}{4} x}^{xxx}$  wakes (two-dimensional fundamental and subharmonic at  $\frac{\pi}{4}$  with various Reynolds numbers).  $\square$ :  $119(0)_{0 \frac{\pi}{4} x}^{xxx}$ .  $\circ$ :  $346(0)_{0 \frac{\pi}{4} x}^{xxx}$ .  $\triangle$ :  $692(0)_{0 \frac{\pi}{4} x}^{xxx}$ .  $\nabla$ :  $1384(0)_{0 \frac{\pi}{4} x}^{xxx}$ . (a) Direct halfwidth  $b$ . (b) Integral halfwidth  $b_i$ .



(a)



(b)

Figure 3.22: Square of normalized wake halfwidth versus normalized time for  $(?)_0^{\frac{\pi}{2}x}$  wakes (two-dimensional fundamental and subharmonic at  $\frac{\pi}{2}$  with various Reynolds numbers).  $\square$ :  $119(0)_0^{\frac{\pi}{2}x}$ .  $\circ$ :  $346(0)_0^{\frac{\pi}{2}x}$ .  $\triangle$ :  $692(0)_0^{\frac{\pi}{2}x}$ .  $\nabla$ :  $1384(0)_0^{\frac{\pi}{2}x}$ . (a) Direct halfwidth  $b$ . (b) Integral halfwidth  $b_i$ .

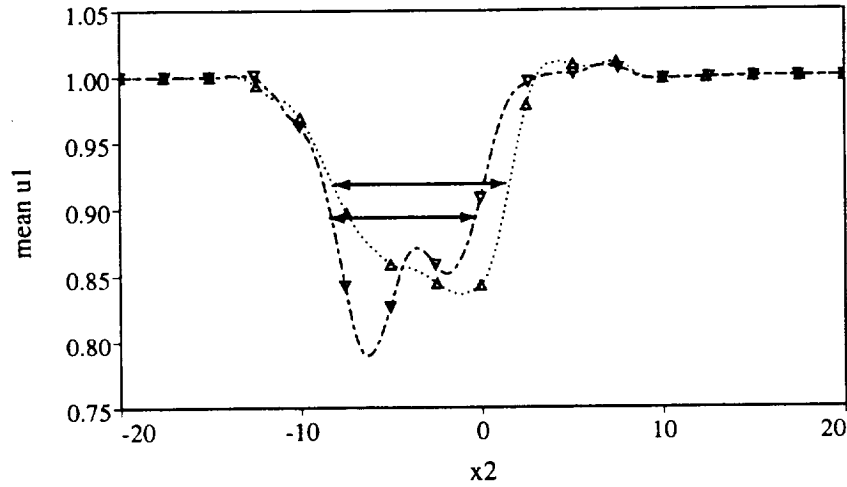


Figure 3.23: Comparison of mean velocity profiles for  $\langle 692 \rangle(0)_{00x}^{xxx}$  and  $\langle 1384 \rangle(0)_{00x}^{xxx}$  wakes (two-dimensional fundamental and subharmonic at 0).  $\triangle$ :  $692(0)_{00x}^{xxx}$ ,  $t = 199.1$ .  $\nabla$ :  $1384(0)_{00x}^{xxx}$ ,  $t = 208.1$ . (Symbols correspond to those in figure 3.20). Arrows indicate locations for measurement of “direct” halfwidths.

profile. The “direct” halfwidth is simply taken as half the width between the two outermost points where the mean streamwise velocity is at the half maximum velocity defect level. If the mean defect velocity profile is non-Gaussian, and in particular if it has “shoulders” or multiple peaks, then large variations in the measured halfwidth can appear between flows that look very similar in terms of vorticity distribution. This is an inherent shortcoming of the “direct” halfwidth measure  $b$  which becomes particularly acute in cases such as this where the mean profiles can be far from Gaussian.

This is illustrated by figure 3.23, which shows mean streamwise velocity profiles for the simulations that are presented in figures 3.13c and 3.13d. The vorticity fields of these flows appear very similar, but due to the way the large scale structures have arranged themselves, they produce very different mean profiles. At the lower Reynolds number, the rollers are more scattered and diffuse, which results in a broad, flattened mean velocity profile. At the higher Reynolds number, however, the fact

that the rollers are compact, and that the top roller has been pulled further toward the bottom of the wake produces a mean profile with a narrow, intense peak. Though the vorticity in both wakes has spread out over approximately the same spanwise extent (which is another possible measure of the width), the “direct” halfwidth  $b$  (arrows) is very different between the two cases.

As noted above, the difference in the integral halfwidth,  $b_i$ , is much smaller than for the “direct” halfwidth  $b$ . There is, however, still a significant difference in the widths of the  $692(0)_{00x}^{xx}$  and  $1384(0)_{00x}^{xx}$  wakes ( $\Delta$  and  $\nabla$  in figure 3.20b respectively). The higher Reynolds number  $1384(0)_{00x}^{xx}$  wake is significantly more compact than the lower Reynolds number flows. This is due to the fact that at this particular subharmonic phasing, one side the wake develops a single region of concentrated vorticity, while the vorticity in the other side of the wake remains in two weaker regions. The difference in the relative strength of the regions of vorticity that form allow the single strong region to capture one of both of the weaker regions from the opposite side of the wake. At the highest Reynolds number shown,  $1384(0)_{00x}^{xx}$ , the very strong concentrated vorticity region at the bottom of the wake captures both of the weaker vorticity concentrations at the top of the wake, resulting in a very compact configuration. At the lower Reynolds numbers shown just one of the upper vorticity concentrations is captured, resulting in a wider wake (see figure 3.13 on page 75). In contrast, the other two subharmonic phasings examined result in wakes in which the vorticity concentrations that develop on opposite sides of the wake are more balanced in strength. Neither side of the wake can capture all of the significant vorticity concentrations from the other side of the wake, independent of the wake Reynolds number (see figures 3.14 and 3.15 on pages 76 and 77).



# Chapter 4

## Three-dimensional Simulations

### 4.1 Motivation

To explore the effects of initial conditions on the development of the three-dimensional incompressible plane wake, a set of three-dimensional simulations has been run using various initial conditions. The effects of disturbance wavelength, phasing, and wake Reynolds number are examined in this section.

### 4.2 Simulation Parameters

#### 4.2.1 Three-dimensional Forcing

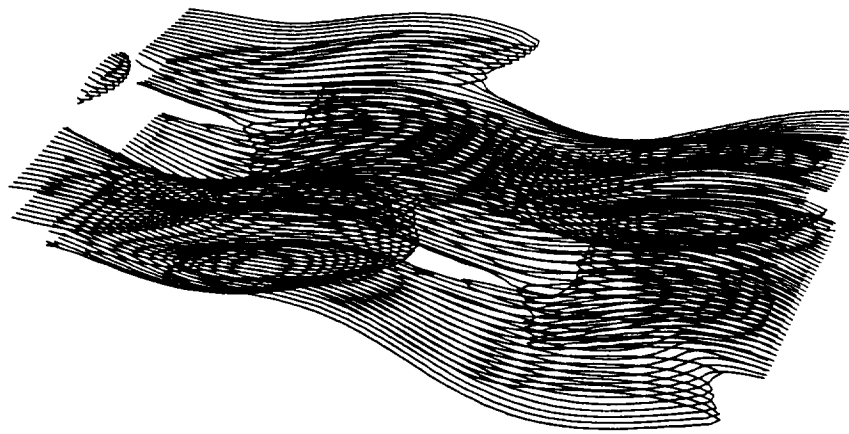
As discussed in section 2.7, the initial conditions for the three-dimensional simulations were composed of a Gaussian mean streamwise velocity profile with sets of small amplitude periodic disturbances superimposed. Simulations were performed at Reynolds numbers based on initial halfwidth and defect velocity of between 69 and 2768. The majority of wakes simulated were at a Reynolds number of  $Re_b = 346$ . Based on the results of the two-dimensional simulations presented in chapter 3, this should be a sufficiently high Reynolds number to capture the main effects of the variety of initial disturbances on the large scale development of the wake. Simulations at the highest Reynolds numbers, which are much more computationally demanding, were run for

only a few select sets of initial disturbances in order to examine the transition to turbulence. Table H.2 in appendix H gives a summary of all of the three-dimensional simulations that have been performed.

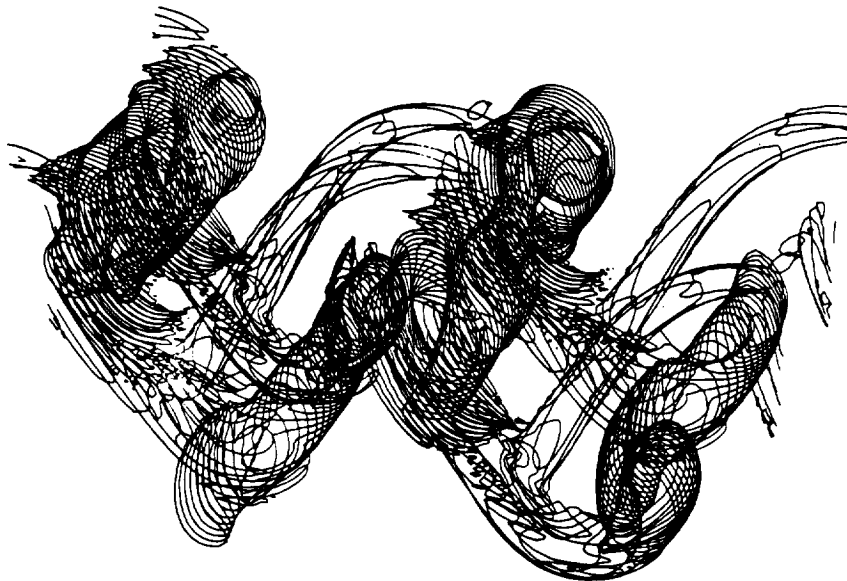
### 4.3 Structural Development of the Three-dimensional Wake

Figure 4.1 shows perspective views of three-dimensional iso-*enstrophy* density contours at four times in the development of the  $346(60)_{0xx}^{x0x}$  wake (two-dimensional fundamental disturbance and a pair of  $60^\circ$  oblique disturbances at the subharmonic wavelength). The freestream flow direction is from left to right. The contour level was chosen to be  $|\omega| = 0.4$ . This corresponds to approximately 60% of the initial mean wake defect velocity divided by the initial wake halfwidth, which serves as a rough measure of the mean gradient in the initial flow.

The development of this wake is typical of the wakes initiated with a two-dimensional fundamental disturbance and a pair of  $60^\circ$  oblique disturbances at the subharmonic wavelength. The initial development is primarily two-dimensional, with the fundamental (Kármán) mode growing most quickly as predicted by linear theory. The flow develops well defined spanwise rollers with relatively weak streamwise structures stretching between rollers on the same side of the wake (figure 4.1b). Once the rollers are established, the three dimensional disturbances grow rapidly in strength under the influence of the resulting straining field. (figure 4.1b,c). As the streamwise structures become more intense, they begin to distort the rollers, breaking up their spanwise coherence (figure 4.1c). Eventually, the streamwise structures, both the original structures and ones which are the result of the distortion of the spanwise rollers, become the dominant features in the flow (figure 4.1d). Note that as the wake spreads with time, the maximum vorticity due to the mean flow drops, so the magnitude of a fixed level of vorticity relative to the gradients of the mean flow becomes substantially larger. The structures which appear in figure 4.1d are at an intensity level far above the vorticity due to the mean shear. Compared to the contour level of



(a)



(b)

Figure 4.1: See caption page 97.



(c)

Figure 4.1: See caption page 97.



Figure 4.1: Iso-entropy density contour for  $346(60)_{0xx}^{x0x}$  wake (two-dimensional fundamental plus three-dimensional subharmonic). Contour level is  $|\omega| = 0.4$ . (a)  $t = 22.8$ . (b)  $t = 52.8$ . (c)  $t = 102.7$ . (d)  $t = 204.8$ .

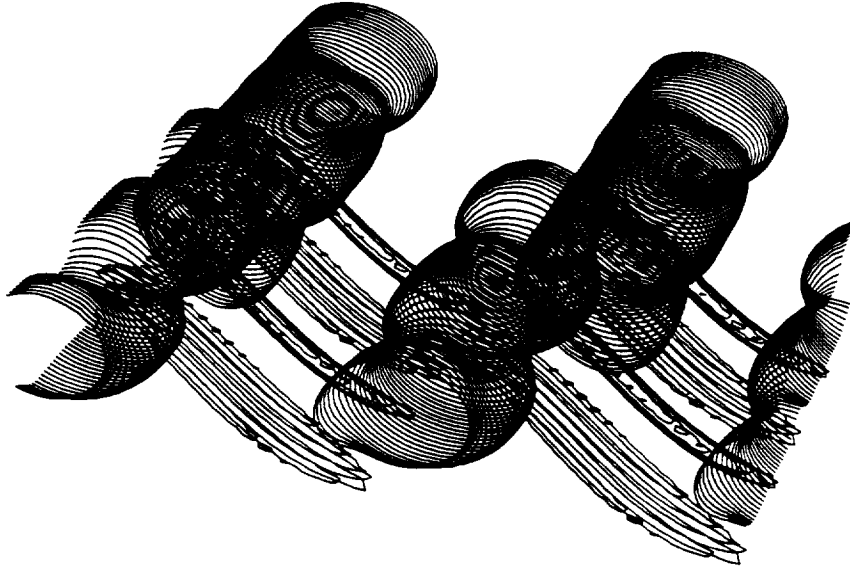


Figure 4.2: Iso-entrophy density contour for  $346(60)_{0xx}^{0xx}$  wake (two-dimensional fundamental plus three-dimensional fundamental).  $t = 196.9$ . Contour level is  $|\omega| = 0.2$ .

$|\omega| = 0.4$  shown, the mean shear at that late time, based on halfwidth and maximum defect velocity, is 0.037, more than an order of magnitude lower.

#### 4.3.1 Effect of Disturbance Wavelength

In stark contrast to the wake shown in figure 4.1 is the wake shown in figure 4.2. This is the  $346(60)_{0xx}^{0xx}$  wake (which has a two-dimensional fundamental disturbance and a pair of oblique disturbances at the *fundamental* wavelength). The contour level here is 0.2, half the level used in figure 4.1. With these initial conditions, strong three-dimensionality fails to develop even by the advanced time shown. The streamwise structures are present (the dominant ones can be seen running between rollers on the bottom side of the wake at this disturbance phasing), but exist as broad flat regions of vorticity, canted to the plane of the wake, as opposed to the intense tube-like structures which appear in the  $346(60)_{0xx}^{x0x}$  wake. The relatively low circulation of these weak streamwise structures is evidenced by their minimal impact on the spanwise rollers. The rollers in the wake in figure 4.2 are only slightly corrugated,

whereas at the corresponding time for the  $346(60)_{0xx}^{x0x}$  wake (figure 4.1d), the spanwise rollers have been entirely overwhelmed by the streamwise structures.

The effects of the addition of longer wavelength disturbances are illustrated by the wakes in figures 4.3, 4.5, and 4.7. Figure 4.3 shows the results from the  $346(60)_{00x}^{0xx}$  simulation. This wake was started from initial conditions similar to those used in figure 4.2, but with the addition of a two-dimensional subharmonic disturbance. Again, the evolution is dominated by two-dimensional dynamics, even at the late time ( $t = 202.8$ ) shown. As in the corresponding two-dimensional wake (figure 3.4), the two bottom rollers have paired to form one coherent roller, captured one of the top rollers, and drawn it down to the bottom of the wake. Although the three-dimensional structures are stronger than those found in the  $346(60)_{0xx}^{0xx}$  simulation, and have a tube-like shape as opposed to a flat shape, they are still substantially weaker than those found in the  $346(60)_{0xx}^{x0x}$  simulation. The effect of the moderate strength streamwise structures is to break up the spanwise coherence of the captured roller, with little impact on the other two (primary) rollers.

The essential two-dimensionality of this flow is reinforced by the plot in figure 4.4. This figure shows a comparison of the evolution of the first few streamwise (two-dimensional) mode energies for the three-dimensional wake  $346(60)_{00x}^{0xx}$  (symbols) and the corresponding two-dimensional wake  $346(60)_{00x}^{xx}$  (lines). Up to a time of approximately  $t = 150$  there is no significant difference in the development of the mean, two-dimensional fundamental or subharmonic mode energies between the two-dimensional and three-dimensional wake. Even at very late times the differences are relatively small. The subharmonic mode energy for the three-dimensional wake is somewhat lower due to energy being transferred into the three-dimensional modes, but the wake dynamics are still essentially those of a two-dimensional wake.

Figure 4.5 shows an iso-entrophy density contour for the  $346(60)_{00x}^{x0x}$  simulation, where a two-dimensional subharmonic has been added to the initial disturbance field. Note that the contour level shown is again  $|\omega| = 0.4$ . The addition of a two-dimensional subharmonic disturbance does not have a major impact on the development of the streamwise structures as compared to the  $346(60)_{0xx}^{x0x}$  simulation in figure 4.1. Similar primary streamwise structures exist in both flows, running between rollers

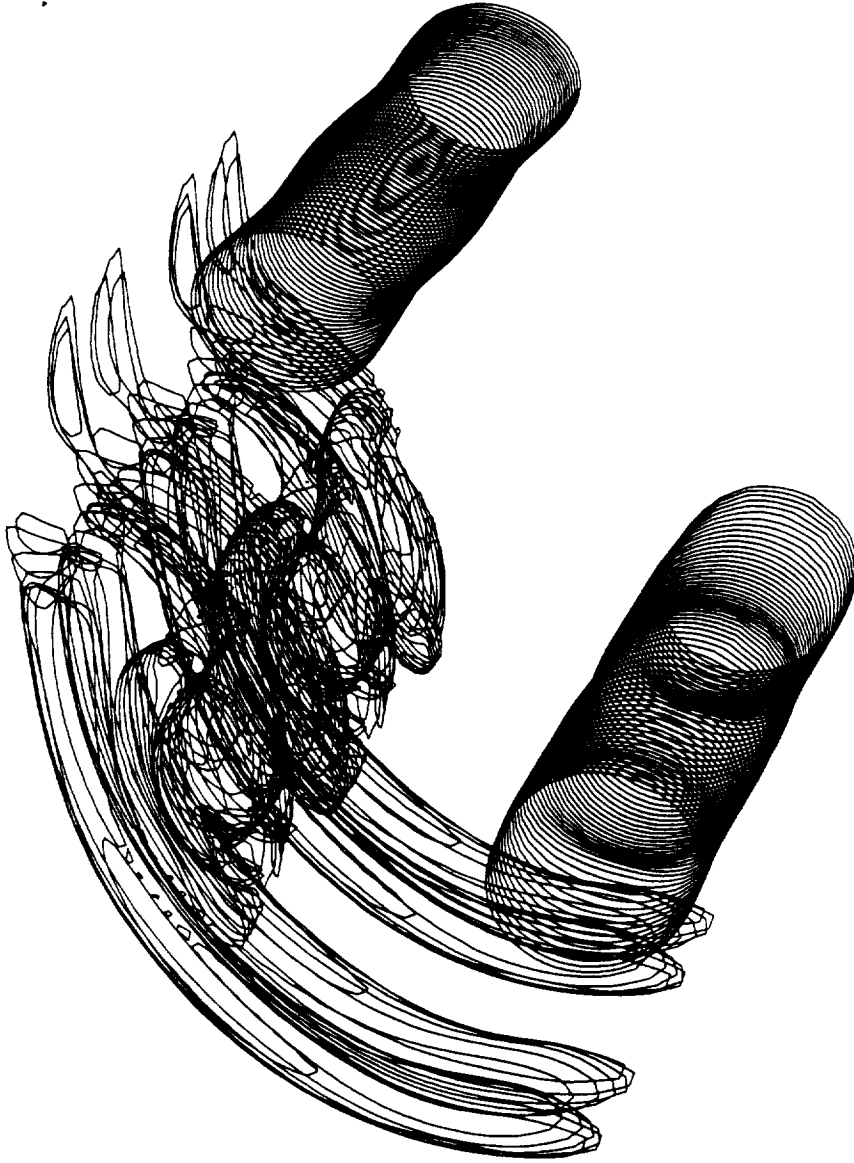


Figure 4.3: Iso-entropy density contour for  $346(60)_{00x}^{0xx}$  wake (two-dimensional fundamental and subharmonic plus three-dimensional fundamental).  $t = 202.8$ . Contour level is  $|\omega| = 0.2$ .



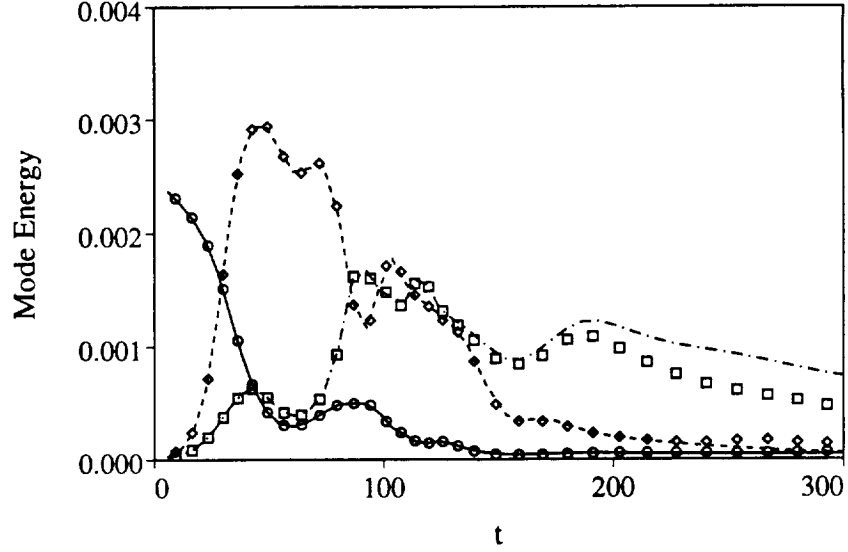


Figure 4.4: Comparison of mean, two-dimensional fundamental, and two-dimensional subharmonic mode energies versus time for  $346(0)_{00x}^{xxx}$  (lines) and  $346(0)_{00x}^{0xx}$  (symbols) wakes. —, o:  $0.1 \times$  mean flow energy. ----,  $\diamond$ : Fundamental mode energy. - · - · - ,  $\square$ : Subharmonic mode energy.

on the same side of the wake. The main effect of the two-dimensional subharmonic disturbance is on the spacing of the rollers, causing the two bottom rollers and one of the top rollers to cluster into a tight group and begin to pair as was observed in the corresponding two-dimensional wake in figure 3.4d and the weakly three-dimensional wake in figure 4.3. In this wake, however, the strong streamwise structures inhibit the pairing process by distorting the rollers.

This is more easily seen by examining the evolution of the streamwise mode energies. Figure 4.6 shows a comparison of the disturbance energies for the two-dimensional  $346(60)_{00x}^{xxx}$  wake (lines) and the three-dimensional  $346(60)_{00x}^{x0x}$  wake (symbols). Note that both the fundamental and subharmonic disturbances in the three-dimensional wake peak earlier and at a lower energy than in the corresponding two-dimensional wake. Furthermore, the late time energy of the subharmonic disturbance is significantly lower in the three-dimensional wake. This is a result of the three-dimensional motions drawing energy out of the long wavelength two-dimensional modes.

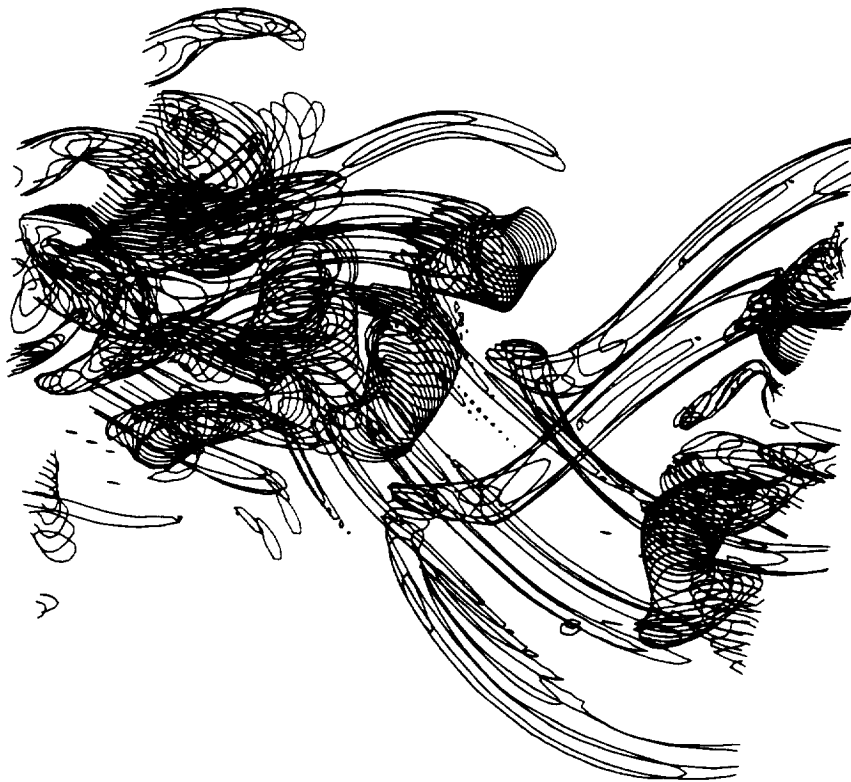


Figure 4.5: Iso-entropy density contour for  $346(60)_{00x}^{x0x}$  wake (two-dimensional fundamental and subharmonic plus three-dimensional subharmonic).  $t = 96.7$ . Contour level is  $|\omega| = 0.4$ .

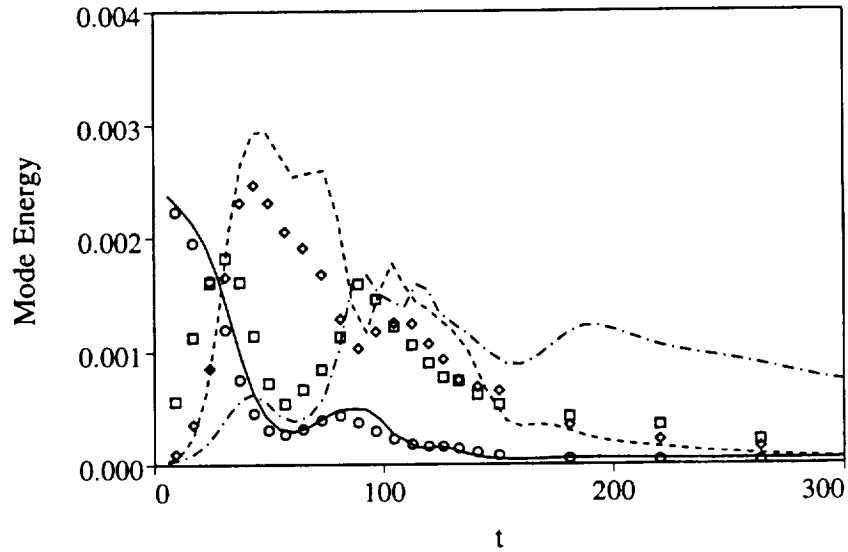


Figure 4.6: Comparison of mean, two-dimensional fundamental, and two-dimensional subharmonic mode energies versus time for  $346(0)_{00x}^{xxx}$  (lines) and  $346(0)_{00x}^{x0x}$  (symbols) wakes. —,  $\circ$ :  $0.1 \times$  mean flow energy. ----,  $\diamond$ : Fundamental mode energy. ····,  $\square$ : Subharmonic mode energy.



Figure 4.7: Iso-entrophy density contour for  $346(60)_{000}^{x00}$  wake (two-dimensional fundamental, subharmonic, and sub-subharmonic plus three-dimensional subharmonic and sub-subharmonic).  $t = 103.2$ . Contour level is  $|\omega| = 0.4$ .

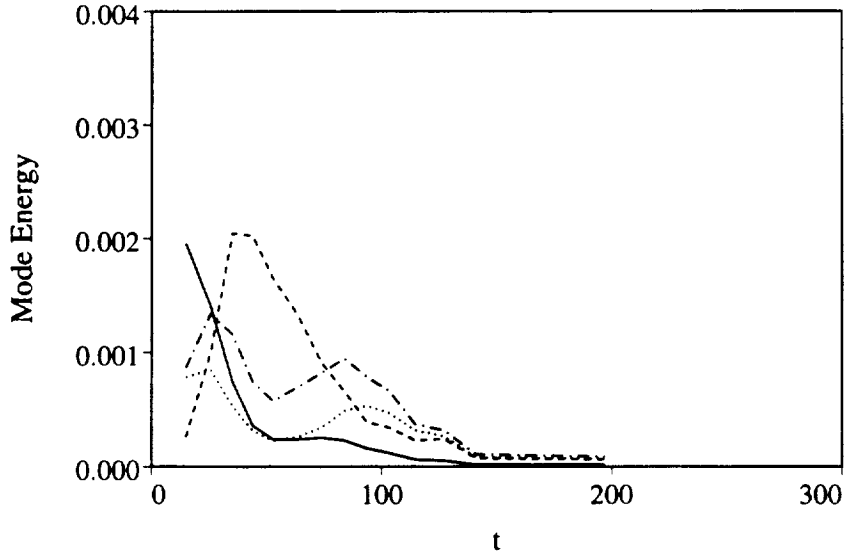


Figure 4.8: Mean and two-dimensional fundamental, two-dimensional subharmonic, and two-dimensional sub-subharmonic mode energies versus time for  $346(0)_{000}^{x_{00}}$  wake. — :  $0.1 \times$  mean flow energy. ---- : Fundamental mode energy. - · - · - : Subharmonic mode energy. · · · · : Sub-subharmonic mode energy.

Figure 4.7 shows iso-entropy density contours for the  $346(60)_{000}^{x_{00}}$  wake, which has the longest wavelength disturbances studied. Note that the streamwise extent of the field shown in figure 4.7 is twice that of the fields in the previous figures (four fundamental wavelengths long instead of two). The effect of the additional two-dimensional sub-subharmonic disturbance is rather minimal up to the time shown. It has caused the sets of paired rollers to be offset slightly in the cross-stream direction, but there is no indication that a second pairing is likely. This conclusion is supported by figure 4.8 which shows the evolution of the energies of the first few streamwise disturbance modes. Note that the sub-subharmonic disturbance (dotted line) is the weakest of the disturbance modes shown, and is decaying rapidly at late times. Since the sub-subharmonic mode is required for a second pairing to occur, such a pairing is impossible in the time frame observed.

At late times the spanwise structures are very similar to the structures in the wake in figure 4.5. The effect the addition of the oblique sub-subharmonic disturbance is to impart a spanwise variation in the strengths of both the streamwise structures

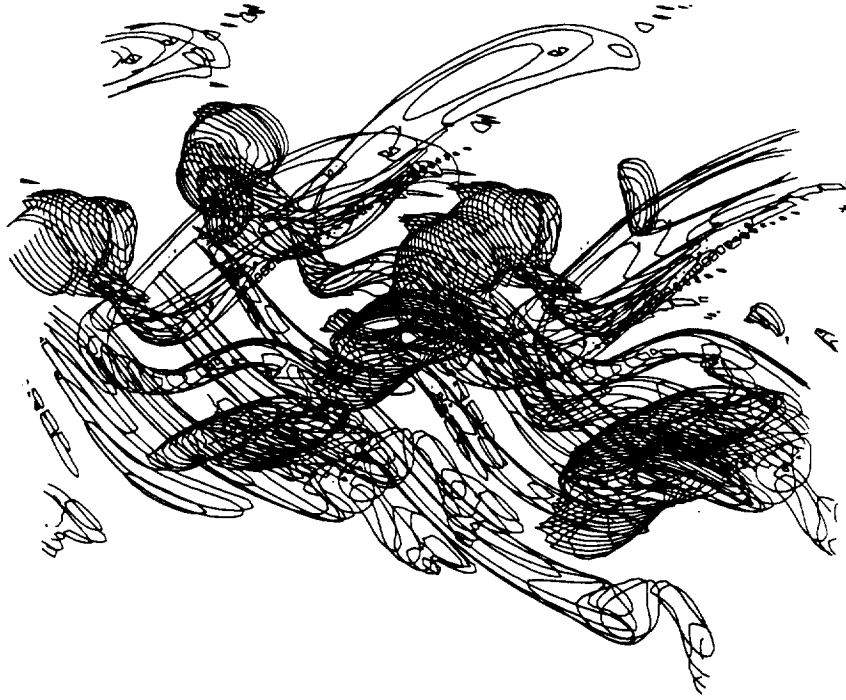


Figure 4.9: Iso-entropy density contour for  $346(60)^{\frac{x}{2}x}_{0xx}$  wake (two-dimensional fundamental plus three-dimensional subharmonic at  $\frac{\pi}{2}$ ).  $t = 96.5$ . Contour level is  $|\omega| = 0.4$ .

and the spanwise rollers. This small increase in the complexity of the overall flow has little impact on the development of the wake.

### 4.3.2 Effect of Disturbance Phase

Figures 4.9, 4.10, 4.11, and 4.12 illustrate the effects of phasing of the oblique disturbance on the structure of the three-dimensional wakes discussed above. The general effect is to decrease the strength of the streamwise structures on one side of the wake and increase the strength of the streamwise structures on the other. For the wakes initiated with an oblique disturbance at the fundamental wavelength (figures 4.10 and 4.2, and figures 4.11 and 4.3) this results in the already weak streamwise structures on the bottom of the wake dropping in intensity below the contour level shown in favor of streamwise structures on the top of the wake, which remain too weak to

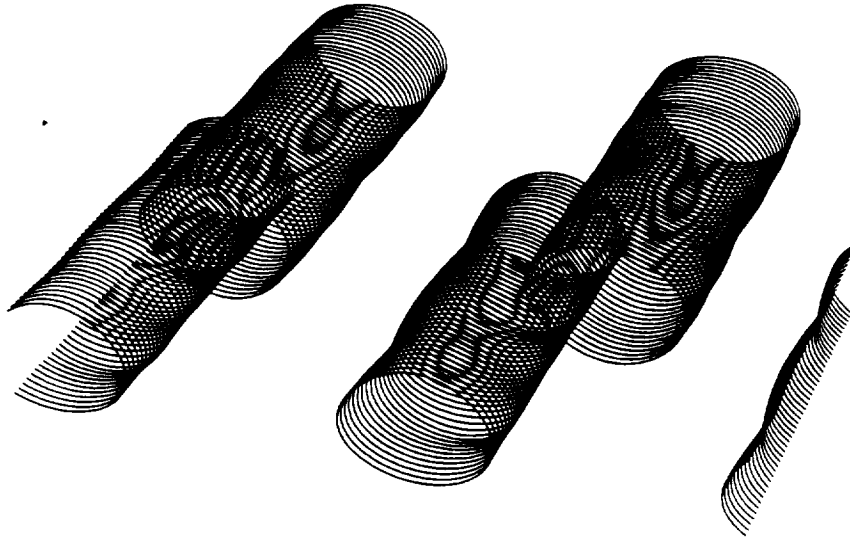


Figure 4.10: Iso-entropy density contour for  $346(60)_{0xx}^{\pi/2}$  wake (two-dimensional fundamental plus three-dimensional fundamental at  $\frac{\pi}{2}$ ).  $t = 197.0$ . Contour level is  $|\omega| = 0.2$ .

appear. For the wakes initiated with a oblique disturbance at the subharmonic wavelength (figures 4.9 and 4.1, and figures 4.12 and 4.5) this results in a balancing of the strengths of the streamwise structures, which previously favored the top of the wake.

### 4.3.3 Effect of Reynolds Number

Figure 4.13 shows a series of iso-entropy density contours for  $\langle ? \rangle(60)_{0xx}^{x0x}$  wakes all at approximately the same time, but with progressively increasing Reynolds number. Note that as the Reynolds number increases, the contour level shown also increases.

Even at a rather low Reynolds number (the  $119(60)_{0xx}^{x0x}$  wake in figure 4.13a), the streamwise structures which arise from the oblique subharmonic disturbance are quite strong and dynamically important. Though they do not overwhelm the spanwise rollers, they do distort the rollers significantly.

As the Reynolds number increases, the relative strengths of the streamwise structures also increase, the spanwise rollers become more distorted, and finer flow scales appear. Even in the highest Reynolds number wake simulated (the  $2768(60)_{0xx}^{x0x}$  wake in figure 4.13e), the influence of the oblique subharmonic is apparent. Very intense

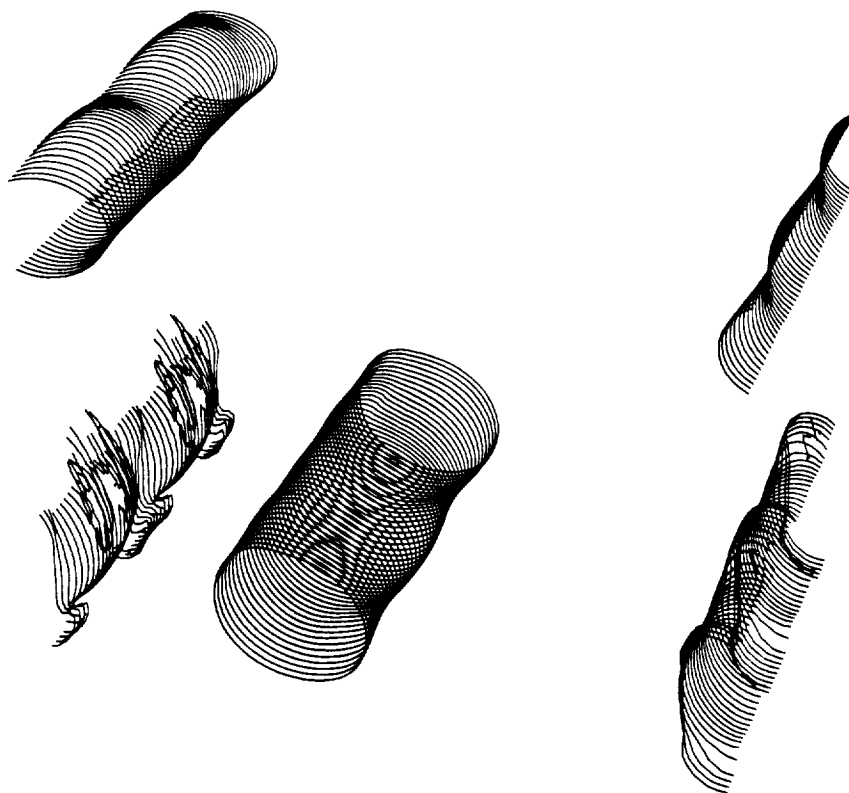
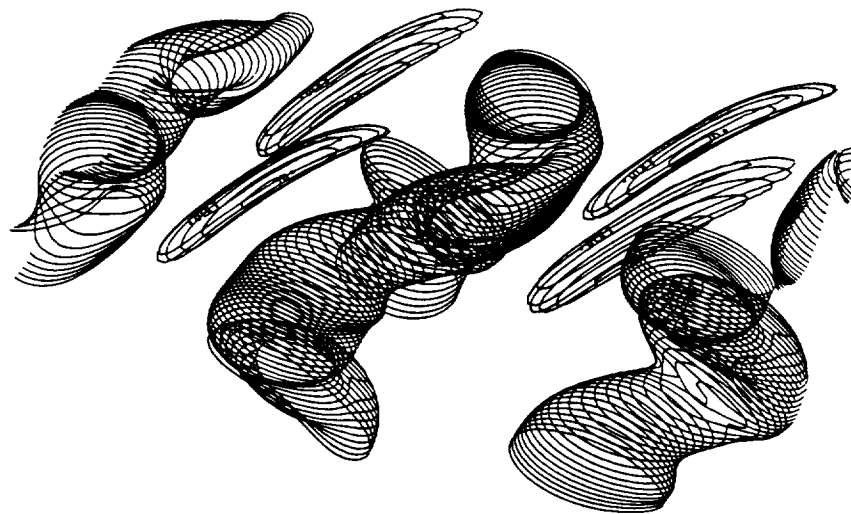


Figure 4.11: Iso-entropy density contour for  $346(60)_{\frac{\pi}{2}xx}$  wake (two-dimensional fundamental and subharmonic plus three-dimensional fundamental at  $\frac{\pi}{2}$ ).  $t = 192.6$ . Contour level is  $|\omega| = 0.2$ .



Figure 4.12: Iso-entropy density contour for  $346(60)_{00x}^{\frac{\pi}{2}x}$  wake (two-dimensional fundamental and subharmonic plus three-dimensional subharmonic at  $\frac{\pi}{2}$ ).  $t = 97.3$ . Contour level is  $|\omega| = 0.4$ .





(a)



(b)

Figure 4.13: See caption page 111.



(c)



(d)

Figure 4.13: See caption page 111.

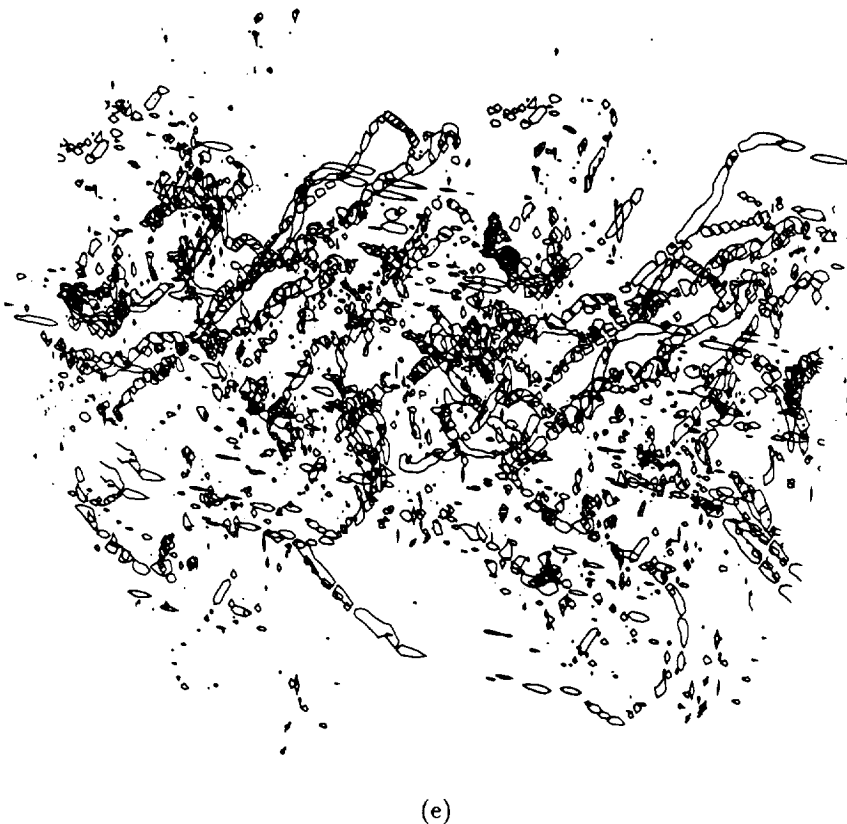


Figure 4.13: Iso-entropy density contours for  $(?) (60)_{0xx}^{x0x}$  wakes (two-dimensional fundamental plus three-dimensional subharmonic) at various Reynolds numbers. (a)  $119(60)_{0xx}^{x0x}$ ,  $t = 97.9$ .  $|\omega| = 0.2$ . (b)  $346(60)_{0xx}^{x0x}$ ,  $t = 102.7$ .  $|\omega| = 0.4$ . (c)  $692(60)_{0xx}^{x0x}$ ,  $t = 101.2$ .  $|\omega| = 0.8$ . (d)  $1384(60)_{0xx}^{x0x}$ ,  $t = 101.5$ .  $|\omega| = 1.6$ . (e)  $2768(60)_{0xx}^{x0x}$ ,  $t = 102.4$ .  $|\omega| = 2.4$ .

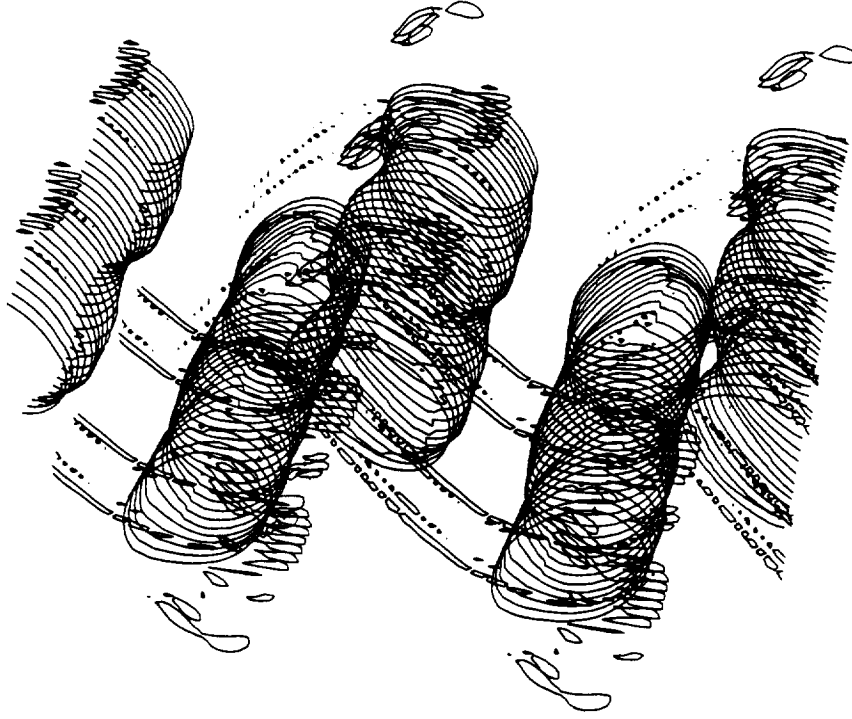


Figure 4.14: Iso-entrophy density contour for  $1384(60)_{0xx}^{0xx}$  wake (two-dimensional fundamental plus three-dimensional fundamental).  $t = 100.2$ . Contour level is  $|\omega| = 0.2$ .

fine scale motions occur at locations where the coherent streamwise structures appear in the lower Reynolds number flows. This is an indication that the generation of small scales in the wake is linked the very intense straining fields created by the streamwise structures.

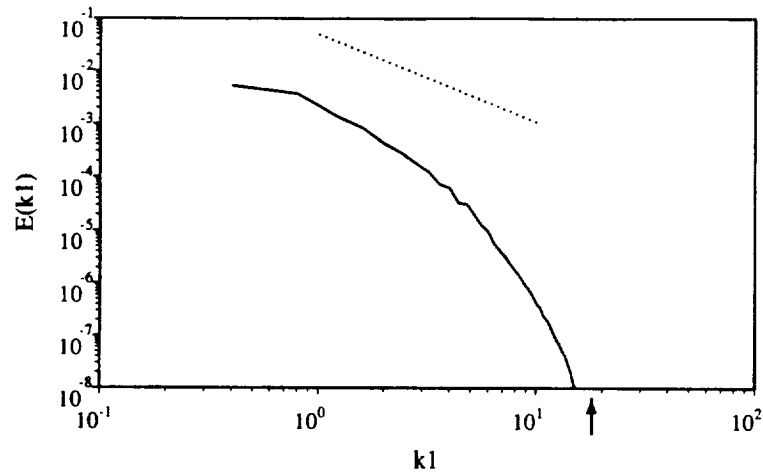
Though the early development of all the wakes calculated is similar, the development of significant strong three-dimensionality does not occur in the absence of the oblique subharmonic. Figure 4.14 shows an iso-entrophy density contour for the  $1384(60)_{0xx}^{0xx}$  wake. The streamwise structures are evident, and, as evidenced by the visible corrugation in the spanwise rollers, have a somewhat greater impact on the flow dynamics than in the corresponding lower Reynolds number  $\langle ? \rangle (60)_{0xx}^{0xx}$  wake presented previously. However, the three-dimensional motions are still very weak,

and the wake remains nearly two dimensional. Similar results are found for computations started from the same set of initial disturbances, but with different disturbance phasings.

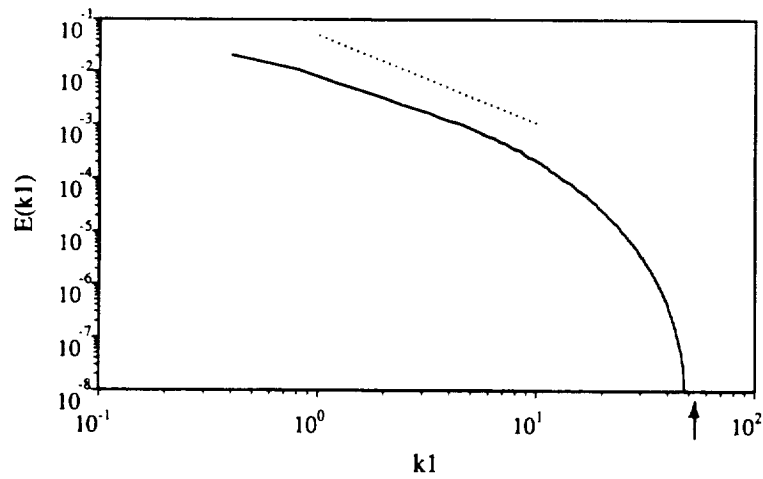
This result differs markedly from the compressible wake computed by Chen *et al.* [10], which showed strong three-dimensional development for certain disturbance phases and only weak three-dimensional development for others. It is unclear why this difference exists. Chen *et al.* attributed the sensitivity to three-dimensional disturbance phase in the compressible wake to the fact that at certain phasings significant amounts of vorticity from the three-dimensional mode resides in the high strain-rate regions between the spanwise rollers where it can be amplified through stretching. Other phases are such that most of the vorticity from the three-dimensional mode gets wrapped into the relative low strain-rate rollers, where it is only weakly amplified. If this were the only process occurring the same results should hold for the incompressible wake. A more careful comparison of the respective datasets needs to be made before the reason for the observed difference can be determined.

At this point it is prudent to check that the wake simulations presented, particularly the simulations of the higher Reynolds number wakes, are well resolved. To do this it should be sufficient to demonstrate that the most extreme case, the  $Re_b = 2768$  wake, is adequately resolved. This was accomplished by calculating the Taylor microscales as was done for the test case in section 2.8.3 (see appendix A for definitions of the microscales used). Analysis of the  $2768(60)^{x_0x}$  wake yielded a minimum (as a function of  $x_2$ ) Taylor microscales of  $\lambda_T = 0.26$  and  $\lambda_{T1} = 0.35$  respectively. The least well resolved direction in this flow is the cross-stream, with a grid size of  $\Delta x_2 = 0.085$  which translates to over three grid cells per microscale length. This resolution is adequate.

This conclusion is reinforced by examining the energy spectra of the simulated wakes. Figure 4.15a shows the energy spectra for the  $346(60)^{x_0x}$  wake and figure 4.15b shows the energy spectra for the  $2768(60)^{x_0x}$  wake. The  $2768(60)^{x_0x}$  wake is the most demanding of the simulations performed. Since the spectra of both wakes show large, clean dropoff of their spectra at high wavenumbers it is clear that both simulations are sufficiently resolved.



(a)



(b)

Figure 4.15: Streamwise energy spectra for 346(60) $_{0xx}^{x0x}$  and 2768(60) $_{0xx}^{x0x}$  wakes. — :  $E(k_1)$ . (a) 346(60) $_{0xx}^{x0x}$ ,  $t = 102.7$ . (b) 2768(60) $_{0xx}^{x0x}$ ,  $t = 102.4$ . Arrows indicate minimum grid wavenumber.

## 4.4 Growth of the Mean Flow

Wynanski, Champagne, & Marasli [58] (hereafter referred to as WCM) studied a set of small defect turbulent plane wakes created with a variety of wake generators. The generators were carefully designed such that the momentum thickness,  $\delta_\theta$ , was constant for all of the experiments. The Reynolds number for the various wakes they studied, based on freestream velocity and momentum thickness, ranged between 640 and 3220 (which, assuming a Gaussian mean initial profile, corresponds to Reynolds numbers based on wake halfwidth and centerline velocity of between  $Re_b = 589$  and  $Re_b = 2962$ , the high end of the computational range studied here.) They found that the far wake growth rates followed

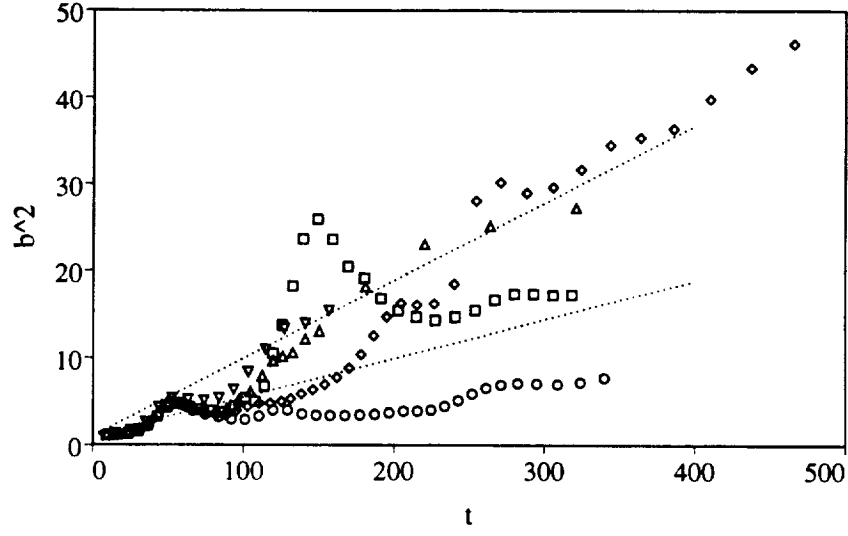
$$\left(\frac{b}{\delta_\theta}\right)^2 = \Delta_0^2 \left(\frac{x - x_0}{\delta_\theta}\right) \quad (4.1)$$

where  $x$  is the streamwise coordinate and  $x_0$  is a virtual origin. The coefficient  $\Delta_0$  was found to vary depending on the particular wake generator used. The limiting values for  $\Delta_0$  that they observed were 0.270 for a solid strip set perpendicular to the flow direction, and 0.382 for a flat plate with a trailing edge flap which was oscillated at the frequency of the Kármán mode.

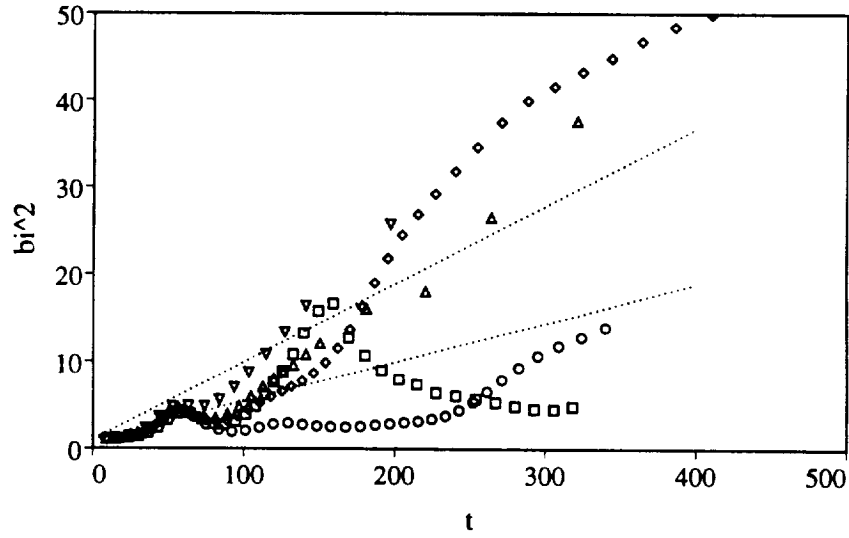
In order to compare with these experiments, straight dotted lines indicating the upper and lower bounds for the growth rates observed by WCM will be plotted in the following figures. These lines have been transformed into the appropriate computational variables using  $x - x_0 = U_0(t - t_0)$ . Note that these lines have not been shifted to account for the virtual origins for the various flows. Only the slopes of the lines are significant.

### 4.4.1 Effect of Disturbance Wavelength

Figure 4.16 shows comparisons of the square of the wake halfwidths,  $b^2$  and  $b_i^2$ , versus non-dimensional time,  $t$ , for computations with a Reynolds number of  $Re_b = 346$  and various combinations of initial disturbances. All the disturbance phases are zero. Up to a time of approximately  $t = 70$ , the growth rate of all the wakes shown is



(a)



(b)

Figure 4.16: Square of normalized wake halfwidth versus normalized time for  $Re = 346$  wakes with various combinations of initial disturbance wavelengths.  $\circ$ :  $346(60)_{0xx}^{0xx}$ .  $\diamond$ :  $346(60)_{0xx}^{x0x}$ .  $\square$ :  $346(60)_{00x}^{0xx}$ .  $\triangle$ :  $346(60)_{00x}^{x0x}$ .  $\nabla$ :  $346(60)_{000}^{x00}$ . (a) Direct halfwidth  $b$ . (b) Integral halfwidth  $b_i$ .



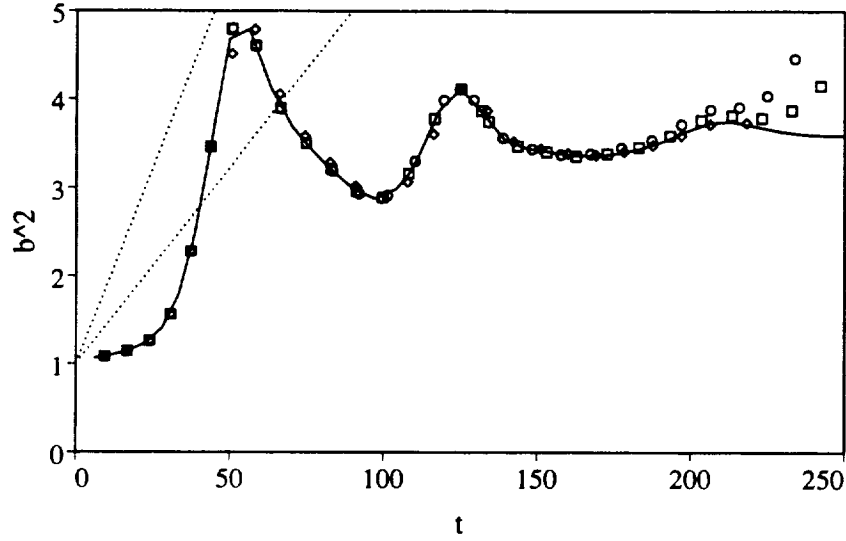
dominated by the initial two-dimensional development of the Kármán vortex street. The presence of disturbances other than the two-dimensional fundamental has little impact.

Between a time of  $t = 70$  and  $t = 200$  the growth rate becomes highly dependent on the particular choice of initial disturbance. The most significant factor is the existence of a two-dimensional subharmonic disturbance. The wakes with the two-dimensional subharmonic ( $346(60)_{00x}^{0xx}$ ,  $346(60)_{00x}^{x0x}$ , and  $346(60)_{000}^{x00}$ ) undergo a period of rapid spreading around a time of  $t = 100$  which corresponds to the pairing of the spanwise rollers, while the wakes with only the two-dimensional fundamental disturbance grow more slowly.

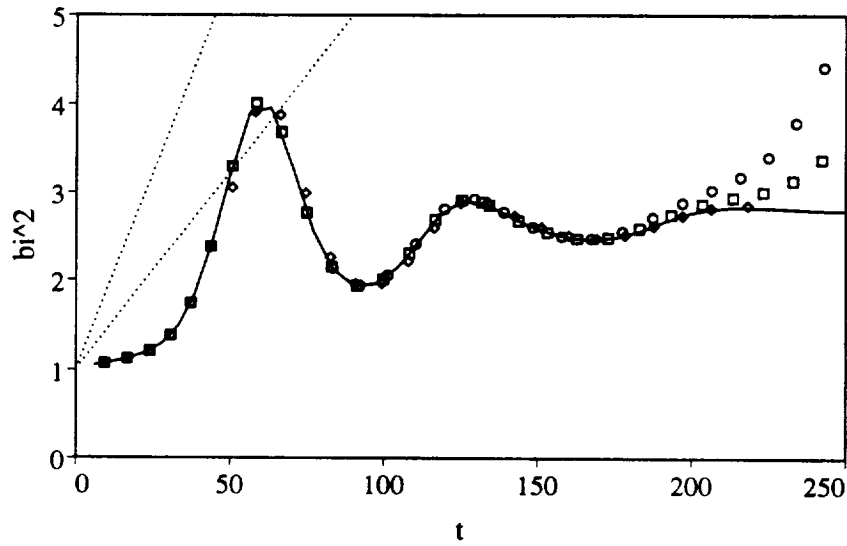
The late time growth rate, after a time of approximately  $t = 200$  is determined by the wavelengths of the oblique disturbances. The wakes initiated with a subharmonic oblique disturbance, which develop strong three-dimensional motions, maintain a growth rate similar to the upper range observed by WCM. The wakes initiated with only a fundamental wavelength oblique disturbance, which are dominated by two-dimensional dynamics, have a late time growth rate well below the experimentally observed level. The late time growth of these wakes is primarily due to the viscous diffusion of the coherent vortex street.

#### 4.4.2 Effect of Disturbance Phasing

Figure 4.17 shows plots of the square of the wake halfwidths versus non-dimensional time for a set of three-dimensional simulation runs started from the  $346(60)_{0xx}^{(?)xx}$  disturbance condition (a two-dimensional fundamental and a three-dimensional oblique fundamental at  $60^\circ$ ) overlayed on the results from the corresponding two-dimensional simulation ( $346(0)_{0xx}^{xxx}$ ). It is readily apparent that the growth of these wakes is dominated by two-dimensional dynamics. This is not surprising given the fact that, as discussed previously, this choice of initial disturbances does not lead to development of strong three-dimensionality. As a result, the phase of the oblique disturbance has no significant effect on the growth of the mean flow. The late time growth rates for these wakes fall well below the levels observed by WCM.

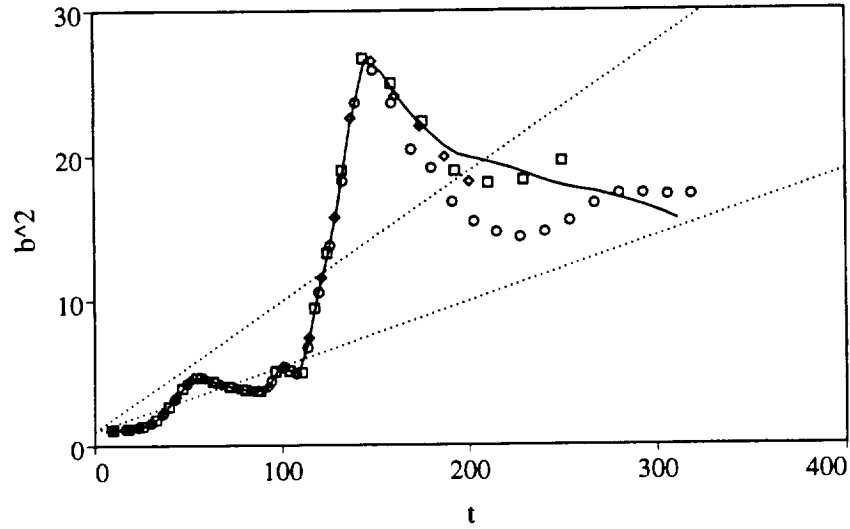


(a)

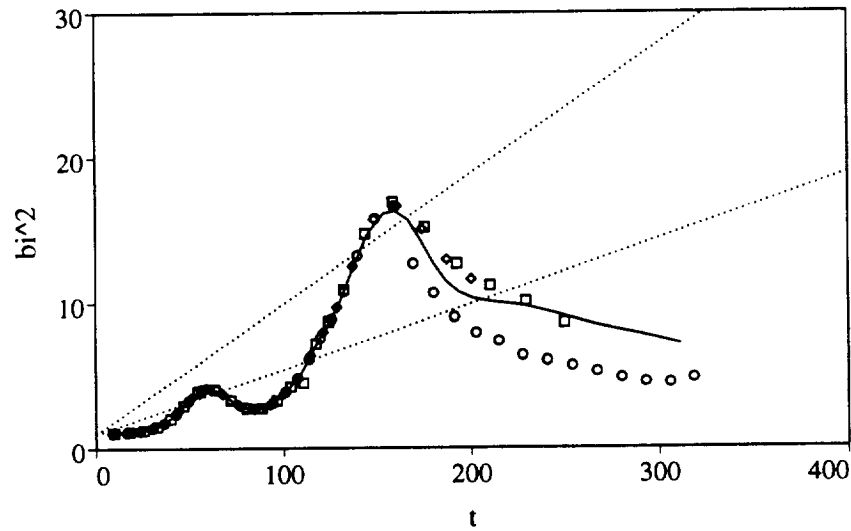


(b)

Figure 4.17: Square of normalized wake halfwidth versus normalized time for  $346(60)_{0xx}^{(?)xx}$  wakes (two-dimensional fundamental plus three-dimensional fundamental at various phases).  $\circ$ :  $346(60)_{0xx}^{0xx}$ .  $\diamond$ :  $346(60)_{0xx}^{\frac{\pi}{4}xx}$ .  $\square$ :  $346(60)_{0xx}^{\frac{\pi}{2}xx}$ . —: Corresponding two-dimensional wake,  $346(0)_{0xx}^{xxx}$ . (a) Direct halfwidth  $b$ . (b) Integral halfwidth  $b_i$ .

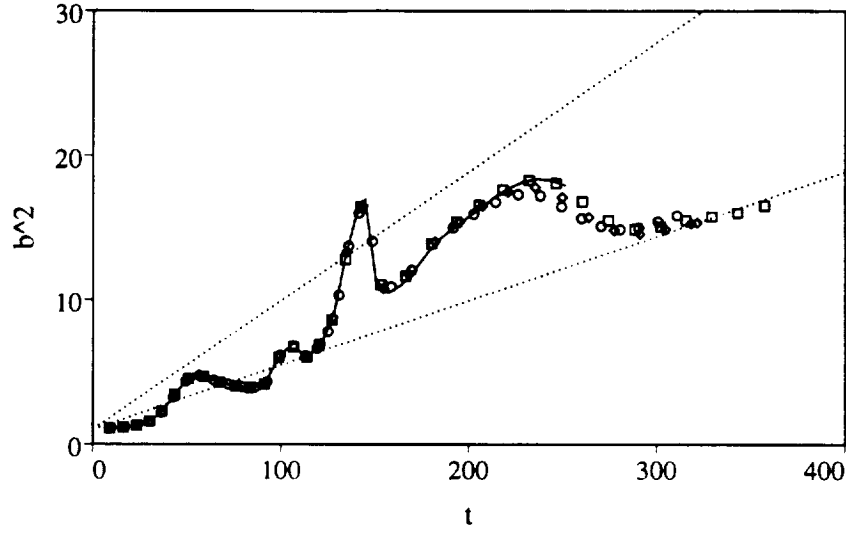


(a)

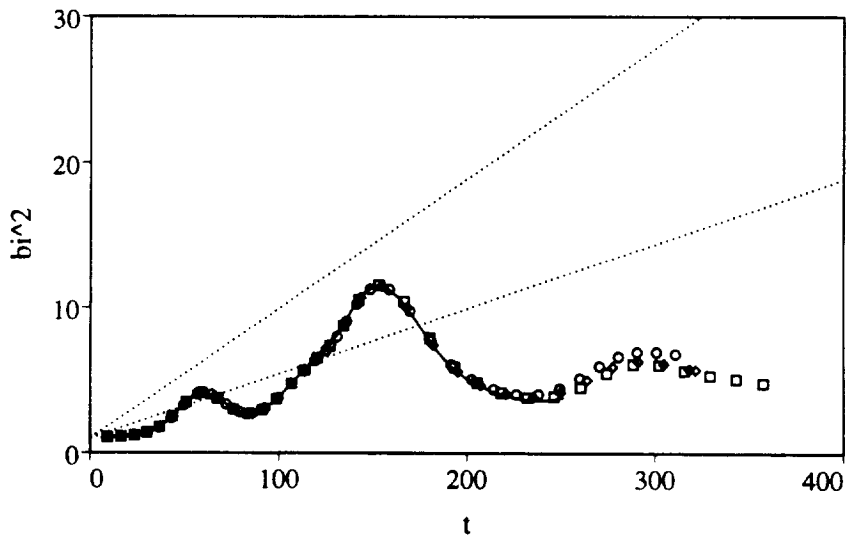


(b)

Figure 4.18: Square of normalized wake halfwidth versus normalized time for  $346(60)^{(\cdot)}_{00x}$  wakes (two-dimensional fundamental and two-dimensional subharmonic plus three-dimensional fundamental at various phases).  $\circ$ :  $346(60)^{0xx}_{00x}$ .  $\diamond$ :  $346(60)^{\frac{\pi}{4}xx}_{00x}$ .  $\square$ :  $346(60)^{\frac{\pi}{2}xx}_{00x}$ . —: Corresponding two-dimensional wake,  $346(0)^{xx}_{00x}$ . (a) Direct halfwidth  $b$ . (b) Integral halfwidth  $b_i$ .

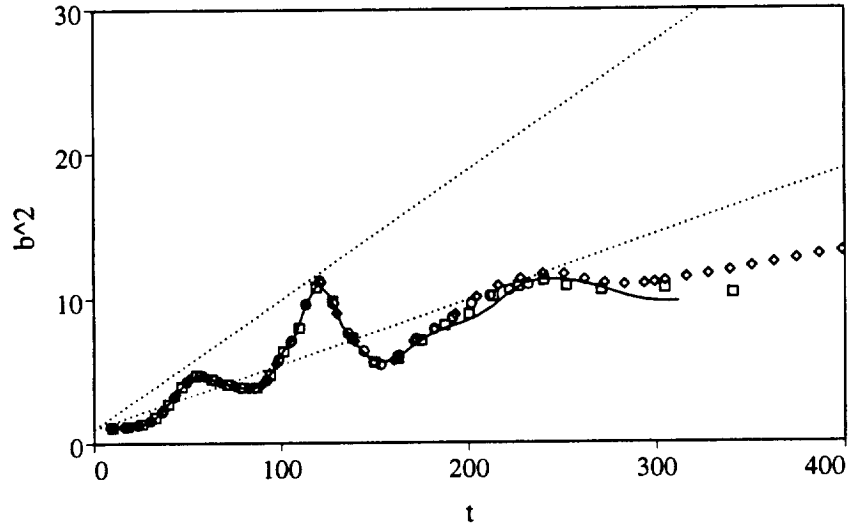


(a)

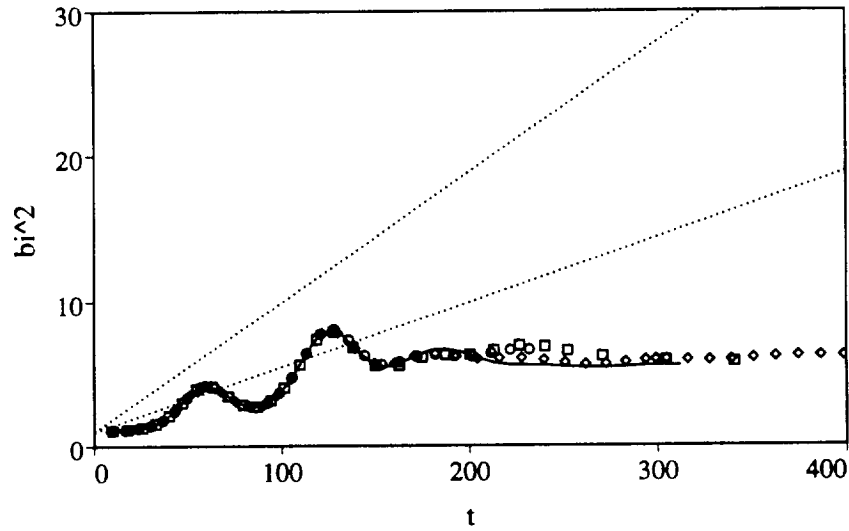


(b)

Figure 4.19: Square of normalized wake halfwidth versus normalized time for  $346(60)_{0\frac{\pi}{4}x}^{(?)xx}$  wakes (two-dimensional fundamental and two-dimensional subharmonic at  $\frac{\pi}{4}$  plus three-dimensional fundamental at various phases).  $\circ$ :  $346(60)_{0\frac{\pi}{4}x}^{0xx}$ .  $\diamond$ :  $346(60)_{0\frac{\pi}{4}x}^{\frac{\pi}{4}xx}$ .  $\square$ :  $346(60)_{0\frac{\pi}{4}x}^{\frac{\pi}{2}xx}$ . —: Corresponding two-dimensional wake,  $346(0)_{0\frac{\pi}{4}x}^{xx}$ . (a) Direct halfwidth  $b$ . (b) Integral halfwidth  $b_i$ .



(a)



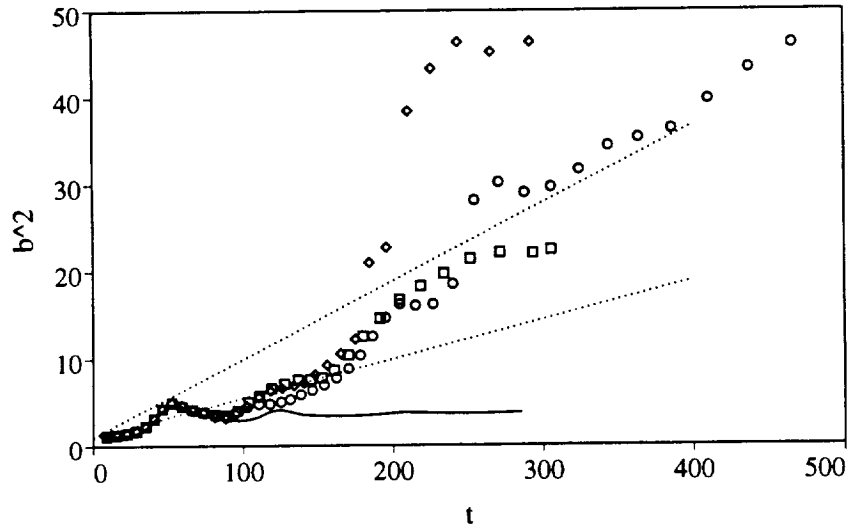
(b)

Figure 4.20: Square of normalized wake halfwidth versus normalized time for  $346(60)_{0\frac{\pi}{4}x}^{(?)xx}$  wakes (two-dimensional fundamental and two-dimensional subharmonic at  $\frac{\pi}{2}$  plus three-dimensional fundamental at various phases).  $\circ$ :  $346(60)_{0\frac{\pi}{2}x}^{0xx}$ .  $\diamond$ :  $346(60)_{0\frac{\pi}{2}x}^{\frac{\pi}{4}xx}$ .  $\square$ :  $346(60)_{0\frac{\pi}{2}x}^{\frac{\pi}{2}xx}$ . — : Corresponding two-dimensional wake,  $346(0)_{0\frac{\pi}{2}x}^{xxx}$ . (a) Direct halfwidth  $b$ . (b) Integral halfwidth  $b_i$ .

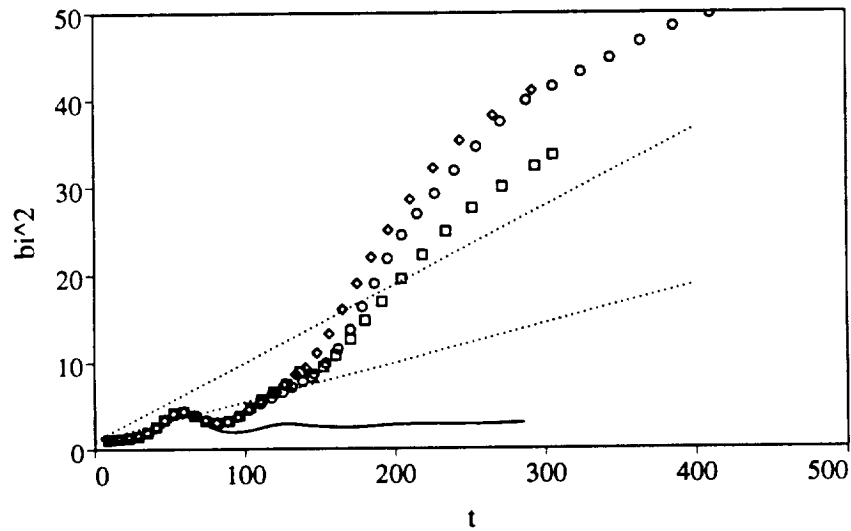
Figures 4.18, 4.19, and 4.20 show plots of the square of the wake halfwidths versus non-dimensional time for a set of three-dimensional simulation runs started from the  $346(60)_{0(?)x}^{(?)xx}$  disturbance condition (a two-dimensional fundamental, a two-dimensional subharmonic, and a three-dimensional oblique fundamental at  $60^\circ$ ). Here again the flow is dynamically two-dimensional and therefore the growth of the mean flow is very insensitive to the phasing of the three-dimensional fundamental disturbance. The phasing of the two-dimensional subharmonic determines the development of the mean flow almost entirely. The small deviations from the corresponding two-dimensional wakes at late times are due to the (relatively weak) three-dimensional structures which develop during the pairing of the spanwise rollers. However, these structures never dominate the flow dynamics. Again the late time growth of these flows is well below the range observed by WCM.

Figure 4.21 shows plots of the square of the wake halfwidths versus non-dimensional time for a set of three-dimensional simulation runs started from the  $346(60)_{0xx}^{x(?)x}$  disturbance condition (a two-dimensional fundamental and a three-dimensional oblique subharmonic at  $60^\circ$ ). In contrast to the wakes with oblique disturbances at the fundamental wavelength, the late time growth of these wakes is substantially different from the corresponding two-dimensional case. The initial growth is still dominated by two-dimensional dynamics, but by a time of  $t = 125$  three-dimensional processes clearly begin to take over, as evidenced by the substantial deviation from the two-dimensional growth curve.

The effect of the phasing of the three-dimensional subharmonic on either halfwidth measure is minimal up to a time of  $t = 200$ . After a time of  $t = 200$ , however, the “direct” halfwidth measure shows what appears to be a strong phase dependence. the apparent dependence on phase is due to the fact that the mean flow profiles for these wakes are highly non-Gaussian, with several local maxima. The oblique disturbance phase has an impact on the details of the shape of the mean profile, as well as an effect on the maximum mean velocity. This has a large impact on the calculation of the “direct” halfwidth,  $b$ , even though the vorticity in the flows has spread over a similar extent. This is illustrated by the mean  $u_1$  velocity profiles shown in figure 4.22, which correspond to the  $\circ$  and  $\diamond$  lines in figure 4.21 at a time of approximately



(a)



(b)

Figure 4.21: Square of normalized wake halfwidth versus normalized time for  $346(60)_{0xx}^{x(?)x}$  wakes (two-dimensional fundamental plus three-dimensional subharmonic at various phases).  $\circ$ :  $346(60)_{0xx}^{x0x}$ .  $\diamond$ :  $346(60)_{0xx}^{x\frac{1}{4}x}$ .  $\square$ :  $346(60)_{0xx}^{x\frac{\pi}{2}x}$ . —: Corresponding two-dimensional wake,  $346(0)_{0xx}^{xxx}$ . (a) Direct halfwidth  $b$ . (b) Integral halfwidth  $b_i$ .

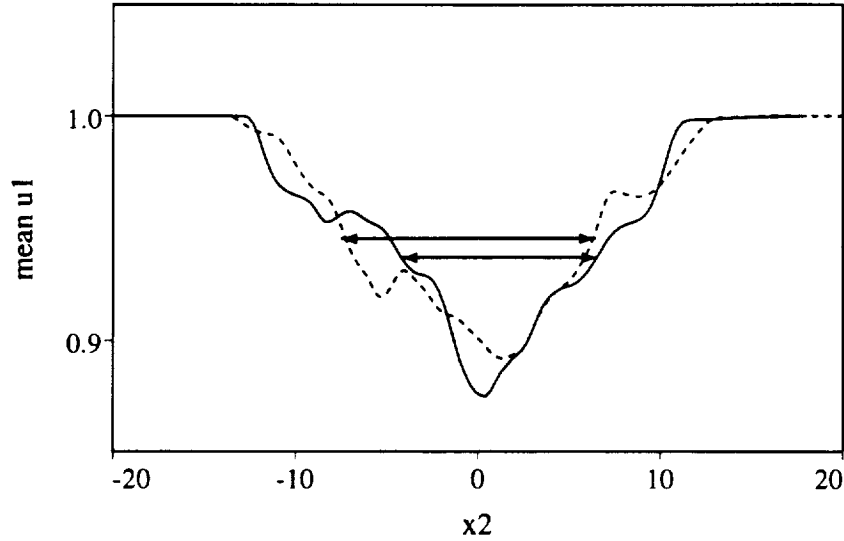


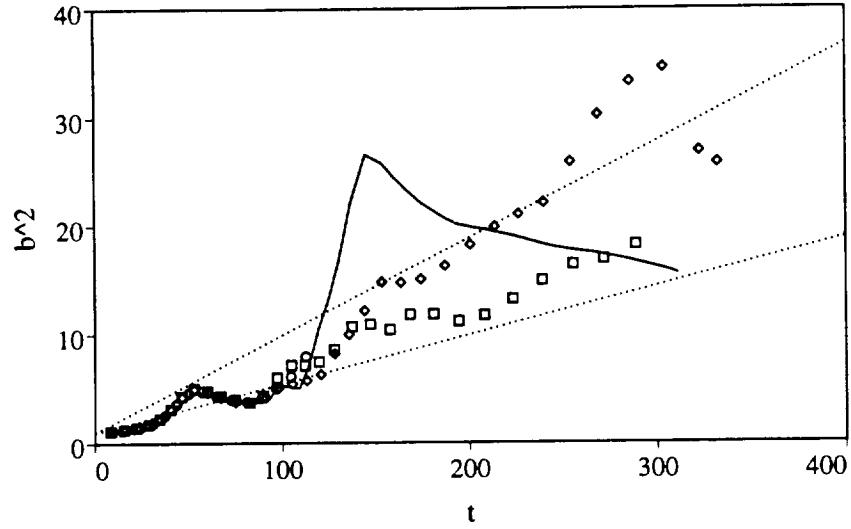
Figure 4.22: Mean velocity profiles for  $346(60)_{0xx}^{x0x}$  and  $346(60)_{0xx}^{x\frac{\pi}{4}x}$  wakes. — :  $692(60)_{0xx}^{x0x}$ ,  $t = 288.2$ . ---- :  $692(60)_{0xx}^{x\frac{\pi}{4}x}$ ,  $t = 292.1$ . Arrows indicate locations for measurement of “direct” halfwidths.

$t = 300$ . The relative small differences in profile height and shape lead to a large difference in “direct” halfwidth  $b$  (see arrows).

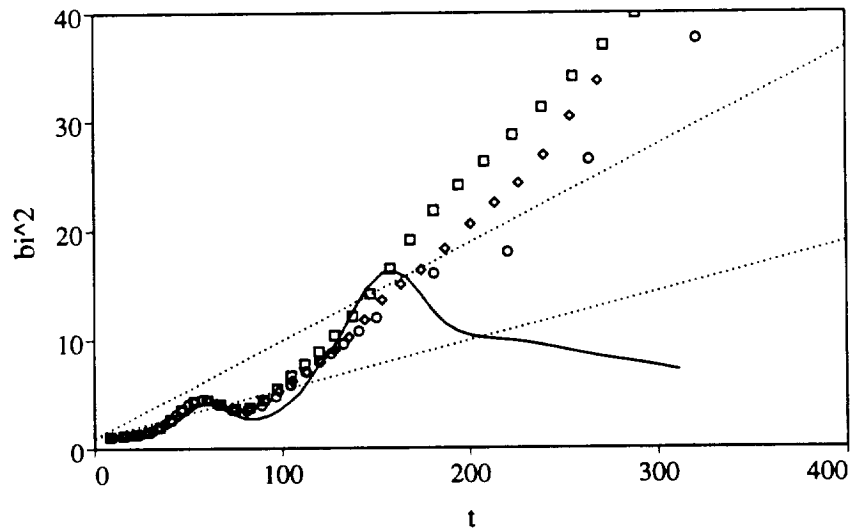
The actual effect of disturbance phase is relatively small as can be concluded from the plot of the integral halfwidth  $b_i$ . What is most significant is that the late time growth rates for all of these wakes are similar and within the range observed by WCM. The presence of a three-dimensional subharmonic allows growth that is in line with natural wakes. This does not occur in the wakes that have a three-dimensional fundamental only.

Figures 4.23, 4.24, and 4.25 show the square of halfwidths versus time for the  $346(60)_{0(\frac{?}{?})x}^{x(\frac{?}{?})x}$  wakes. Again, the oblique disturbance phasing has only a small impact on the growth of the mean flow. Though the *magnitude* of the late time width varies somewhat with the phasing of the oblique disturbances, the *growth rate* is not significantly impacted. Note also that so long as a three-dimensional subharmonic is present, the late time growth rate of the three-dimensional wakes varies little with the phase of



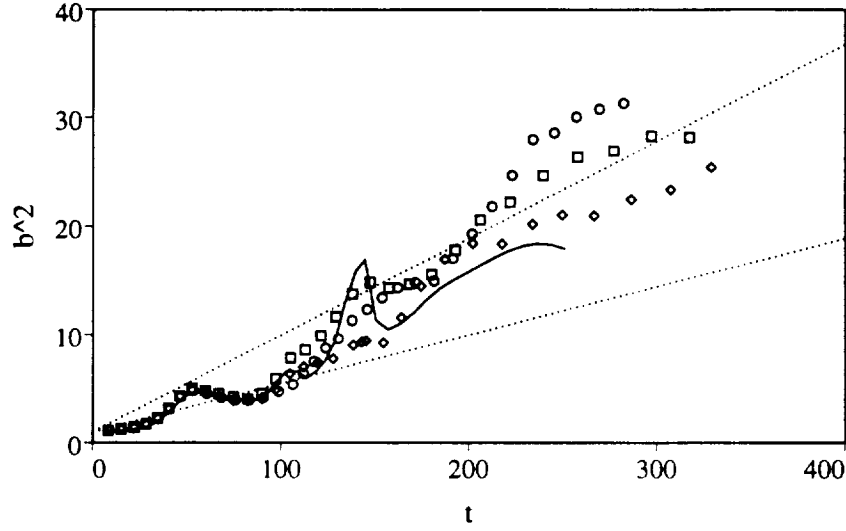


(a)

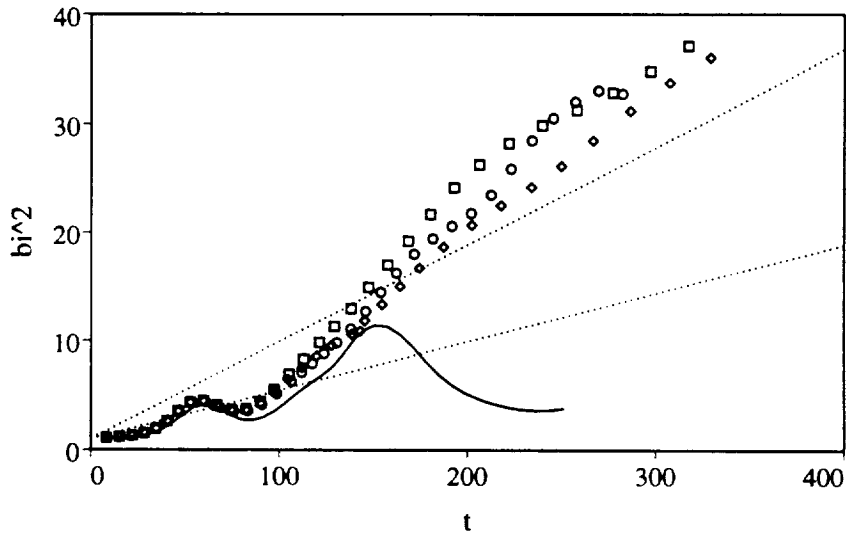


(b)

Figure 4.23: Square of normalized wake halfwidth versus normalized time for  $346(60)_{00x}^{x(?)x}$  wakes (two-dimensional fundamental and two-dimensional subharmonic plus three-dimensional subharmonic at various phases).  $\circ$ :  $346(60)_{00x}^{x0x}$ .  $\diamond$ :  $346(60)_{00x}^{x\frac{\pi}{4}x}$ .  $\square$ :  $346(60)_{00x}^{x\frac{\pi}{2}x}$ . —: Corresponding two-dimensional wake,  $346(0)_{00x}^{xxx}$ . (a) Direct halfwidth  $b$ . (b) Integral halfwidth  $b_i$ .

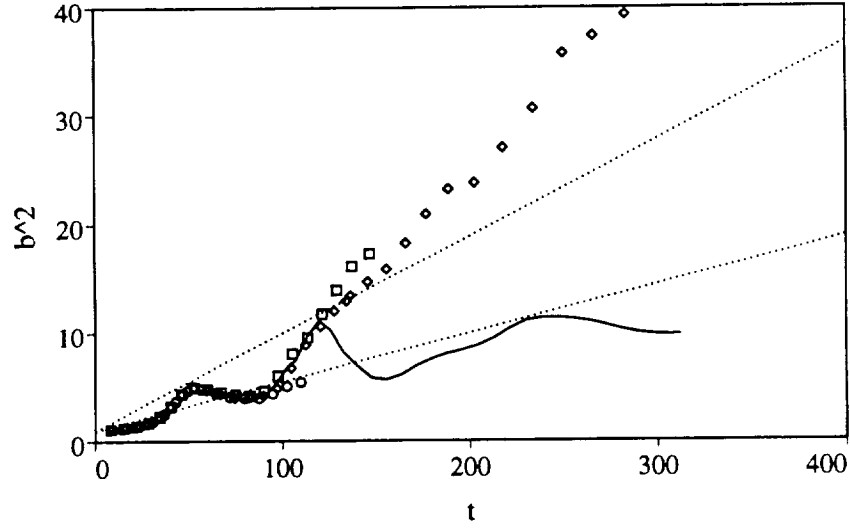


(a)

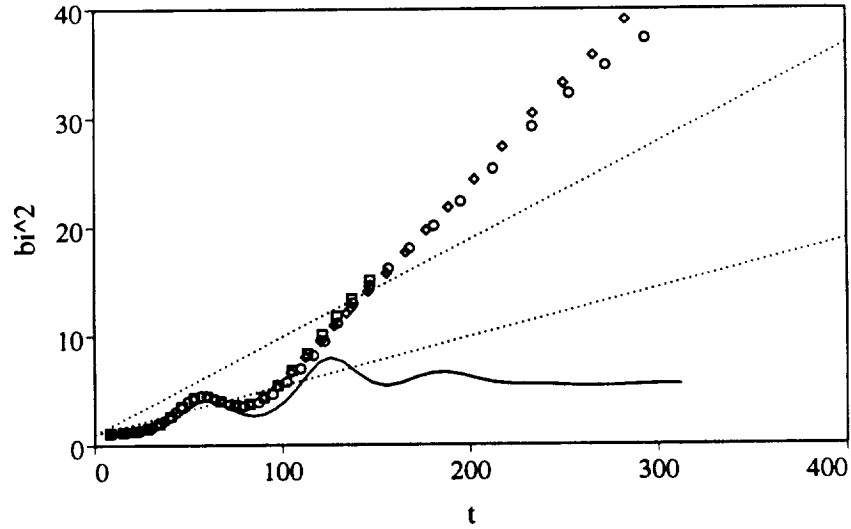


(b)

Figure 4.24: Square of normalized wake halfwidth versus normalized time for  $346(60)_{0\frac{\pi}{4}x}^{x(?)x}$  wakes (two-dimensional fundamental and two-dimensional subharmonic at  $\frac{\pi}{4}$  plus three-dimensional subharmonic at various phases).  $\circ$ :  $346(60)_{0\frac{\pi}{4}x}^{x0x}$ .  $\diamond$ :  $346(60)_{0\frac{\pi}{4}x}^{x\frac{\pi}{4}x}$ .  $\square$ :  $346(60)_{0\frac{\pi}{4}x}^{x\frac{\pi}{2}x}$ . — : Corresponding two-dimensional wake,  $346(0)_{0\frac{\pi}{4}x}^{xx}$ . (a) Direct halfwidth  $b$ . (b) Integral halfwidth  $b_i$ .



(a)



(b)

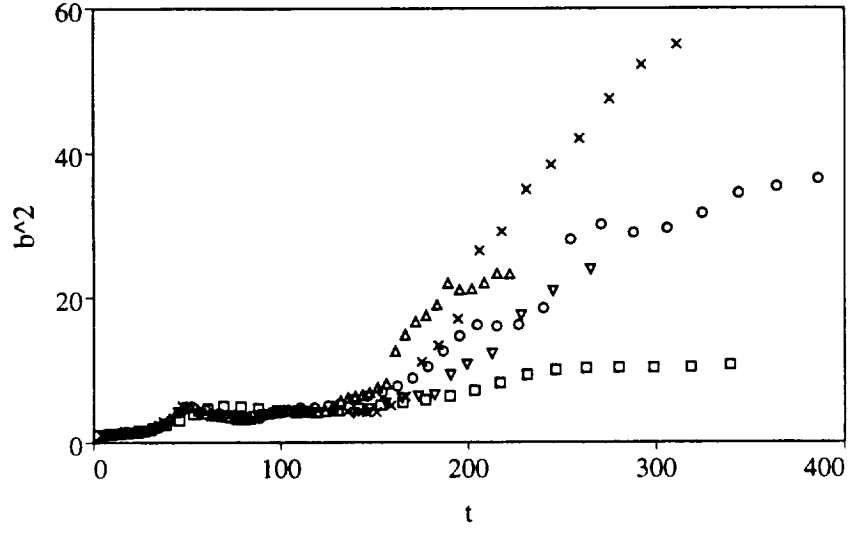
Figure 4.25: Square of normalized wake halfwidth versus normalized time for  $346(60)_{0\frac{\pi}{2}x}^{x(?)x}$  wakes (two-dimensional fundamental and two-dimensional subharmonic at  $\frac{\pi}{4}$  plus three-dimensional subharmonic at various phases).  $\circ$ :  $346(60)_{0\frac{\pi}{2}x}^{x0x}$ .  $\diamond$ :  $346(60)_{0\frac{\pi}{2}x}^{x\frac{\pi}{4}x}$ .  $\square$ :  $346(60)_{0\frac{\pi}{2}x}^{x\frac{\pi}{2}x}$ . —: Corresponding two-dimensional wake,  $346(0)_{0\frac{\pi}{2}x}^{xx}$ . (a) Direct halfwidth  $b$ . (b) Integral halfwidth  $b_i$ .

the two-dimensional subharmonic disturbance, or for that matter, with the *presence* or *absence* of the two-dimensional subharmonic (compare with the  $346(60)_{0xx}^{x(?)x}$  wakes in figure 4.21). The late time growth rates are again similar, though in some cases slightly above, the bounds observed by WCM.

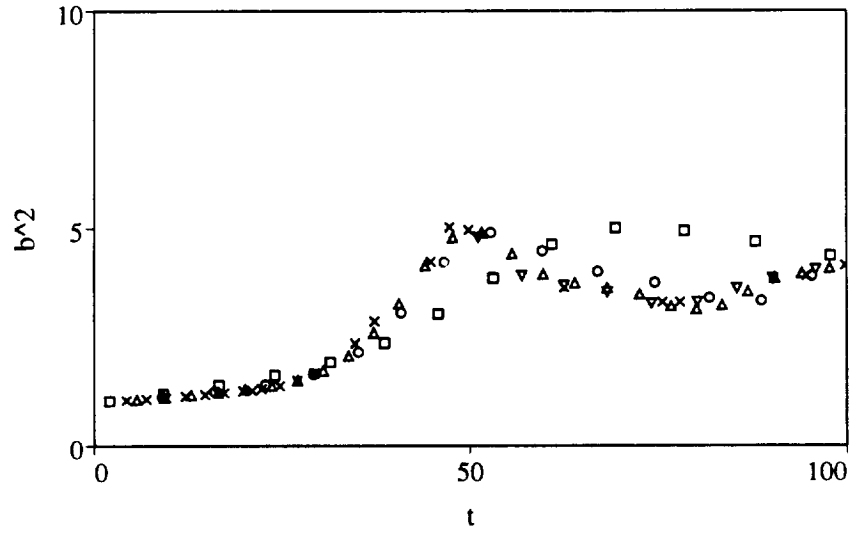
### 4.4.3 Effect of Reynolds Number

Figure 4.26 shows a comparison of the square of the wake “direct” halfwidth versus time for a set of computations all initiated with the  $(?)_{0xx}^{x0x}$  disturbance condition, but at different Reynolds numbers. Figure 4.27 are similar plots of the integral halfwidth. At early times (figure 4.26b and 4.27b), the low Reynolds number wake rolls up more slowly and peaks in width later than the other wakes. This is due to viscous effects. The  $346(60)_{0xx}^{x0x}$  wake shows a similar, though much less pronounced effect.

From the time the wake rolls up into the initial vortex street until a time of approximately  $t = 150$ , the wake growth is insensitive to Reynolds number. During this period the three-dimensional structures are growing in strength but have not yet become the dynamically dominant features in the wakes. After a time of  $t = 150$ , the growth begins to show some sensitivity to Reynolds number. The three-dimensional structures in the lowest Reynolds number wake,  $119(60)_{0xx}^{x0x}$ , are quickly diffused by viscosity and therefore never become strong enough to overwhelm the two-dimensional dynamics of the early flow. At higher Reynolds numbers, however, coherent three-dimensional structures dominate the late time growth. Though there is some variation in the late time widths of the wakes as the Reynolds number is varied, the late time growth rate for all of the higher Reynolds number flows is similar. In fact the growth rates of the highest Reynolds number flows are somewhat lower than the growth rate for the  $346(60)_{0xx}^{x0x}$  wake. The reason for this is that the  $346(60)_{0xx}^{x0x}$  wake develops very strong three-dimensional structures that remain coherent for long periods. Those organized structures can efficiently work to spread the wake. At higher Reynolds numbers the coherent structures are disrupted, though not destroyed, by disorganized fine scale motions. The resulting reduced organization of the coherent structures slightly reduces the wake growth rate.

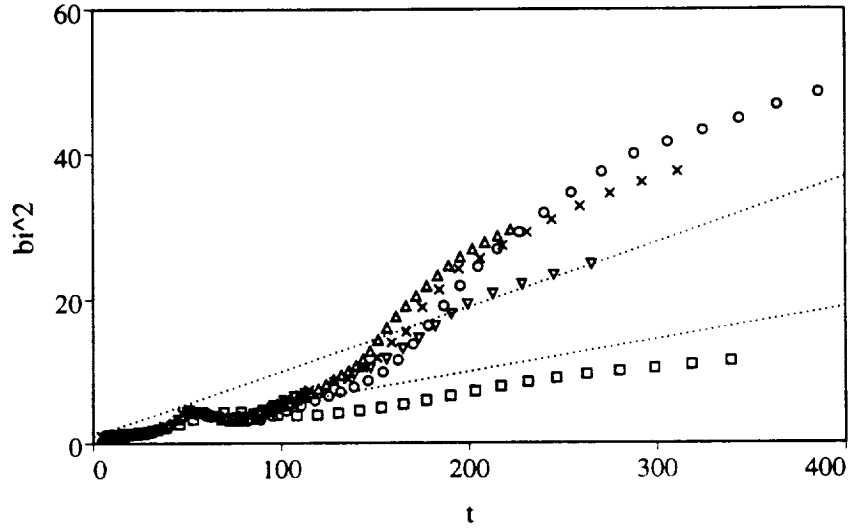


(a)

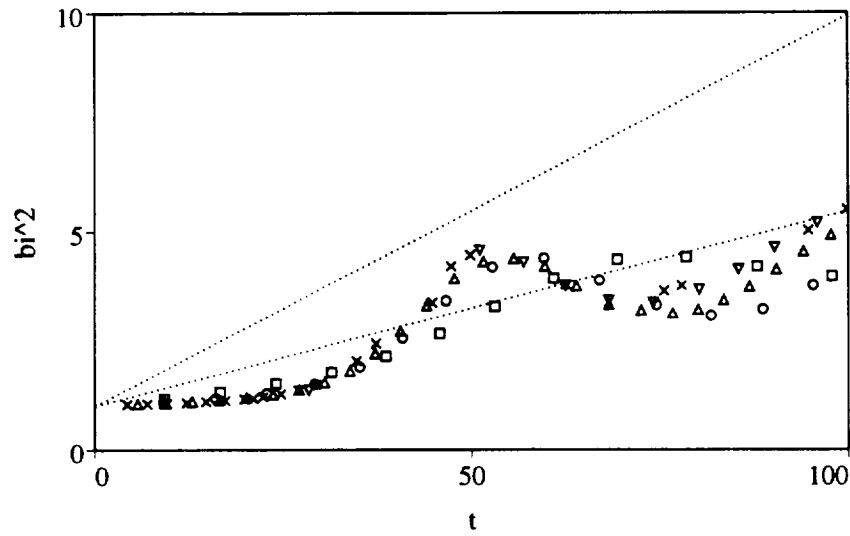


(b)

Figure 4.26: Square of normalized wake direct halfwidth versus normalized time for  $(?)(60)_{0xx}^{x0x}$  wakes (two-dimensional fundamental plus three-dimensional subharmonic with various Reynolds numbers).  $\square$ :  $119(60)_{0xx}^{x0x}$ .  $\circ$ :  $346(60)_{0xx}^{x0x}$ .  $\triangle$ :  $692(60)_{0xx}^{x0x}$ .  $\nabla$ :  $1384(60)_{0xx}^{x0x}$ .  $\times$ :  $2768(60)_{0xx}^{x0x}$ . (b) is a magnification of the early time region of (a).



(a)



(b)

Figure 4.27: Square of normalized wake integral halfwidth versus normalized time for  $(?) (60)_{0xx}^{x0x}$  wakes (two-dimensional fundamental plus three-dimensional subharmonic with various Reynolds numbers).  $\square$ :  $119(60)_{0xx}^{x0x}$ .  $\circ$ :  $346(60)_{0xx}^{x0x}$ .  $\triangle$ :  $692(60)_{0xx}^{x0x}$ .  $\nabla$ :  $1384(60)_{0xx}^{x0x}$ .  $\times$ :  $2768(60)_{0xx}^{x0x}$ . (b) is a magnification of the early time region of (a).

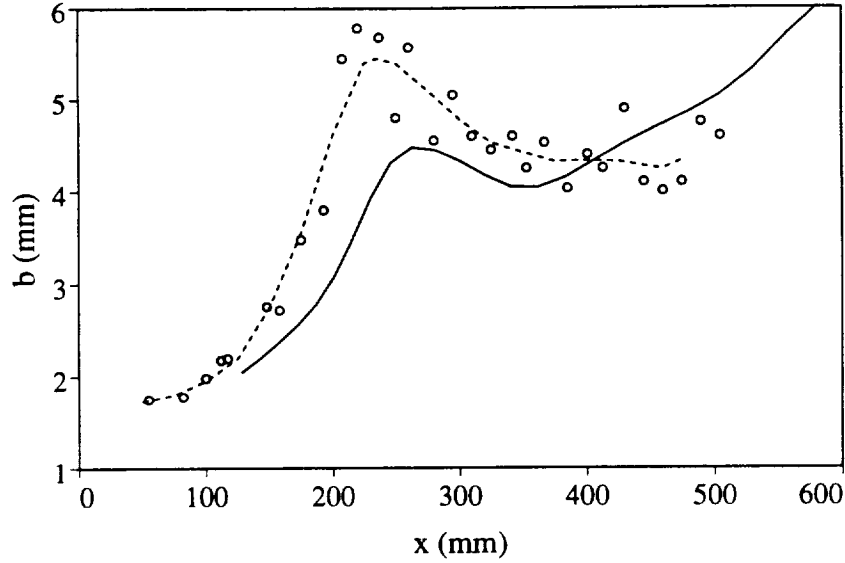


Figure 4.28: Comparison of halfwidth versus downstream distance for  $119(60)_{0xx}^{x0x}$  wake and experiments of Corke, Krull, & Ghassemi [14] (CKG). o: CKG experimental data. ----: CKG curve fit. —:  $119(60)_{0xx}^{x0x}$ .

## 4.5 Comparison with Experiment

The  $119(60)_{0xx}^{x0x}$  and  $346(60)_{0xx}^{x0x}$  wakes in figures 4.26 and 4.27 has slight undulations in the late time growth curve visible in plots of both width measures. This starts at a time of approximately 80 with the peak which corresponds to the rollup and saturation of the Kármán mode, and is followed by a period of neutral or negative growth, followed by growth again. This cycle of stronger growth followed by weaker growth continues as both wakes develop.

Corke, Krull, & Ghassemi [14] (hereafter referred to as CKG) studied this phenomenon in a  $Re = 119$  spatially developing wake produced by a symmetric airfoil at zero angle of attack. They forced their wake with a two-dimensional disturbance at the fundamental frequency and a pair of oblique modes at the subharmonic in a manner similar to the computations presented here. They concluded that the fluctuations in the growth of the wake were due to a parametric resonance between the fundamental mode and the oblique subharmonic mode. The two-dimensional mode saturates and begins to feed energy into the three-dimensional oblique disturbance

through a secondary instability mechanism. The oblique mode in turn saturates, and the two-dimensional disturbance begins to grow again.

Figure 4.28 shows a comparison between the direct wake width for the  $119(60)_{0xx}^{x0x}$  wake and data from figure 4 in CKG. The computed flow has been renormalized to match momentum thickness and shifted to put the virtual origin for the computed flow at  $x = 0$ . The coordinates were transformed using  $x/\theta_{CKG} = U_0(t-t_0)/\theta_{computation}$  and  $(b/\theta)_{CKG} = (b/\theta)_{computation}$ . This rescaling does not account for differences in initial forcing magnitude between the experiment and the computation, or for the virtual origin of the experimental wake. Nevertheless, the match between the computed flow and the experimental data is quite reasonable.

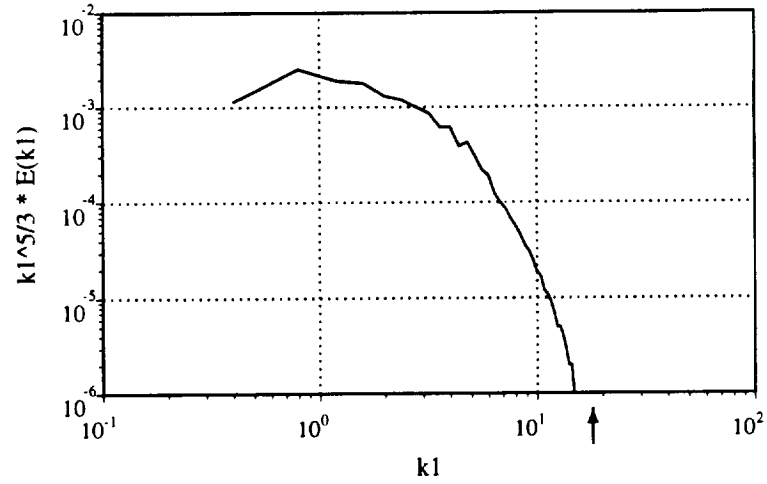
## 4.6 Selected Spectra, Mean Profiles, and Turbulence Statistics

Figure 4.29 shows rescaled streamwise energy spectra ( $k_1^{5/3}E(k_1)$ ) for the velocity fields in two of the computed wakes. The data has been plotted in this way in order to bring out regions of  $k_1^{-5/3}$  spectra which are expected in turbulent flows. In these coordinates, regions of  $k_1^{-5/3}$  spectra will appear as horizontal lines. The spanwise and cross-stream ( $E(k_2)$  and  $E(k_3)$ ) spectra are very similar to the streamwise spectra and are not shown here.

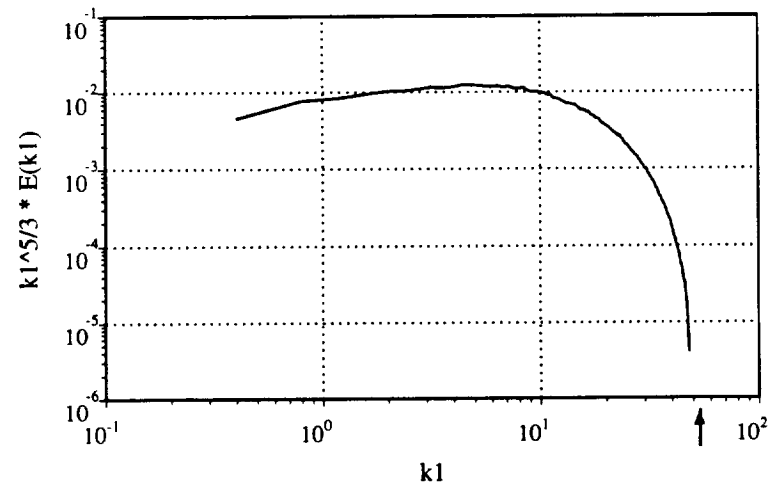
Figure 4.29a shows the rescaled streamwise energy spectrum for the moderate Reynolds number  $346(60)_{0xx}^{x0x}$  wake which appears in figure 4.13b. There is clearly no significant inertial ( $k_1^{-5/3}$ , horizontal line in the plot) range in this flow. This is consistent with the fact that the flow is dominated by large coherent structures and has few small scales. This wake can not be considered turbulent.

Figure 4.29b shows the streamwise energy spectrum for the highest Reynolds number wake computed,  $2768(60)_{0xx}^{x0x}$ . This is the wake which appears in figure 4.13b. This flow has a spectrum which is much more consistent with the expected spectrum of a turbulent flow. It shows a range in the spectrum that is close to the expected  $k_1^{-5/3}$  law (horizontal line). Since the range of  $k_1$  over which the spectrum goes like  $k_1^{-5/3}$  is



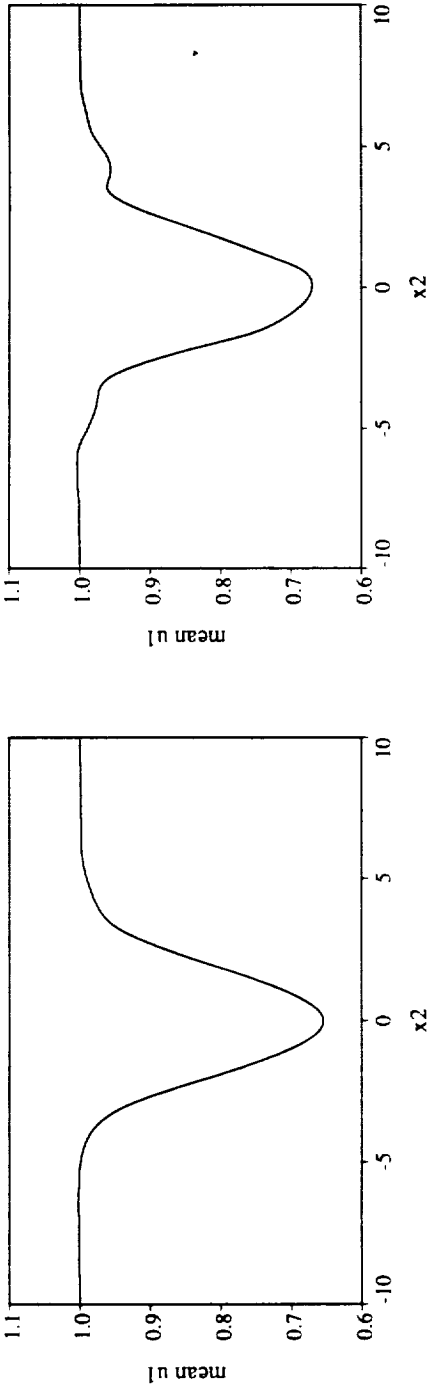


(a)

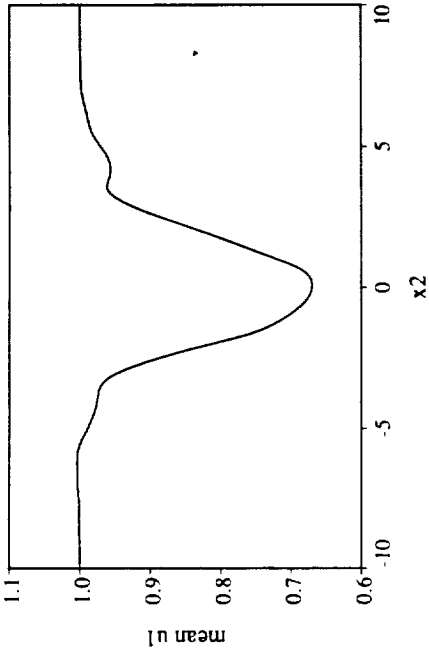


(b)

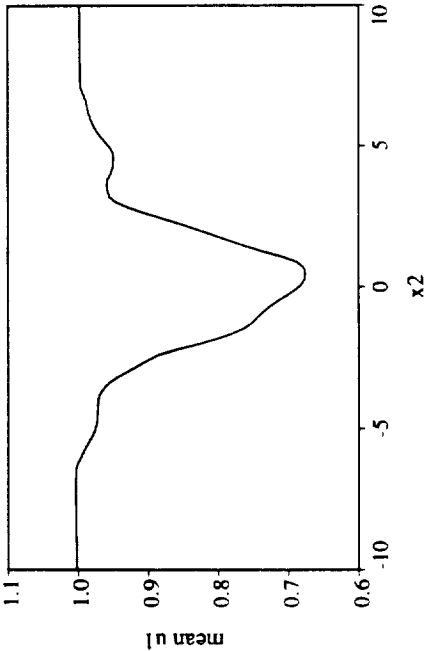
Figure 4.29: Rescaled streamwise energy spectra for  $346(60)_{0xx}^{x0x}$  and  $2768(60)_{0xx}^{x0x}$  wakes. —:  $k_1^{5/3} E(k_1)$ . (a)  $346(60)_{0xx}^{x0x}$ ,  $t = 102.7$ . (b)  $2768(60)_{0xx}^{x0x}$ ,  $t = 102.4$ . Arrows indicate minimum grid wavenumber.



(a)



(b)



(c)

Figure 4.30: See caption page 135.

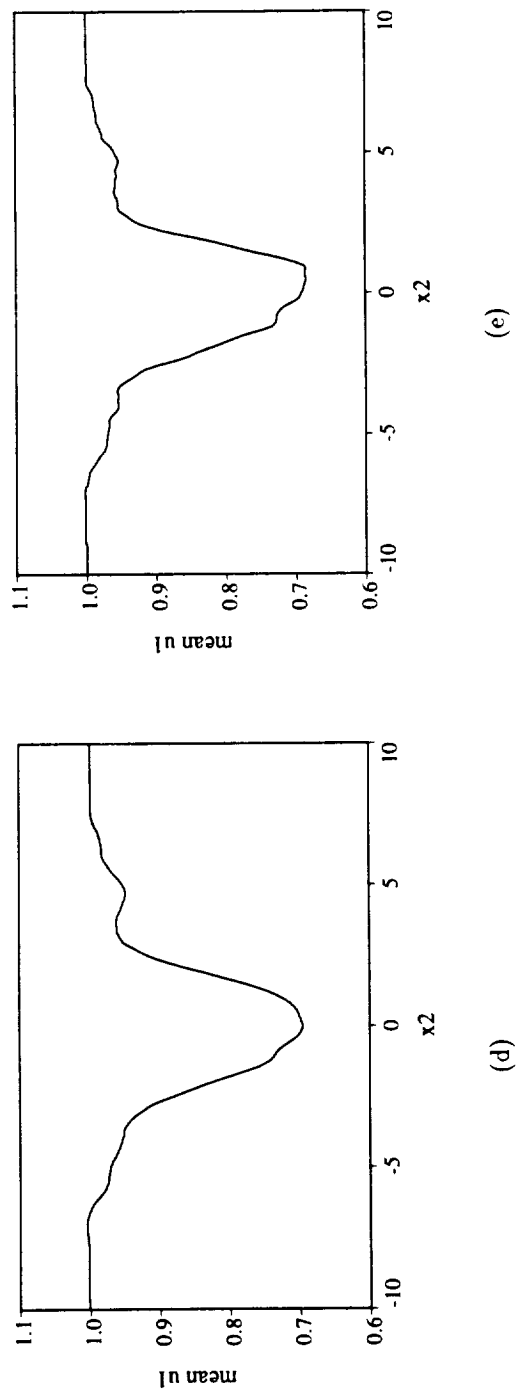
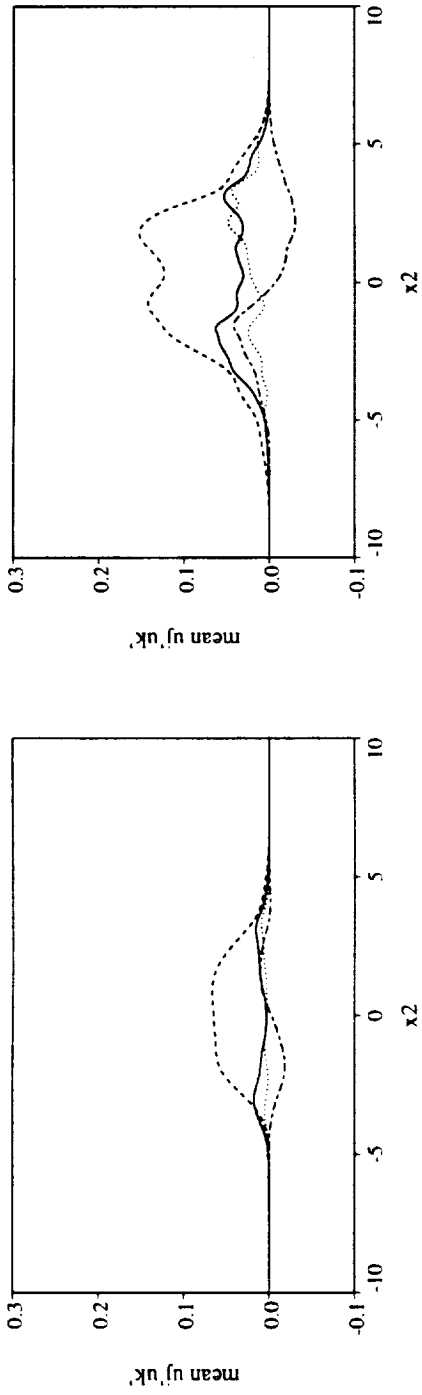
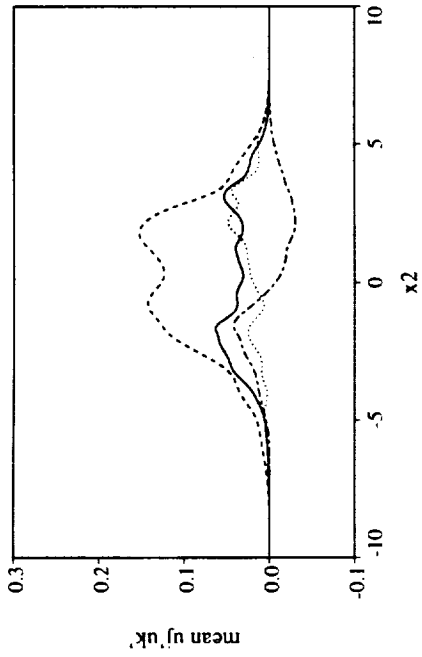


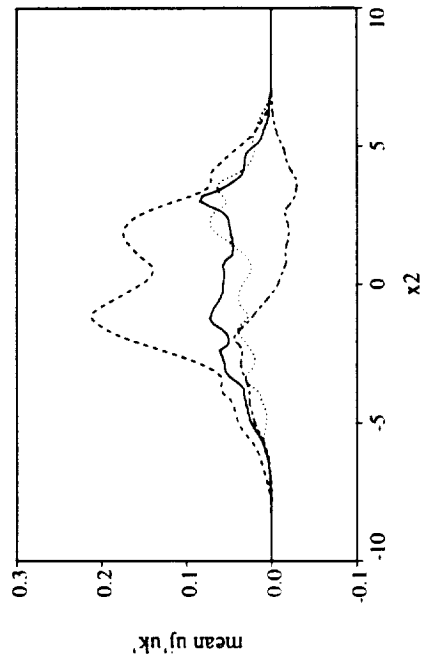
Figure 4.30: Mean streamwise velocity profiles for  $\langle ? \rangle(60)^{x_{0x}}_{0_{xx}}$  wakes.  $t \sim 100.0$ . (a)  $119(60)^{x_{0x}}_{0_{xx}}$ ,  $t = 97.9$ . (b)  $346(60)^{x_{0x}}_{0_{xx}}$ ,  $t = 102.7$ . (c)  $692(60)^{x_{0x}}_{0_{xx}}$ ,  $t = 101.2$ . (d)  $1384(60)^{x_{0x}}_{0_{xx}}$ ,  $t = 101.5$ . (e)  $2768(60)^{x_{0x}}_{0_{xx}}$ ,  $t = 102.4$ .



(a)



(b)



(c)

Figure 4.31: See caption page 137.

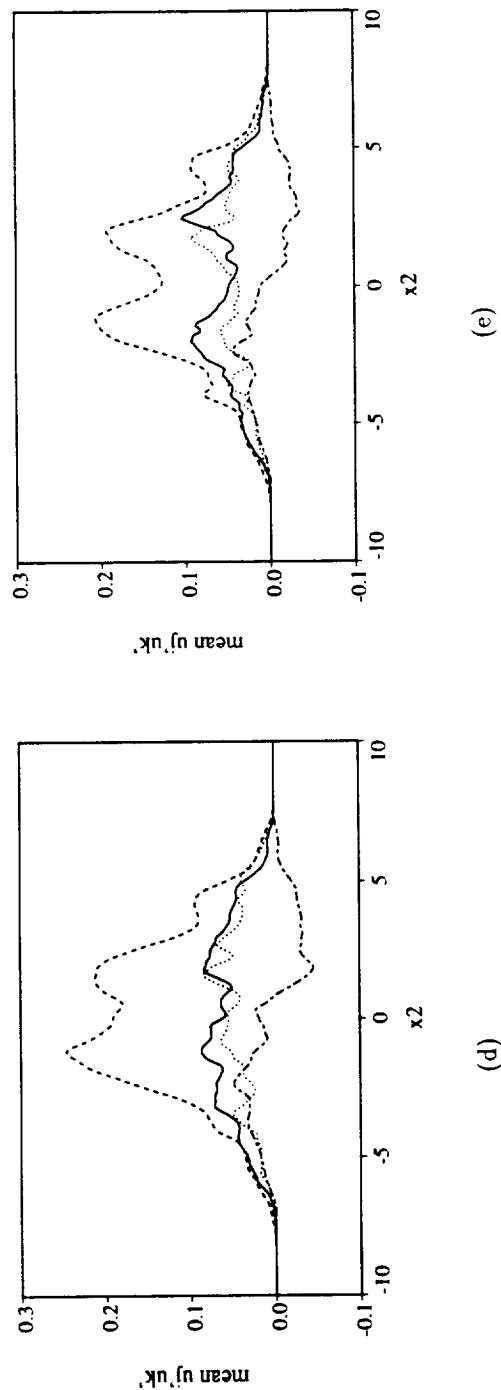


Figure 4.31: Second order velocity correlations for  $\langle ? \rangle (60)_{0xx}^{x0x}$  wakes.  $t \sim 100.0$ . — :  $\overline{u'_1 u'_1}$ . - - - - :  $\overline{u'_2 u'_2}$ . . . . :  $\overline{u'_3 u'_3}$ . - . . . - :  $\overline{u'_1 u'_2}$ . (a) 119(60) $_{0xx}^{x0x}$ ,  $t = 97.9$ . (b) 346(60) $_{0xx}^{x0x}$ ,  $t = 102.7$ . (c) 692(60) $_{0xx}^{x0x}$ ,  $t = 101.2$ . (d) 1384(60) $_{0xx}^{x0x}$ ,  $t = 101.5$ . (e) 2768(60) $_{0xx}^{x0x}$ ,  $t = 102.4$ .

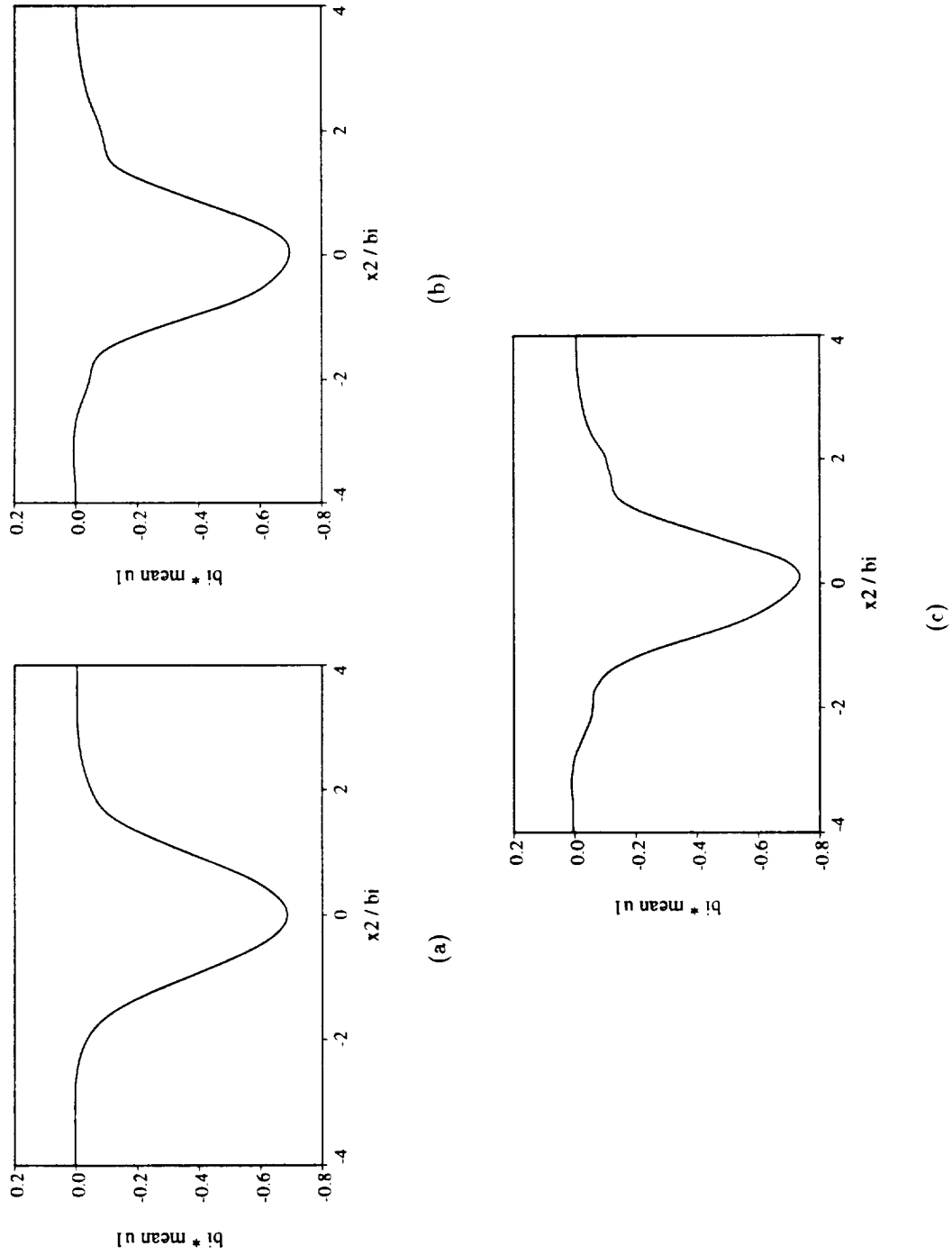


Figure 4.32: See caption page 139.

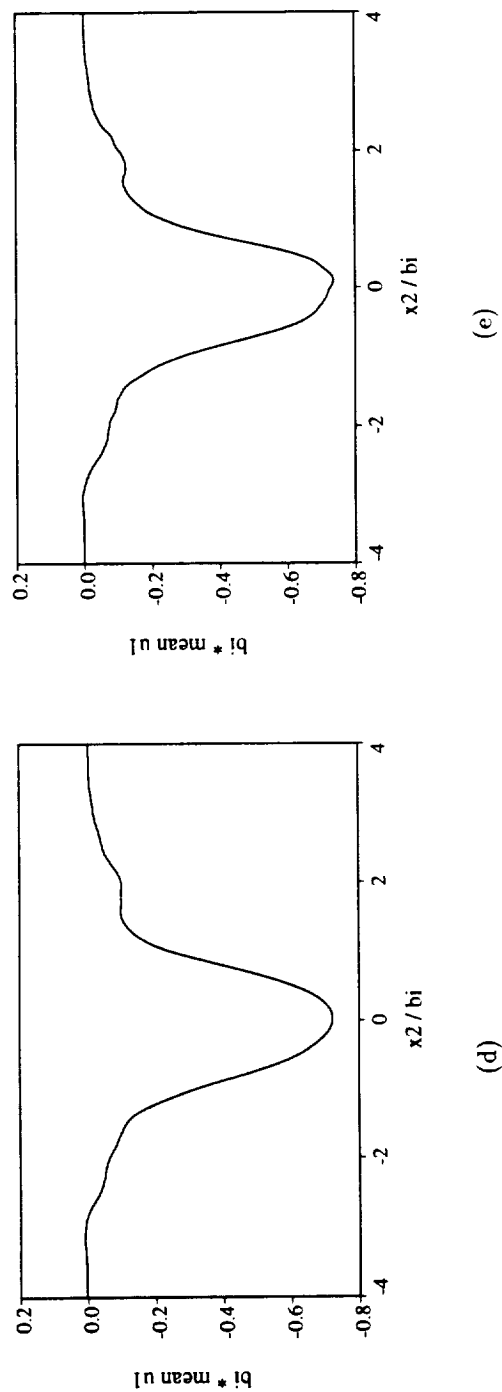


Figure 4.32: Normalized long time mean streamwise velocity defect profiles for  $(?) (60)_{0xx}^{x0x}$  wakes.  $t \sim 100.0$ .  
 (a)  $119(60)_{0xx}^{x0x}$ . (b)  $346(60)_{0xx}^{x0x}$ . (c)  $692(60)_{0xx}^{x0x}$ . (d)  $1384(60)_{0xx}^{x0x}$ . (e)  $2768(60)_{0xx}^{x0x}$ .

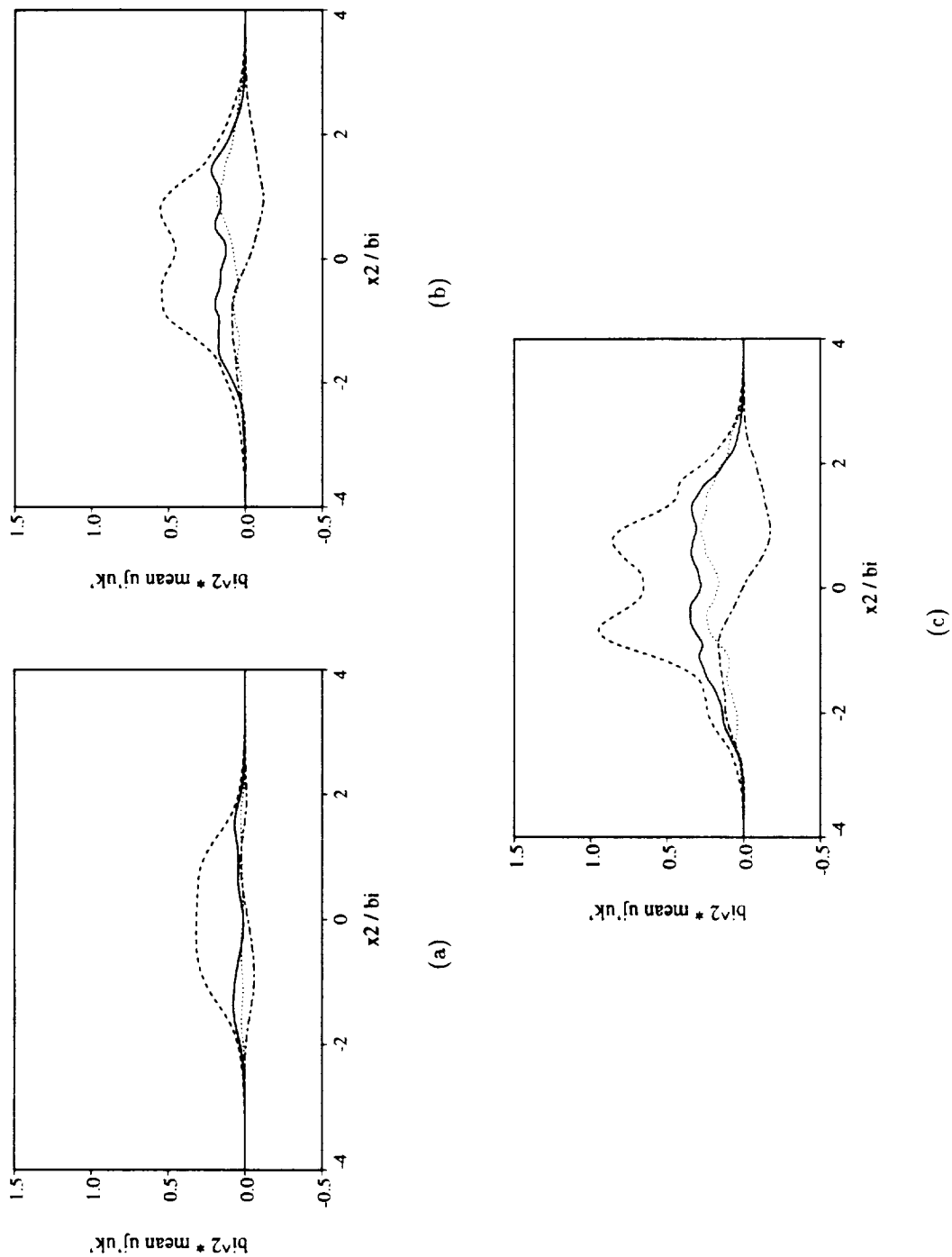


Figure 4.33: See caption page 141.



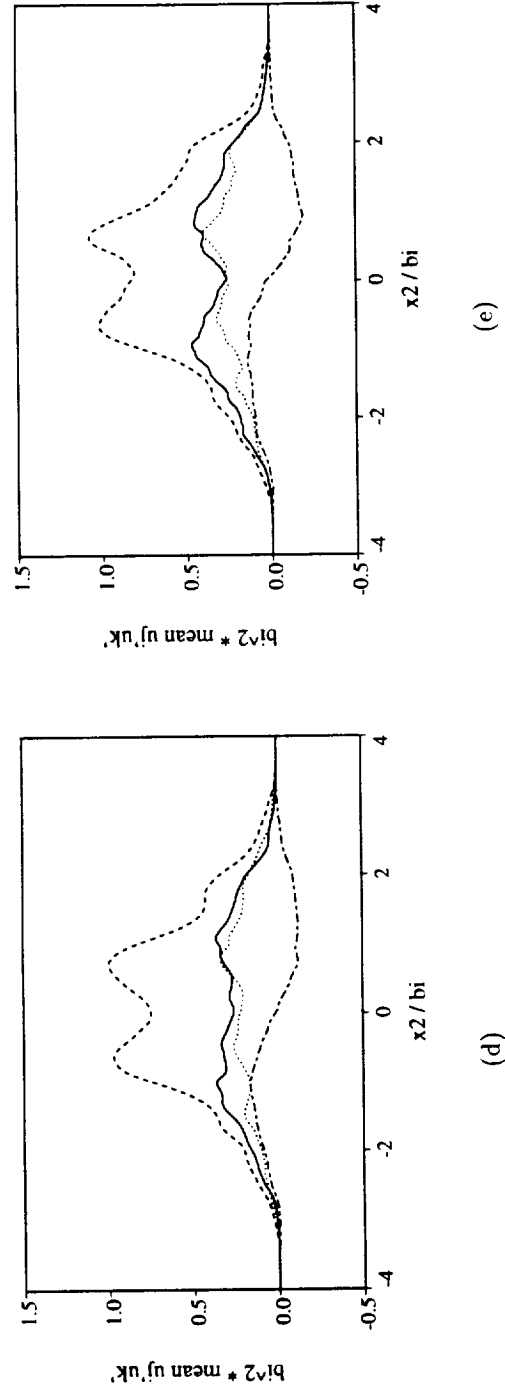


Figure 4.33: Normalized long time second order velocity correlations for  $\langle ? \rangle (60)_{0xx}^{x0x}$  wakes.  $t \sim 100.0$ . —:  $\overline{u'_1 u'_1}$ . - - - -:  $\overline{u'_2 u'_2}$ . . . .:  $\overline{u'_3 u'_3}$ . - . - . -:  $\overline{u'_1 u'_2}$ . (a) 119(60) $_{0xx}^{x0x}$ . (b) 346(60) $_{0xx}^{x0x}$ . (c) 692(60) $_{0xx}^{x0x}$ . (d) 1384(60) $_{0xx}^{x0x}$ . (e) 2768(60) $_{0xx}^{x0x}$ .

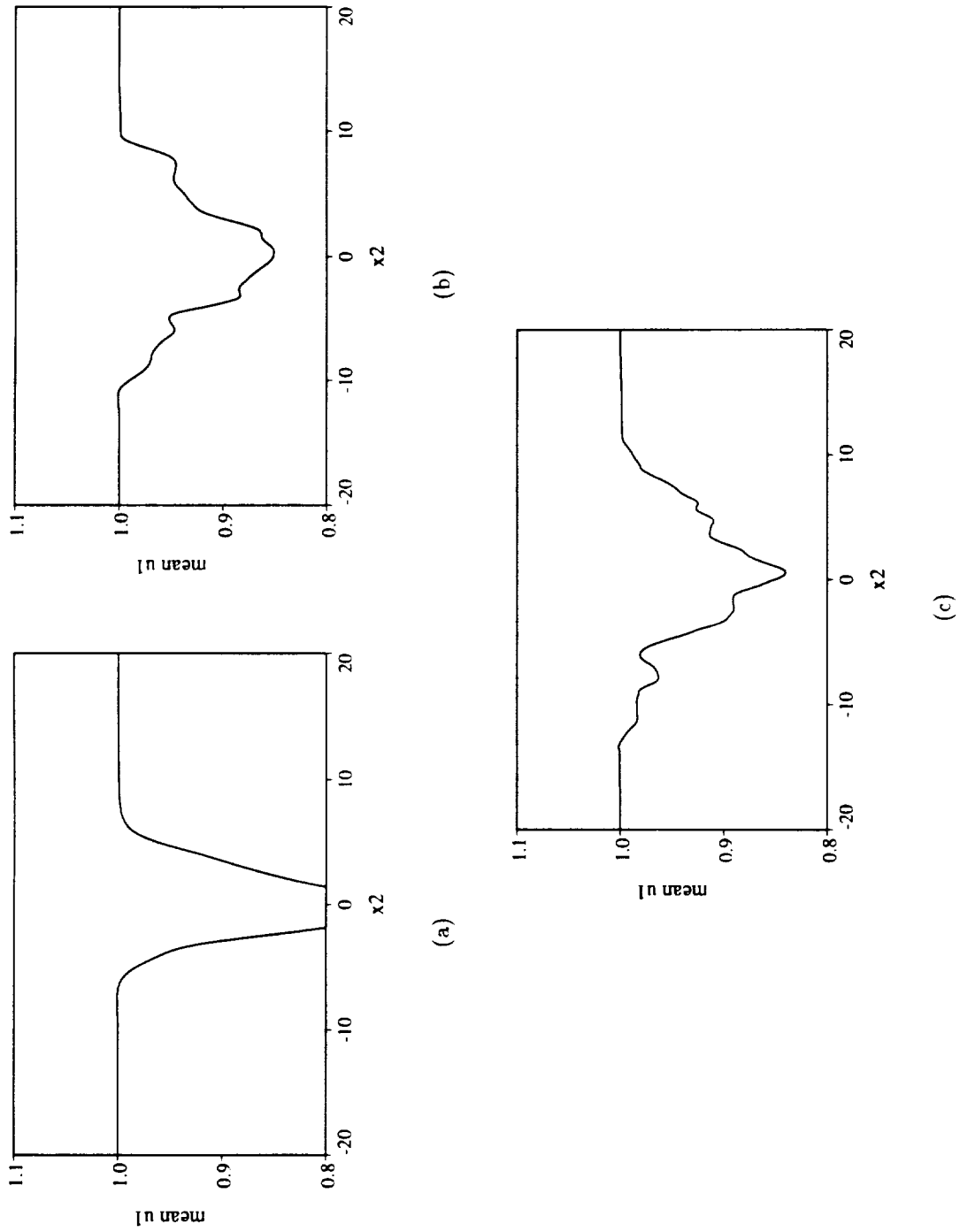


Figure 4.34: See caption page 143.

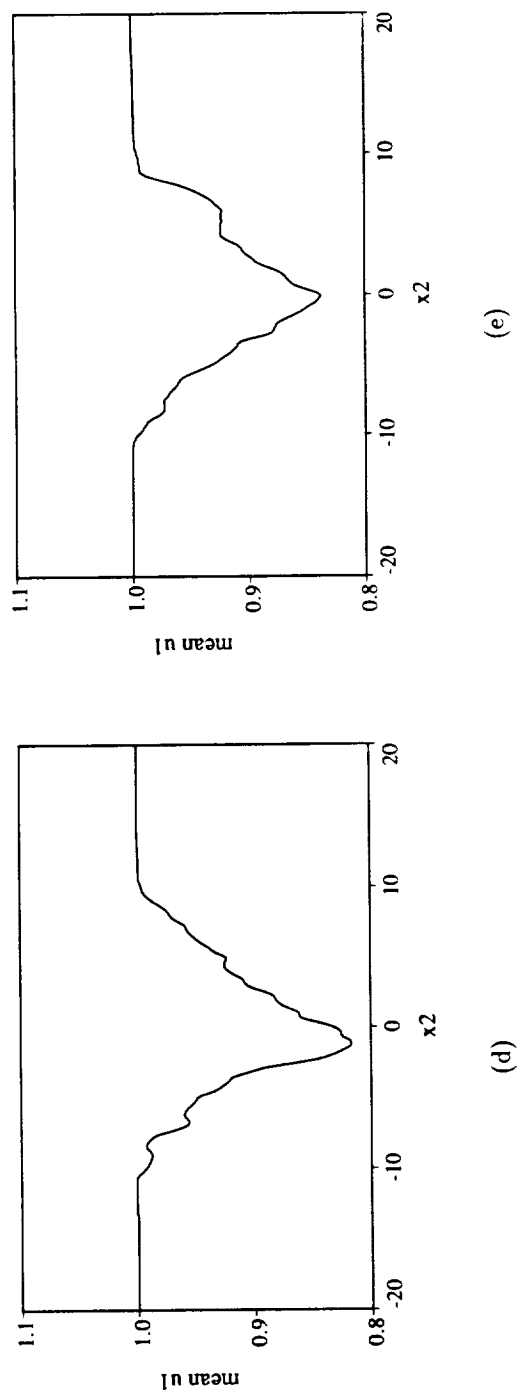


Figure 4.34: Mean streamwise velocity profiles for  $(?) (60)_{0xx}^{x0x}$  wakes.  $t \sim 200.0$ . (a)  $119(60)_{0xx}^{x0x}$ ,  $t = 203.3$ . (b)  $346(60)_{0xx}^{x0x}$ ,  $t = 204.8$ . (c)  $692(60)_{0xx}^{x0x}$ ,  $t = 201.9$ . (d)  $1384(60)_{0xx}^{x0x}$ ,  $t = 199.3$ . (e)  $2768(60)_{0xx}^{x0x}$ ,  $t = 194.6$ .

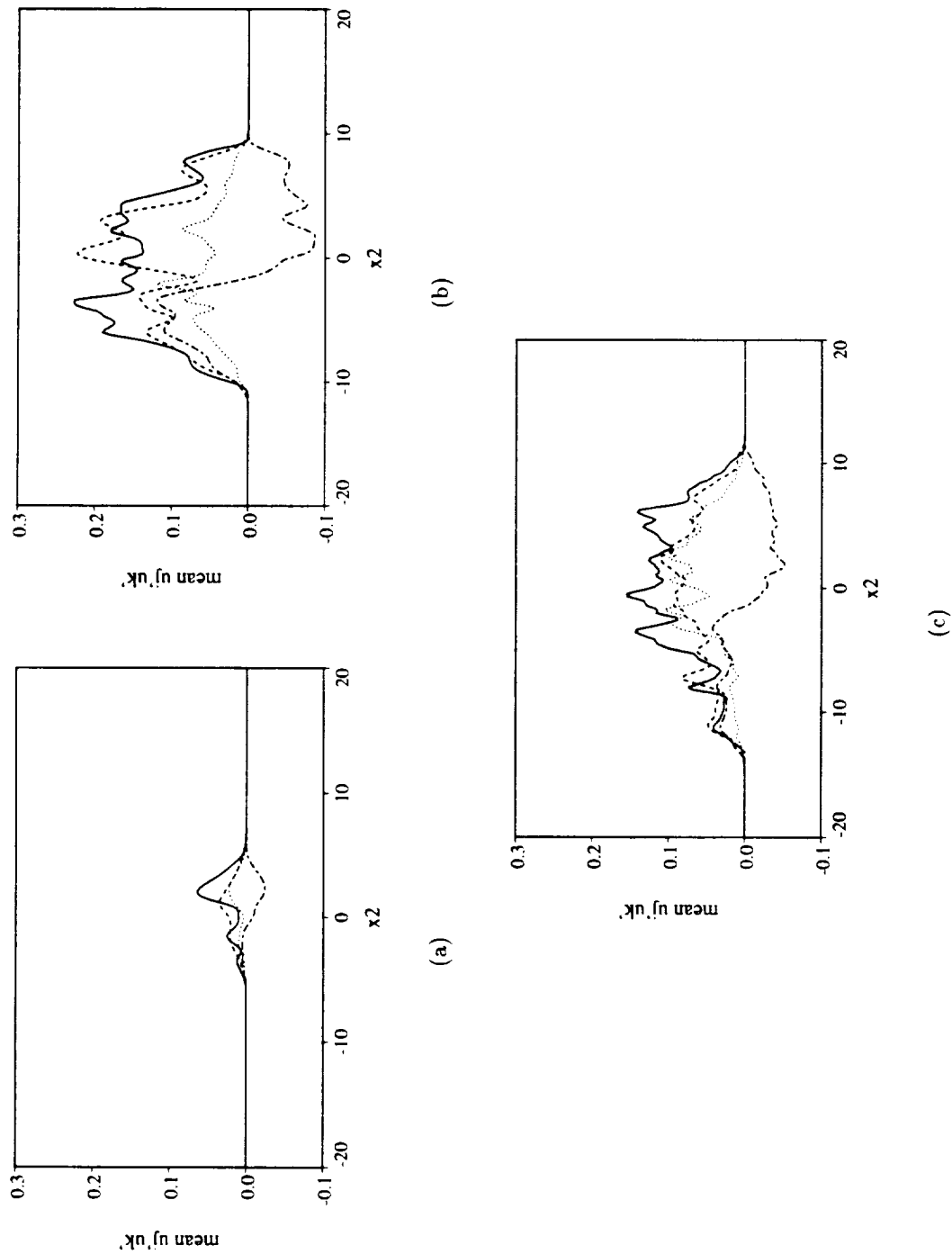


Figure 4.35: See caption page 145.

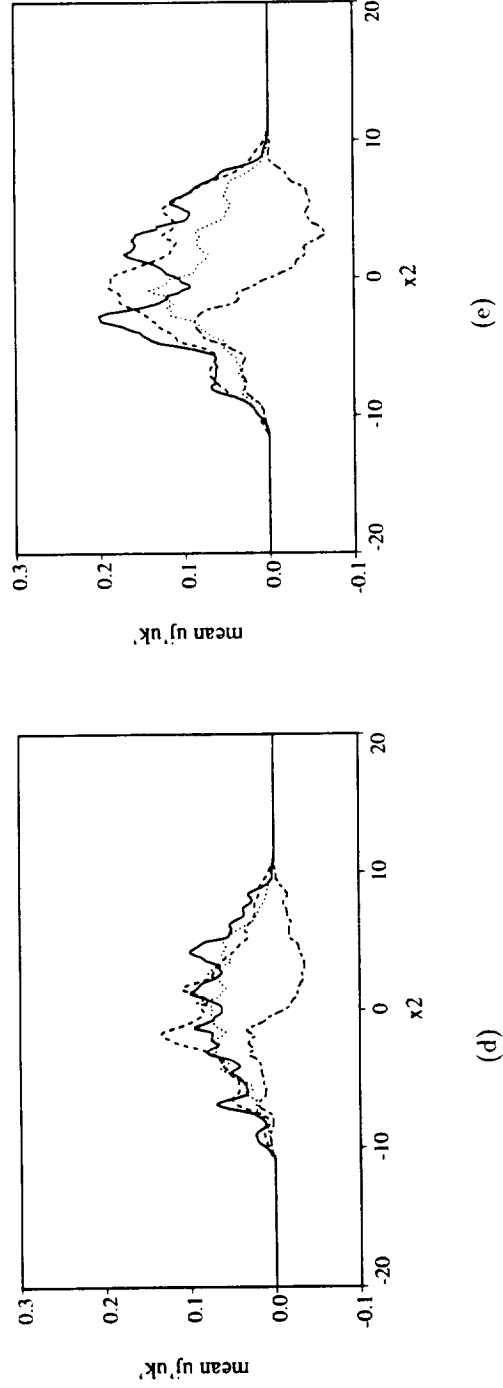


Figure 4.35: Second order velocity correlations for  $\langle ? \rangle (60)_{0xx}^{x0x}$  wakes.  $t \sim 200.0$ . — :  $u_1' u_1'$ . - - - :  $u_2' u_2'$ . . . . :  $u_3' u_3'$ . - . . . :  $u_1' u_2'$ . (a)  $119(60)_{0xx}^{x0x}$ ,  $t = 203.3$ . (b)  $346(60)_{0xx}^{x0x}$ ,  $t = 204.8$ . (c)  $692(60)_{0xx}^{x0x}$ ,  $t = 201.9$ . (d)  $1384(60)_{0xx}^{x0x}$ ,  $t = 199.3$ . (e)  $2768(60)_{0xx}^{x0x}$ ,  $t = 194.6$ .

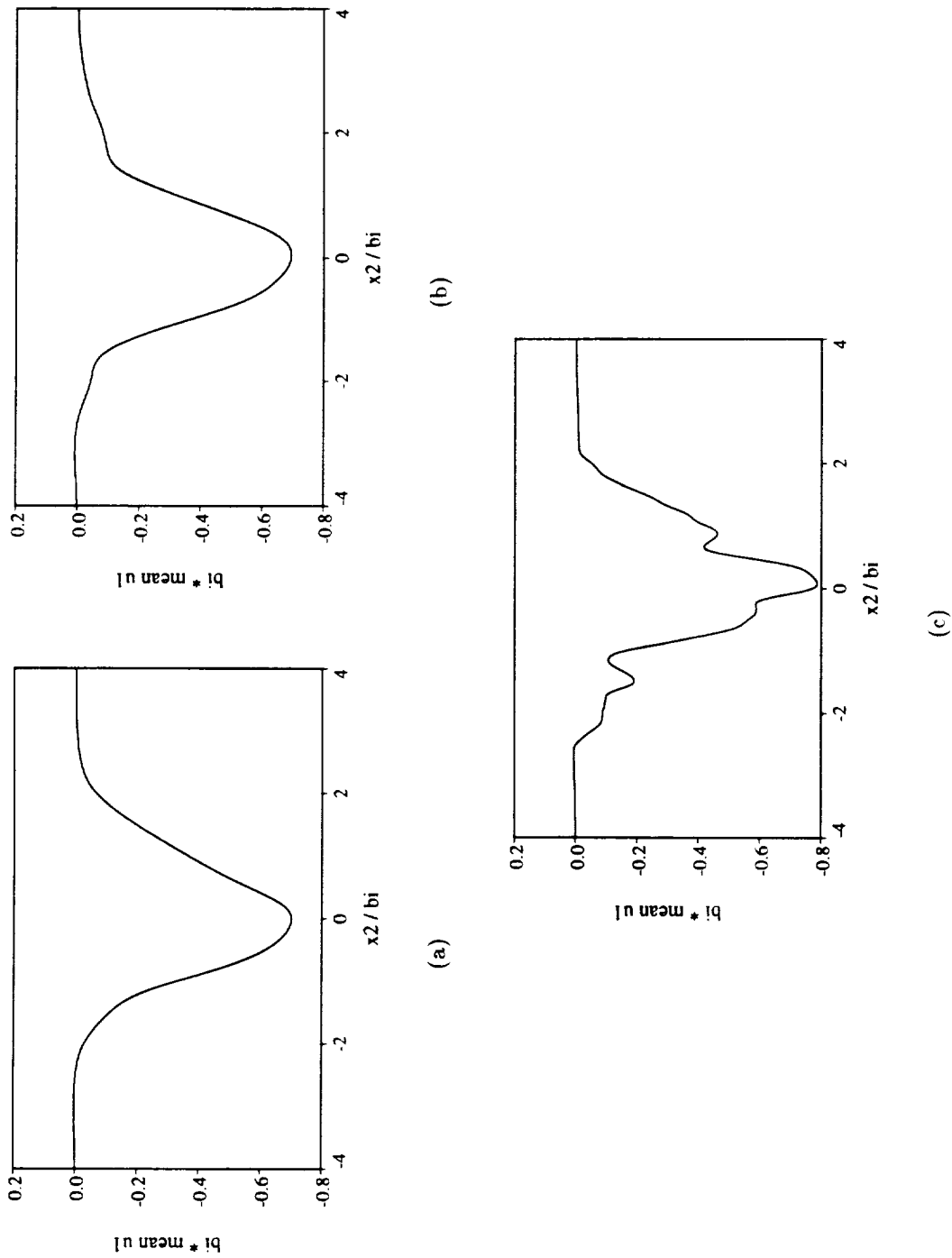


Figure 4.36: See caption page 147.

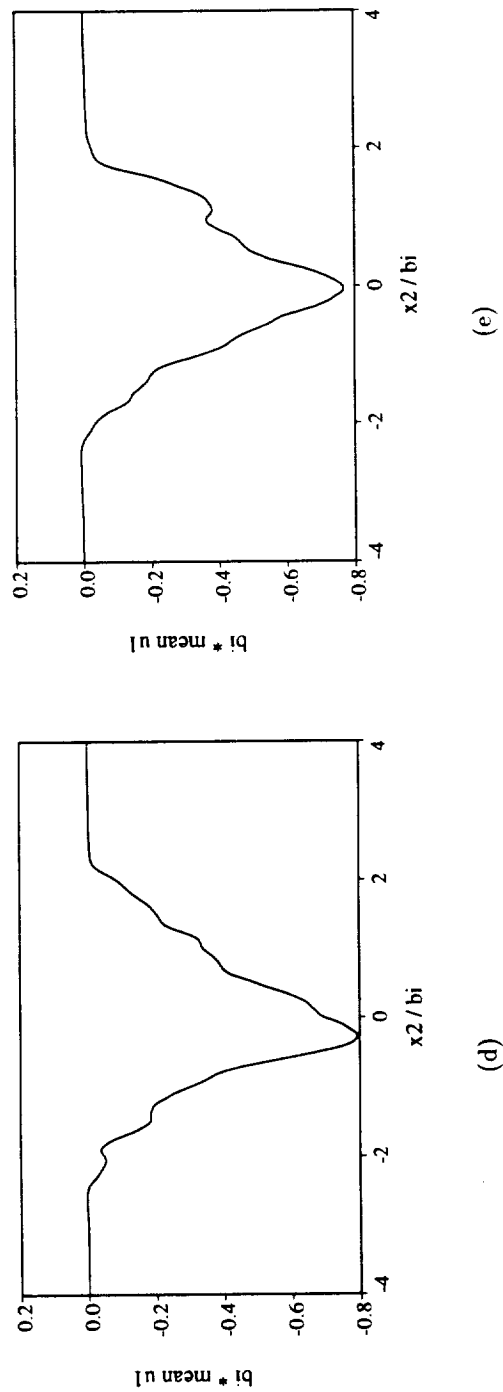


Figure 4.36: Normalized long time mean streamwise velocity defect profiles for  $\langle ? \rangle (60)_{0xx}^{x0x}$  wakes.  $t \sim 200.0$ .  
 (a)  $119(60)_{0xx}^{x0x}$ . (b)  $346(60)_{0xx}^{x0x}$ . (c)  $692(60)_{0xx}^{x0x}$ . (d)  $1384(60)_{0xx}^{x0x}$ . (e)  $2768(60)_{0xx}^{x0x}$ .

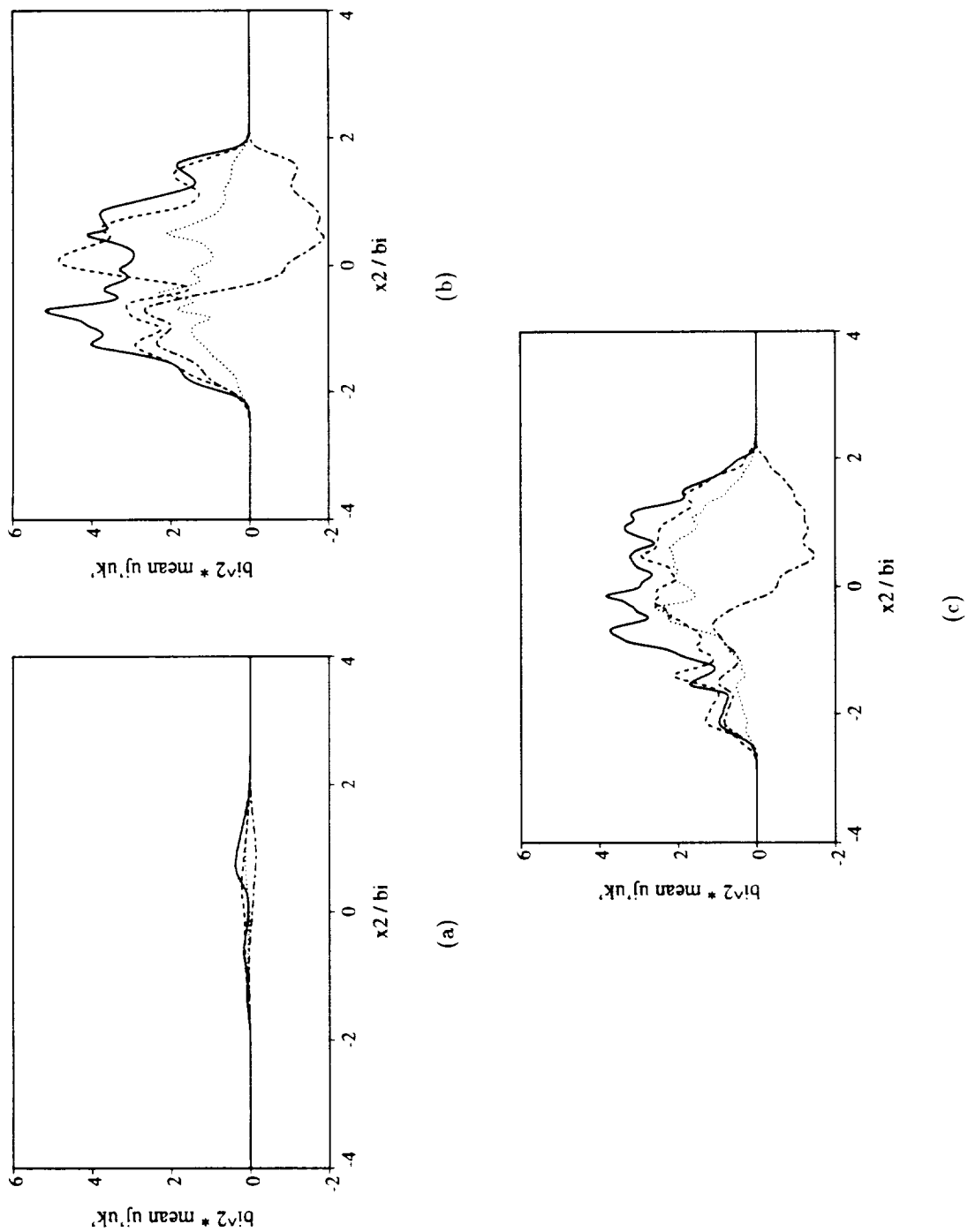


Figure 4.37: See caption page 149.



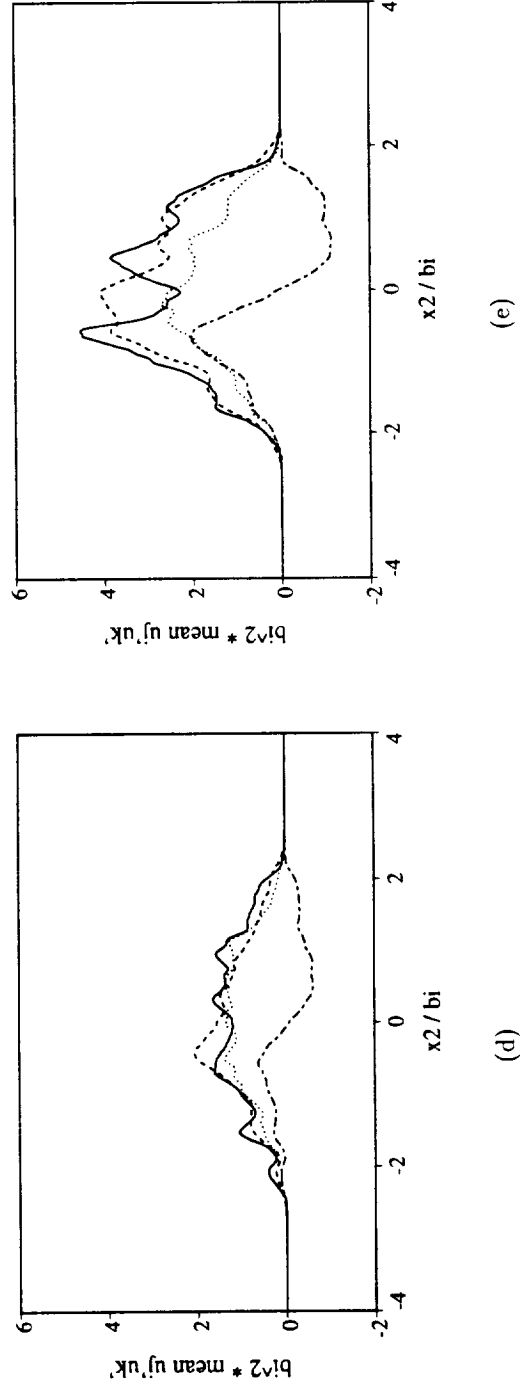


Figure 4.37: Normalized long time second order velocity correlations for  $(u'v')_{0xx}^{x0x}$  wakes.  $t \sim 200.0$ . —:  $\overline{u'_1 u'_1}$ . ----:  $\overline{u'_2 u'_2}$ . ....:  $\overline{u'_3 u'_3}$ . -.-.-.-:  $\overline{u'_1 u'_2}$ . (a) 119(60) $_{0xx}^{x0x}$ . (b) 346(60) $_{0xx}^{x0x}$ . (c) 692(60) $_{0xx}^{x0x}$ . (d) 1384(60) $_{0xx}^{x0x}$ . (e) 2768(60) $_{0xx}^{x0x}$ .

fairly short, the wake can not be considered fully turbulent. A proper classification for this wake is “transitional”.

This “transitional” classification is borne out by the mean streamwise ( $u_1$ ) velocity profiles which appear in figure 4.30. (The symmetry of the initial conditions is such that the spanwise and cross-stream velocities have zero mean). These profiles correspond to the wakes which appear in figure 4.13. Only for the lowest Reynolds number case ( $119(60)_{0xx}^{x0x}$  in figure 4.30a) where no significant three-dimensionality develops, is the mean profile Gaussian. For all of the higher Reynolds number wakes (figures 4.30b–e) the coherent structures in the flow distort the shape of the mean profiles. Specifically, the “lumps” in the profiles that appear in the vicinity of  $x_2 = \pm 5.0$  are a result of the strong streamwise structures that appear in figures 4.13b–e. The shape of the profile for the  $2768(60)_{0xx}^{x0x}$  wake (figure 4.30e), which is significantly non-Gaussian again indicates that that flow is not fully turbulent, but instead is still transitional.

Figure 4.31 shows the second order velocity correlations,  $\overline{u'_j u'_k}$  versus the cross-stream coordinate  $x_2$  corresponding to the mean profiles in figure 4.30. Again, because of the symmetry of the initial conditions,  $\overline{u'_1 u'_3}$  and  $\overline{u'_2 u'_3}$  are zero, so they are not shown. These profiles are typical of plane wakes, with the most intense unsteady motions occurring away from the wake centerline. As expected, the intensity of the unsteady motions increases with increasing Reynolds number. Once again the effects of the coherent structures are on the profiles in the vicinity of  $x_2 = \pm 5.0$ . This is particularly apparent in the  $\overline{u'_2 u'_2}$  profiles for the wakes in figures 4.31c–e. This implies that the coherent structures shown in figure 4.13 are still responsible for significant unsteadiness in the wakes.

In a physical flow, the effects of coherent structures on long time averages are smeared out. This is due to the presence of low amplitude long wavelength motions that cause each set of coherent structures to be offset in space slightly from the other sets. Since the longest wavelength available in any of the simulations presented is not very large, the effective averaging domain is not large, and the effects of coherent structures on the averages are more pronounced than would be seen in a physical experiment. figures 4.32 and 4.33 are an attempt to get around this shortcoming. This has been done by taking mean data from several times near the time of interest

(approximately  $t \pm 0.1t$  in this case) for each simulation. The separate mean data sets are normalized using the integral halfwidth at each time,  $b_i(t)$ , and forming a combined mean. This effectively increases the sample size, and introduces the sort of jitter in the coherent motions that one would expect in a physical flow.

The long time mean streamwise velocity profiles in figure 4.32 are considerably smoother than the single time mean profiles for the same datasets in figure 4.30. The profiles are significantly more Gaussian in appearance, though the effects of the coherent three-dimensional structures are still evident near the edges of the wakes.

The same smoothing effect can be seen in the long time second order correlations in figure 4.33. The general shapes remain unchanged from the single time plots in figure 4.31, but the bimodal form of the  $\overline{u'_1 u'_1}$ ,  $\overline{u'_2 u'_2}$ , and  $\overline{u'_3 u'_3}$  correlations are more clearly evident, particularly for the higher Reynolds number cases.

Figure 4.34 shows single time mean streamwise velocity profiles for the same set of simulations shown in figure 4.30 but at a later time of approximately  $t = 200$  for each wake. Again the single time means for all of the higher Reynolds number wakes simulated are quite non-Gaussian due to the strong coherent streamwise structures that appear in the flow. Taking a long time average (figure 4.36) makes the mean velocity profiles appear more Gaussian, but the highest Reynolds number wakes continue to have distinctly non-Gaussian mean profiles.

Figure 4.35 shows the single time second order velocity correlations for the same set of wake simulations, again at a time of approximately  $t = 200$  for each wake. Figure 4.37 shows the corresponding long time correlations. The most significant thing to note is that the  $Re = 119$  wake (figure 4.35a) has significantly weaker unsteady motions than the wakes at Reynolds numbers. This is due to the fact that at that low Reynolds number, the wake never develops strong fine scale motions.

The effect of fine scale motions is also apparent in the relative magnitudes of the second order velocity auto-correlations for the higher Reynolds number wakes. At the earlier time of  $t \sim 100$  shown in figures 4.31 and 4.33 the  $\overline{u'_2 u'_2}$  correlation was approximately twice the magnitude of the  $\overline{u'_1 u'_1}$  and  $\overline{u'_3 u'_3}$  correlations. At  $t \sim 200$ , the onset of significant small scale motions have caused these three quantities to be both much larger in magnitude relative to the mean flow (note difference in scales in

figures 4.33 and 4.37) and much closer in magnitude to each other. This is due to the fact that at the earlier time, most of the velocity fluctuations are due to large scale coherent structures, which favor the  $\overline{u'_2 u'_2}$  correlation. At the later time more of the velocity fluctuations are due to the more randomly distributed fine scales, which contribute equally to all three second order auto-correlations.

## Chapter 5

# Three-dimensional Topological Description

In order to study the fine scale (high wavenumber), high gradient motions in the computed wakes, a topological classification method has been applied. The method is based on concisely summarizing the local flow structures in the space of the invariants of the velocity gradient, strain rate, and rotation rate tensors. This allows information about the local flow geometry for every point in the incompressible flow to be presented in the form of two-dimensional joint probability density functions (pdfs) of various combinations of the invariants. These pdf plots facilitate the study of global trends in the local structure of the fine scales in the velocity field.

Only a small subset of the invariant space plots for the wakes that have been simulated will be presented here. See appendix E for a more complete set of plots.

### 5.1 Topological Method

An abbreviated description of the topological method used will be presented in this section. An extended description can be found in appendix D.

The velocity gradient tensor

$$A_{jk} \equiv u_{j,k} \tag{5.1}$$

can be split into a symmetric and an antisymmetric part

$$A_{jk} = S_{jk} + W_{jk} \quad (5.2)$$

where the symmetric part

$$S_{jk} \equiv \frac{1}{2}(u_{j,k} + u_{k,j}) \quad (5.3)$$

is the rate-of-strain tensor, and the anti-symmetric part

$$W_{jk} \equiv \frac{1}{2}(u_{j,k} - u_{k,j}) \quad (5.4)$$

is the rate-of-rotation tensor. The eigenvalues  $\lambda$  of  $A_{jk}$  satisfy the characteristic equation

$$\lambda^3 + P\lambda^2 + Q\lambda + R = 0 \quad (5.5)$$

where  $P$ ,  $Q$ , and  $R$  are referred to as the *invariants* of the tensor  $A_{jk}$  and are given by

$$P = -A_{kk} = -S_{kk} \quad (5.6)$$

$$\begin{aligned} Q &= \frac{1}{2}(P^2 - A_{jk}A_{kj}) \\ &= \frac{1}{2}(P^2 - S_{jk}S_{kj} - W_{jk}W_{kj}) \end{aligned} \quad (5.7)$$

$$\begin{aligned} R &= -\det[A_{jk}] \\ &= \frac{1}{3}(-P^3 + 3PQ - A_{jk}A_{kl}A_{lj}) \\ &= \frac{1}{3}(-P^3 + 3PQ - S_{jk}S_{kl}S_{lj} - 3W_{jk}W_{kl}S_{lj}). \end{aligned} \quad (5.8)$$

The values of the three invariants  $P$ ,  $Q$ , and  $R$  completely determine the eigenvalues, and therefore the eigenvectors, of the velocity gradient tensor  $A_{jk}$ . Since the eigenvectors of  $A_{jk}$  determine the local flow kinematics, the local flow geometry is determined to within an arbitrary rotation by the location of the three invariants in  $(P, Q, R)$  space. See Chong, Perry, and Cantwell [12] for a detailed discussion of the local flow geometries associated with the various regions of  $(P, Q, R)$  space.

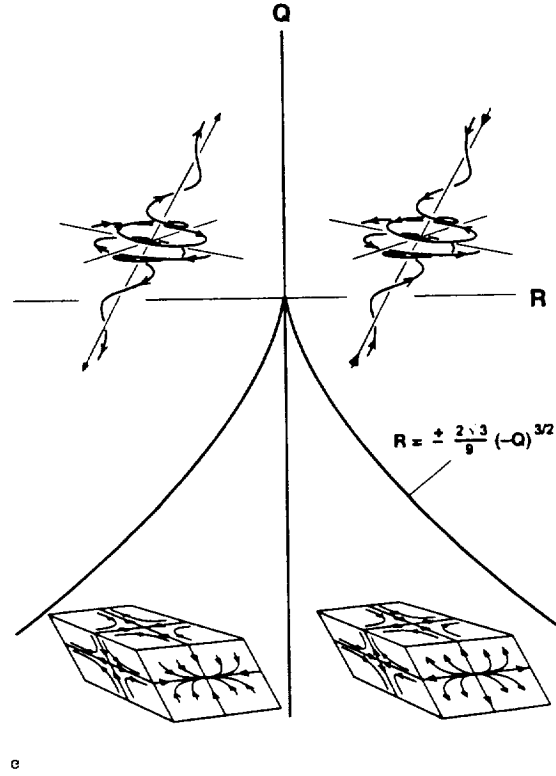


Figure 5.1: Invariant Space for Incompressible Flows

For incompressible flow

$$P = 0 \quad (5.9)$$

and the second and third invariants reduce to

$$Q = -\frac{1}{2}(S_{jk}S_{kj} + W_{jk}W_{kj}) \quad (5.10)$$

$$R = -\frac{1}{3}(S_{jk}S_{kl}S_{lj} + 3W_{jk}W_{kl}S_{lj}). \quad (5.11)$$

Hence the local flow geometry is completely determined by the location of the second and third invariants of the velocity gradient tensor in  $(Q, R)$  space.

The curve in  $(Q, R)$  space that separates characteristic equations with all real solutions (strain dominated local flow) from those with one real and two complex

solutions (rotation dominated local flow) is given by

$$27R^2 + 4Q^3 = 0. \quad (5.12)$$

This curve, along with the  $Q$  axis, separates the  $(Q, R)$  space into four regions as shown in figure 5.1:

- Above the separator and to the left of the  $Q$  axis, the local flow spirals in towards the local origin in a plane and then flow out along the third direction. This local flow geometry is referred to as a stable-vortex/stretching.
- Above the separator and to the right of the  $Q$  axis, the local flow is toward the local origin along one axis and spirals out in a plane. This local flow geometry is referred to as an unstable-vortex/contracting.
- Below the separator and to the left of the  $Q$  axis, the local flow approaches the origin along two axes and flows outward along the third. This local flow geometry is referred to as a stable-node/saddle/saddle.
- Below the separator and to the right of the  $Q$  axis, the local flow approaches the origin along one axis and flows outward along the other two. This local flow geometry is referred to as an unstable-node/saddle/saddle.

The flow geometry for a single data point can be determined simply by calculating the invariants and determining where they lie in  $(Q, R)$  space. Global trends for large quantities of data can be examined by calculating the invariants for each point in the data set and constructing joint probability density functions (pdf's) in  $(Q, R)$  space for the entire data set. Moreover, motions with high gradients will tend to lie far from the origin in  $(Q, R)$  space, so the most intense motions will tend to separate themselves visually when viewed in the space of invariants.

Other quantities related to the invariants of the velocity gradients tensor are also of interest. The second invariant,  $Q$ , may be written as the sum of quantities

$$\begin{aligned} Q &= -\frac{1}{2}(S_{jk}S_{jk} + W_{jk}W_{jk}) \\ &= Q_s + Q_u \end{aligned} \quad (5.13)$$



where

$$Q_s = -\frac{1}{2}S_{jk}S_{jk} \quad (5.14)$$

is the negative-definite second invariant of the rate-of-strain tensor and

$$Q_w = \frac{1}{2}W_{jk}W_{jk} \quad (5.15)$$

is the positive-definite second invariant of the rate-of-rotation tensor.

The second invariant of the rate-of-strain tensor is directly proportional to the mechanical dissipation rate

$$\varphi = 2\nu S_{jk}S_{kj} = -4\nu Q_s. \quad (5.16)$$

Points with a large negative value for  $Q_s$  have large dissipation. The second invariant of the rate-of-rotation tensor is equal to the enstrophy density

$$\omega_j\omega_j = Q_w. \quad (5.17)$$

Points with large positive values of  $Q_w$  have high associated enstrophy density. Thus, the second invariant of the velocity-gradient tensor can be thought of as a measure of the relative importance of strain and rotation. Plots of  $-Q_s$  vs.  $Q_w$  reveal correlations between strain and rotation fields. Plots of  $Q_s$  vs.  $R_s$ , the third invariant of the rate-of-strain tensor

$$R_s = -\frac{1}{3}S_{jk}S_{kl}S_{lj} \quad (5.18)$$

reveal trends in the type of rate-of-strain field associated with high dissipation regions. Since the rate-of-strain tensor is symmetric it only has real eigenvalues, hence its second and third invariant will always fall underneath the separator, and the possible rate-of-strain topologies will be limited to either stable-node/saddle/saddle or unstable-node/saddle/saddle.

Finally, the vortex stretching rate,  $\sigma$ , may be expressed in terms of the invariants of the velocity-gradient and rate-of-strain tensors

$$\sigma = W_{jk}W_{kl}S_{lj} = R_s - R. \quad (5.19)$$

Plots of the enstrophy density versus stretching,  $Q_w$  vs.  $\sigma$  can be examined to reveal global trends.

## 5.2 Effect of Initial Conditions

Figure 5.2 shows plots of the joint pdf of  $Q$  and  $R$  for a set of  $Re_b = 346$  wakes with a variety of combinations of initial disturbance wavelengths. The first feature that is apparent is that, as one would expect from the discussion of the wakes in physical space presented earlier, the wake initiated with only a two-dimensional fundamental and a three-dimensional fundamental ( $346(60)_{0xx}^{0xx}$  in figure 5.2a) has fine scale motions which have much lower gradients (are much weaker) than the other wakes (recall that high gradient motions tend to appear far from the origin in invariant space). Further, though the wake which has an additional two-dimensional subharmonic disturbance ( $346(60)_{00x}^{0xx}$  in figure 5.2e) has gradients that are on par with the wakes that have a three-dimensional subharmonic disturbance (figures 5.2b–d), those high gradients account for a much smaller percentage of the flow as evidenced by the relative small area inside the second contour level. Note that the contour levels shown are logarithmic, with each contour level being ten times the value of the previous level, thus large differences in the area inside of a given contour level equate to very large differences in the relative volume of the fluid in physical space represented.

The second feature that is readily apparent is that the overall shape of the joint pdf of  $Q$  and  $R$  is the same for all of the wakes, with high gradients motions favoring the upper left (stable-vortex/stretching) and lower right (unstable-node/saddle/saddle) regions of  $(Q, R)$  space. This same “skewed teardrop” shape has been observed by Soria *et al.* [42] and Chen *et al.* [11] in studies of the gradients in compressible and incompressible temporally evolving mixing layers, Blackburn, Mansour, & Cantwell

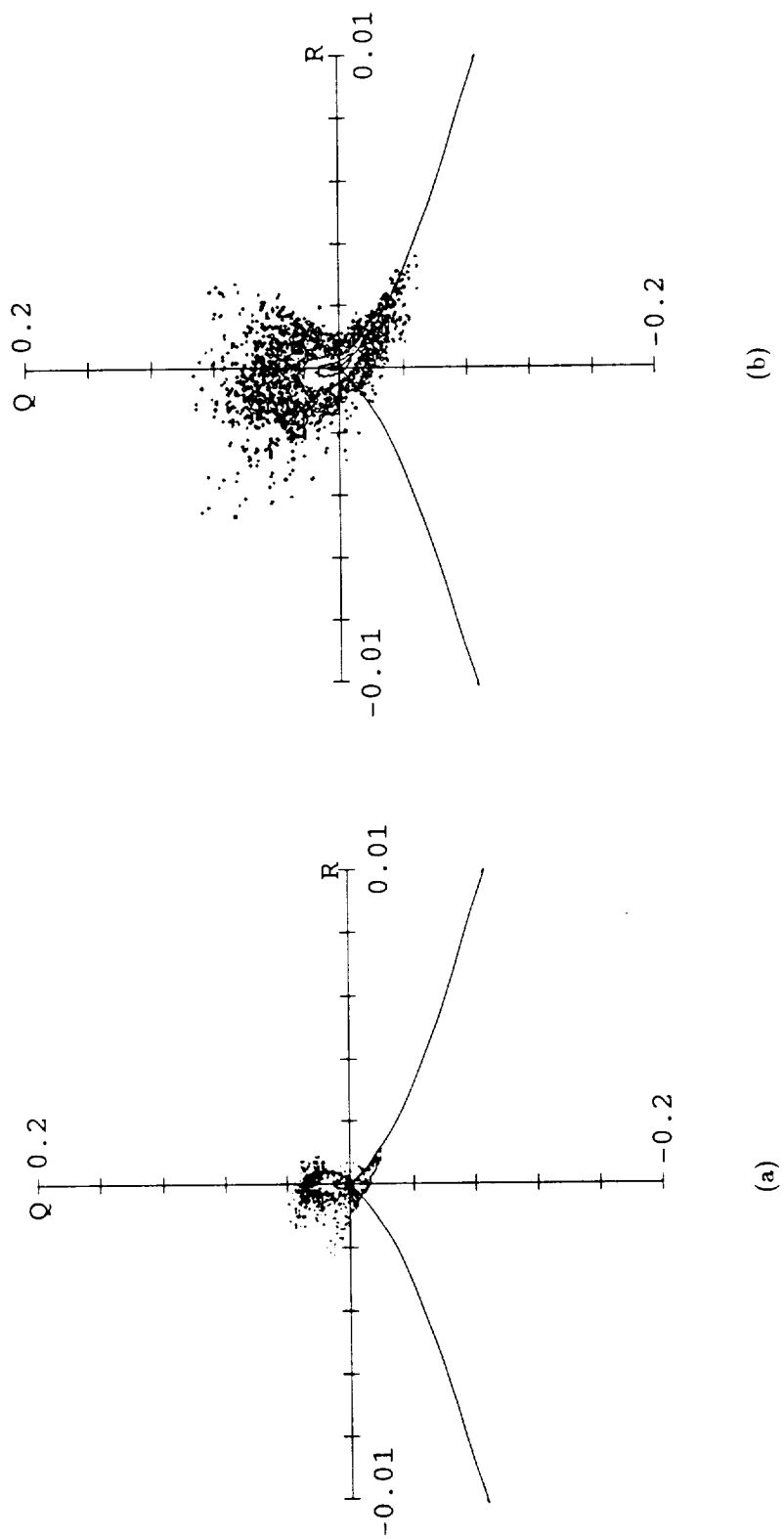


Figure 5.2: See caption page 161.

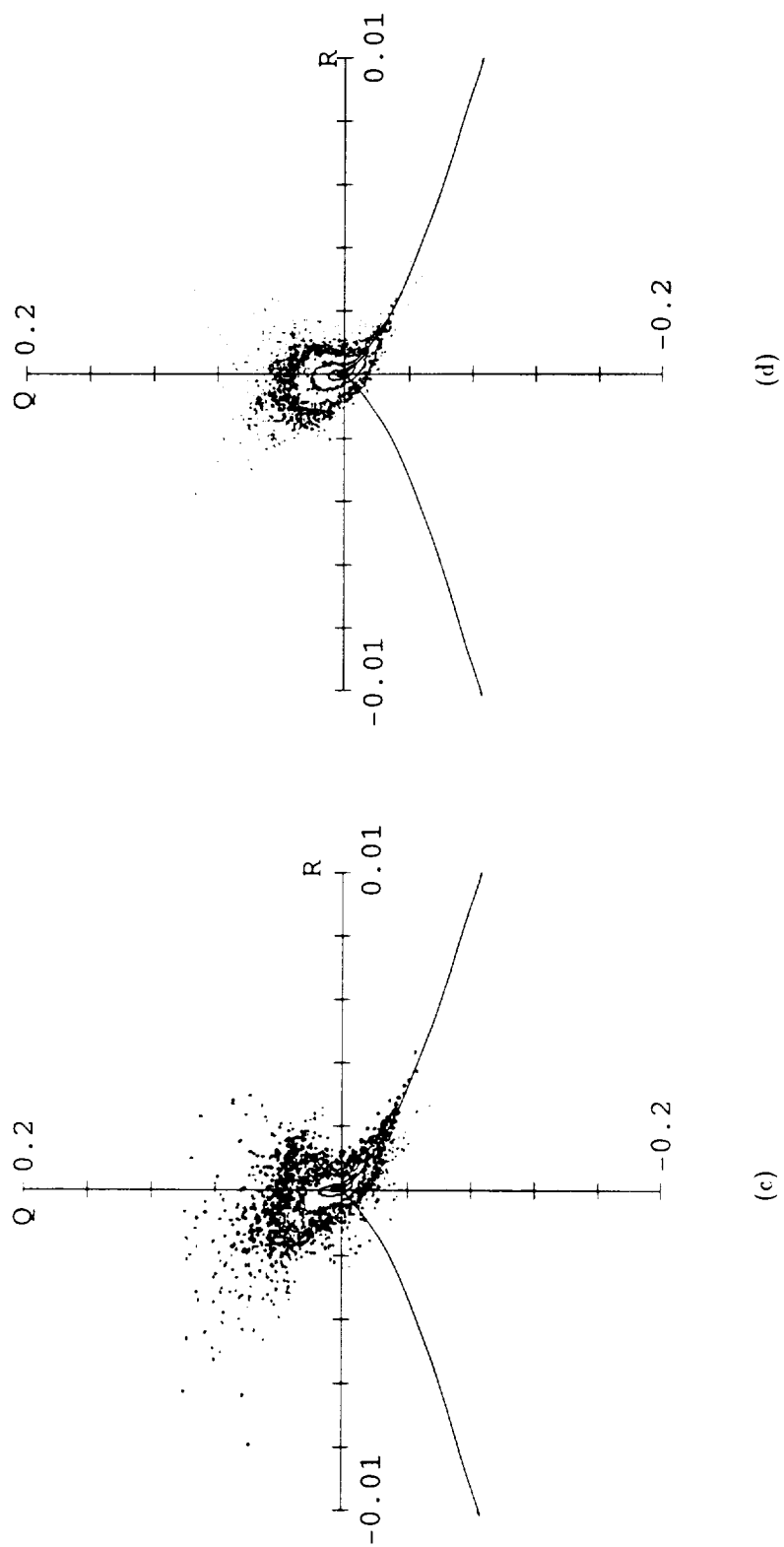


Figure 5.2: See caption page 161.

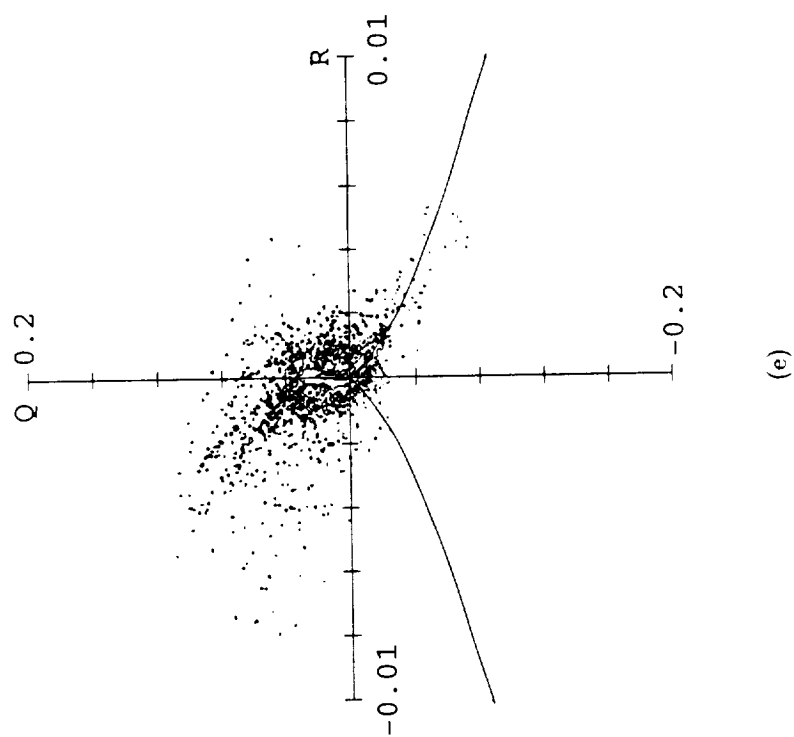


Figure 5.2: Contour plots of joint pdf of  $Q$  vs.  $R$  for  $Re_b = 346$  wakes with various initial disturbance wavelengths.  
 (a)  $346(60)_{0xx}^{0xx}$ ,  $t = 196.9$ . (b)  $346(60)_{0xx}^{x0x}$ ,  $t = 181.1$ . (c)  $346(60)_{0xx}^{x00}$ ,  $t = 197.0$ .  
 (d)  $346(60)_{0xx}^{0xx}$ ,  $t = 202.8$ . (e)  $346(60)_{0xx}^{0xx}$ ,  $t = 204.8$ .

[3] in a computation of a turbulent channel flow, and Sondergaard *et al.* [41] in a survey of computations of compressible and incompressible shear flows including mixing layers, wakes, and isotropic and sheared homogeneous turbulence.

It is apparent from the wide variety of flow fields which exhibit this feature that it is a characteristic of solutions to the Navier-Stokes equations (the pdf of  $Q$  and  $R$  generated from random gradient fields do not exhibit this feature). Cantwell [6] performed an analysis of the evolution of the velocity gradient tensor in incompressible flows and found that, given certain assumptions, the second and third invariants were restricted to an attractor in invariant space with a shape similar to the one which has been observed.

Figure 5.3 shows plots of the joint probability density functions of the second and third invariants of the rate-of-strain tensor ( $Q_s$  and  $R_s$ ) for the same wakes shown in figure 5.2. Once again, the much weaker gradients in the two-dimensional fundamental / three-dimensional oblique fundamental case ( $346(60)_{0xx}^{0xx}$  in figure 5.3a) are apparent. And again, the  $346(60)_{00x}^{0xx}$  wake (figure 5.3e) shows gradients on par with the simulations which have a three-dimensional subharmonic, but with a much smaller volume of high gradient motions occurring.

All of the pdf's have the same general shape, with highly dissipating motions (large negative  $Q_s$ ) showing a strong preference for the unstable-node/saddle/saddle type topology. This strong preference continues even for more moderately dissipating regions as demonstrated by figure 5.4, which is a magnified version of figure 5.3b. These moderately dissipating motions account for the majority of the total dissipation in the flow. Again, these same trends were observed by Chen *et al.*, Soria *et al.*, Blackburn *et al.*, and Sondergaard *et al.* in a wide range of other flows.

Figure 5.5 shows plots of the joint pdf of  $-Q_s$  (dissipation) and  $Q_w$  (enstrophy density) for the same set of simulations shown in figures 5.2 and 5.3. Once again the much lower gradients for the three-dimensional fundamental cases (figures 5.5a and 5.5e) is apparent. These wakes also have a pdf shape which is different than those for the wakes with a three-dimensional subharmonic (figures 5.5b-d). The “L” shaped pdf in figures 5.5a and 5.5e, which tends to hug the axes, is common in non-turbulent flows and flows in which the turbulent motions have not had time to fully

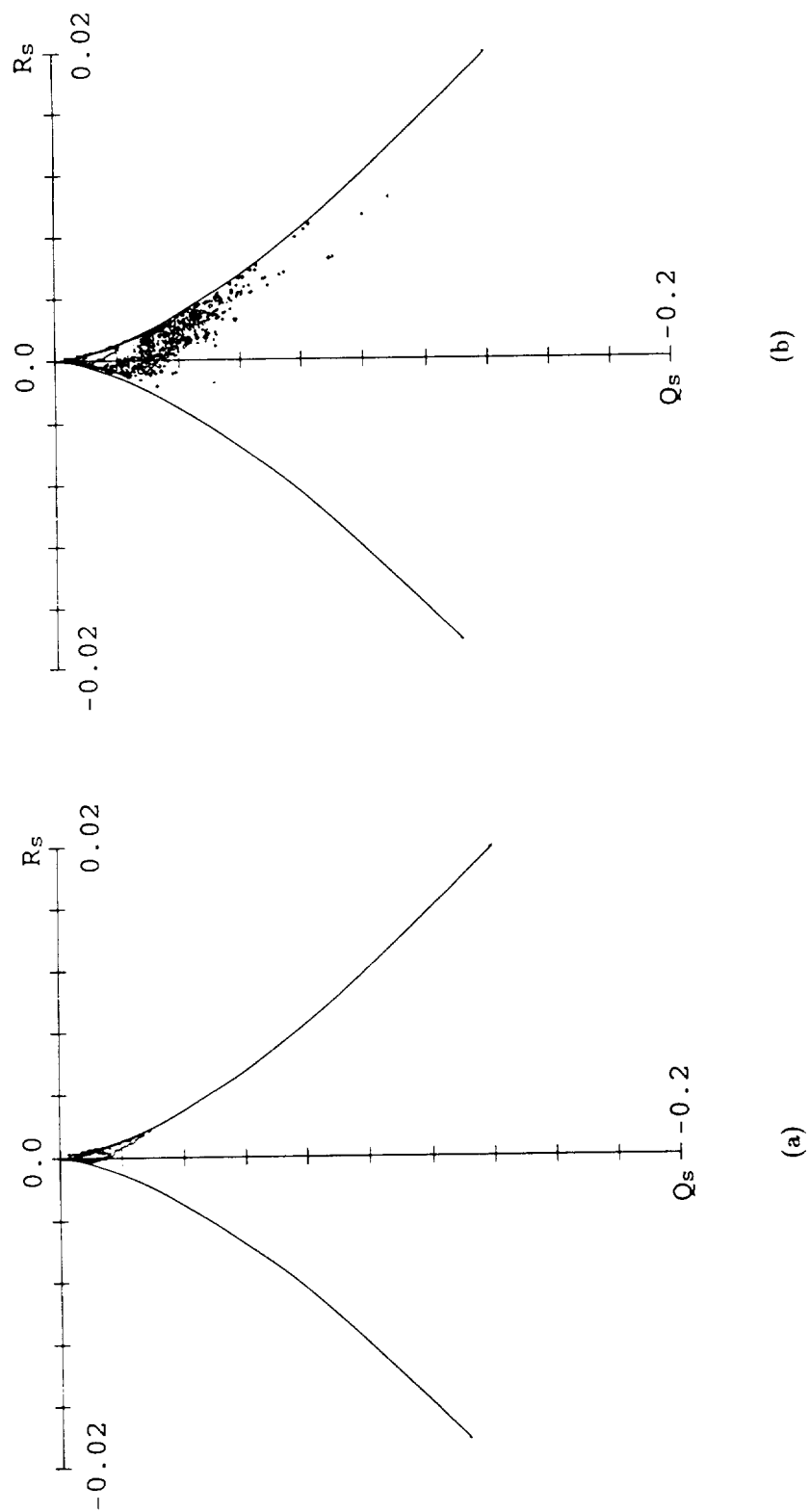


Figure 5.3: See caption page 165.

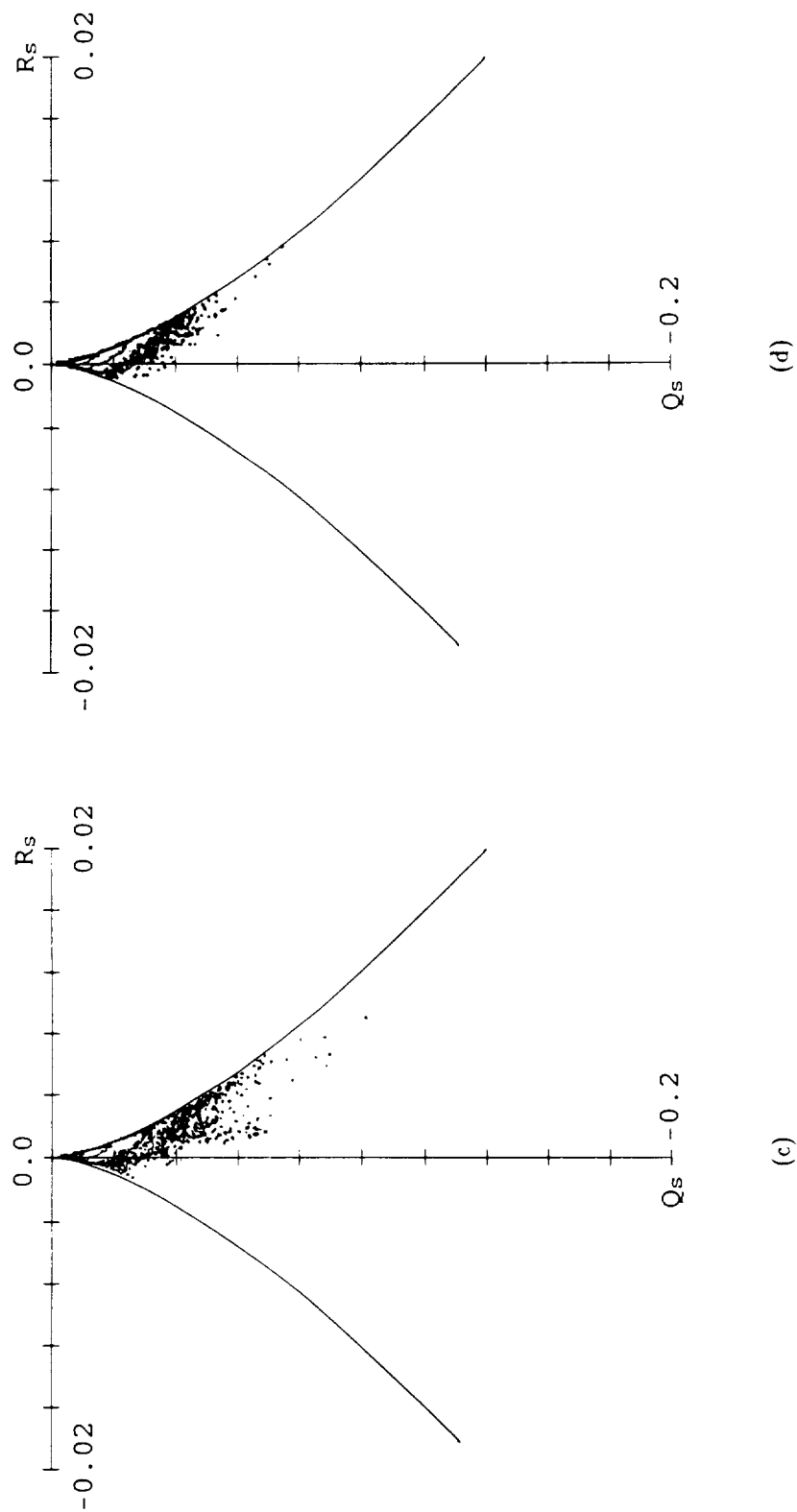
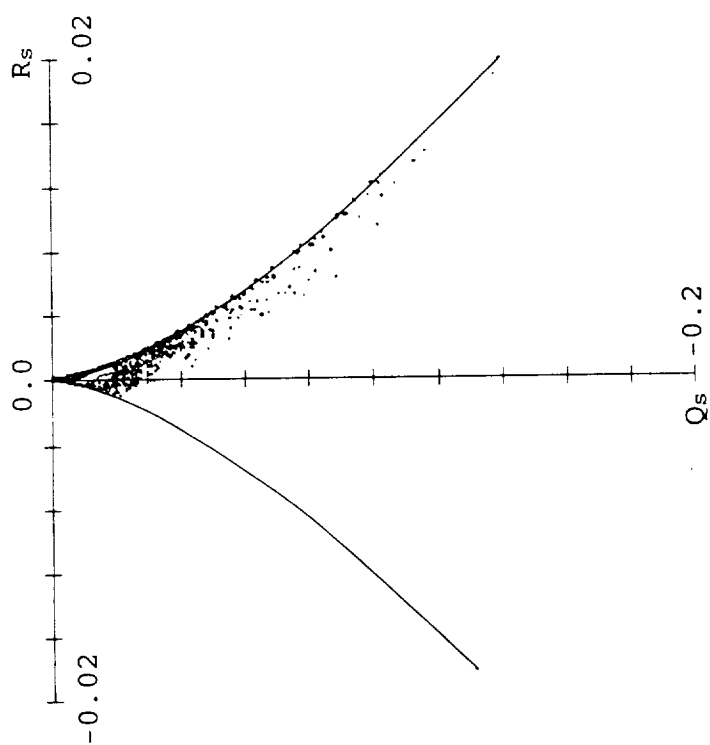


Figure 5.3: See caption page 165.





(e)

Figure 5.3: Contour plots of joint pdf of  $Q_s$  vs.  $R_s$  for  $Re_b = 346$  wakes with various initial disturbance wavelengths.  
 (a)  $346(60)_{0xx}^{0xx}$ ,  $t = 196.9$ . (b)  $346(60)_{0xx}^{x0x}$ ,  $t = 204.8$ . (c)  $346(60)_{00x}^{x0x}$ ,  $t = 181.1$ . (d)  $346(60)_{000}^{x00}$ ,  $t = 197.0$ .  
 (e)  $346(60)_{00x}^{0xx}$ ,  $t = 202.8$ .

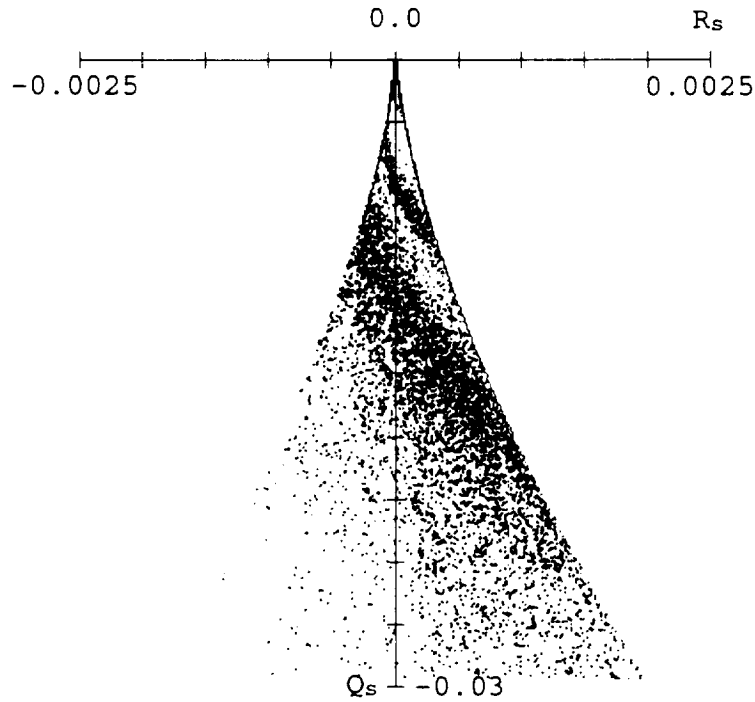


Figure 5.4: Enlarged plot of pdf of  $Q_s$  vs.  $R_s$  for  $346(60)_{0xx}^{x0x}$ .  $t = 204.8$ . Corresponds to figure 5.3b.

develop. The highest mechanical dissipation rates in such flows tend to occur in the high strain-rate regions between large organized vortical structures, thus the shape of the pdf. The half ellipsoid shape seen in figures 5.5b-d is much more typical of strongly three-dimensional flows, where regions of high strain-rate are closely intermingled with regions of high vorticity.

The “tongues” of highly rotational points that appear in the flows with a three-dimensional subharmonic, particularly in figures 5.5b and 5.5c, correspond to the centers of the strong streamwise structures seen in physical space (since those structures contain the highest enstrophy density motions in the wake). It is clear from figure 5.5 that while the most dissipating motions (largest  $|Q_s|$ ) tend to be associated with the regions of highest enstrophy density (scattered points near  $-Q_s = Q_w$  line, most obvious in figures 5.5a.b and e), the bulk of the high enstrophy density points in

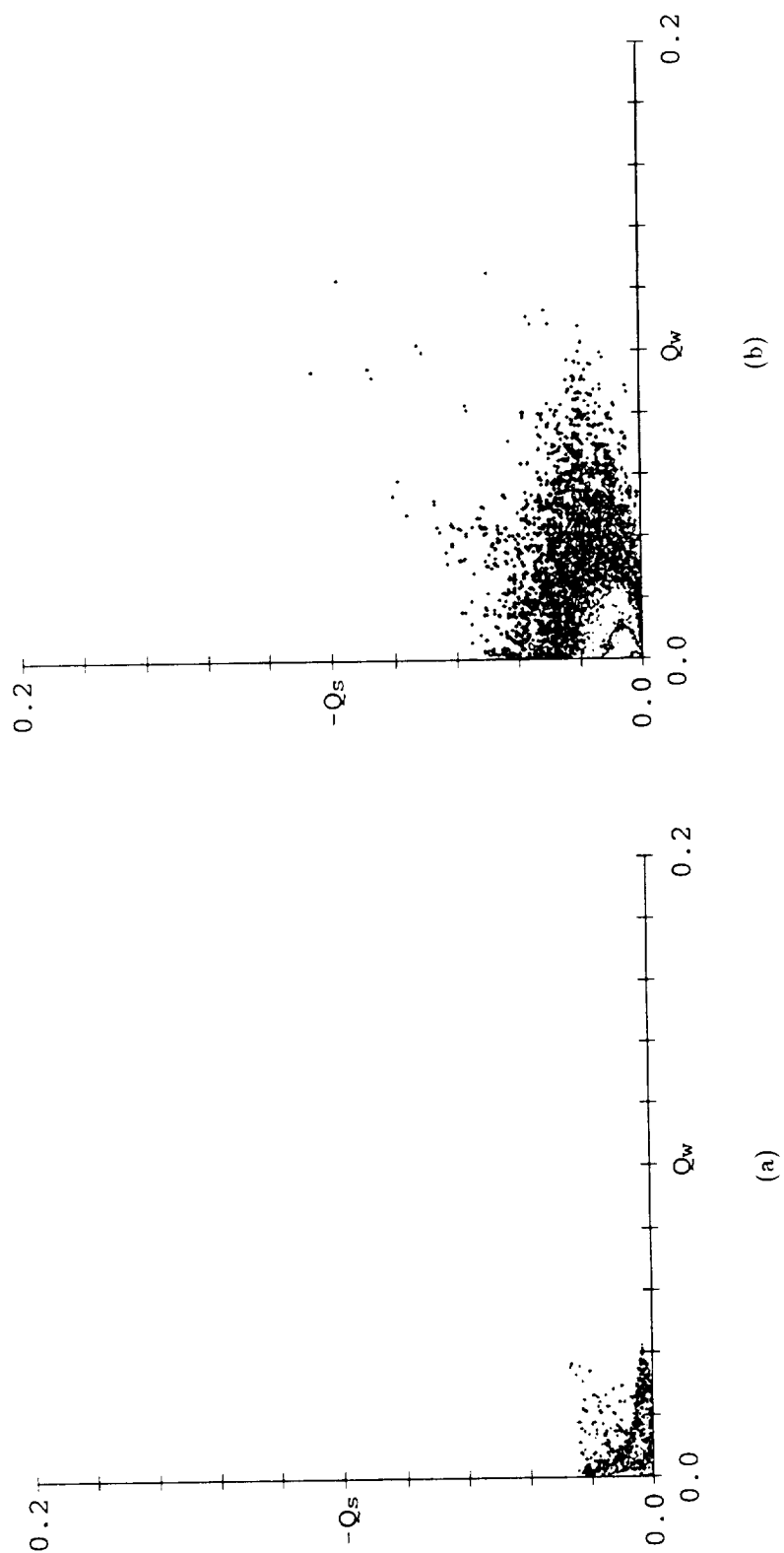


Figure 5.5: See caption page 169.

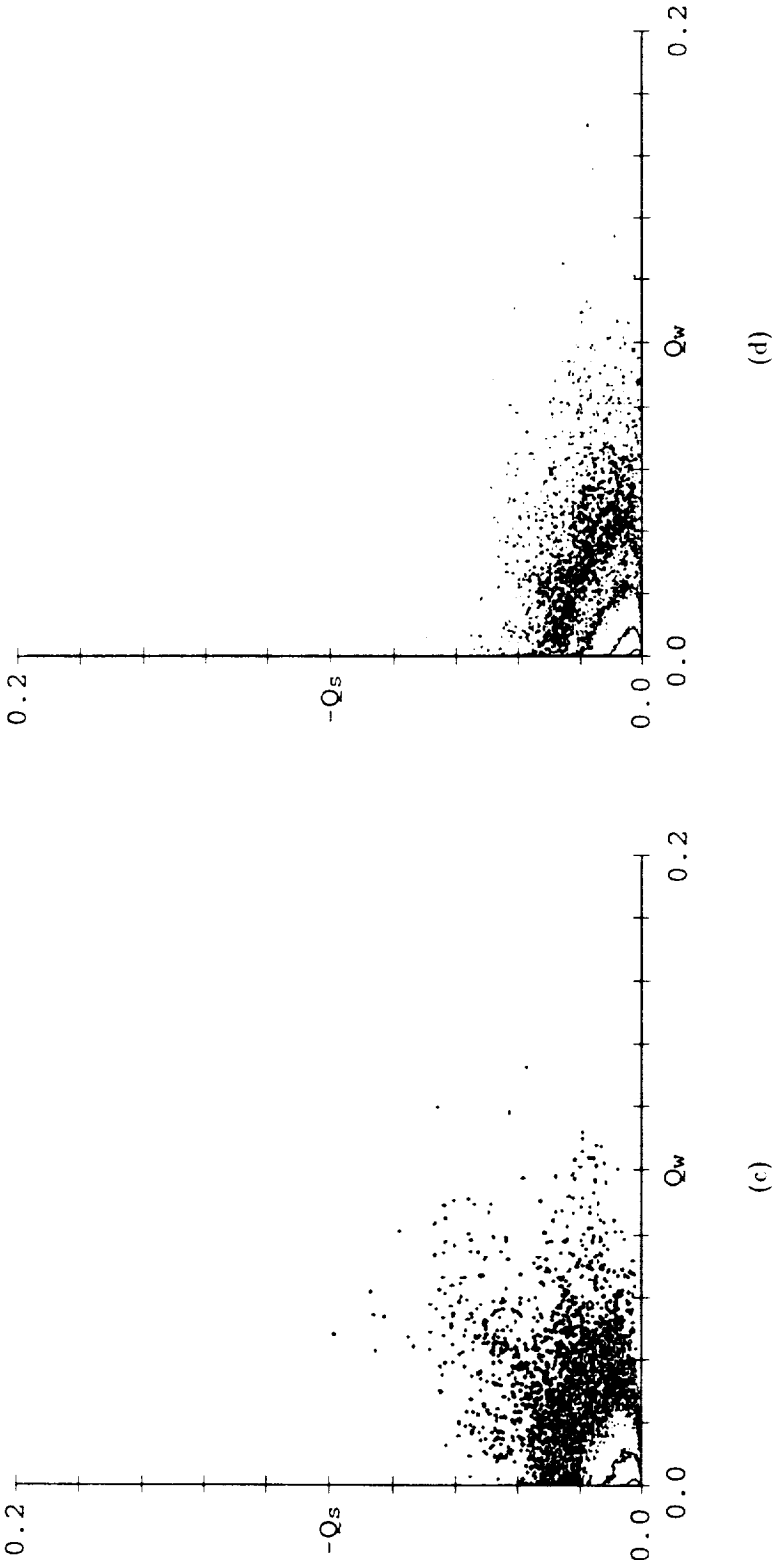


Figure 5.5: See caption page 169.

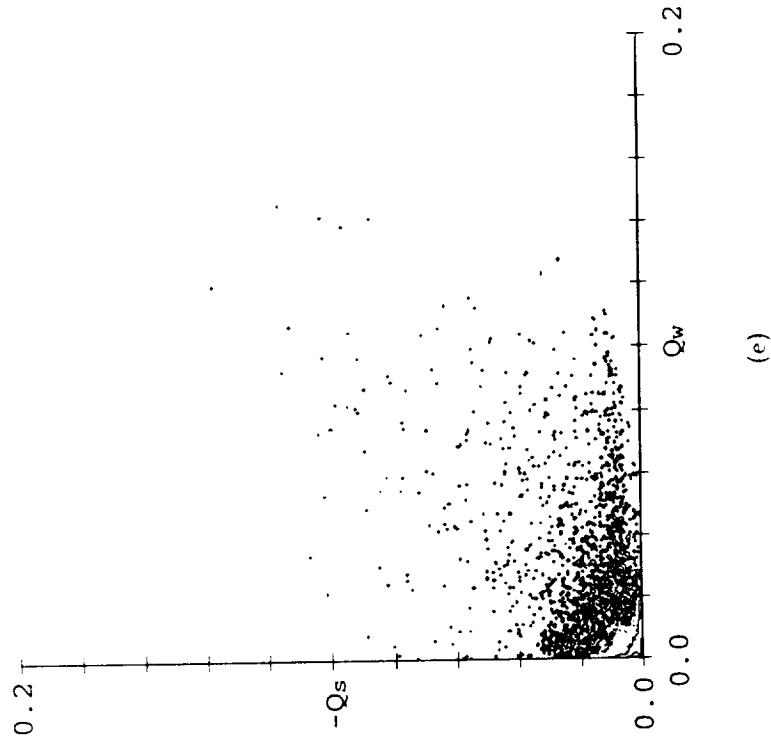


Figure 5.5: Contour plots of joint pdf of  $-Q_s$  vs.  $Q_w$  for  $Re_b = 346$  wakes with various initial disturbance wavelengths. (a)  $346(60)_{0xx}^{0xx}$ ,  $t = 196.9$ . (b)  $346(60)_{0xx}^{x0x}$ ,  $t = 204.8$ . (c)  $346(60)_{00x}^{x0x}$ ,  $t = 181.1$ . (d)  $346(60)_{000}^{x00}$ ,  $t = 197.0$ . (e)  $346(60)_{00x}^{0xx}$ ,  $t = 202.8$ .

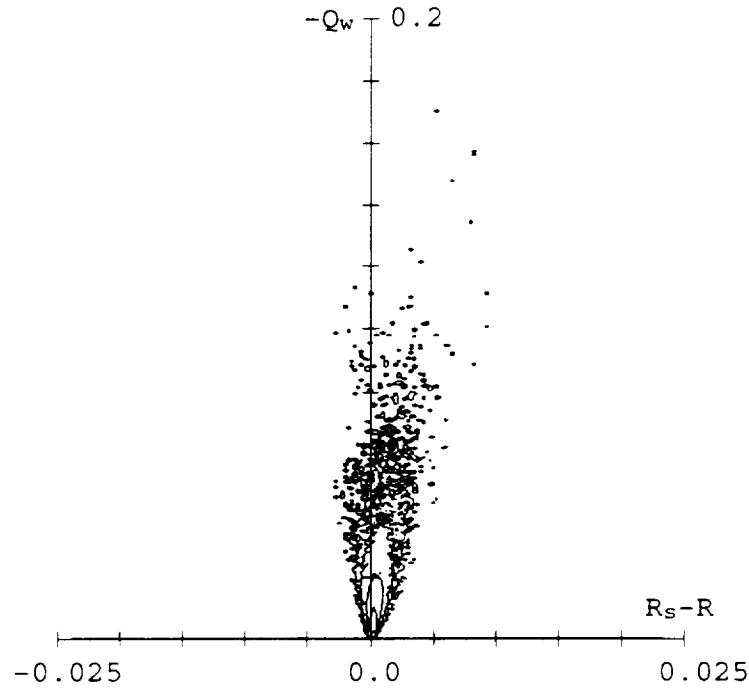


Figure 5.6: Contour plots of joint pdf of  $Q_w$  vs.  $R_s - R$  for  $346(60)_{000}^{00}$ .  $t = 197.0$ .

the wake have only moderate dissipation rates. This leads to the conclusion that the bulk of the most mechanically dissipating motions in the wake occur in the vicinity of the highest enstrophy density motions, but are in fact associated with more moderate enstrophy density levels. This is not entirely unexpected, since many models of the structure of turbulent motions produce peak dissipation rates separated from the peak enstrophy density location (c.f. Burger's vortex).

Figure 5.6 shows the joint pdf of  $Q_w$  (enstrophy density) and  $R_s - R$  (vortex stretching rate) for the  $346(60)_{000}^{00}$  wake. The points with the highest enstrophy density occur in regions of the flow that have the strongest vortex stretching. This comes as no surprise since the effect of stretching is to amplify the vorticity aligned with the strain field. This result is typical of all the three-dimensional flows which have been studied.

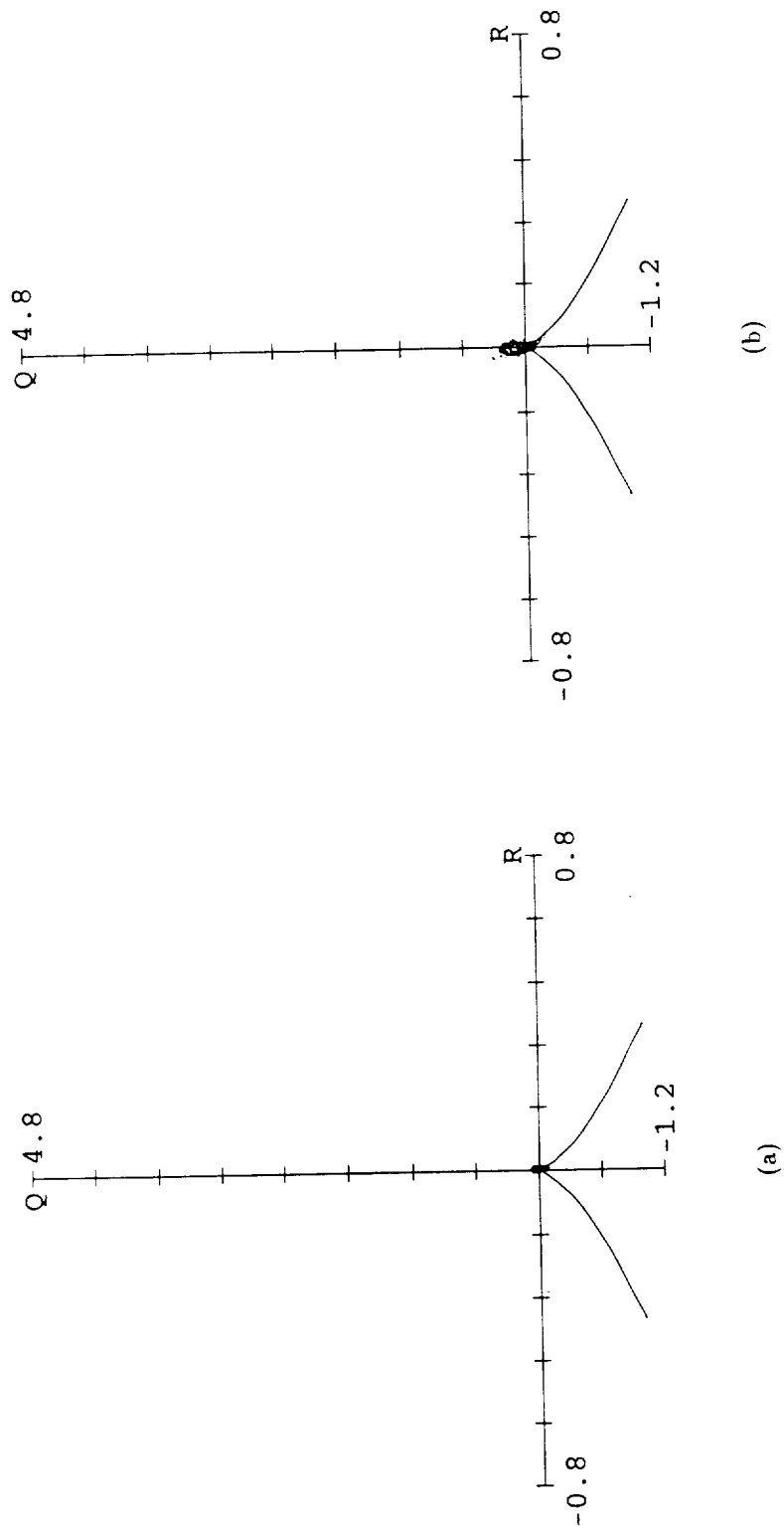


Figure 5.7: See caption page 172.

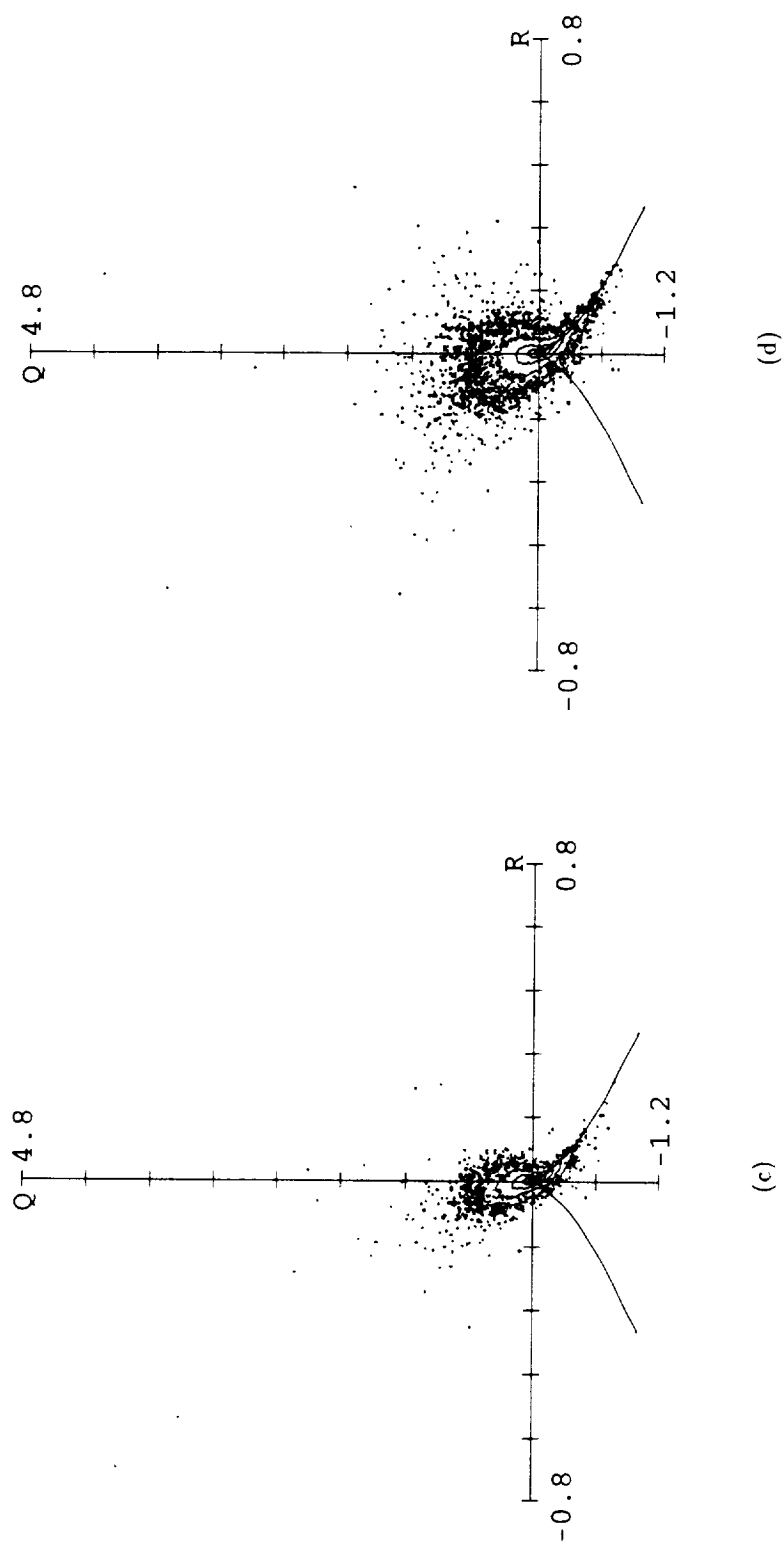


Figure 5.7: Contour plots of joint pdf of  $Q$  vs.  $R$  for  $\langle ? \rangle (60)_{0,r}^{x_{0,r}}$  wakes (two-dimensional fundamental plus three-dimensional subharmonic with various Reynolds numbers). (a)  $Re_b = 346$ ,  $t = 204.8$ . (b)  $Re_b = 692$ ,  $t = 201.9$ . (c)  $Re_b = 1384$ ,  $t = 199.3$ . (d)  $Re_b = 2768$ ,  $t = 194.6$ .



### 5.3 Effect of Reynolds Number

Figure 5.7 illustrates the effect of Reynolds number on the invariant pdf's. Shown is the joint pdf of  $Q$  and  $R$  for  $\langle \cdot \rangle (60)_{0xx}^{x0x}$  wakes all at approximately the same developmental time. The effects of increasing the Reynolds number is to greatly increase both the magnitude of the highest gradients and the fraction of the flow which contains high gradient motions.

Changing the Reynolds number has minimal effect on the overall shape of the pdf's (given that the Reynolds number is high enough to allow for strong three-dimensional motions). The only effect of increasing the Reynolds number is to make the highest gradient regions appear a bit more scattered (compare figure 5.7d and figure 5.2b on page 159).

### 5.4 Time Evolution in Invariant Space

Figure 5.8 illustrates the time evolution of the wake flows in invariant space. Shown is the joint pdf of  $Q_s$  and  $R_s$  for the  $346(60)_{0xx}^{x0x}$  wake. The initial shape of the pdf is determined by the initial conditions of the flow (figure 5.8a), but it rapidly relaxes to the general shape which has been observed in the other flows, and which will be maintained throughout the remainder of the evolution (figure 5.8b).

The strong gradient motions, which are associated with strong three-dimensionality, become much more significant (note the much larger area encompassed by the second and third contour levels in figure 5.8c as compared to figure 5.8b). The magnitude of the highest gradient motions then begin drop as the wake approaches a self similar regime where all the gradients should decay like  $t^{-1/2}$ . At the time shown these wakes have not yet entered the self similar decay regime.

This developmental cycle is common to all of the invariants for all of the three-dimensional wakes simulated, and is independent of Reynolds number.

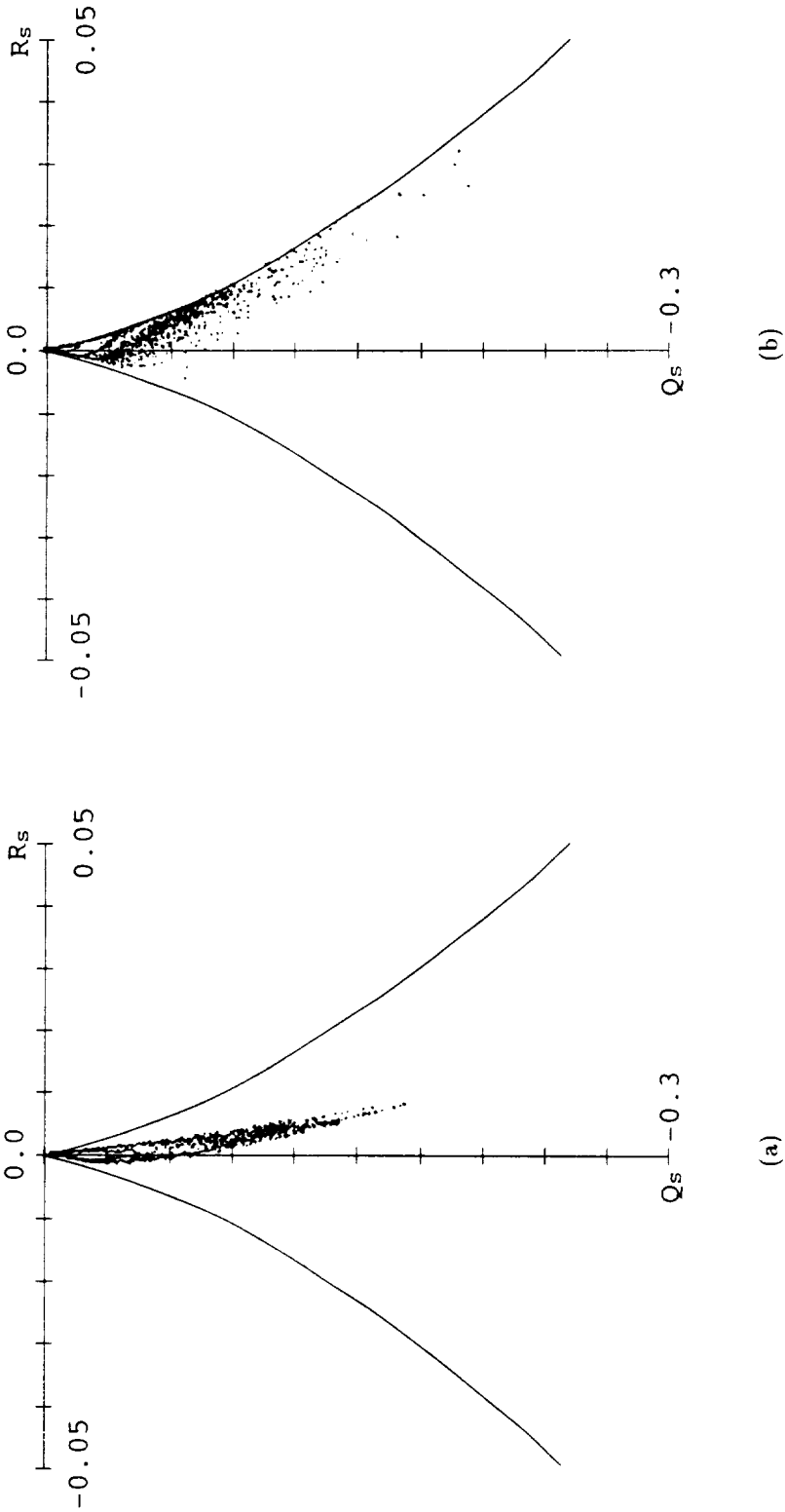


Figure 5.8: See caption page 175.

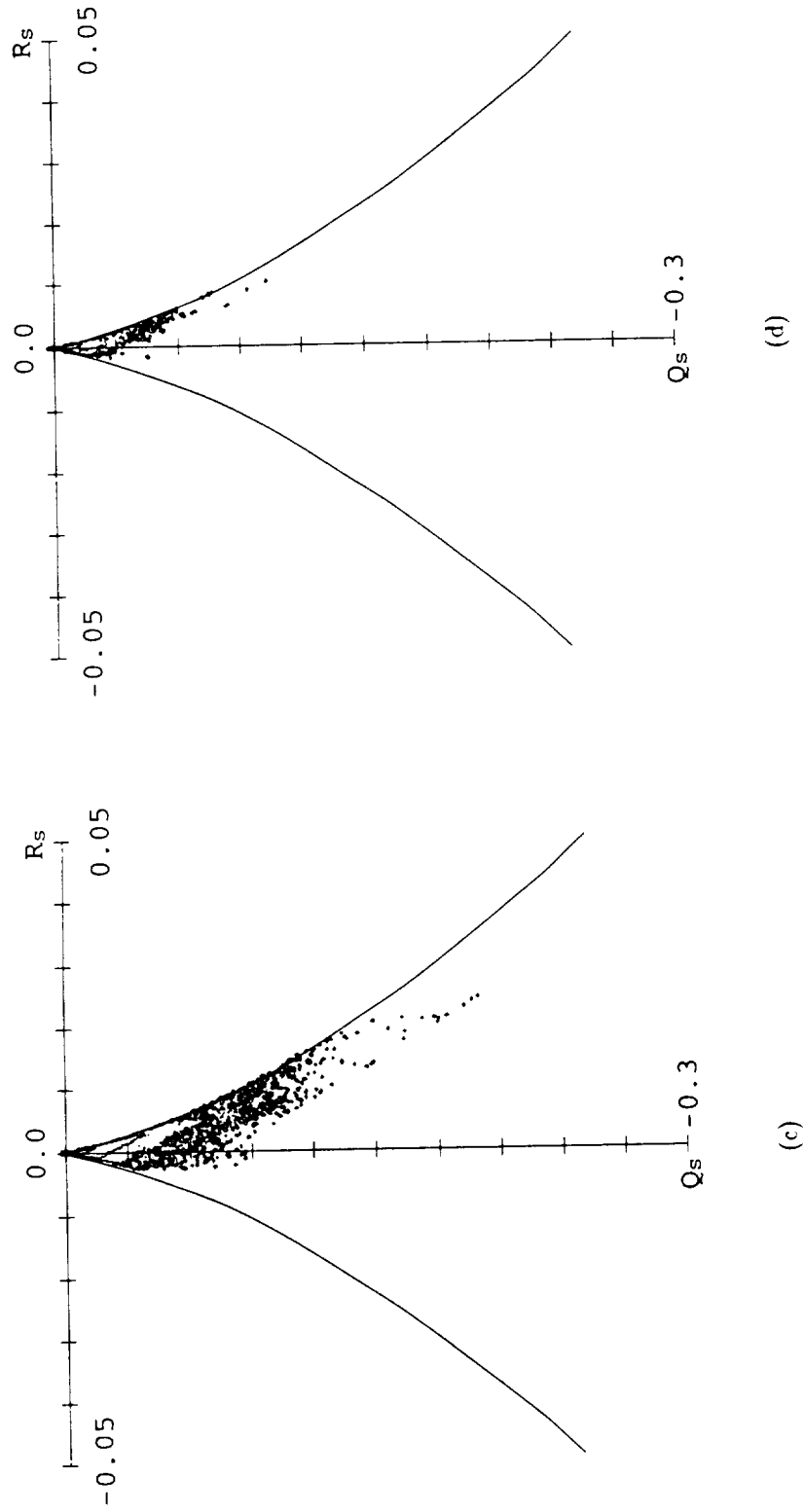


Figure 5.8: Time evolution of contour plots of joint pdf of  $Q_s$  vs.  $R_s$  for  $346(60)^{x_{0x}}$  wake (two-dimensional fundamental plus three-dimensional subharmonic). (a)  $t = 22.8$ . (b)  $t = 52.8$ . (c)  $t = 102.7$ . (d)  $t = 204.8$ .

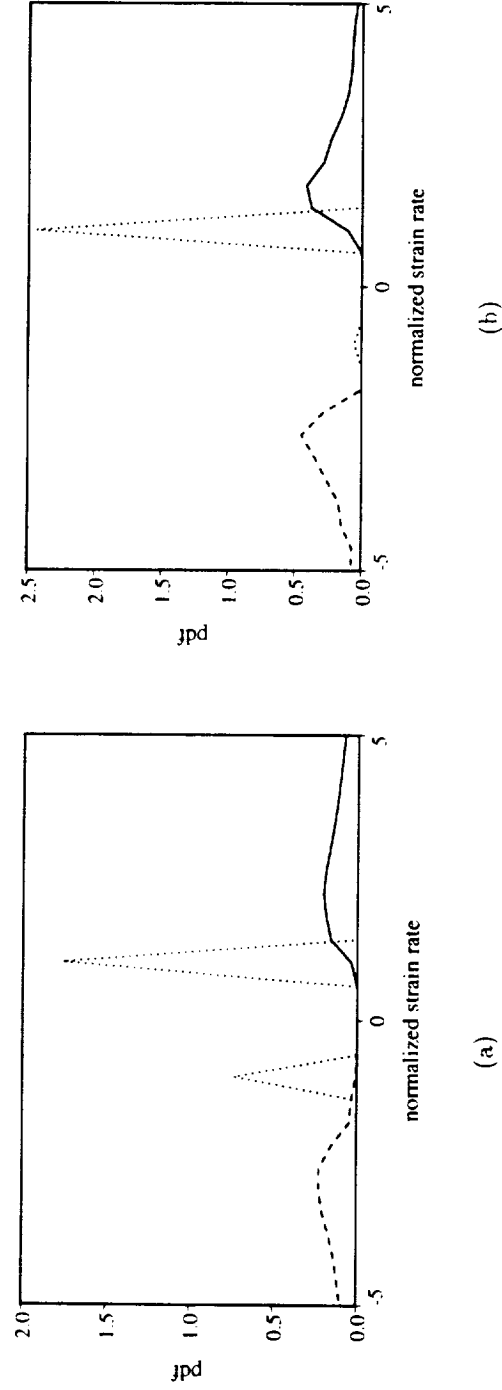


Figure 5.9: Pdf of normalized rates-of-strain for  $346(60)_{0x}^{0x}$  wake (two-dimensional fundamental plus three-dimensional subharmonic).  $t = 204.8$ . — : Most positive strain-rate,  $\alpha$ . ..... : Intermediate strain-rate,  $\beta$ . - - - - : Most negative strain-rate,  $\gamma$ . (a)  $|Q_s| > 0.00$ . (b)  $|Q_s| > 0.03$ .

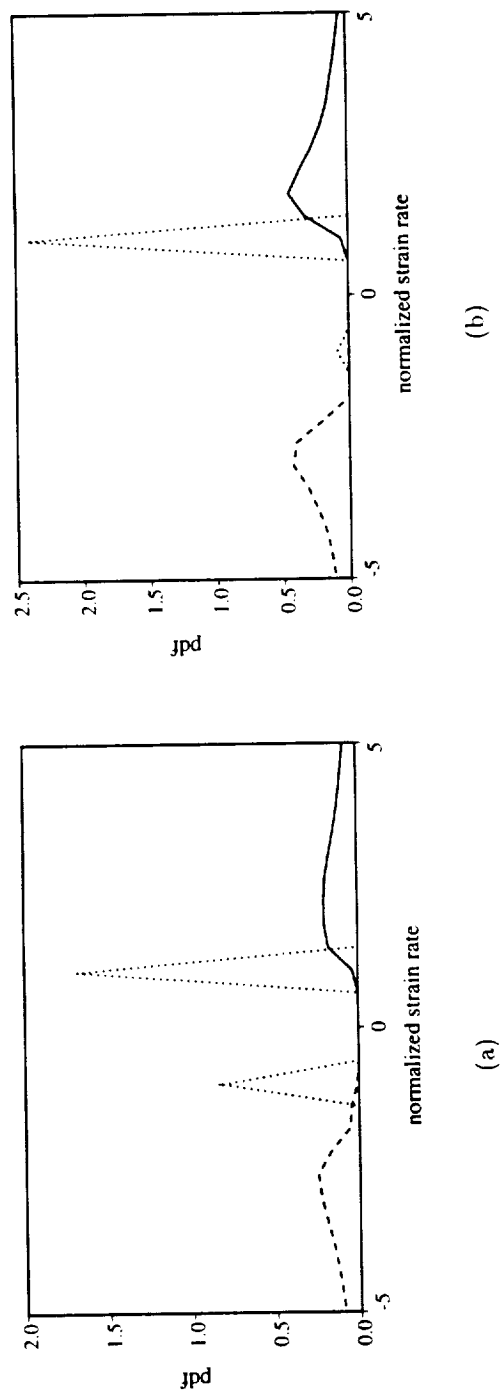


Figure 5.10: Pdf of normalized rates-of-strain for 1384(60) $_{0rx}^{x0x}$  wake (two-dimensional fundamental plus three-dimensional subharmonic).  $t = 199.3$ . — : Most positive strain-rate,  $\alpha$ . ..... : Intermediate strain-rate,  $\beta$ . ---- : Most negative strain-rate,  $\gamma$ . (a)  $|Q_s| > 0.00$ . (b)  $|Q_s| > 0.15$ .

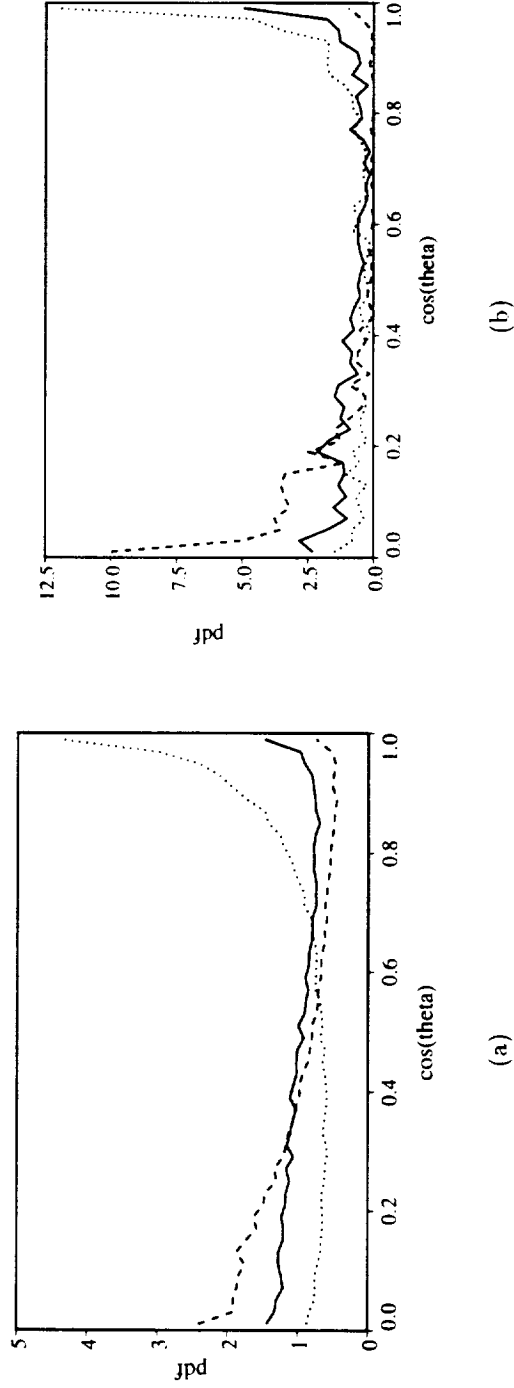


Figure 5.11: Pdf of cosine of angle between vorticity vector and principal strain rate directions for  $346(60)_{0_{rr}}^{0_{rr}}$  wake (two-dimensional fundamental plus three-dimensional subharmonic).  $t = 204.8$ . — : Most positive strain-rate. .... : Intermediate strain-rate. - - - - : Most negative strain-rate. (a)  $|Q_s| > 0.00$ . (b)  $|Q_s| > 0.03$ .

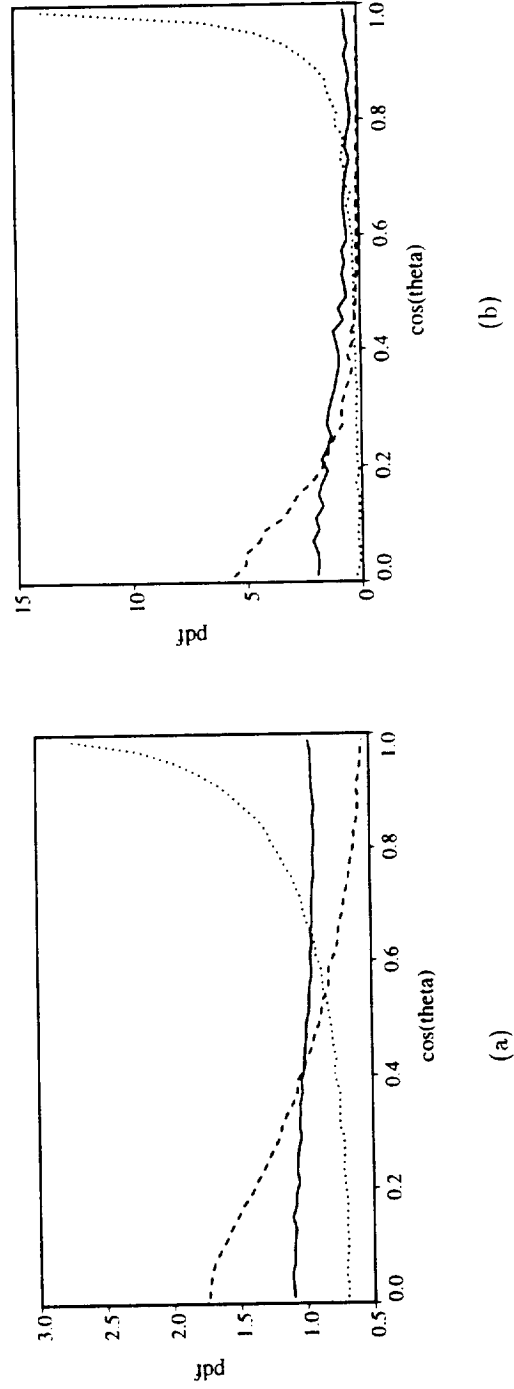


Figure 5.12: Pdf of cosine of angle between vorticity vector and principal strain rate directions for 1384(60) $_{0xx}^{x0x}$  wake (two-dimensional fundamental plus three-dimensional subharmonic).  $t = 199.3$ . — : Most positive strain-rate. .... : Intermediate strain-rate. - - - - : Most negative strain-rate. (a)  $|Q_s| > 0.00$ . (b)  $|Q_s| > 0.15$ .

## 5.5 Rate-of-Strain Distribution and Vorticity-Strain Alignment

Figures 5.9 and 5.10 show plots of the probability density functions of the normalized principal rates-of-strain,  $\alpha$ ,  $\beta$ , and  $\gamma$ , for the  $346(60)_{0xx}^{x0x}$  and  $1384(60)_{0xx}^{x0x}$  wakes respectively. The strain rates are sorted such that they are in descending order

$$\alpha \geq \beta \geq \gamma \quad (5.20)$$

and the rate-of-strain in each principal strain direction has been normalized by the magnitude of the intermediate rate-of-strain,  $|\beta|$ . Thus the normalized intermediate rate-of-strain,  $\beta$ , can take on values of positive or negative one only

$$\beta = \pm 1.0. \quad (5.21)$$

This is the reason for the delta function distribution for  $\beta$ .

There is a direct correspondence between the sign of  $\beta$  and the local rate-of-strain topology. If  $\beta = +1.0$ , then the local rate-of-strain topology is of the type unstable-node/saddle/saddle. If  $\beta = -1.0$ , then the local rate-of-strain topology is of the type stable-node/saddle/saddle.

If the pdf's are formed using all of the grid points in the computational domain (including those in the freestream), they appear as in figures 5.9a and 5.10a. Approximately two-thirds of the points have a rate-of-strain field consisting of two positive and one negative rate-of-strain ( $\beta = 1.0$ ). The other two rates-of-strain have broad distributions with peaks around  $\alpha \approx 2.0$  and  $\gamma \approx -3.0$ .

If the pdf's are conditioned so as to include only those points with high mechanical dissipation, which is proportional to  $-Q_s$ , then they appear as in figures 5.9b and 5.10b. The high dissipation points have rate-of-strain fields which almost exclusively consist of two positive and one negative rate-of-strain ( $\beta = 1.0$ , unstable-node/saddle/saddle rate-of-strain topology as was apparent from figure 5.3b). The distributions of  $\alpha$  and  $\gamma$  still have rather broad distributions, but with more distinct peaks at  $\alpha \approx 1.5$



and  $\gamma \approx -2.5$ . This result is insensitive to Reynolds number, and holds for all of the three-dimensional wakes computed, even those with relative weak three-dimensional motions (e.g.  $346(60)_{0xx}^{0xx}$ ).

Ashurst *et al.* [2] studied a direct numerical simulation of isotropic turbulence and found that the strain-rates for the most dissipating motions were in the ratio of  $\alpha : \beta : \gamma = 3 : 1 : -4$ , which they speculated might be a universal ratio. The studies of Soria *et al.* [42] and Chen *et al.* [11] and Sondergaard *et al.* [41] found that the ratio of principal rates-of-strain depended on the specific flow examined. The strain-rate ratio of  $\alpha : \beta : \gamma \approx 1.5 : 1 : -2.5$  found here for the three-dimensional incompressible plane wake adds weight to the conclusion that the ratio is indeed flow-dependent.

Figures 5.11 and 5.12 show plots of the probability density function of cosine of the angle between the vorticity vector and each of the three principal strain-rate directions for the  $346(60)_{0xx}^{0xx}$  and  $1384(60)_{0xx}^{0xx}$  wakes. The pdf of the cosine is plotted because in those coordinates randomly distributed three-dimensional vorticity vectors will result in uniform pdf's.

There is a clear tendency for the vorticity vector to be aligned (cosine equals one) with the intermediate rate-of-strain ( $\beta$ ) direction and nonaligned (cosine equals zero) with the most compressive rate-of-strain ( $\gamma$ ) direction in both wakes (figures 5.11a and 5.12a). When only the points with the highest dissipation rates, and hence the most intense local rate-of-strain fields, are included in the pdf, this tendency is strongly enhanced (figures 5.11b and 5.12b). The vorticity aligns almost exclusively with the intermediate rate-of-strain direction and is nearly always approximately perpendicular to the most compressive rate-of-strain direction.

Again, similar results were observed by Ashurst *et al.* [2] for isotropic turbulence. They also found that the vorticity tended to align with the intermediate rate-of-strain direction. The studies of Soria *et al.* [42] and Chen *et al.* [11], Sondergaard *et al.* [41], Blackburn *et al.* [3] and Tsinober *et al.* [47] found the same tendency for a wide variety of other flows. The evidence that this is a universal characteristic of turbulence is becoming very convincing.

# Chapter 6

## Conclusions

### 6.1 Numerical Method

The numerical method developed to perform the simulations used for this study has proven to be both effective and efficient. For planar flows with compact vorticity fields, matching of the velocities at the edge of a finite sized computational domain to irrotational flow solutions is a workable alternative to nonlinear mapping of the infinite direction to a finite domain.

The velocity matching method provides uniform resolution of the vortical region of the flow without wasting large fractions of the available grid points on the freestream or over-resolution of the centerplane of the flow. Use of a Fourier method on the uniform grid also allows for changes in resolution to be accomplished by simply truncating the transformed data or padding it with zeros at runtime. No special routine or extra computational time is needed to rebuild the grid or dataset after a resolution change.

The addition of a growing grid in the cross-stream direction allows the computational domain to adapt to the changing size of the vorticity field as the simulation evolves. This permits the flow to remain resolved even over long simulation times with minimal need for intervention on the part of the user. Changes in grid size of a factor of two or more while the simulated wake grew in extent by factors of five were routine when running the simulations for this study.

## 6.2 The Incompressible Plane Wake

### 6.2.1 Physical Development

The results presented here indicate that oblique disturbances at the subharmonic wavelength are very important to the development of strong three-dimensionality in the temporally evolving incompressible plane wake. Simulations started with a two-dimensional fundamental disturbance and a three-dimensional disturbance at the subharmonic wavelength developed strong streamwise structures stretching between corrugated spanwise rollers on the same side of the wake. These structures create very high rates-of-strain which lead to the appearance of fine scale motions and rapid growth rates in the far wake. Simulations started with three dimensional disturbances at only the fundamental wavelength remain almost two-dimensional, with relatively weak rate-of-strain fields, no significant small scale motions, and sluggish late time growth patterns which nearly match the corresponding purely two-dimensional wakes.

Varying the Reynolds number affects the intensity and scale of the structures in the flow. This effect is especially strong in wakes which develop strong coherent three-dimensional structures (wakes initiated with an oblique subharmonic). At high Reynolds number these wakes develop very intense fine scale motions even at moderate Reynolds numbers. The most intense fine scales tend to appear in the vicinity of the coherent three-dimensional structures. Wakes which do not develop strong three-dimensional coherent structures (wakes initiated with an oblique fundamental) develop small scales only at the very highest Reynolds numbers. The Reynolds number of the wake has minimal impact on the growth rate of the far wake. Wakes with very low Reynolds number do not develop strong three-dimensional structures, and grow somewhat more slowly at late times. Wakes with moderate to high Reynolds numbers grow at similar rates given similar initial conditions.

The addition of longer wavelength disturbances allows for scale changes in the flow and can temporarily augment the growth rate of the wake. This has implications for the interpretation of temporal simulations, where the flow is restricted to a maximum wavelength corresponding to the longest wavelength in the initial disturbance field.

At late times in the simulation the flow will not follow a growth path which can be related to that of a spatially developing wake.

This result also has implications for experiments involving spatially developing wakes. Any experiment is by necessity limited by the dimensions of the facility in which it is performed. The sensitivity of the wake to subharmonic disturbances which has been observed in these computations suggests that the rate of growth of experimentally studied wakes may be sensitive to the low frequency spectral content of naturally occurring disturbances in experimental facilities.

### 6.2.2 Topological Development

Topological analysis of the fine scale, high gradient motions in the incompressible wakes revealed that the wakes with a three-dimensional subharmonic have a greater quantity of more intense high gradient motions as compared to wakes with a three-dimensional fundamental only. Changes in the phase of the initial disturbances were found to have minimal impact on the overall distribution of the high gradient motions. Increasing the wake Reynolds number increased the intensity of the gradients while preserving the shape of the pdf's in invariant space.

All of the three-dimensional wakes simulated had joint probability density functions which were similar to those observed in other three-dimensional flows:

- Joint pdf's of the second and third invariants of the velocity gradient tensor have a characteristic “skewed teardrop” shape, with high gradient motions tending to be of stable-vortex/stretching and unstable-node/saddle/saddle topological types.
- Joint pdf's of the second and third invariants of the rate-of-strain tensor indicate that the most dissipative motions are associated exclusively with an unstable-node/saddle/saddle type strain topology. More moderately dissipating motions, which account for the majority of the dissipation in the flow, are also very strongly associated with an unstable-node/saddle/saddle type strain topology.

- Joint pdf's of the enstrophy density and vortex stretching indicate that the highly rotational motions occur in regions where the vortex stretching is positive, even at late times when the intensity of all gradients are decreasing in the wake.

Examination of the rate-of-strain distributions and the vorticity-strain alignment indicates that highly dissipating motions have a strong tendency to have two positive and one negative principal rates-of-strain (which corresponds to an unstable-node/saddle/saddle type rate-of-strain topology) in the ratio of  $1.5 : 1 : -2.5$ . These motions also tend to have the vorticity vector aligned with the intermediate (positive) strain rate direction and nearly perpendicular to the most compressive (negative) strain rate direction. These results appear to be insensitive to both Reynolds number and initial condition.

### 6.3 Future Work

As a direct extension of this study, the following work is recommended:

- The effect of the angle of the oblique disturbance needs to be examined, at least to the extent of verifying the broad range of amplified secondary instabilities predicted by the work of Flemming [16].
- With the recent availability of larger and faster parallel machines, the existing code should be used to simulate wakes at higher Reynolds numbers and for longer times. This is necessary to verify that the profound difference between wakes with short wavelength oblique disturbances and wakes with long wavelength oblique disturbances continue to exist at very high Reynolds numbers and at late times.
- To adequately simulate late time behavior, the wake simulations need to be run with the addition of longer wavelength disturbances to allow for continued unconfined growth. This should also allow for much realistic calculation of late time mean profiles and turbulence statistics.

In addition, the code which was developed for this study can readily be used to study a wide variety of planar free shear flows, including mixing layers (as demonstrated in section 2.8.1), skewed mixing layers, and momentumless wakes. Application of the code to these flows requires only that the proper initial conditions for the vorticity field and free stream flow velocities be defined.

# Appendix A

## Classical Similarity Theory

This appendix will present a brief review of the arguments and conclusions of similarity theory as applied to free shear flows in general and the incompressible plane wake in particular.

### A.1 Preliminaries

#### A.1.1 Energy Transport Equation

The Navier-Stokes equations for incompressible flow may be written as

$$u_{j,j} = 0 \tag{A.1}$$

$$u_{j,t} + \left( u_j u_l + \frac{p}{\rho} \delta_{jl} - 2\nu S_{jl} \right)_{,l} = 0 \tag{A.2}$$

where  $S_{jk}$  is the rate-of-strain tensor defined by

$$S_{jk} = \frac{1}{2} (u_{j,k} + u_{k,j}) . \tag{A.3}$$

Multiplying equation A.2 by  $u_k$  gives

$$\begin{aligned}
 & u_k \left[ u_{j,t} + \left( u_j u_l + \frac{p}{\rho} \delta_{jl} - 2\nu S_{jl} \right)_{,l} \right] \\
 &= (u_j u_k)_{,t} + \left( u_j u_k u_l + \frac{p}{\rho} (u_k \delta_{jl} + u_j \delta_{kl}) - 2\nu (u_k S_{jl} + u_j S_{kl}) \right)_{,l} \\
 &\quad - 2\frac{p}{\rho} S_{jk} + 2\nu (S_{jl} (S_{kl} + W_{kl}) + S_{kl} (S_{jl} + W_{jl})) = 0
 \end{aligned} \tag{A.4}$$

where  $W_{jk}$  is the rate-of-rotation tensor defined by

$$W_{jk} = \frac{1}{2} (u_{j,k} - u_{k,j}). \tag{A.5}$$

Taking the trace of equation A.4 and noting  $S_{ii} = 0$  for incompressible flow gives the transport equation for the kinetic energy  $E \equiv u_k u_k / 2$

$$E_{,t} + \left( E u_k + \frac{p}{\rho} u_k - 2\nu u_j S_{jk} \right)_{,k} + \Phi = 0 \tag{A.6}$$

where  $\Phi$  is the dissipation of (total) kinetic energy

$$\Phi = 2\nu S_{jk} S_{kj} \geq 0. \tag{A.7}$$

The flow variables may be split into mean and fluctuating parts

$$u_j = \bar{u}_j + u'_j \quad p = \bar{p} + p' \tag{A.8}$$

where the overbar signifies an appropriate average of the variable (temporal or ensemble for spatially developing flows, spatial or ensemble for temporally developing flows) and the primed quantities are deviations from that mean.

Using this decomposition, and applying the averaging procedure to the Navier-Stokes equations A.2 yields the Reynolds equations

$$\bar{u}_{j,j} = u'_{j,j} = 0 \tag{A.9}$$



$$\bar{u}_{j,t} + \left( \bar{u}_j \bar{u}_k + \frac{\bar{p}}{\rho} \delta_{jk} - 2\nu \bar{S}_{jk} + \frac{1}{\rho} \overline{u'_j u'_k} \right)_{,k} = 0 \quad (\text{A.10})$$

with a mean kinetic energy defined by

$$\begin{aligned} \bar{E} &= (\bar{u}_j \bar{u}_j + \overline{u'_j u'_j}) / 2 \\ &= \hat{E} + \bar{q}^2 \end{aligned} \quad (\text{A.11})$$

where  $\hat{E}$  is the energy of the mean flow and  $\bar{q}^2$  is the turbulent kinetic energy.

A transport equation for the energy of the mean flow may be derived from equation A.10 by multiplying by  $\bar{u}_j$  and rearranging

$$\hat{E}_{,t} + \left( \bar{u}_k \hat{E} + \frac{\bar{p}}{\rho} \bar{u}_k - 2\nu \bar{u}_j \bar{S}_{jk} + \bar{u}_j \overline{u'_j u'_k} \right)_{,k} + 2\nu \bar{S}_{jk} \bar{S}_{kj} - \overline{u'_j u'_k} \bar{S}_{jk} = 0 \quad (\text{A.12})$$

Similarly, a transport equation for the total mean energy can be derived from equation A.6.

$$\begin{aligned} \hat{E}_{,t} + \bar{q}^2_{,t} + \left( \hat{E} \bar{u}_k + \bar{q}^2 \bar{u}_k + \frac{\bar{p}}{\rho} \bar{u}_k - 2\nu \bar{u}_j \bar{S}_{jk} + \bar{u}_j \overline{u'_j u'_k} + \overline{q^2 u'_k} + \frac{\bar{p}'}{\rho} \bar{u}'_k \right. \\ \left. - 2\nu \overline{u'_j S_{jk}} \right)_{,k} + 2\nu \bar{S}_{jk} \bar{S}_{kj} + 2\nu \overline{S'_{jk} S'_{kj}} = 0. \end{aligned} \quad (\text{A.13})$$

Subtracting out the equation for the mean flow energy, equation A.12, from the above equation yields an equation for the transport of mean turbulent kinetic energy

$$\bar{q}^2_{,t} + \left( \bar{q}^2 \bar{u}_k + \overline{q^2 u'_k} + \frac{\bar{p}'}{\rho} \bar{u}'_k - 2\nu \overline{u'_j S'_{jk}} \right)_{,k} = \Pi - \varphi \quad (\text{A.14})$$

where

$$\Pi = -\overline{u'_j u'_k} \bar{S}_{jk} \quad (\text{A.15})$$

is known as the turbulence production, and

$$\varphi = 2\nu \overline{S'_{jk} S'_{kj}} \quad (\text{A.16})$$

is the dissipation of turbulent kinetic energy. The production,  $\Pi$  serves to transfer kinetic energy from the mean flow to the unsteady flow, while the dissipation serves to convert turbulent kinetic energy into heat.

It has been observed in a number of flows with simple geometries that at sufficiently high Reynolds number the production scales locally with the dissipation

$$\Pi \sim \varphi. \quad (\text{A.17})$$

or

$$-\overline{u'_j u'_k} \overline{S}_{jk} \sim 2\nu \overline{S'_{jk} S'_{kj}} \quad (\text{A.18})$$

A complete theoretical understanding of this relationship between production and dissipation is still lacking. The evidence for equation A.18 is empirical and confined to a limited range of flows. However this is used as the basis for arguments presented in the following sections.

## A.2 Scales of Motion

Equation A.18 allows for an estimate of the relative size of the large and small scales in the flow. Assume that the velocity fluctuations and the mean velocity both scale with the same reference velocity

$$u'_j \sim \overline{u_j} \sim U_0 \quad (\text{A.19})$$

and that the largest scales in the flow scale with some reference length  $\delta$ . This allows an estimate of the scale of the left hand side of equation A.18

$$\Pi = -\overline{u'_j u'_k} \overline{S}_{jk} \sim \frac{U_0^3}{\delta} \quad (\text{A.20})$$

The scaling of the right hand side is more problematic, since it involves the mean of products of the gradient of the fluctuations. Clearly the appropriate velocity scale to use is  $U_0$  since  $u'_j \sim U_0$ , but the appropriate length scale to use is unclear.

There are two turbulence length scales, or microscales, that are commonly used to complete the above scaling: The Taylor microscale, and the Kolmogorov microscale.

### A.2.1 The Taylor Microscale

The Taylor microscale,  $\lambda$ , is defined such that the proportionality given in equation A.18 is satisfied

$$\frac{U_0^3}{\delta} \sim \nu \frac{U_0^2}{\lambda^2} \quad (\text{A.21})$$

giving

$$\boxed{\frac{\lambda}{\delta} \sim \left( \frac{\nu}{U_0 \delta} \right)^{1/2} \equiv \frac{1}{Re_\delta^{1/2}}.} \quad (\text{A.22})$$

This microscale represents an upper bound on the range of scales that contribute to significant turbulent kinetic energy dissipation.

In this study, two version of the Taylor microscale were calculated for use in estimating the resolution of the simulations that were performed. The first version is one that appears in many experimental studies where obtaining the three-dimensional velocity and velocity gradient field is very difficult. It relies on the measurement of only one velocity (usually  $u_1$ )

$$\boxed{\lambda_{T1} \equiv \frac{\overline{u'_1 u'_1}}{\left( \overline{u'_{1,1} u'_{1,1}} \right)}}. \quad (\text{A.23})$$

The second version used here includes the velocities and gradients in all three directions

$$\boxed{\lambda_T \equiv \frac{\overline{u'_j u'_j}}{\left( \overline{u'_{j,k} u'_{j,k}} \right)}} \quad (\text{A.24})$$

which is derived from the definition which appears above for the general case.

The Taylor microscale also arises in correlation functions which appear in the theory of isotropic turbulence. For a complete description see the discussions in Hinze [18].

### A.2.2 The Kolmogorov Microscale

The second scale is a result of introducing both a new turbulence length scale and a new turbulence velocity scale so as satisfy the proportionality in equation A.18

$$\frac{U_0^3}{\delta} \sim \nu \frac{v^2}{\eta^2}. \quad (\text{A.25})$$

To close the definition, the Reynolds number of the resulting scale is chosen to be one

$$\frac{\eta v}{\nu} \equiv 1. \quad (\text{A.26})$$

These lead to the relations

$$\boxed{\frac{\eta}{\delta} \sim \frac{1}{Re_\delta^{3/4}}} \quad (\text{A.27})$$

and

$$\boxed{\frac{v}{U_0} \sim \frac{1}{Re_\delta^{1/4}}}. \quad (\text{A.28})$$

The Kolmogorov microscale represents a lower bound on the on the range of scales that contribute to significant turbulent kinetic energy dissipation. For both the Taylor and Kolmogorov microscales it should be kept in mind that they are only estimates of the actual turbulent length scales.

## A.3 Evolution of the Spatially Evolving Incompressible Plane Wake

### A.3.1 Momentum Balance

Figure A.1 shows schematically the wake behind a symmetric body with a drag force per unit span of  $D$ .

For a sufficiently large control volume (the dotted box in figure A.1), only the downstream edge of the control volume and the drag on the body contribute to the momentum balance in the control volume. The upstream boundary and top

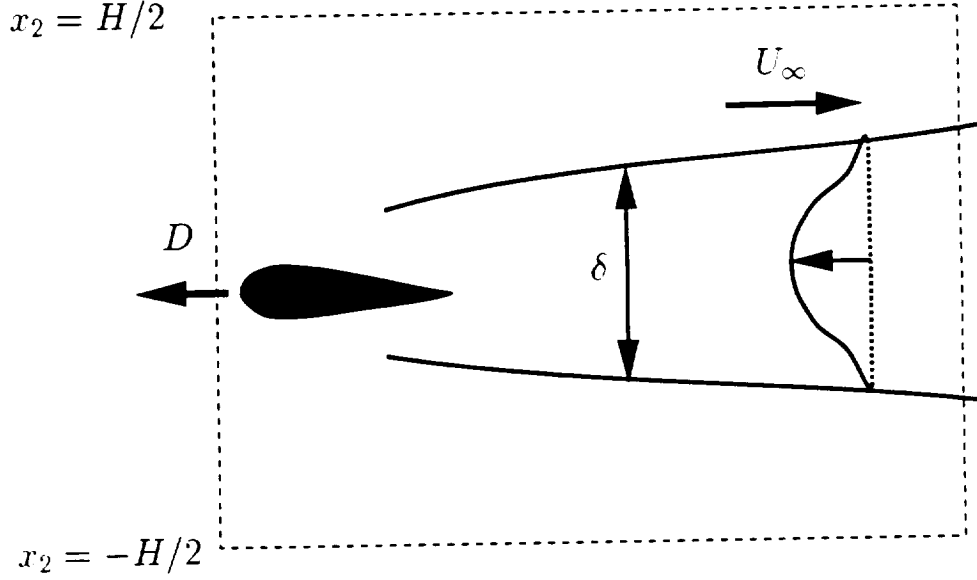


Figure A.1: Schematic of spatially evolving wake. Control volume for momentum balance.

and bottom of the control volume are at free stream conditions, and therefore have negligible contribution to the momentum. Thus, for sufficiently large  $H$ , an integral momentum balance over the control volume becomes

$$\frac{D}{\rho} = \int_{-H/2}^{H/2} \left[ \bar{u}_1(x_2) (\bar{u}_1(x_2) - u_\infty) + \left( \frac{\bar{p}(x_2) - p_\infty}{\rho} \right) - \frac{\tau_{11}(x_2) - \tau_{11\infty}}{\rho} \right] dx_2 \quad (\text{A.29})$$

where  $\tau_{ij}$  is the stress tensor.

In the far wake,

$$\frac{u_1 - u_\infty}{u_\infty} \ll 1. \quad (\text{A.30})$$

Combining this with the similarity assumptions

$$\frac{u_\infty - \bar{u}_1(x_2)}{U_0} = \hat{u} \left( \frac{x_2}{\delta} \right) \quad (\text{A.31})$$

and

$$\left( \frac{\bar{p}(x_2) - p_\infty}{\rho} - \frac{\tau_{11}(x_2) - \tau_{11\infty}}{\rho} \right) / U_0^2 = \hat{f} \left( \frac{x_2}{\delta} \right) \quad (\text{A.32})$$

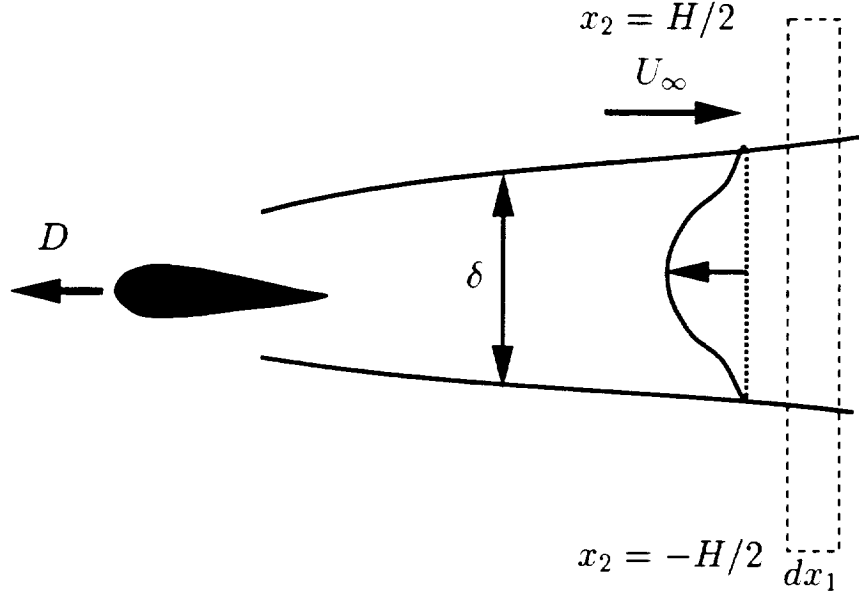


Figure A.2: Schematic of spatially evolving wake. Control volume for energy balance.

where  $\delta$  is a measure of the mean flow width and  $U_0 = u_\infty - \bar{u}_Q$  is a reference velocity, allows the momentum balance to be written as

$$\frac{D}{\rho u_\infty} = U_0 \delta \int_{-H/2\delta}^{H/2\delta} \hat{u}\left(\frac{x_2}{\delta}\right) d\left(\frac{x_2}{\delta}\right) + U_0^2 \delta \int_{-H/2\delta}^{H/2\delta} \hat{f}\left(\frac{x_2}{\delta}\right) d\left(\frac{x_2}{\delta}\right). \quad (\text{A.33})$$

In the far wake, the second integral is much smaller than the first, and the momentum balance can be approximated as

$$\frac{D}{\rho u_\infty} \approx U_0 \delta \int_{-H/2\delta}^{H/2\delta} \hat{u}\left(\frac{x_2}{\delta}\right) d\left(\frac{x_2}{\delta}\right). \quad (\text{A.34})$$

Under the assumption of self-similarity (the profile is a function of  $x_2/\delta$  only), the integral is a constant, in this case of order one. Thus, in the far wake

$$\boxed{U_0 \delta \sim \frac{D}{\rho u_\infty}}. \quad (\text{A.35})$$

### A.3.2 Mean Kinetic Energy

The evolution of the mean kinetic energy can be derived from the integral of equation A.12 over the infinitesimal control volume shown in figure A.2

$$\begin{aligned} \int_V [\tilde{E}_{,t}] dV &+ \int_V \left[ \left( \bar{u}_k \tilde{E} + \frac{\bar{p}}{\rho} \bar{u}_k - 2\nu \bar{u}_j \bar{S}_{jk} + \bar{u}_j \overline{u'_j u'_k} \right)_{,k} + 2\nu \bar{S}_{jk} \bar{S}_{kj} \right] dV \\ &= - \int_V [\overline{u'_j u'_k} \bar{S}_{jk}] dV. \end{aligned} \quad (\text{A.36})$$

Assuming the flow is stationary, the first integral is zero (constant total energy in the control volume). The second integral may be converted into a contour integral, giving

$$\begin{aligned} \int_{\Omega} \left[ \bar{u}_k \tilde{E} + \frac{\bar{p}}{\rho} \bar{u}_k - 2\nu \bar{u}_j \bar{S}_{jk} + \bar{u}_j \overline{u'_j u'_k} + 2\nu \bar{S}_{jk} \bar{S}_{kj} \right] d\Omega_k \\ = - \int_V [\overline{u'_j u'_k} \bar{S}_{jk}] dV. \end{aligned} \quad (\text{A.37})$$

where  $\Omega$  is the contour surface and  $\Omega_k$  is a surface normal.

Let  $\Delta \bar{U} = U_{\infty} - \bar{u}_1$  and  $\Delta \bar{p} = p_{\infty} - \bar{p}$ . Evaluating over the volume in A.2 and assuming the mean flow is in the  $x_1$  direction yields

$$\begin{aligned} &- \left[ \int_{-H/2}^{H/2} \left( \frac{U_{\infty} p_{\infty}}{\rho} + \frac{U_{\infty}^3}{2} \right) dx_2 \right]_{,1} - \left[ \int_{-H/2}^{H/2} \left( \frac{p_{\infty}}{\rho} + \frac{3U_{\infty}^2}{2} \right) \Delta \bar{U} dx_2 \right]_{,1} \\ &- \left[ \int_{-H/2}^{H/2} U_{\infty} \left( \frac{\Delta \bar{p}}{\rho} + \frac{3\Delta \bar{U}^2}{2} \right) dx_2 \right]_{,1} \\ &+ \left[ \int_{-H/2}^{H/2} \left( \frac{\Delta \bar{p} \Delta \bar{U}}{\rho} - \frac{\Delta \bar{U}^3}{2} - \Delta \bar{U} \overline{U' U'} \right) dx_2 \right]_{,1} \\ &= - \int_V [\overline{u'_j u'_k} \bar{S}_{jk}] dV. \end{aligned} \quad (\text{A.38})$$

Introducing the similarity assumptions

$$\frac{\Delta \bar{U}}{U_0} = \hat{u} \left( \frac{x_2}{\delta} \right) \quad (\text{A.39})$$

$$\left( \frac{\Delta \bar{p}}{\rho} - \frac{3\Delta \bar{U}^2}{2} \right) / U_0^2 = \hat{f} \left( \frac{x_2}{\delta} \right) \quad (\text{A.40})$$

$$\left( \frac{\Delta \bar{p} \Delta \bar{U}}{\rho} - \frac{\Delta \bar{U}^3}{2} - \Delta \bar{U} \overline{U' U'} \right) / U_0^3 = \hat{g} \left( \frac{x_2}{\delta} \right) \quad (\text{A.41})$$

$$\frac{\overline{u'_j u'_k S_{jk}}}{U_0^3} = \hat{h} \left( \frac{x_2}{\delta} \right) \quad (\text{A.42})$$

yields

$$\begin{aligned} & - \left( \frac{p_\infty}{\rho} + \frac{3U_\infty^2}{2} \right) (U_0 \delta)_{,1} \int_{-H/2\delta}^{H/2\delta} \hat{u} \left( \frac{x_2}{\delta} \right) d \left( \frac{x_2}{\delta} \right) - U_\infty (U_0^2 \delta)_{,1} \int_{-H/2\delta}^{H/2\delta} \hat{f} \left( \frac{x_2}{\delta} \right) d \left( \frac{x_2}{\delta} \right) \\ & + (U_0^3 \delta)_{,1} \int_{-H/2\delta}^{H/2\delta} \hat{g} \left( \frac{x_2}{\delta} \right) d \left( \frac{x_2}{\delta} \right) = -U_0^3 \int_{-H/2\delta}^{H/2\delta} \hat{h} \left( \frac{x_2}{\delta} \right) d \left( \frac{x_2}{\delta} \right) \end{aligned} \quad (\text{A.43})$$

The first term on the left is zero since, by equation A.35,  $U_0 \delta$  is constant. The third term dies off much more rapidly in the far wake than either of the remaining terms, so it may be dropped. This leaves the approximate relation

$$U_\infty (U_0^2 \delta)_{,1} \int_{-H/2\delta}^{H/2\delta} \hat{f} \left( \frac{x_2}{\delta} \right) d \left( \frac{x_2}{\delta} \right) \approx U_0^3 \int_{-H/2\delta}^{H/2\delta} \hat{h} \left( \frac{x_2}{\delta} \right) d \left( \frac{x_2}{\delta} \right) \quad (\text{A.44})$$

The integrals are constants of order one, hence

$$U_\infty (U_0^2 \delta)_{,1} \sim U_0^3. \quad (\text{A.45})$$



Combining this with equation A.35 gives

$$\delta \sim \frac{1}{U_\infty^{1/2}} \left( \frac{D}{\rho U_\infty} \right) x_1^{1/2} \quad (\text{A.46})$$

and

$$U_0 \sim U_\infty^{1/2} \left( \frac{D}{\rho U_\infty} \right) x_1^{-1/2}, \quad (\text{A.47})$$

the asymptotic growth laws for the spatially evolving incompressible plane wake.

## A.4 Evolution of the Temporally Evolving Incompressible Plane Wake

### A.4.1 Momentum Balance

For the temporally evolving plane wake the total momentum deficit per unit plan area  $M$  (momentum per unit span per unit length) is a constant. Thus

$$\frac{M}{\rho} = \int_{-H/2}^{H/2} (u_\infty - \bar{u}_1(x_2)) dx_2. \quad (\text{A.48})$$

Applying the similarity assumption from equation A.31 yields

$$\frac{M}{\rho} = U_0 \int_{-H/2\delta}^{H/2\delta} \hat{u} \left( \frac{x_2}{\delta} \right) d \left( \frac{x_2}{\delta} \right). \quad (\text{A.49})$$

Again, the integral is a constant of order one, thus

$$U_0 \delta \sim \frac{M}{\rho}. \quad (\text{A.50})$$

### A.4.2 Mean Kinetic Energy

The development of the results for the mean kinetic energy are identical to those for the spatially evolving wake except that the time derivative of the mean energy is not dropped. The equivalent to equation A.38 is

$$\begin{aligned}
& \frac{1}{2} \left[ \int_{-H/2}^{H/2} (U_\infty^2 - 2U_\infty \Delta \bar{U} + \Delta \bar{U}^2) dx_2 \right]_{,t} - \left[ \int_{-H/2}^{H/2} \left( \frac{U_\infty p_\infty}{\rho} + \frac{U_\infty^3}{2} \right) dx_2 \right]_{,1} \\
& - \left[ \int_{-H/2}^{H/2} \left( \frac{p_\infty}{\rho} + \frac{3U_\infty^2}{2} \right) \Delta \bar{U} dx_2 \right]_{,1} - \left[ \int_{-H/2}^{H/2} U_\infty \left( \frac{\Delta \bar{p}}{\rho} + \frac{3\Delta \bar{U}^2}{2} \right) dx_2 \right]_{,1} \\
& + \left[ \int_{-H/2}^{H/2} \left( \frac{\Delta \bar{p} \Delta \bar{U}}{\rho} - \frac{\Delta \bar{U}^3}{2} - \Delta \bar{U} \bar{U}' \bar{U}' \right) dx_2 \right]_{,1} \\
& = - \int_V [\overline{u'_j u'_k} \bar{S}_{jk}] dV. \tag{A.51}
\end{aligned}$$

Applying the similarity assumptions from equations A.39 through A.42 gives

$$\begin{aligned}
& \frac{(U_\infty^2 H)_{,t}}{2} - (U_\infty U_0 \delta)_{,t} \int_{-H/2\delta}^{H/2\delta} \hat{u} \left( \frac{x_2}{\delta} \right) d \left( \frac{x_2}{\delta} \right) + \frac{(U_0^2 \delta)_{,t}}{2} \int_{-H/2\delta}^{H/2\delta} \hat{u}^2 \left( \frac{x_2}{\delta} \right) d \left( \frac{x_2}{\delta} \right) \\
& - \left( \frac{p_\infty}{\rho} + \frac{3U_\infty^2}{2} \right) (U_0 \delta)_{,1} \int_{-H/2\delta}^{H/2\delta} \hat{u} \left( \frac{x_2}{\delta} \right) d \left( \frac{x_2}{\delta} \right) \\
& - U_\infty (U_0^2 \delta)_{,1} \int_{-H/2\delta}^{H/2\delta} \hat{f} \left( \frac{x_2}{\delta} \right) d \left( \frac{x_2}{\delta} \right) \\
& + (U_0^3 \delta)_{,1} \int_{-H/2\delta}^{H/2\delta} \hat{g} \left( \frac{x_2}{\delta} \right) d \left( \frac{x_2}{\delta} \right) = -U_0^3 \int_{-H/2\delta}^{H/2\delta} \hat{h} \left( \frac{x_2}{\delta} \right) d \left( \frac{x_2}{\delta} \right). \tag{A.52}
\end{aligned}$$

The first term is zero since  $H$  is a constant. The same holds for the second term since, by equation A.50,  $U_0 \delta$  is a constant. All of the terms which are differentiated with respect to  $x_1$  are zero since in a temporal wake there is no spatial variation of

the mean. This leaves the third term on the left and the term on the right

$$\frac{(U_0^2 \delta)_{,t}}{2} \int_{-H/2\delta}^{H/2\delta} \hat{u}^2 \left( \frac{x_2}{\delta} \right) d \left( \frac{x_2}{\delta} \right) = -U_0^3 \int_{-H/2\delta}^{H/2\delta} \hat{h} \left( \frac{x_2}{\delta} \right) d \left( \frac{x_2}{\delta} \right). \quad (\text{A.53})$$

Again, the integrals are constants of order one, hence

$$\frac{(U_0^2 \delta)_{,t}}{2} \sim -U_0^3. \quad (\text{A.54})$$

Combining this with the result from equation A.50 yields

$$\boxed{\delta \sim \left( \frac{4M}{\rho} \right)^{1/2} t^{1/2}} \quad (\text{A.55})$$

and

$$\boxed{U_0 \sim \left( \frac{M}{4\rho} \right)^{1/2} t^{-1/2}}, \quad (\text{A.56})$$

the asymptotic growth laws for the temporally evolving incompressible plane wake.

# Appendix B

## Linear Stability Theory

In the interest of completeness, this appendix will present a brief overview of linear stability theory. A brief outline of the methodology used in the present study to generate the disturbance eigenfunctions will also be presented.

### B.1 Mean Flow

The mean base wake flow for all of the present simulation runs was the parallel Gaussian profile (properly non-dimensionalized)

$$\bar{u}_1 = 1 - \Delta u_{\mathbb{Q}0} e^{-c_1 x_2^2} \quad (\text{B.1})$$

$$\bar{u}_2 = \bar{u}_3 = 0 \quad (\text{B.2})$$

$$\bar{p} = \text{const} \quad (\text{B.3})$$

where  $\Delta u_{\mathbb{Q}0}$  is the dimensionless centerline velocity deficit, and  $c_1$  is a scaling factor. The scaling factor  $c_1$  was chosen to be 0.69315 and  $\Delta u_{\mathbb{Q}0}$  was chosen to be 0.692 which gives an initial wake halfwidth  $b_0$  of 1.0, and an initial Reynolds number based on halfwidth of  $0.692/\nu$ . These values were used in the previous experiments of Sato & Kuriki [39], Corke, Krull, & Ghassemi [14], and in the computations of Chen, Cantwell, & Mansour [10].

## B.2 Linearized Disturbance Equations

Starting with the full incompressible, uniform density Navier-Stokes equations

$$u_{j,j} = 0 \quad (\text{B.4})$$

$$u_{j,t} + u_k u_{j,k} + \frac{p_{,j}}{\rho} = \nu u_{j,kk} \quad (\text{B.5})$$

$$p_{,kk} = \rho u_{k,l} u_{l,k} \quad (\text{B.6})$$

a total flow consisting of the mean base flow defined in equations B.1 through B.3 plus a small perturbation

$$u_j = \bar{u}_1 \delta_{1j} + u'_j \quad (\text{B.7})$$

$$p = \bar{p} + p' \quad (\text{B.8})$$

is substituted into equations B.4 through B.6.

$$u'_{j,j} = 0 \quad (\text{B.9})$$

$$\bar{u}_{1,t} \delta_{1j} + u'_{j,t} + (\bar{u}_1 \delta_{1k} + u'_k)(\bar{u}_{1,k} \delta_{1j} + u'_{j,k}) + \frac{\bar{p}_{,j} + p'_{,j}}{\rho} = \nu(\bar{u}_{1,kk} \delta_{1j} + u'_{j,kk}) \quad (\text{B.10})$$

$$\bar{p}_{,kk} + p'_{,kk} = \rho(\bar{u}_{1,k} \delta_{1j} + u'_{j,k})(\bar{u}_{1,j} \delta_{1k} + u'_{k,j}) \quad (\text{B.11})$$

The mean flow satisfies the Navier-Stokes equations, hence the mean flow terms may be subtracted out from equations B.9 through B.11 leaving the nonlinear disturbance equations

$$u'_{j,j} = 0 \quad (\text{B.12})$$

$$u'_{j,t} + \bar{u}_1 u'_{j,1} + u'_2 \bar{u}_{1,2} \delta_{1j} + u'_k u'_{j,k} + \frac{p'_{,j}}{\rho} = \nu u'_{j,kk} \quad (\text{B.13})$$

$$p'_{,kk} = \rho(2\bar{u}_{1,2} u'_{2,1} + u'_{k,l} u'_{l,k}) \quad (\text{B.14})$$

The perturbations are assumed to be small and products of perturbation terms are dropped, giving the linearized disturbance equations

$$u'_{j,j} = 0 \quad (\text{B.15})$$

$$u'_{j,t} + \bar{u}_1 u'_{j,1} + u'_k \bar{u}_{1,k} \delta_{1j} + \frac{p'_j}{\rho} = \nu u'_{j,kk} \quad (\text{B.16})$$

$$p'_{,kk} = 2\rho \bar{u}_{1,2} u'_{2,1} \quad (\text{B.17})$$

The disturbance flow is assumed to have the form of a traveling wave

$$u'_j = \check{u}_j(x_2) e^{i(\alpha x_1 + \beta x_3 - ct)} \quad (\text{B.18})$$

$$p' = \check{p}(x_2) e^{i(\alpha x_1 + \beta x_3 - ct)} \quad (\text{B.19})$$

where  $\alpha$  and  $\beta$  are real wavenumbers which determine the wavelength and wave angle, and  $c = c_\phi + ic_i$  is a complex wavespeed.

Substituting into the linearized disturbance equations

$$i\alpha \check{u}_1 + \check{u}_{2,2} + i\beta \check{u}_3 = 0 \quad (\text{B.20})$$

$$i(\alpha \bar{u}_1 - c) \check{u}_1 + \bar{u}_{1,2} \check{u}_2 = -\frac{i\alpha}{\rho} \check{p} + \nu(\check{u}_{1,22} - (\alpha^2 + \beta^2) \check{u}_1) \quad (\text{B.21})$$

$$i(\alpha \bar{u}_1 - c) \check{u}_2 = -\frac{1}{\rho} \check{p}_{,2} + \nu(\check{u}_{2,22} - (\alpha^2 + \beta^2) \check{u}_2) \quad (\text{B.22})$$

$$i(\alpha \bar{u}_1 - c) \check{u}_3 = -\frac{i\beta}{\rho} \check{p} + \nu(\check{u}_{3,22} - (\alpha^2 + \beta^2) \check{u}_3) \quad (\text{B.23})$$

$$\check{p}_{,22} - (\alpha^2 + \beta^2) \check{p} = 2i\alpha\rho \bar{u}_{1,2} \check{u}_2 \quad (\text{B.24})$$

Equations B.20 through B.23 may be combined to eliminate the pressure. After some manipulations, equations B.20 through B.23 can be reduced to the equations

$$\left[ \nu \left( D^2 - (\alpha^2 + \beta^2) \right)^2 - i(\alpha \bar{u}_1 - c) \left( D^2 - (\alpha^2 + \beta^2) \right) + i\alpha(D^2 \bar{u}_1) \right] \check{u}_2 = 0 \quad (\text{B.25})$$

and

$$\nu \left[ \left( D^2 - (\alpha^2 + \beta^2) \right) - i(\alpha \bar{u}_1 - c) \right] (\alpha \check{u}_3 - \beta \check{u}_1) = -\beta (D \bar{u}_1) \check{u}_2. \quad (\text{B.26})$$

Here the differentiation operator  $D \equiv (\cdot)_{,2}$  has been introduced for the sake of clarity.

Any physically meaningful disturbance must decay to zero as  $|x_2| \rightarrow \infty$ , thus the appropriate boundary conditions for these equations are

$$[\check{u}_2, D \check{u}_2] \rightarrow 0 \quad \text{as } |x_2| \rightarrow \infty \quad (\text{B.27})$$

and

$$\alpha \check{u}_3 - \beta \check{u}_1 \rightarrow 0 \quad \text{as } |x_2| \rightarrow \infty \quad (\text{B.28})$$

Equation B.25 is the well known Orr-Sommerfeld equation. Equation B.26 is known as the Squire equation. The form of equations B.25 and B.26 indicate that there are two classes of solutions to the set of linear equations B.20 through B.23 ([8]). The first class is comprised of solutions to equations B.25 and B.27 with equations B.26 and B.28 used only to solve for  $\check{u}_1$  and  $\check{u}_3$  once  $\check{u}_2$  is known. The second class is comprised of solutions with  $\check{u}_2 \equiv 0$  which satisfy equations B.26 and B.28. The solutions we will seek here are in the first class.

### B.3 Solution of the Linear Equations

The technique used to solve equation B.25 subject to B.27 was the spectral method developed by Spalart *et al.* A brief overview of the procedure will be given here. The reader is directed to Spalart, Moser, and Rogers [44] for a complete detailed description.

Spalart *et al.* begin by defining a vorticity perturbation component perpendicular to the wave vector  $(\alpha, \beta)$

$$\check{\omega}^\perp \equiv \frac{-\beta \check{\omega}_1 + \alpha \check{\omega}_3}{\sqrt{\alpha^2 + \beta^2}} \quad (\text{B.29})$$

where

$$\check{\omega}_1 \equiv D \check{u}_3 - i \beta \check{u}_2 \quad (\text{B.30})$$

and

$$\check{\omega}_3 \equiv i\alpha\check{u}_2 - D\check{u}_1 \quad (\text{B.31})$$

are the perturbation vorticities.

Applying continuity (equation B.20) allows  $\check{\omega}^\perp$  to be written in terms of  $\check{u}_2$  only

$$i\sqrt{\alpha^2 + \beta^2}\check{\omega}^\perp = [D^2 - (\alpha^2 + \beta^2)]\check{u}_2. \quad (\text{B.32})$$

Substituting equation B.32 into equation B.25 gives

$$\left[ \nu (D^2 - (\alpha^2 + \beta^2)) - i(\alpha\bar{u}_1 - c) \right] \sqrt{\alpha^2 + \beta^2}\check{\omega}^\perp = -\alpha(D^2\bar{u}_1)\check{u}_2 \quad (\text{B.33})$$

with boundary conditions

$$\check{\omega}^\perp \rightarrow 0 \quad \text{as } |x_2| \rightarrow \infty. \quad (\text{B.34})$$

Equations B.33 and B.34, along with B.32, are solved using a standard Galerkin method. The known and unknown functions,  $f(x_2)$ , are expanded in terms of a set of orthogonal basis functions  $R_j$  derived from the (1,1) Jacobi polynomials on a mapped coordinate  $\eta$

$$\check{\omega}^\perp(\eta) = a_j R_j(\eta) \quad (\text{B.35})$$

$$\check{u}_2(\eta) = b_{N-1}\Gamma_{N-1}(\eta) + b_N\Gamma_N(\eta) + b_j R_j(\eta) \quad (\text{B.36})$$

$$\bar{u}_1(\eta) = c_j R_j(\eta) \quad (\text{B.37})$$

$$R_j(\eta) = (1 - \eta^2)P_j^{(1,1)}(\eta) \quad (\text{B.38})$$

$$\eta \equiv \tanh\left(\frac{x_2}{x_2^0}\right) \quad (\text{B.39})$$

where  $x_2^0$  is a scaling factor for the mapping and  $\Gamma_j$  are exponential “extra” functions determined from

$$[D^2 - (\alpha^2 + \beta^2)]\Gamma_j = R_j \quad (\text{B.40})$$

which come about from the inversion of the Poisson equation B.32.



Derivatives of the basis functions  $R_j(\eta)$  can be expressed in terms of the basis functions themselves using the recursion relation

$$\begin{aligned} DR_j &= \frac{j+1}{x_2^0(2j+3)} ((j+1)R_{j-1} - (j+3)R_{j+1}) \\ &\equiv L_{jk}R_k \end{aligned} \quad (\text{B.41})$$

Substituting equations B.35, B.36, and B.41 into equation B.32 allows the unknown coefficients  $a_j$  to be written explicitly in terms of the unknown coefficients  $b_j$

$$\begin{aligned} a_j &= \frac{-i}{\sqrt{\alpha^2 + \beta^2}(x_2^0)^2} \begin{cases} d_{j-2}b_{j-2} + (e_j - (x_2^0)^2(\alpha^2 + \beta^2))b_j \\ \quad + f_{j+2}b_{j+2}, & j = 1, \dots, N-2; \\ d_{j-2}b_{j-2} + (x_2^0)^2b_j, & j = N-1, N; \end{cases} \\ &\equiv M_{jk}b_k \end{aligned} \quad (\text{B.42})$$

where  $d_j$ ,  $e_j$ , and  $f_j$  are known rational functions of the expansion index  $j$ .

Substituting the above into equation B.33 and applying a scalar Galerkin method with test function  $R_k$  results in an  $N \times N$  matrix eigenvalue problem for the coefficients  $a_j$  of the form

$$E_{jk}a_k = ca_j \quad (\text{B.43})$$

where  $E_{jk}$  is a complicated matrix (which will not be presented explicitly here) formed from  $L_{jk}$  (the derivative recursion matrix),  $M_{jk}$  (which relates the unknown coefficients  $a_j$  to the unknown coefficients  $b_j$ ), the known expansion for  $\bar{u}_1$ , and the known parameters  $\alpha$  and  $\beta$ .

This eigenvalue problem is solved using a standard numerical package which returns the  $N$  complex eigenvalues,  $c$ , and their corresponding eigenvectors. The most unstable eigenfunction for the given input parameters ( $\bar{u}_1$ ,  $\alpha$ , and  $\beta$ ) is the one corresponding to the eigenvalue with the largest complex component  $c_i$ . That eigenfunction is normalized and used to form the needed disturbance function.

# Appendix C

## Aliasing and Alias Control

This appendix presents an overview of numerical aliasing and the techniques used in this study to control the associated errors.

### C.1 Discrete Fourier Transforms and Aliasing

The one-dimensional discrete Fourier transform (DFT) of a series  $a_j$  of length  $N$  is given by

$$\hat{a}_n = \frac{1}{N} \sum_{j=0}^{N-1} a_j e^{-2\pi i \frac{jn}{N}} \quad (\text{C.1})$$

with inverse transform

$$a_j = \sum_{n=0}^{N-1} \hat{a}_n e^{2\pi i \frac{jn}{N}}. \quad (\text{C.2})$$

Consider a series  $a_j$  which represents a complex sinusoid with integer wavenumber  $k$  and constant amplitude  $C$

$$a_j = C e^{2\pi i \frac{jk}{N}}. \quad (\text{C.3})$$

The DFT of this series is

$$\hat{a}_n = \frac{C}{N} \sum_{j=0}^{N-1} e^{-2\pi i \frac{j(n-k)}{N}} = C \delta((k-n) \bmod N) \quad (\text{C.4})$$

where  $\delta$  is the discrete delta function

$$\delta(j) \equiv \begin{cases} 1, & \text{if } j = 0 \\ 0, & \text{otherwise.} \end{cases} \quad (\text{C.5})$$

Hence a wave with wavenumber  $k$  in physical space is transformed into Fourier space with a wavenumber  $(k - n) \bmod N$ . For example, if  $k = N + L$ , the series is transformed as if it were a series with a wavenumber of  $n = L = k - N$ . This effect can be seen directly in physical space since for any integer  $M$

$$a_i = C e^{2\pi i \frac{ik}{N}} = C e^{2\pi i \frac{i(k+MN)}{N}}. \quad (\text{C.6})$$

Thus data separated by  $M$  periods  $N$  in physical space are the same. Wavenumbers  $k + MN$  are said to be “aliased” to wavenumber  $k$ .

Aliasing errors occur in practice when operations on data with wavenumber span  $N$  increases the wavenumber span to greater than  $N$ . Such is the case with the non-linear terms in the Navier-Stokes equations, which are bi-linear products of the dependent variables. The remainder of this discussion will be limited to such products.

To examine aliasing in bi-linear terms, consider the one dimensional product of two series of length  $N$

$$\begin{aligned} c_j = a_j b_j &= \sum_{n=0}^{N-1} \hat{a}_n e^{2\pi i \frac{jn}{N}} \sum_{m=0}^{N-1} \hat{b}_m e^{2\pi i \frac{jm}{N}} \\ &= \sum_{n=0}^{N-1} \sum_{m=0}^{N-1} \hat{a}_n \hat{b}_m e^{2\pi i \frac{j(n+m)}{N}}. \end{aligned} \quad (\text{C.7})$$

This product has an *unaliased* wavenumber span of  $2N - 1$ , nearly twice the span of  $a_j$  and  $b_j$ . The length  $N$  DFT of  $c_j$  is

$$\hat{c}_k = \sum_{n=0}^{N-1} \sum_{m=0}^{N-1} \hat{a}_n \hat{b}_m \delta((n + m - k) \bmod N). \quad (\text{C.8})$$

Hence modes with  $(n + m) \geq N$  are aliased to modes with  $k = (n + m) - N$ .

The standard numerical DFT algorithms in use today have a span  $N$  which is even (typically a power of 2 with optionally one or more factors of 3) and span a wavenumber space of  $(1 - \frac{N}{2}) \leq k \leq \frac{N}{2}$ . Products of such series span a wavenumber range of  $(2 - N) \leq k \leq N$ . Figure C.1 illustrates aliasing with such a modal arrangement.

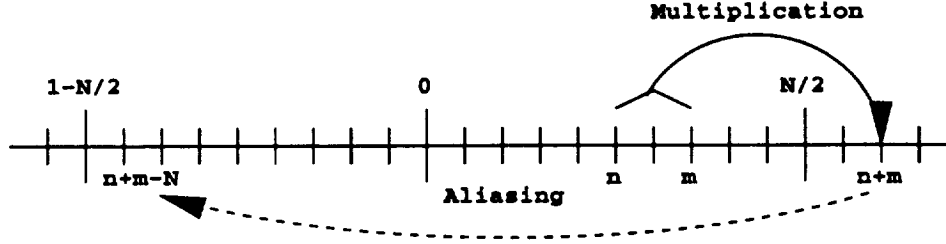


Figure C.1: Example of aliasing

In order to properly handle products of length  $N$  series, length  $N$  alias free products must be formed. The alias error from such products can be eliminated in one of two ways, by truncation and by phase shifting. These methods are outlined below.

## C.2 Dealiasing using Truncation

Since the product of two series each with a wavenumber span of  $N$  results in a series with a wavenumber span of  $(2N - 1)$  a simple method of obtaining an alias free product is to use transforms of length  $2N$ . The length  $N$  transforms  $\hat{a}_j$  and  $\hat{b}_j$  are padded with zeros to form length  $2N$  transforms and transformed to physical space to form length  $2N$  series. The series are used to form the needed products and transformed back to wave space with a length  $2N$  transform. An alias free length  $N$  transform can then be extracted by discarding modes beyond the desired span in wavespace.

For the case of a wavenumber space  $(1 - \frac{N}{2}) \leq k \leq \frac{N}{2}$  identical results can be obtained using transforms of length  $\frac{3}{2}N$  rather than  $2N$ , with resulting savings of time and storage space. This can be understood by considering that the worst cases for aliasing are when two modes of wavenumber  $\frac{N}{2}$  are combined, giving a product which is aliased to  $(N - \frac{3}{2}N) = -\frac{N}{2}$  and when two modes of wavenumber  $(1 - \frac{N}{2})$  are

combined, giving a product which is aliased to  $(\frac{3}{2}N - N - 2) = (\frac{N}{2} - 2)$ , both of which are outside of the desired alias free wavenumber space of  $(1 - \frac{N}{2}) \leq k \leq \frac{N}{2}$ .

In practice, the maximum transform length  $N$  is determined by the limitations imposed by the available computer hardware, so the alias free wavenumber space carried is in practice  $1 - \frac{N}{3} \leq k \leq \frac{N}{3}$ . Since two thirds of the available transform length  $N$  can be made alias free using truncation, this method of dealiasing is commonly referred to as the 2/3 rule.

### C.3 Dealiasing using Phase Shifts

Equation C.8 can be rewritten in the form

$$\hat{c}_j = \underbrace{\sum_{n+m=j} \hat{a}_n \hat{b}_m}_{\text{alias free}} + \underbrace{\sum_{n+m=j \pm N} \hat{a}_n \hat{b}_m}_{\text{alias error}}. \quad (\text{C.9})$$

If the transforms are performed on a shifted mesh (which manifests in wavespace as a multiplication of each Fourier mode  $a_j$  by a phase factor  $e^{ij\Delta}$ ) and then shifted back to the original mesh the results are

$$\begin{aligned} \hat{c}_j &= e^{-ij\Delta} \left( \sum_{n+m=j} \hat{a}_n e^{in\Delta} \hat{b}_m e^{im\Delta} + \sum_{n+m=j \pm N} \hat{a}_n e^{in\Delta} \hat{b}_m e^{im\Delta} \right) \\ &= \underbrace{\sum_{n+m=j} \hat{a}_n \hat{b}_m}_{\text{alias free}} + e^{\pm iN\Delta} \underbrace{\sum_{n+m=j \pm N} \hat{a}_n \hat{b}_m}_{\text{alias error}}. \end{aligned} \quad (\text{C.10})$$

The unaliased part of the product is unaffected by the phase shift while the alias error part is multiplied by a phase factor  $e^{\pm iN\Delta}$ . This can be used to exactly eliminate the aliasing error by evaluating  $\hat{c}_j$  on two meshes shifted by half a cell width from each other. Then

$$e^{\pm iN\Delta_2} = e^{\pm iN(\Delta_1 \pm \frac{\pi}{N})} = -e^{\pm iN\Delta_1} \quad (\text{C.11})$$

and the alias free product is simply the average of the two evaluations of  $\hat{c}_j$ .

If exact dealiasing is not essential, as is the case for most time accurate simulations, multiple evaluations at each time substep can be avoided by evaluating the bi-linear products on a shifted grid at each time substep. By choosing a random phase shift  $e^{\pm iN\Delta}$  at every other time substep, and using the half-cell offset shift  $e^{\pm iN(\Delta \pm \frac{\pi}{N})}$  for the subsequent time substep aliasing error is eliminated to the same order as the time advance algorithm. This random shift method is used in the present code to control one-dimensional aliasing errors.

## C.4 Multidimensional Dealiasing

Multi-dimensional Fourier transforms are obtained by applying separate one dimensional transforms in each direction

$$\hat{a}_{mnq\dots} = \frac{1}{MNQ\dots} \sum_{j=0}^{M-1} \sum_{k=0}^{N-1} \sum_{l=0}^{Q-1} \dots a_{jkl\dots} e^{-2\pi i(\frac{jm}{M} + \frac{kn}{N} + \frac{lq}{M} + \dots)} \quad (\text{C.12})$$

The transform in each direction is independent of the other directions, hence aliasing in each direction may be treated independently.

For the three-dimensional DFT, each pair of modes in a bi-linear product can combine to form one of four types of terms: an unaliased term, a term aliased in one direction, a term aliased in two of the three directions, or a term aliased in all three directions. Hence

$$\begin{aligned} \hat{c}_{\vec{k}=\{j,k,l\}} = & \underbrace{\sum_{\vec{m}+\vec{n}=\vec{k}} \hat{a}_{\vec{m}=\{m,n,q\}} \hat{b}_{\vec{n}=\{r,s,t\}}}_{\text{alias free}} \\ & + \underbrace{\sum_{\substack{\vec{m}+\vec{n}=\vec{k} \\ \vec{k}+\{\pm M,0,0\}}} \hat{a}_{\vec{m}} \hat{b}_{\vec{n}} + \sum_{\substack{\vec{m}+\vec{n}=\vec{k} \\ \vec{k}+\{0,\pm N,0\}}} \hat{a}_{\vec{m}} \hat{b}_{\vec{n}} + \sum_{\substack{\vec{m}+\vec{n}=\vec{k} \\ \vec{k}+\{0,0,\pm Q\}}} \hat{a}_{\vec{m}} \hat{b}_{\vec{n}}}_{\text{aliased in one direction only}} \\ & + \underbrace{\sum_{\substack{\vec{m}+\vec{n}=\vec{k} \\ \vec{k}+\{\pm M,\pm N,0\}}} \hat{a}_{\vec{m}} \hat{b}_{\vec{n}} + \sum_{\substack{\vec{m}+\vec{n}=\vec{k} \\ \vec{k}+\{\pm M,0,\pm Q\}}} \hat{a}_{\vec{m}} \hat{b}_{\vec{n}} + \sum_{\substack{\vec{m}+\vec{n}=\vec{k} \\ \vec{k}+\{0,\pm N,\pm Q\}}} \hat{a}_{\vec{m}} \hat{b}_{\vec{n}}}_{\text{aliased in two of three directions}} \end{aligned}$$

$$+ \sum_{\substack{\vec{m} + \vec{n} = \\ \vec{k} \pm \{\pm M, \pm N, \pm Q\}}} \hat{a}_{\vec{m}} \hat{b}_{\vec{n}} \quad (\text{C.13})$$

*aliased in all three directions*

Dealiasing in multiple dimensions can be accomplished in the same ways as in one dimension, with truncation, shifting, or a combination of the two. Using only truncation is inconvenient since it reduces the number of useful modes to less than one third of the available modes. Dealiasing by pure phase shifting is also inconvenient since it would require two evaluations for each direction dealiased, for a total of six evaluations per time substep.

The present code uses a combination of the two methods. Following Patterson and Orszag [31], modes with

$$\left(\frac{j}{M}\right)^2 + \left(\frac{k}{N}\right)^2 + \left(\frac{l}{Q}\right)^2 \geq 2\left(\frac{1}{3}\right)^2 \quad (\text{C.14})$$

are truncated. This eliminates the two and three dimensional aliasing as per the 2/3 rule, leaving only the one dimensional aliasing. Truncating in this way increased the useful modes to approximately half of the total modes. Rogallo [34] advocates the somewhat less severe rule of truncating *only* those modes which are aliased in more than one direction (as opposed to the ellipsoid in C.14 which also truncates some modes which are aliased in only one direction) however the increased number of useful nodes (to approximately two thirds of the total number of nodes) is not significant when the resulting shape of the useful wavespace is considered.

The remaining one dimensional aliasing errors can be handled using phase shifting as described above for the one dimensional case. The transform is evaluated twice on grids shifted by half a cell width in each direction, and the alias free product is the average of the two evaluations.

Since exact dealiasing is not required for the present code, random phase shifting in each direction at alternate time substeps as outlined above for the one dimensional case is used to cancel out the aliasing error to the order of the time advance algorithm. The remaining aliasing error appears as a small amplitude random forcing function

at low wavenumbers [34]. So long as the computed flow remains well resolved (hence the energy in the highest wavenumber motions is several orders of magnitude below the most energetic wavenumbers) any residual aliasing error will be at least several orders of magnitude below the energy of the alias free solution.



# Appendix D

## Topological Classification

Topological methods are useful in the description of vector fields and are coming increasingly into use as a means to study the large data sets produced by numerical simulations. Chong, Perry, and Cantwell [12] have carried out a general classification of the various types of linearized three-dimensional flows which can occur in compressible and incompressible flow. This classification method was used by Cantwell, Chen, and Lewis [7] and Chen, Cantwell and Mansour [9] to analyze the the topology of flow structures in experimental measurements of a pulsed low-speed diffusion flame and direct numerical simulations of a compressible plane wake. Chen et. al. [11] and Soria et. al. [42] used this method to study the small scale motions in numerical simulations of a variety of compressible and incompressible flows including wakes, mixing layers, isotropic turbulence, and homogeneous shear flows.

The method is based on concisely summarizing local flow structures in the space of invariants of the velocity gradient tensor. In these studies, the velocity gradient tensor,  $A_{ij} = u_{i,j}$  is calculated at each point in the flow, and the invariants of the velocity gradient tensor, as well as the invariants of the rate-of-strain and rate-of-rotation tensors are calculated. Plots of the joint probability density functions (pdf's) of the invariants for the entire flow reveal global trends in the geometry of the velocity field which would be difficult if not impossible to discover using other techniques. They also allow the study of how structures in invariant space (which correspond to specific local flow geometries) correspond to structures observed in physical space.

There are several good reasons for studying the velocity gradient tensor as opposed to the raw velocity field. Primary among them is that results are coordinate independent (invariant under any affine transformation) and independent of the frame of reference of the observer. Moreover, in the case of incompressible flow where the first invariant is zero, the three dimensional physical field, which can be infinite in extent, can be represented in a finite region of the two dimensional space of the second and third invariants. Finally, large scale motions are associated with relatively low gradients while small scale motions are associated with high gradients. Thus different length scales in the physical flow naturally tend to be sorted into different regions in invariant space, and thus may be examined separately.

While the present study focuses on the velocity field, it should be noted that this method may also be applied to any smooth vector field of interest. These can include the vorticity field, the scalar gradient field, or the pressure gradient field.

## D.1 Local Flow Trajectories

The instantaneous trajectory of any fluid particle in a flow field is determined by the solution of the convection equation

$$\dot{x}_{j,t} = u_j \quad (\text{D.1})$$

where  $x_j$  is the location of the given fluid particle and  $u_j$  is the flow velocity evaluated at the particle position.

For fluid in the neighborhood of some reference fluid particle at location  $x_j^c$  moving with the local flow velocity  $u_j^c$ , equation D.1 may be used to obtain an equation for the local relative flow.

$$\begin{aligned} x_{j,t} - x_{j,t}^c &= u_j - u_j^c \\ &= (x_k - x_k^c)u_{j,k} + (x_k - x_k^c)(x_l - x_l^c)u_{j,kl} + \dots \\ &\approx u_{j,k}(x_k - x_k^c). \end{aligned} \quad (\text{D.2})$$

Hence, in a frame of reference moving with some particle in the flow,  $x'_j = x_j - x_j^c$ , the trajectories of fluid particles near the reference particle with respect to the reference particle are determined by the solutions to the linear equation

$$x'_{j,t} = u_{j,k} x'_k. \quad (\text{D.3})$$

The flow in this local frame of reference is completely determined by the eigenvectors of the velocity gradient tensor

$$A_{jk} \equiv u_{j,k} \quad (\text{D.4})$$

the symmetric part of which

$$S_{jk} \equiv \frac{1}{2}(u_{j,k} + u_{k,j}) \quad (\text{D.5})$$

is the rate-of-strain tensor, and the anti-symmetric part of which

$$W_{jk} \equiv \frac{1}{2}(u_{j,k} - u_{k,j}) \quad (\text{D.6})$$

is the rate-of-rotation tensor. If  $A_{jk}$  has only real eigenvalues, the local flow is strain dominated and the local flow consists of fluid moving inward to or outward from the origin along distinct axes.. If  $A_{jk}$  has a pair of complex eigenvalues, the local flow is rotation dominated and the local flow consists of fluid spiraling around the origin in one plane and flowing inward or outward along the third direction.

## D.2 Eigenvalues

The eigenvalues,  $\lambda$ , and complex eigenvectors,  $e_j$ , of  $A_{jk}$  satisfy the eigenvalue equation

$$[A_{jk} - \lambda \delta_{jk}]e_j = 0 \quad (\text{D.7})$$

where the eigenvalues  $\lambda$  are solutions to the characteristic equation

$$\det[A_{jk} - \lambda\delta_{jk}] = 0. \quad (\text{D.8})$$

Equation D.8 expands to the third order algebraic equation

$$\lambda^3 + P\lambda^2 + Q\lambda + R = 0 \quad (\text{D.9})$$

where  $P$ ,  $Q$ , and  $R$  are referred to as the *invariants* of the tensor  $A_{jk}$  and are given by

$$P = -A_{kk} = -S_{kk} \quad (\text{D.10})$$

$$\begin{aligned} Q &= \frac{1}{2}(P^2 - A_{jk}A_{kj}) \\ &= \frac{1}{2}(P^2 - S_{jk}S_{kj} - W_{jk}W_{kj}) \end{aligned} \quad (\text{D.11})$$

$$\begin{aligned} R &= -\det[A_{jk}] \\ &= \frac{1}{3}(-P^3 + 3PQ - A_{jk}A_{kl}A_{lj}) \\ &= \frac{1}{3}(-P^3 + 3PQ - S_{jk}S_{kl}S_{lj} - 3W_{jk}W_{kl}S_{lj}). \end{aligned} \quad (\text{D.12})$$

The set of solutions for  $\lambda$  from equation D.9 fall into one of three categories: All three  $\lambda$  are real and distinct; All three  $\lambda$  are real and at least two of them equal; Or one  $\lambda$  is real and the other two are complex conjugates. The category which a given set of  $\lambda$  falls into is completely determined by the location of the three invariants in  $(P, Q, R)$  space.

The surface in  $(P, Q, R)$  space that separates characteristic equations with all real solutions from those with one real and two complex solutions (and hence the surface on which the characteristic equation has three real solution with at least two equal) is given by

$$27R^2 + (4P^3 - 18PQ)R + (4Q^3 - P^2Q^2) = 0 \quad (\text{D.13})$$

A detailed discussion of the properties of this surface and a guide to the solutions for the resulting sets of  $e_j$  (and hence the local flow geometry) that can occur in the various domains in  $(P, Q, R)$  space is given in Chong, Perry, and Cantwell [12].

### D.3 Incompressible Flows

For incompressible flows,

$$P = A_{jj} = 0 \quad (\text{D.14})$$

and equations D.11 and D.12 simplify to

$$Q = -\frac{1}{2}(S_{jk}S_{kj} + W_{jk}W_{kj}) \quad (\text{D.15})$$

$$R = -\frac{1}{3}(S_{jk}S_{kl}S_{lj} + 3W_{jk}W_{kl}S_{lj}). \quad (\text{D.16})$$

The surface which divides real from imaginary solutions described by equation D.13 simplifies to the curve

$$27R^2 + 4Q^3 = 0. \quad (\text{D.17})$$

Hence, for incompressible flows, the local flow geometry is completely determined by the location of the  $Q$  and  $R$  invariants in  $(Q, R)$  space.

Figure D.1 shows all of the possible local flow geometries for incompressible flow. Below the curve given by equation D.17 all three eigenvalues of  $A_{jk}$  are real, and the flow is dominated by strain type motions. To the left of the  $R = 0$  axis, the local flow has fluid moving inwards toward the origin along two of the principal directions and outward from it along the third principal direction (stable node/saddle/saddle). To the right of the  $R = 0$  axis, the local flow has fluid moving outward from reference point along two of the principal directions and inward towards the reference point along the third direction (unstable node/saddle/saddle).

Above the curve given by equation D.17 two of the eigenvalues of  $A_{ij}$  are complex, and the local flow is dominated by rotational motions. To the left of the  $R = 0$  axis, the local flow has fluid spiraling inwards toward the reference point in a plane and moving outward from it in the third direction (stable focus/stretching). To the right

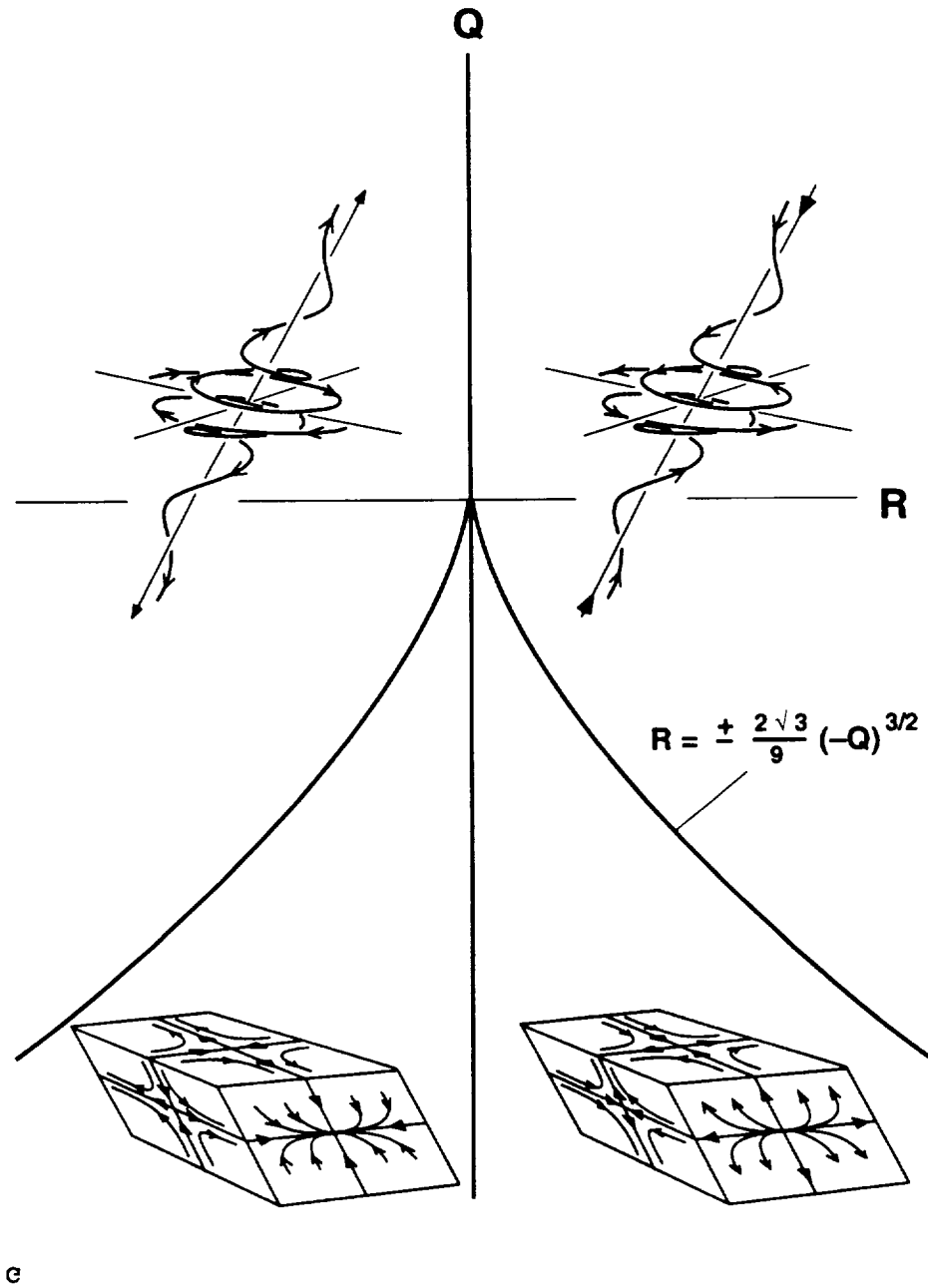


Figure D.1: Invariant Space for Incompressible Flows

of the  $R = 0$  axis, the local flow has fluid moving toward reference point in one direction and spiraling outward in a plane (unstable focus/contracting).

## D.4 Joint Pdf's of Invariants

This relatively simple mapping of the location of the  $Q$  and  $R$  invariants in  $(Q, R)$  space to the local flow geometry allows for a very concise summary of local geometry of a large numbers of points in a flow field.  $Q$  and  $R$  are calculated for each point of interest (often the whole flow) and the resulting data is presented as a joint probability density function (pdf) in the invariant plane. This allows the local flow geometries to be studied in a global framework which allows overall trends to be easily distinguished. This technique is especially useful for studying the smallest scales in the flow, since small scales will have high gradients and their invariants will tend to lie far from the origin in  $(Q, R)$  space where any trends can easily be distinguished.

## D.5 Enstrophy Density, Dissipation, and Vortex Stretching

Other quantities related to the  $Q$  and  $R$  invariants are also of interest. In particular,  $Q$  and  $R$  may be split into contributions from the rate-of-strain and rate-of-rotation tensors. These contributions can be directly related to physical quantities in the flow.

The second invariant of the velocity gradient tensor can be rewritten as the difference of two positive-definite quantities

$$\begin{aligned} Q &= -\frac{1}{2}(S_{jk}S_{jk} - W_{jk}W_{jk}) \\ &= Q_s + Q_w \end{aligned} \tag{D.18}$$

where  $Q_s$  is the second invariant of the rate-of-strain tensor  $S_{jk}$  and  $Q_w$  is the second invariant of the rate-of-rotation tensor  $W_{jk}$ . This decomposition allows the study of the relative importance of strain and rotation (enstrophy density) in the local flow geometry. If  $Q$  is large and positive, then the local enstrophy density is large and

dominates the strain ( $Q_w \gg Q_s$ ). If  $Q$  is large and negative, then the local strain is large and dominates the enstrophy density ( $Q_s \gg Q_w$ ). Plots of joint pdf of  $Q_s$  versus  $Q_w$  will reveal correlations between strain and rotation in the flow.

The third invariant,  $R$  can be similarly split

$$\begin{aligned} R &= -\frac{1}{3}(S_{jk}S_{kl}S_{lj} + 3W_{jk}W_{kl}S_{lj}) \\ &= R_s - \sigma \end{aligned} \tag{D.19}$$

where  $R_s$  is the third invariant of the rate-of-strain tensor  $S_{jk}$  and  $\sigma = W_{jk}W_{kl}S_{lj}$  represents stretching of vorticity. Plots of the joint pdf of  $\sigma = R_s - R$  and the other invariants will reveal correlations between vortex stretching and other quantities. Of particular interest is the correlation between vortex stretching and the enstrophy density ( $2Q_w$ ).

The invariants of the rate-of-strain tensor  $S_{jk}$  are of additional interest. For incompressible flow, the rate mechanical dissipation of energy due to viscosity is related to the second invariant of  $S_{jk}$  by

$$\varphi = 2\nu S_{jk}S_{kj} = -4\nu Q_s. \tag{D.20}$$

Hence strongly dissipating regions in a flow have large negative values of  $Q_s$ . Since  $S_{jk}$  is symmetric, all its eigenvalues must be real, hence its invariants lie under the real-imaginary dividing curve given by equation D.17. By studying plots of  $Q_s$  versus  $R_s$  correlations between the mechanical dissipation and the local flow geometry can be examined.



## Appendix E

### Invariant Space Pdf's for Selected Datasets

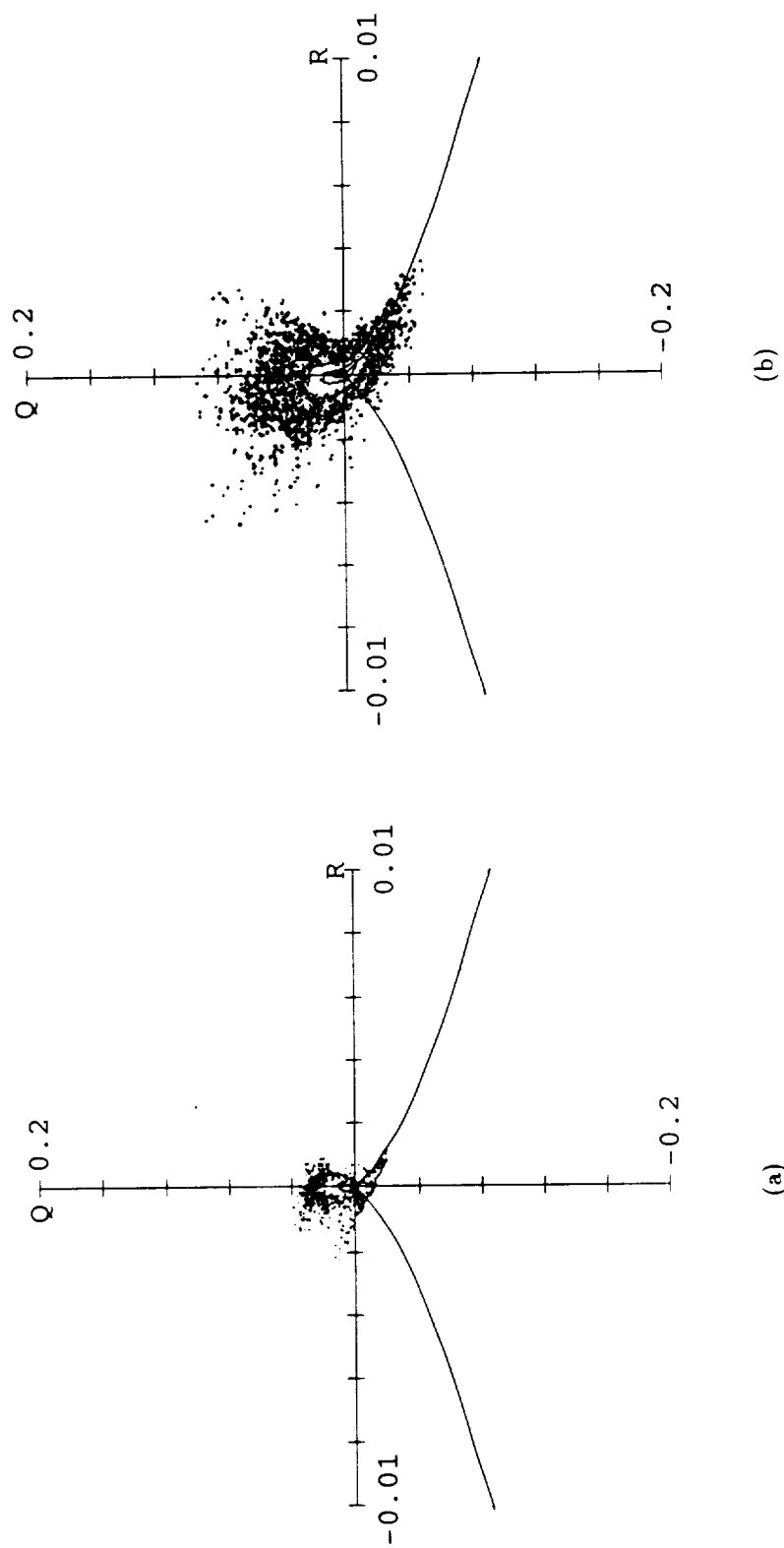


Figure E.1: See caption page 224.

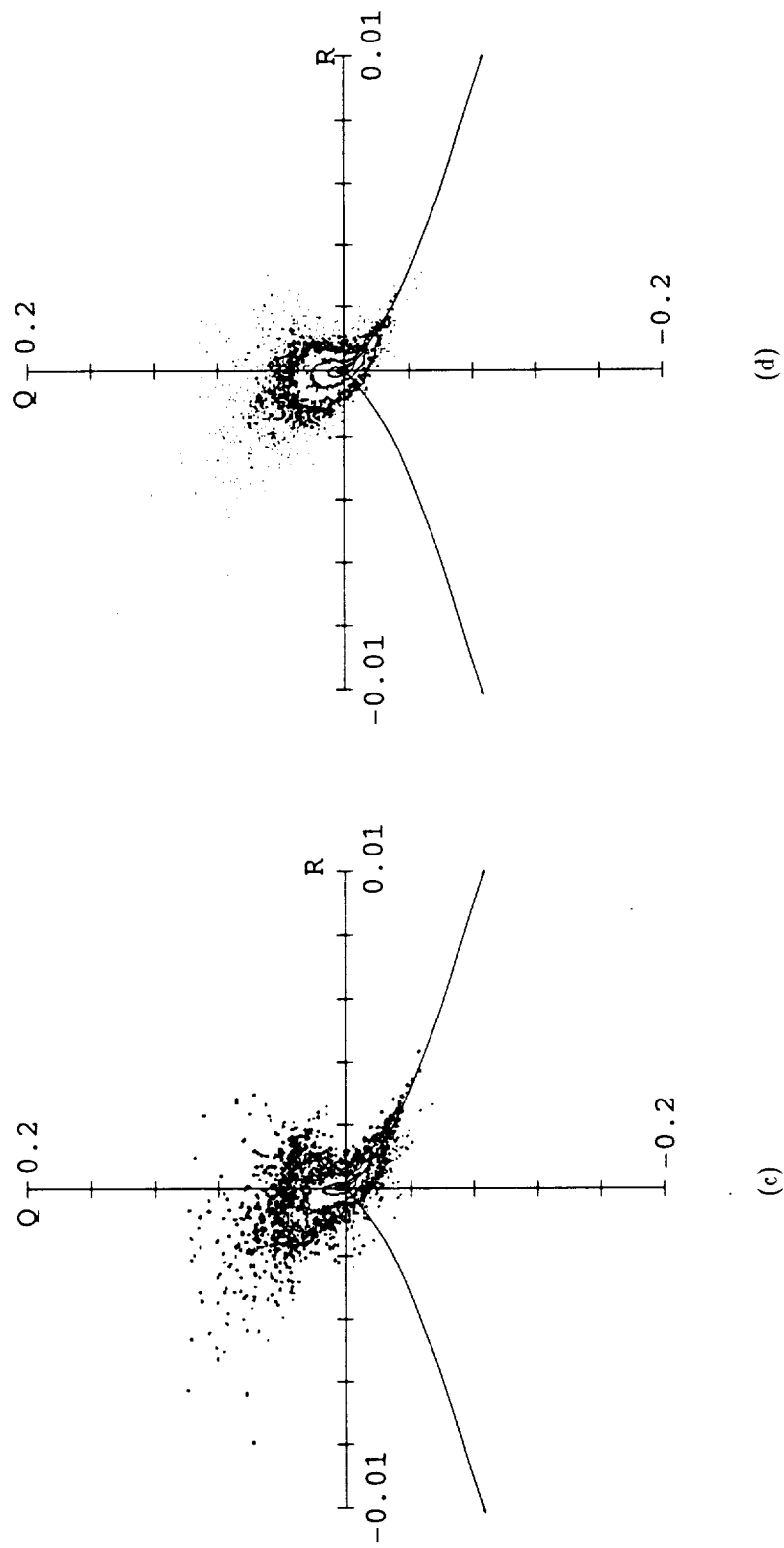


Figure E.1: See caption page 224.

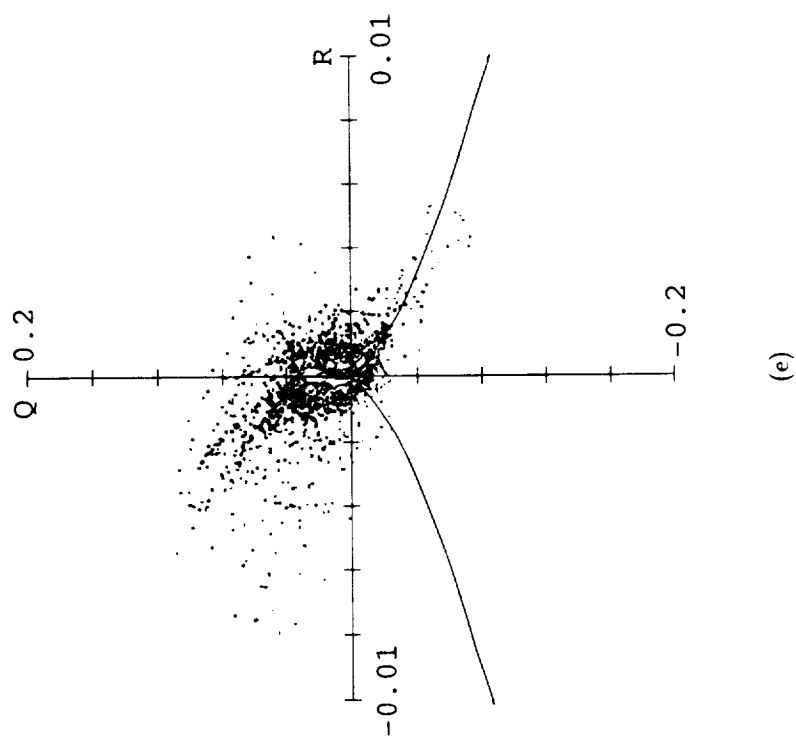


Figure E.1: Contour plots of joint pdf of  $Q$  vs.  $R$  for  $Re_b = 346$  wakes with various initial disturbance wavelengths.  
 (a)  $346(60)_{0xx}^{0xx}$ ,  $t = 196.9$ . (b)  $346(60)_{0xx}^{x0x}$ ,  $t = 204.8$ . (c)  $346(60)_{0xx}^{x0x}$ ,  $t = 181.1$ . (d)  $346(60)_{000}^{x00}$ ,  $t = 197.0$ .  
 (e)  $346(60)_{00x}^{0xx}$ ,  $t = 202.8$ .

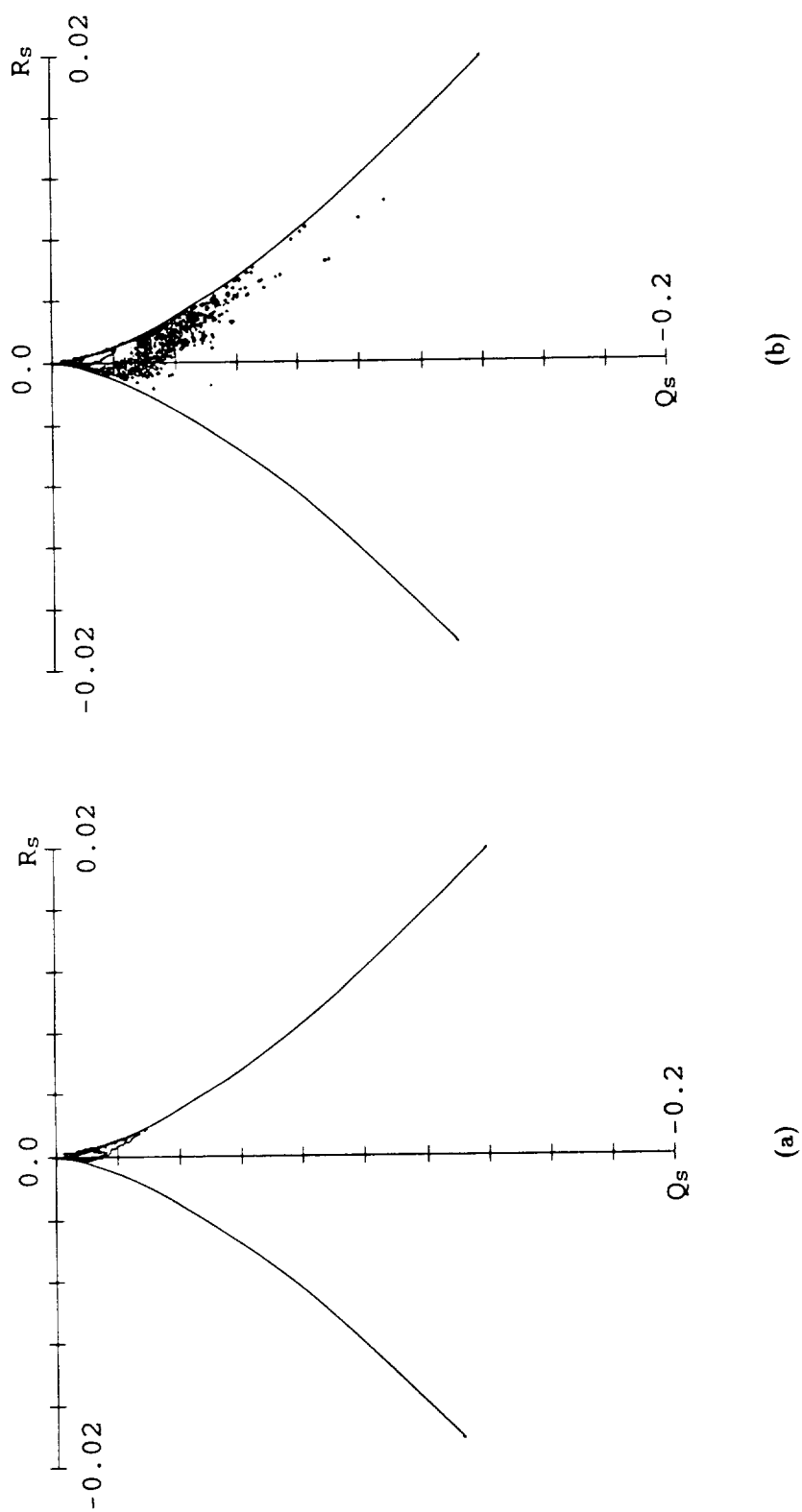


Figure E.2: See caption page 227.

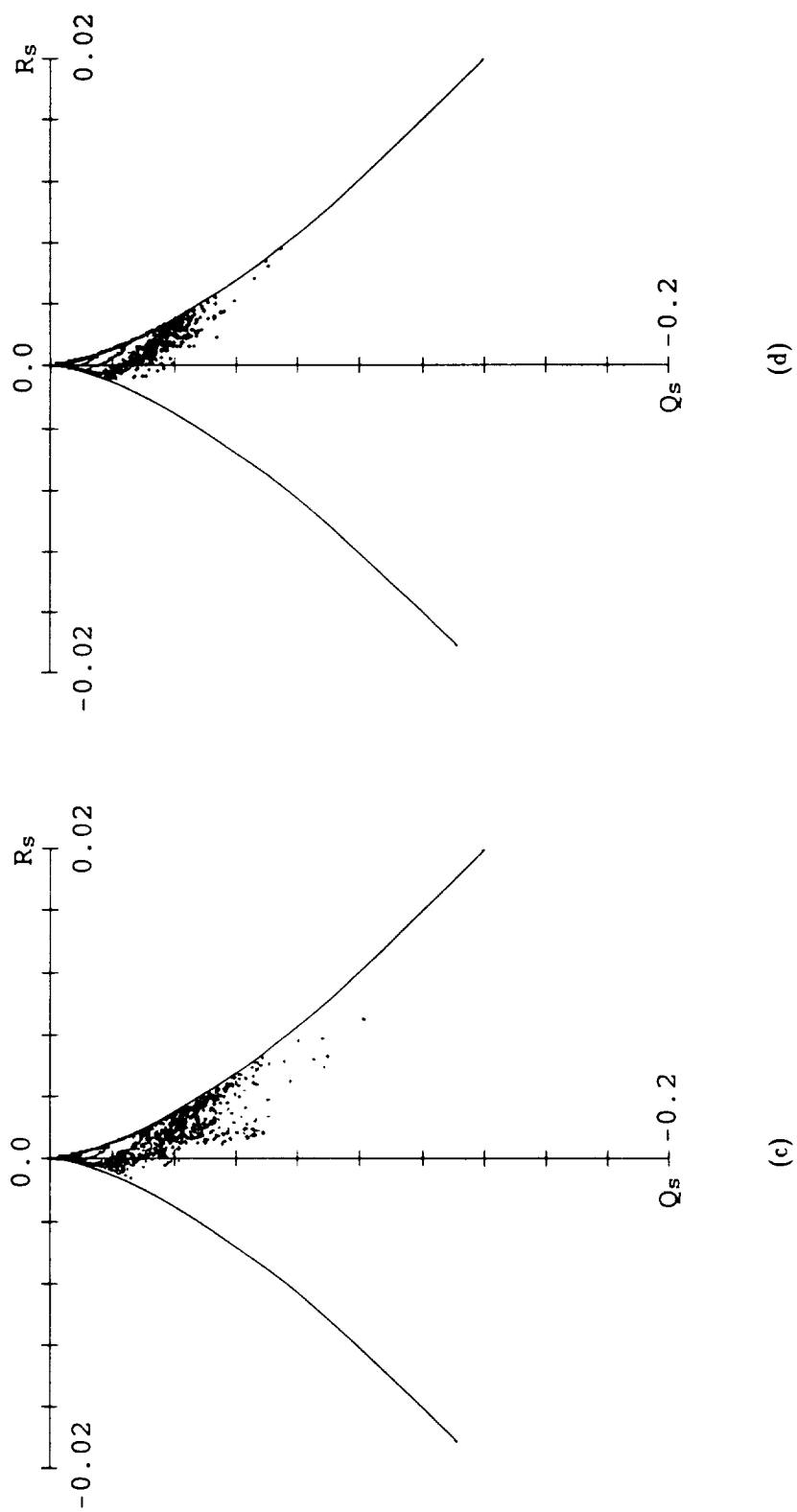
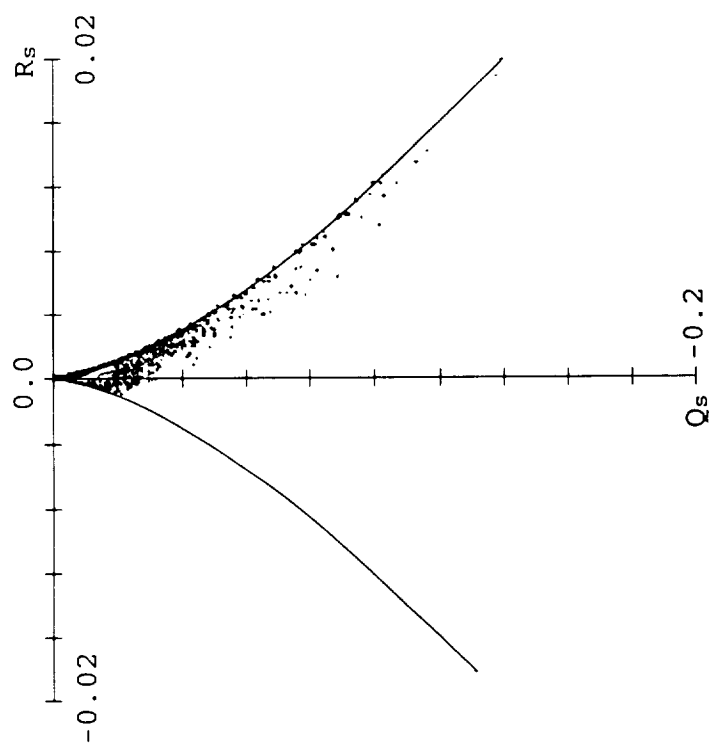


Figure E.2: See caption page 227.



(e)

Figure E.2: Contour plots of joint pdf of  $Q_s$  vs.  $R_s$  for  $Re_b = 346$  wakes with various initial disturbance wavelengths. (a)  $346(60)_{0xz}^{0xz}$ ,  $t = 196.9$ . (b)  $346(60)_{0xz}^{x0x}$ ,  $t = 204.8$ . (c)  $346(60)_{00x}^{x0x}$ ,  $t = 181.1$ . (d)  $346(60)_{000}^{x00}$ ,  $t = 197.0$ . (e)  $346(60)_{00x}^{0xz}$ ,  $t = 202.8$ .

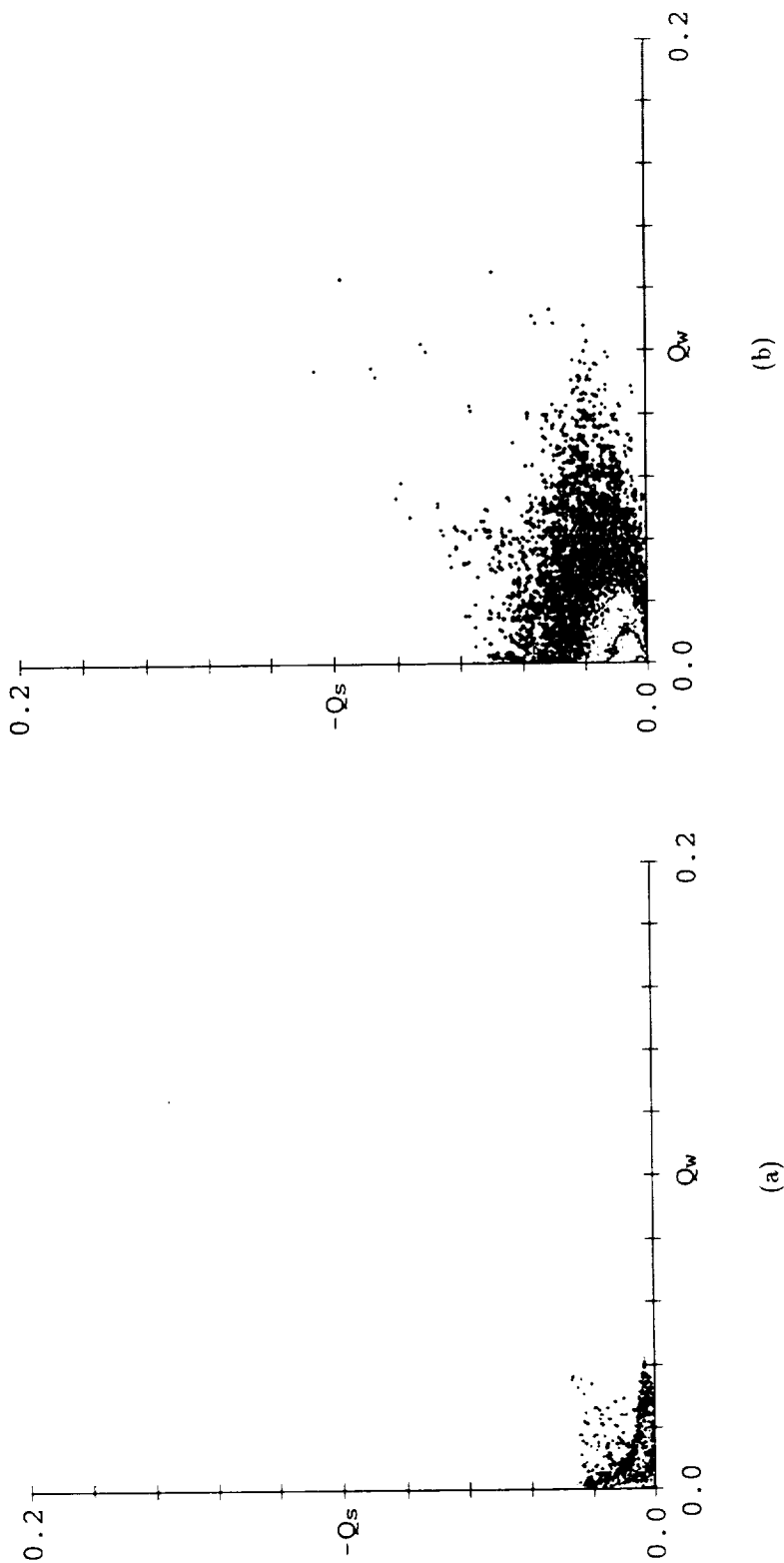


Figure E.3: See caption page 230.



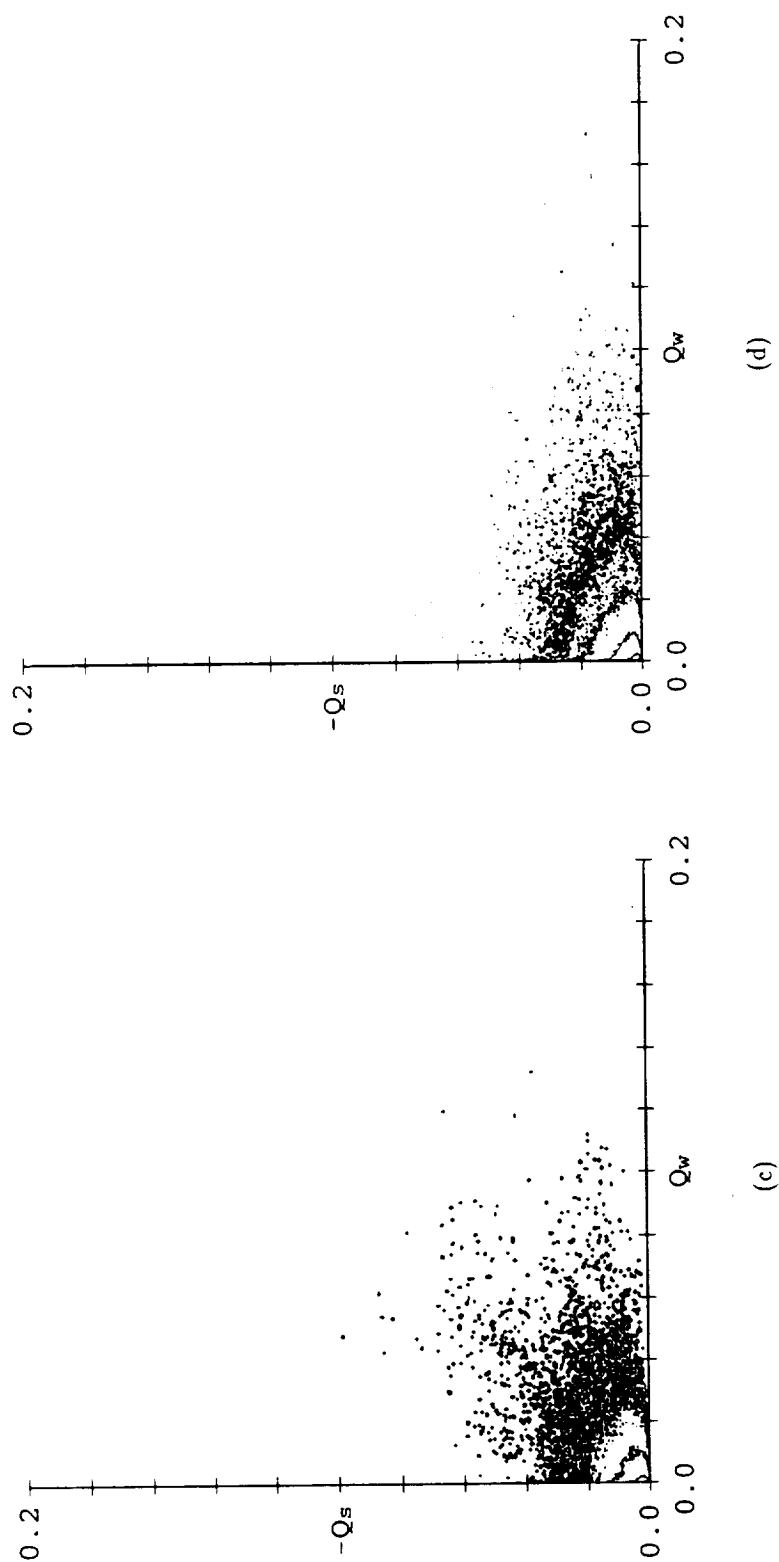


Figure E.3: See caption page 230.

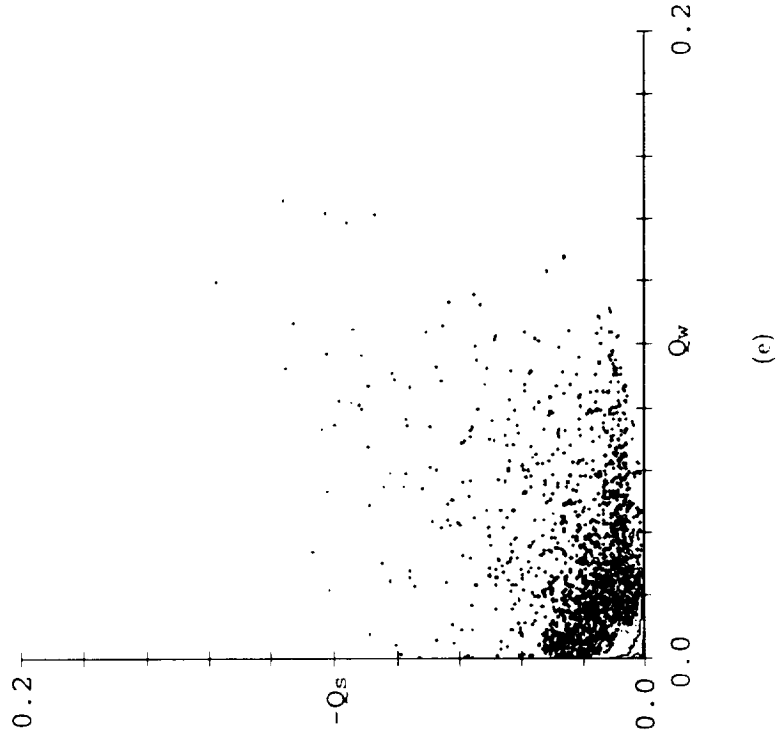


Figure E.3: Contour plots of joint pdf of  $-Q_s$  vs.  $Q_w$  for  $Re_b = 346$  wakes with various initial disturbance wavelengths. (a)  $346(60)_{0rr}^{0rx}$ ,  $t = 196.9$ . (b)  $346(60)_{0rr}^{0rx}$ ,  $t = 204.8$ . (c)  $346(60)_{00r}^{0rx}$ ,  $t = 181.1$ . (d)  $346(60)_{000}^{000}$ ,  $t = 197.0$ . (e)  $346(60)_{00r}^{0rx}$ ,  $t = 202.8$ .

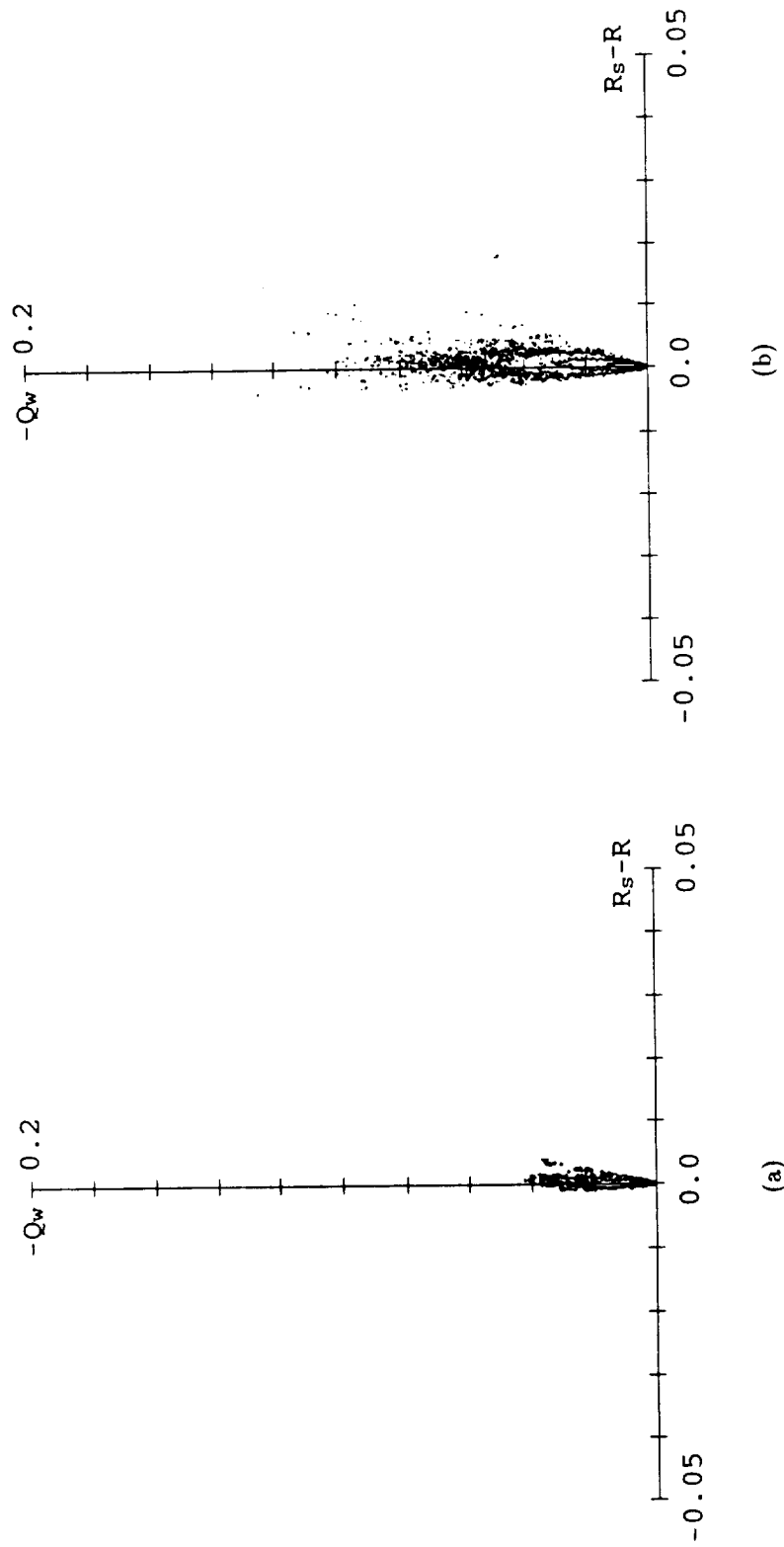


Figure E.4: See caption page 233.

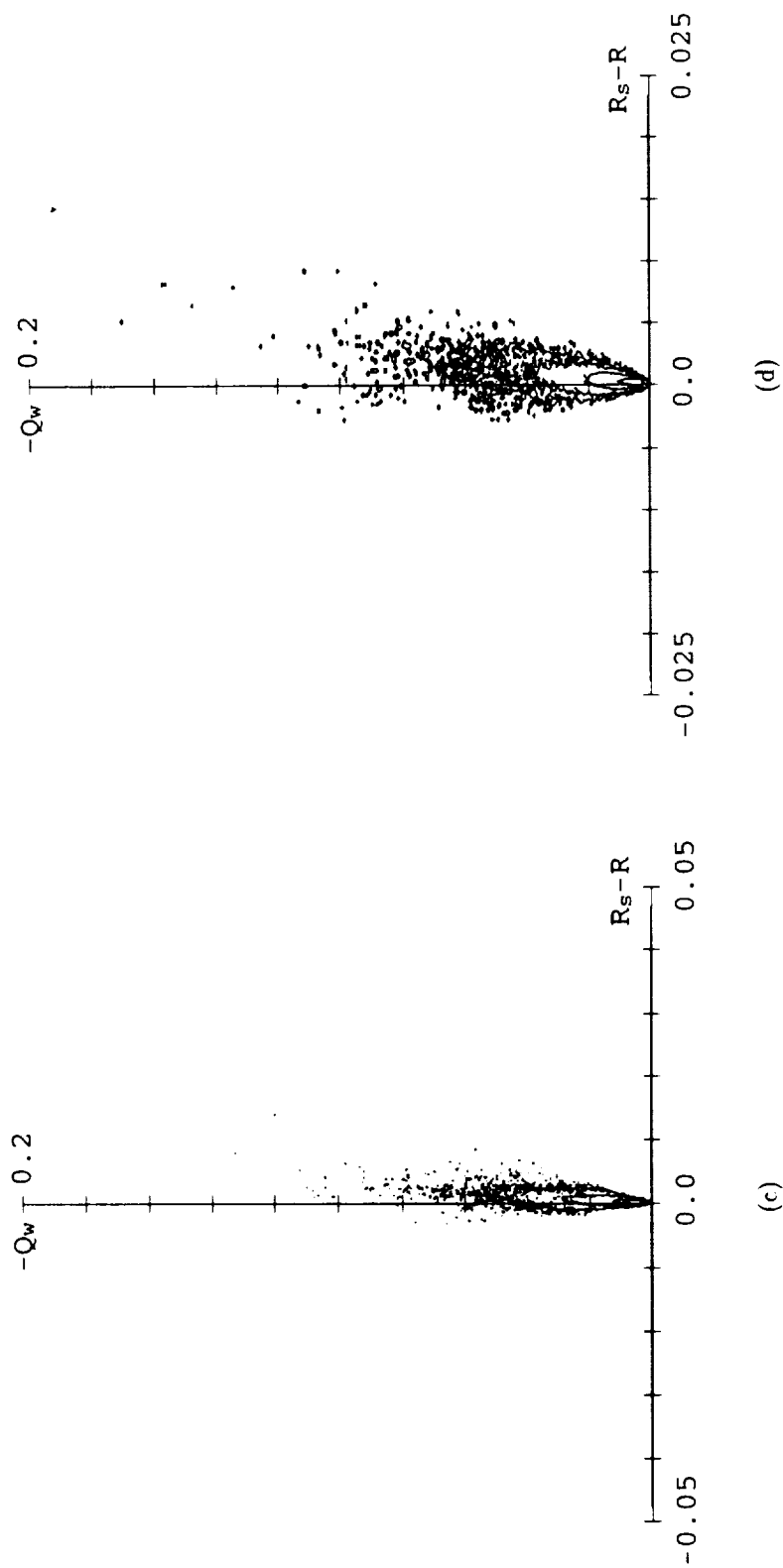


Figure E.4: See caption page 233.

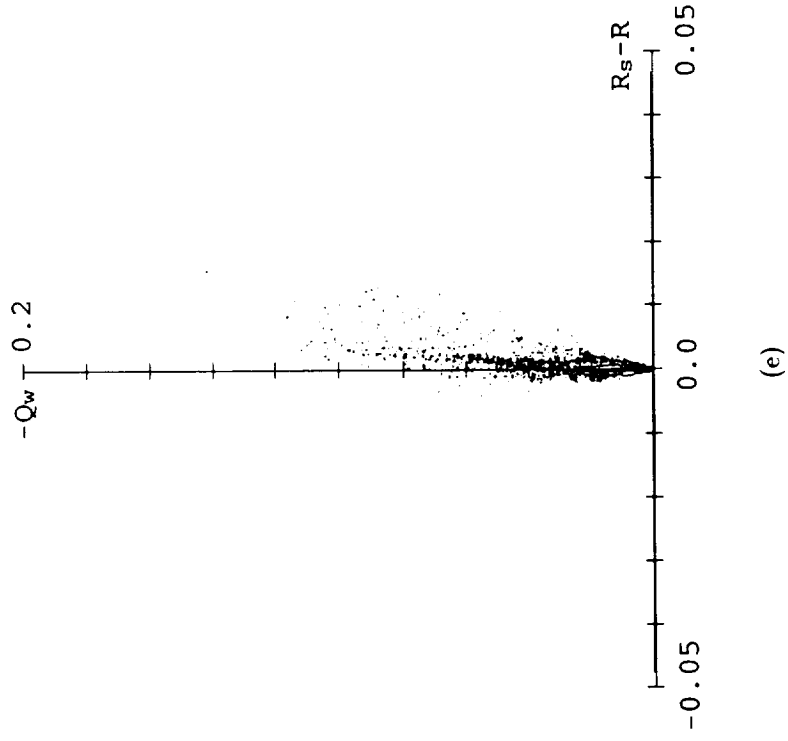


Figure E.4: Contour plots of joint pdf of  $Q_w$  vs.  $R_s - R$  for  $Re_b = 346$  wakes with various initial disturbance wavelengths. (a)  $346(60)_{0xx}^{0xx}$ ,  $t = 196.9$ . (b)  $346(60)_{0xx}^{x0x}$ ,  $t = 204.8$ . (c)  $346(60)_{00x}^{x0x}$ ,  $t = 181.1$ . (d)  $346(60)_{000}^{x00}$ ,  $t = 197.0$ . (e)  $346(60)_{00x}^{0xx}$ ,  $t = 202.8$ .

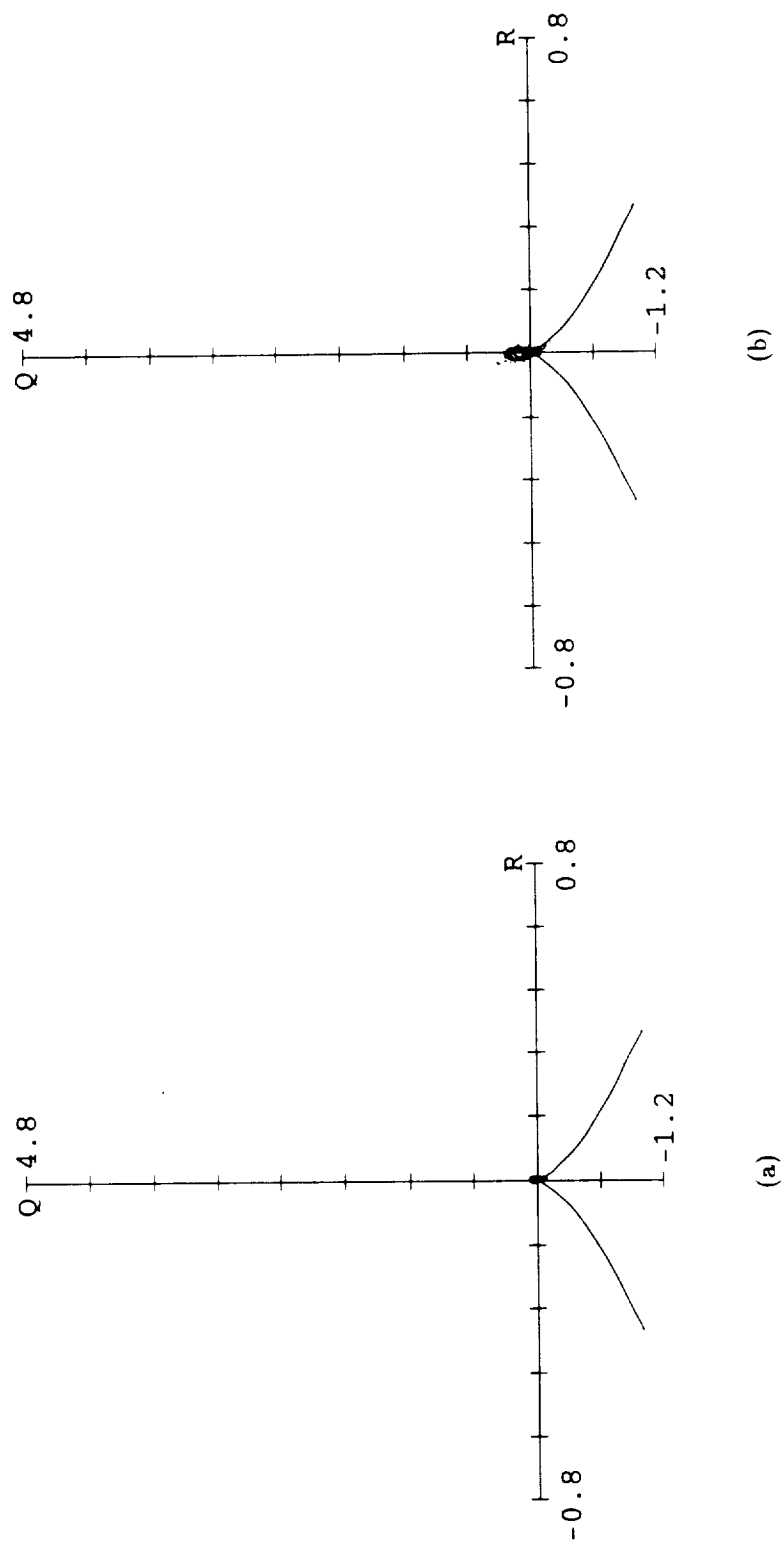


Figure E.5: See caption page 235.

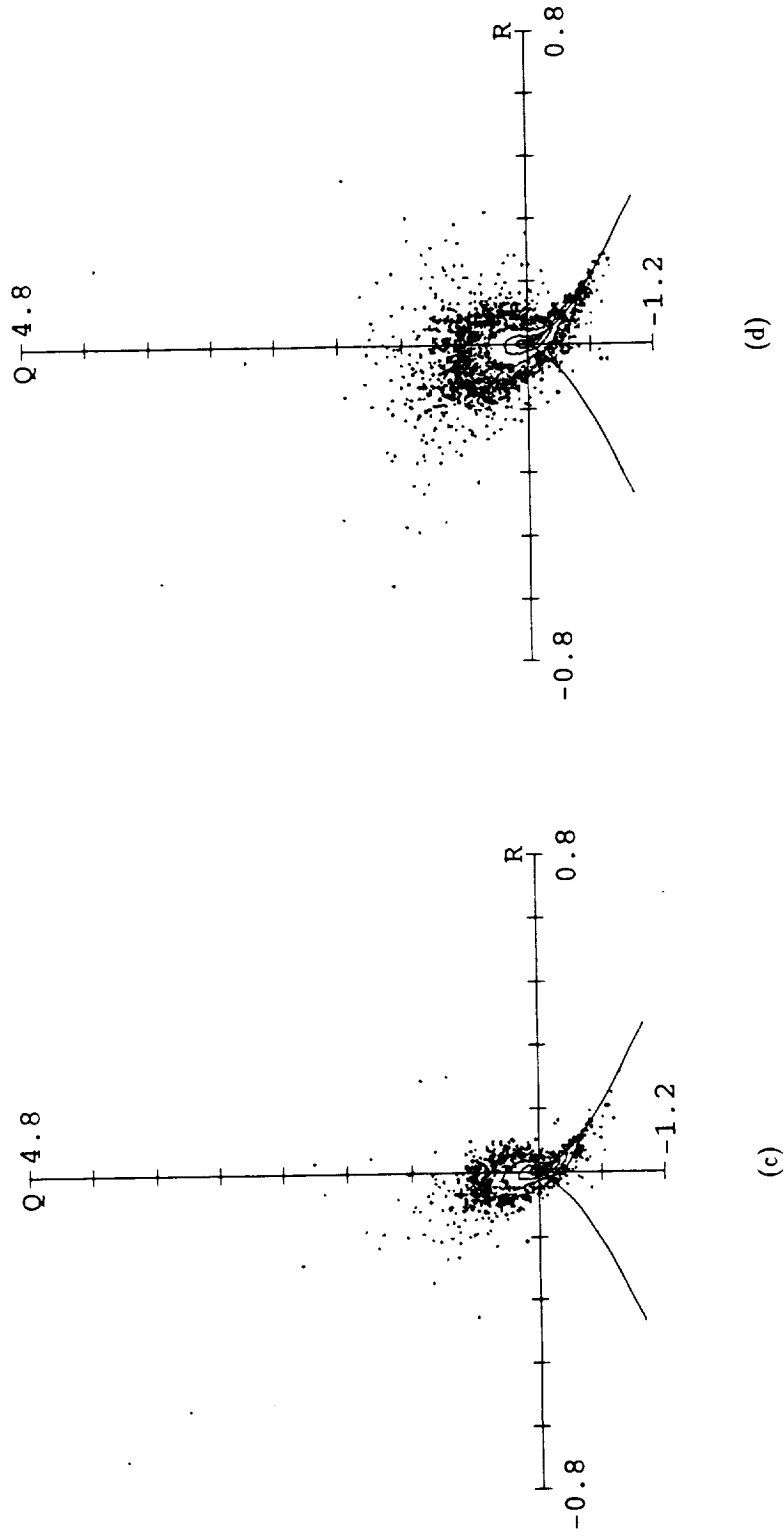


Figure E.5: Contour plots of joint pdf of  $Q$  vs.  $R$  for  $\langle ? \rangle (60)_{0xx}^{x0x}$  wakes (two-dimensional fundamental plus three-dimensional subharmonic with various Reynolds numbers). (a)  $Re_b = 346$ ,  $t = 204.8$ . (b)  $Re_b = 692$ ,  $t = 201.9$ . (c)  $Re_b = 1384$ ,  $t = 199.3$ . (d)  $Re_b = 2768$ ,  $t = 194.6$ .

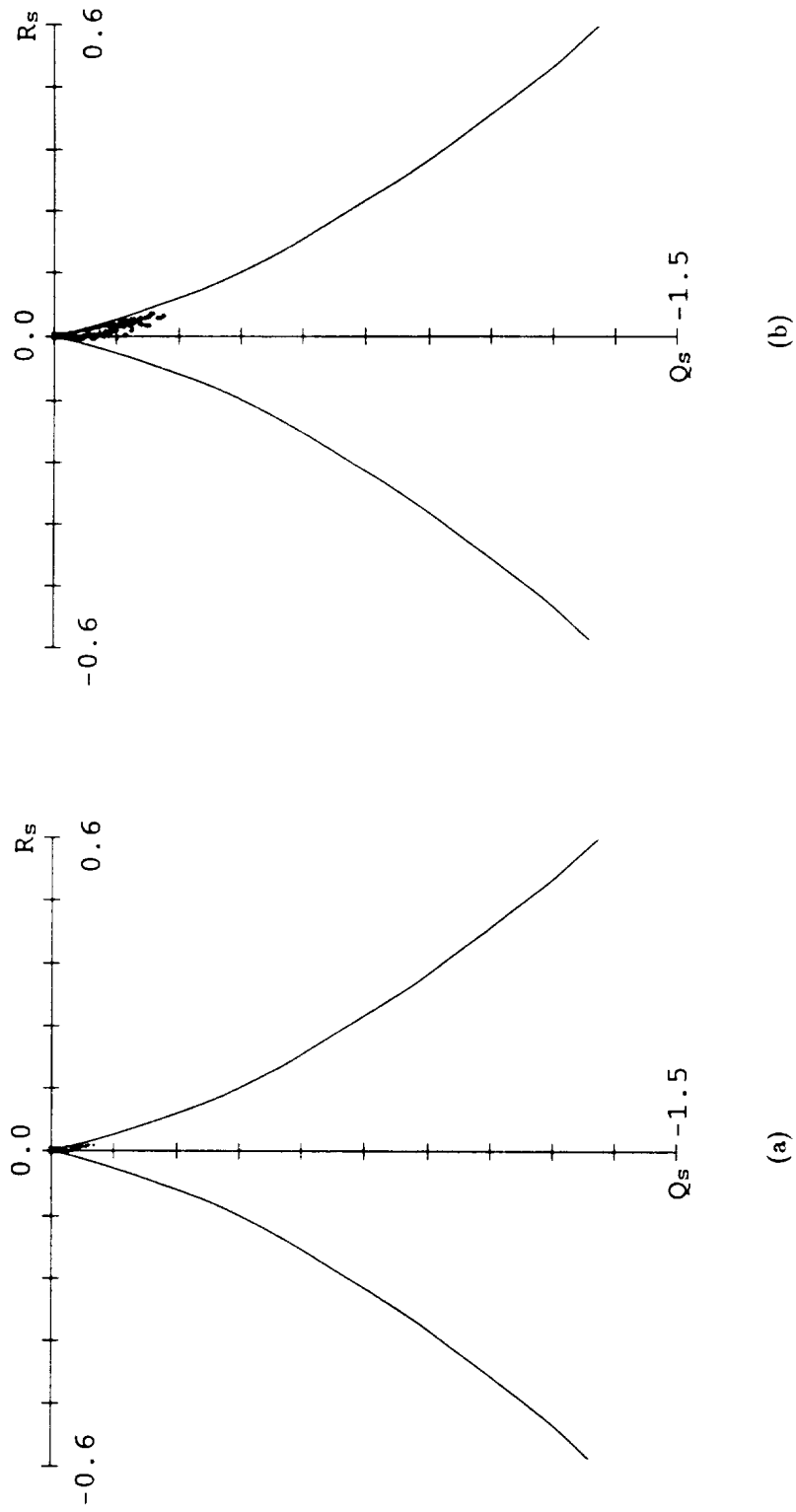


Figure E.6: See caption page 237.



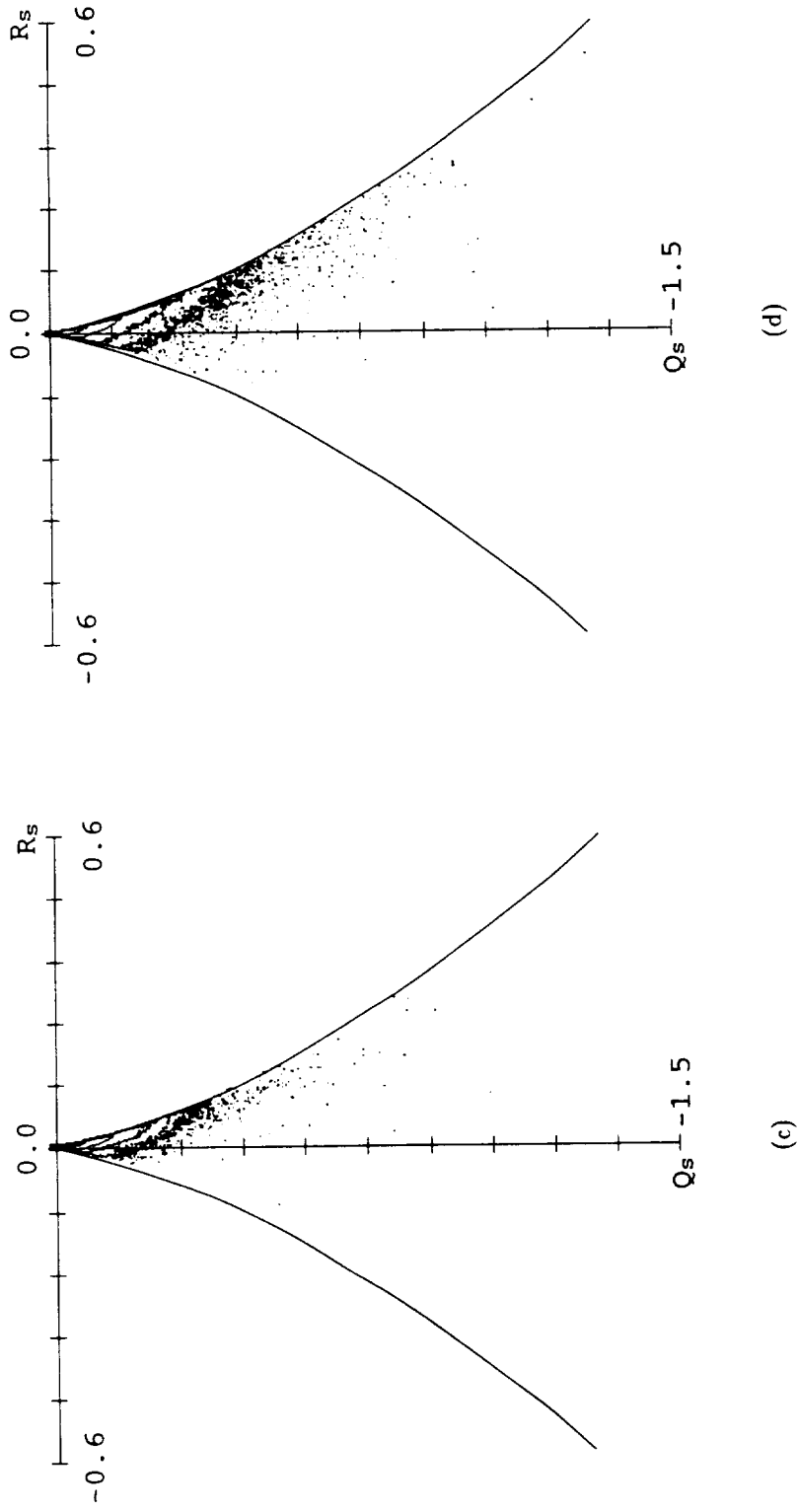


Figure E.6: Contour plots of joint pdf of  $Q_s$  vs.  $R_s$  for  $(?) (60)_{0xx}^{x0x}$  wakes (two-dimensional fundamental plus three-dimensional subharmonic with various Reynolds numbers). (a)  $Re_b = 346$ ,  $t = 204.8$ . (b)  $Re_b = 692$ ,  $t = 201.9$ . (c)  $Re_b = 1384$ ,  $t = 199.3$ . (d)  $Re_b = 2768$ ,  $t = 194.6$ .

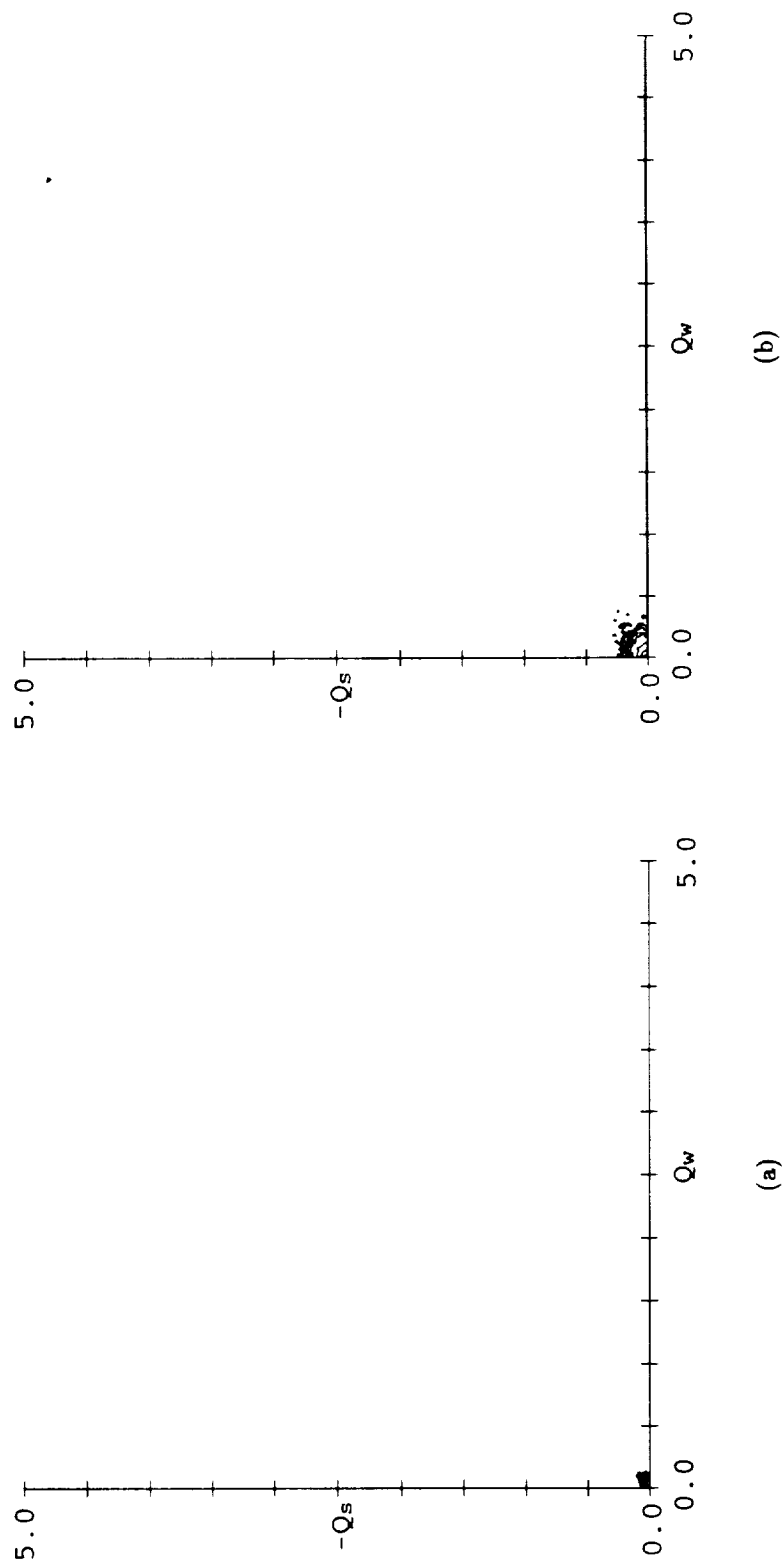


Figure E.7: See caption page 239.

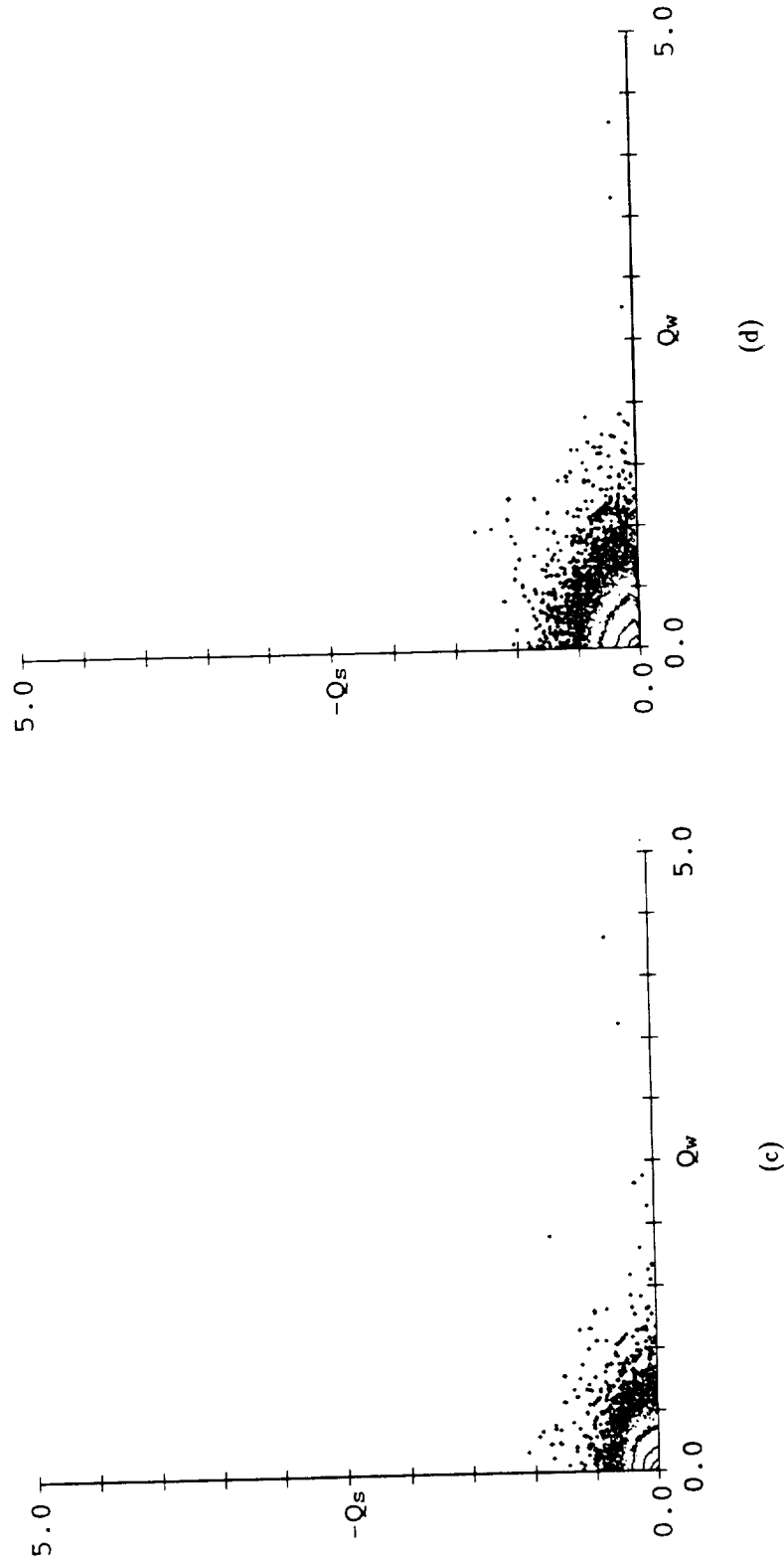


Figure E.7: Contour plots of joint pdf of  $-Q_s$  vs.  $Q_w$  for  $\langle ? \rangle (60)_{0xx}^{x0x}$  wakes (two-dimensional fundamental plus three-dimensional subharmonic with various Reynolds numbers). (a)  $Re_b = 346$ ,  $t = 204.8$ . (b)  $Re_b = 692$ ,  $t = 201.9$ . (c)  $Re_b = 1384$ ,  $t = 199.3$ . (d)  $Re_b = 2768$ ,  $t = 194.6$ .

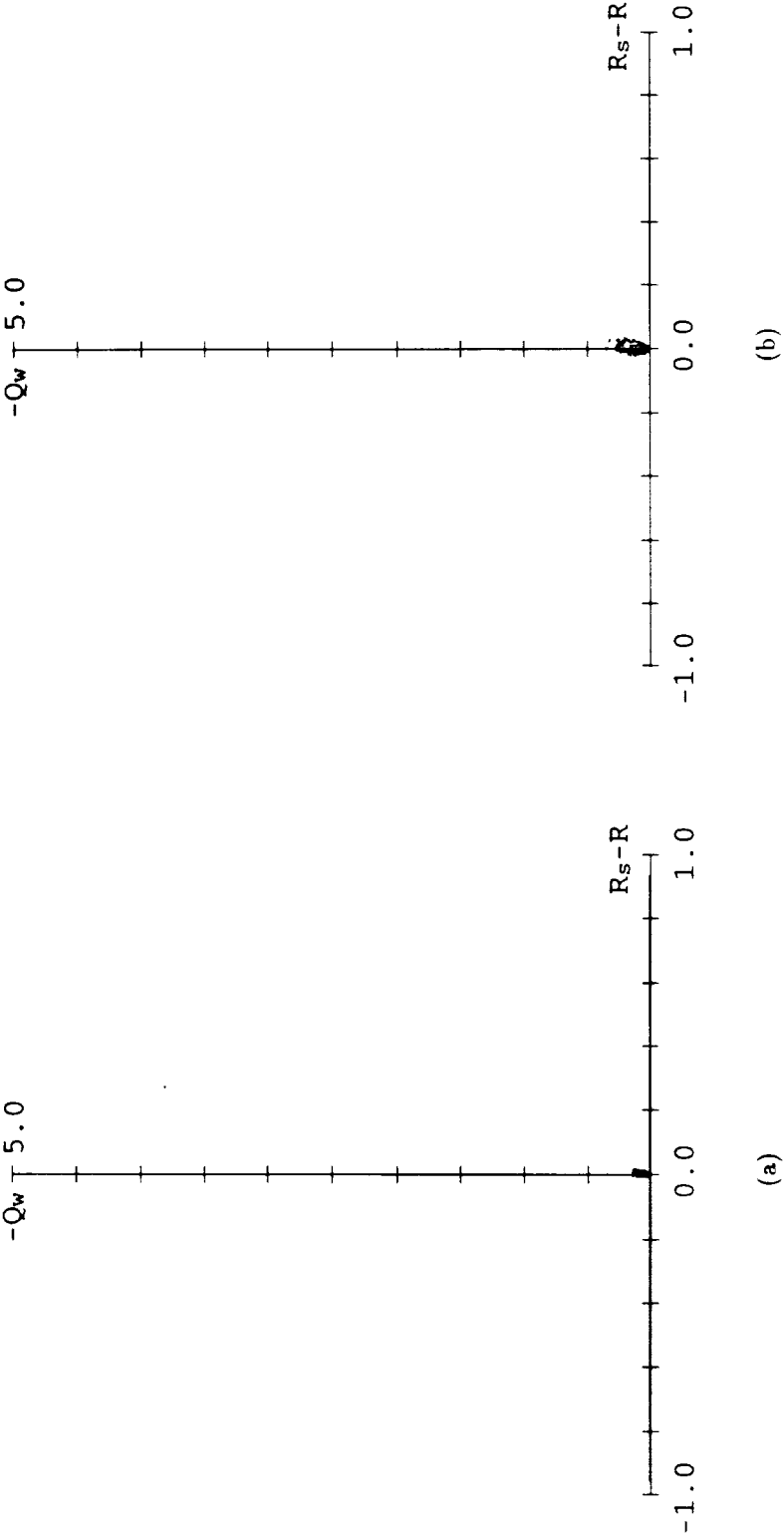


Figure E.8: See caption page 241.

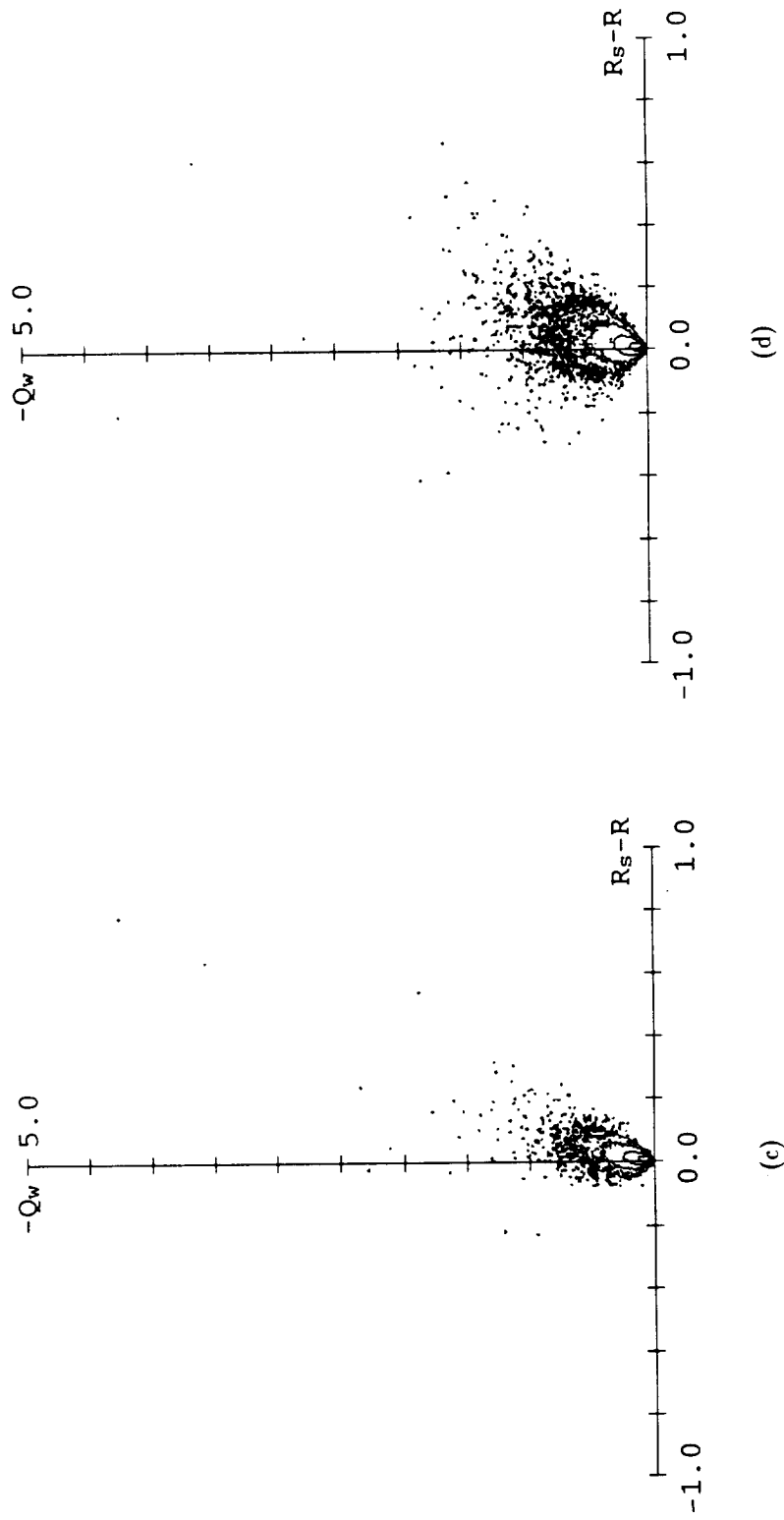


Figure E.8: Contour plots of joint pdf of  $Q_w$  vs.  $R_s - R$  for  $(60)_{0xx}^{x0x}$  wakes (two-dimensional fundamental plus three-dimensional subharmonic with various Reynolds numbers). (a)  $Re_b = 346$ ,  $t = 204.8$ . (b)  $Re_b = 692$ ,  $t = 201.9$ . (c)  $Re_b = 1384$ ,  $t = 199.3$ . (d)  $Re_b = 2768$ ,  $t = 194.6$ .

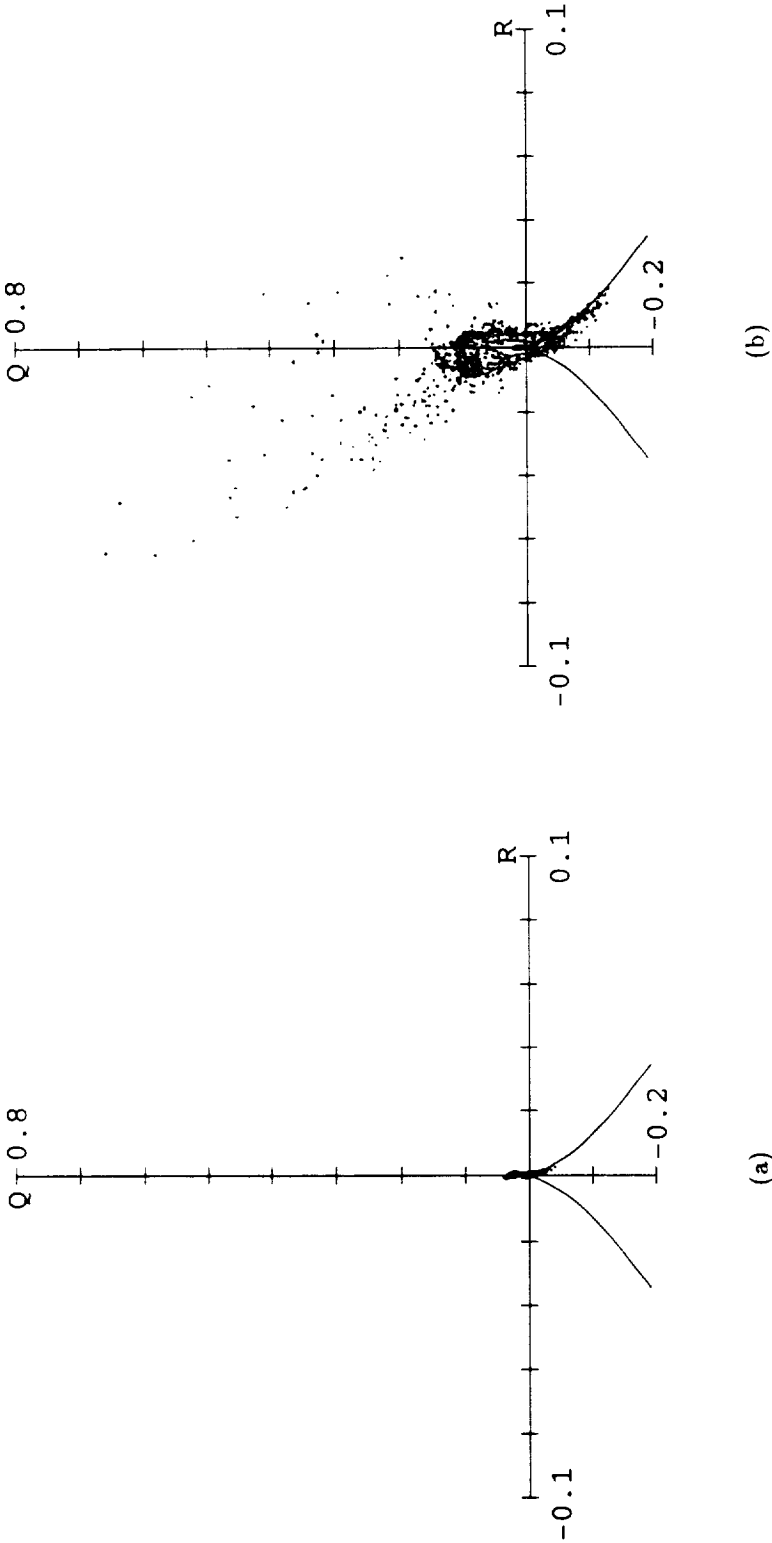


Figure E.9: See caption page 243.

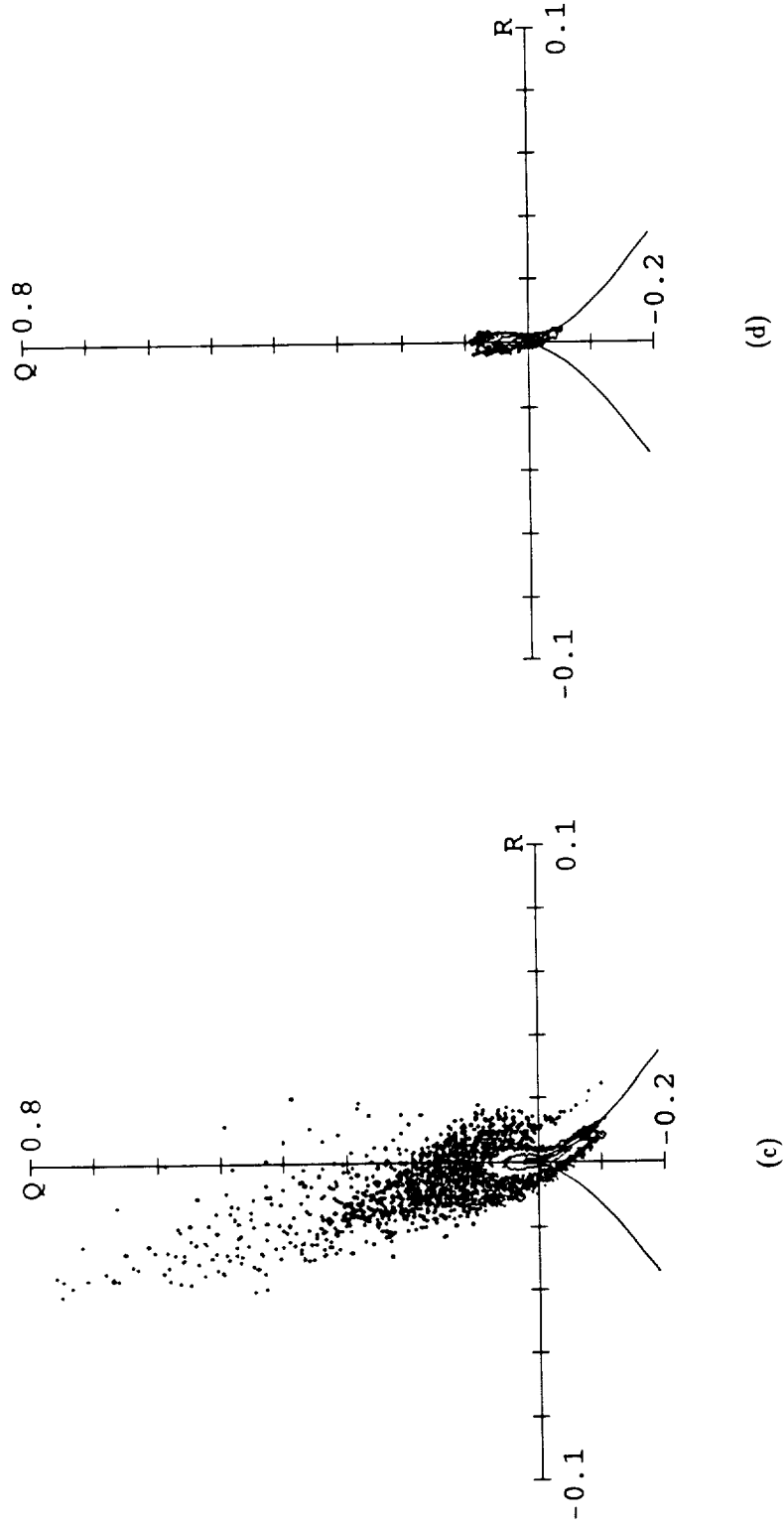


Figure E.9: Time evolution of contour plots of joint pdf of  $Q$  vs.  $R$  for  $346(60)_{0rx}^{x0x}$  wake (two-dimensional fundamental plus three-dimensional subharmonic). (a)  $t = 22.8$ . (b)  $t = 52.8$ . (c)  $t = 102.7$ . (d)  $t = 204.8$ .

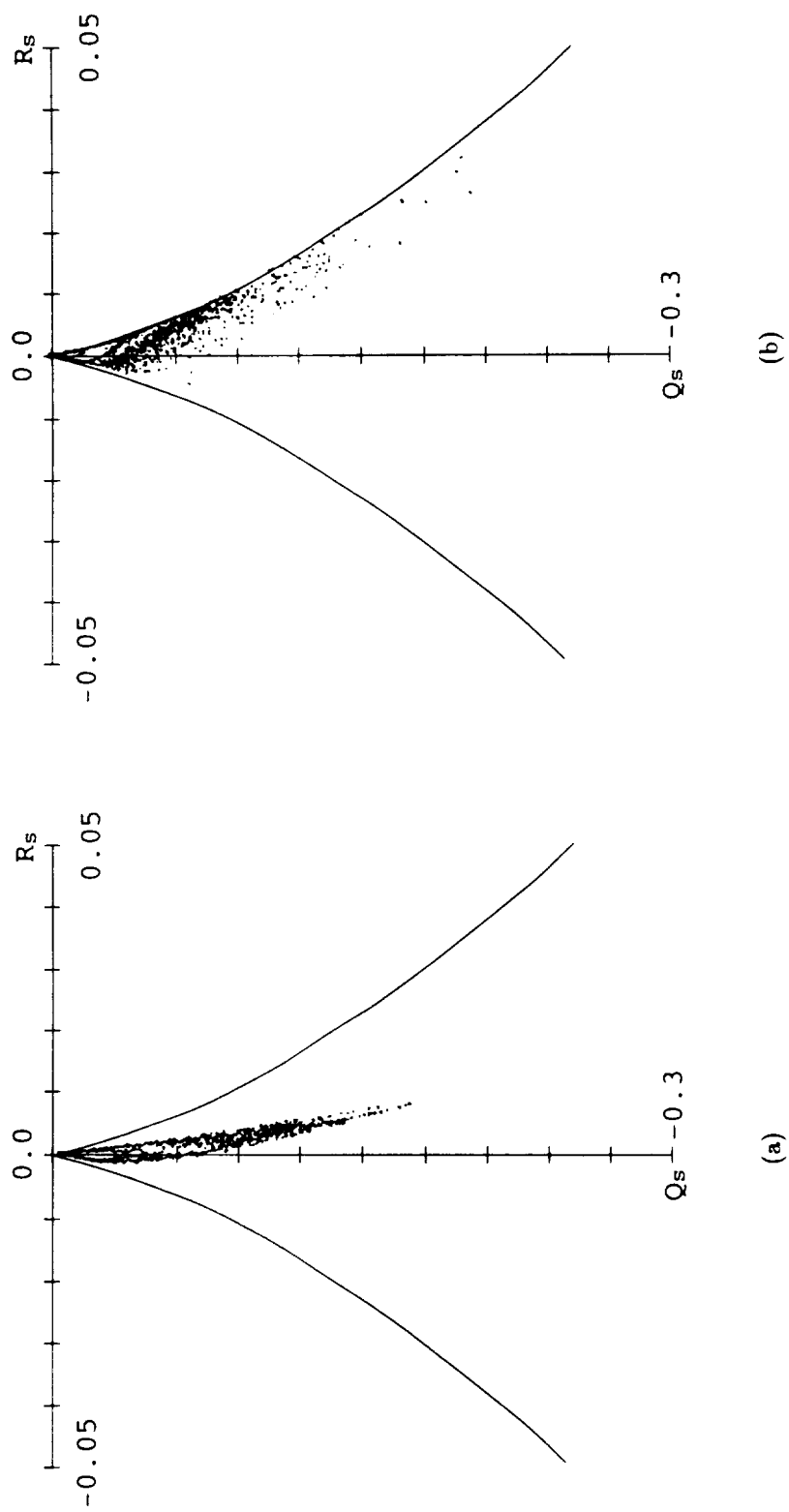


Figure E.10: See caption page 245.



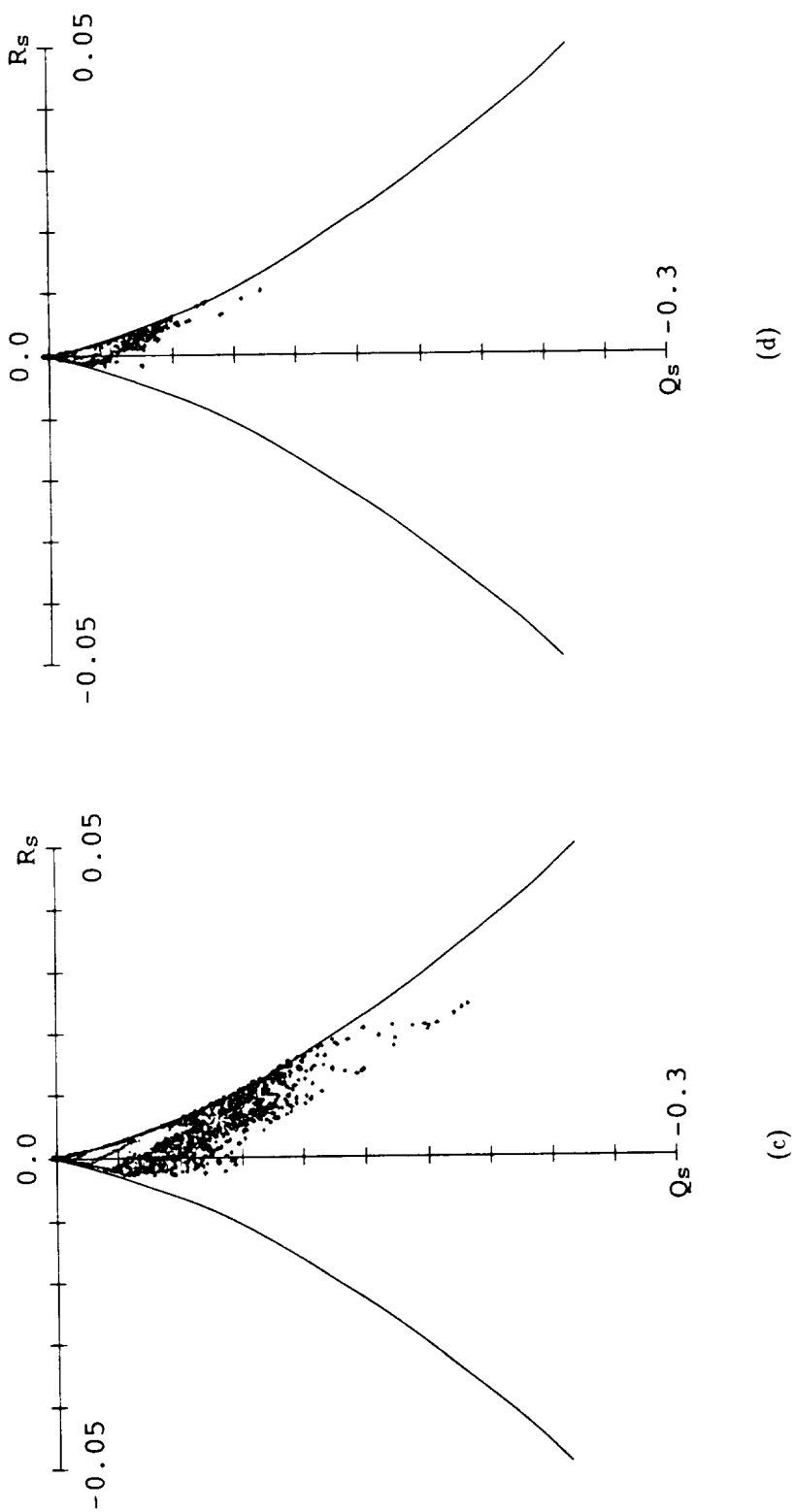


Figure E.10: Time evolution of contour plots of joint pdf of  $Q_s$  vs.  $R_s$  for  $346(60)^{x_{0z}}_{0xz}$  wake (two-dimensional fundamental plus three-dimensional subharmonic). (a)  $t = 22.8$ . (b)  $t = 52.8$ . (c)  $t = 102.7$ . (d)  $t = 204.8$ .

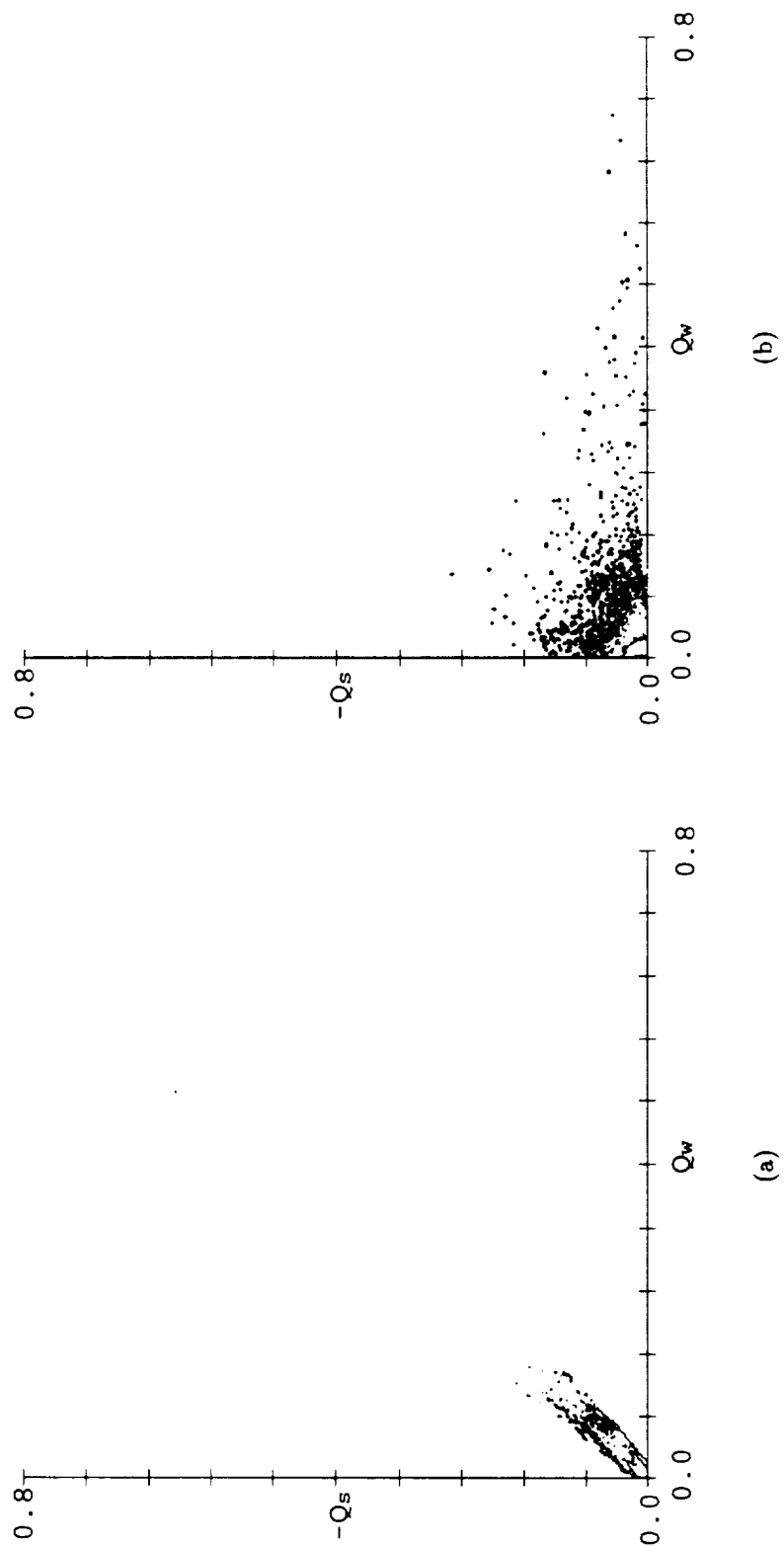


Figure E.11: See caption page 247.

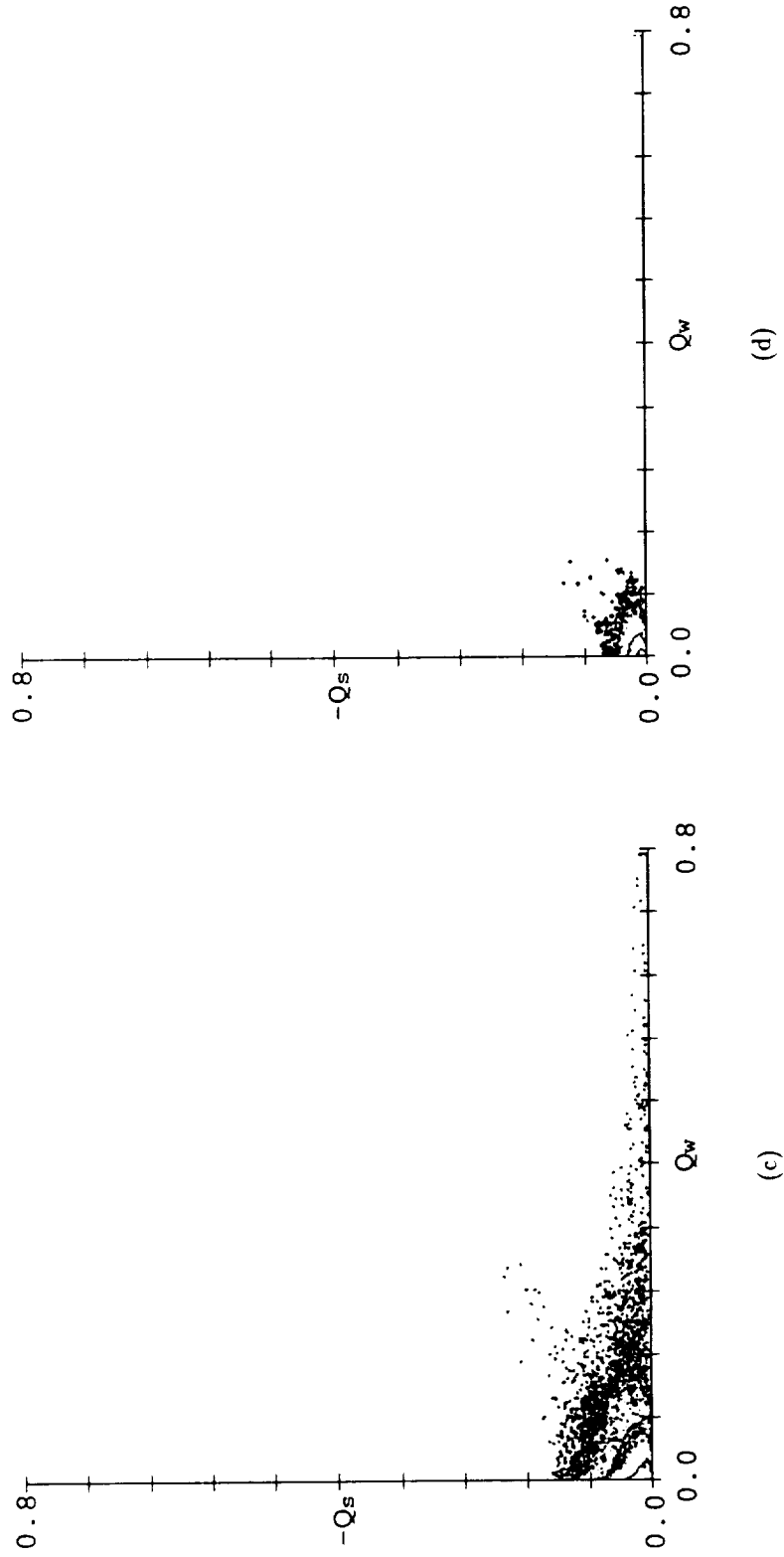


Figure E.11: Time evolution of contour plots of joint pdf of  $-Q_s$  vs.  $Q_w$  for 346(60) $_{0xz}^{x0x}$  wake (two-dimensional fundamental plus three-dimensional subharmonic). (a)  $t = 22.8$ . (b)  $t = 52.8$ . (c)  $t = 102.7$ . (d)  $t = 204.8$ .

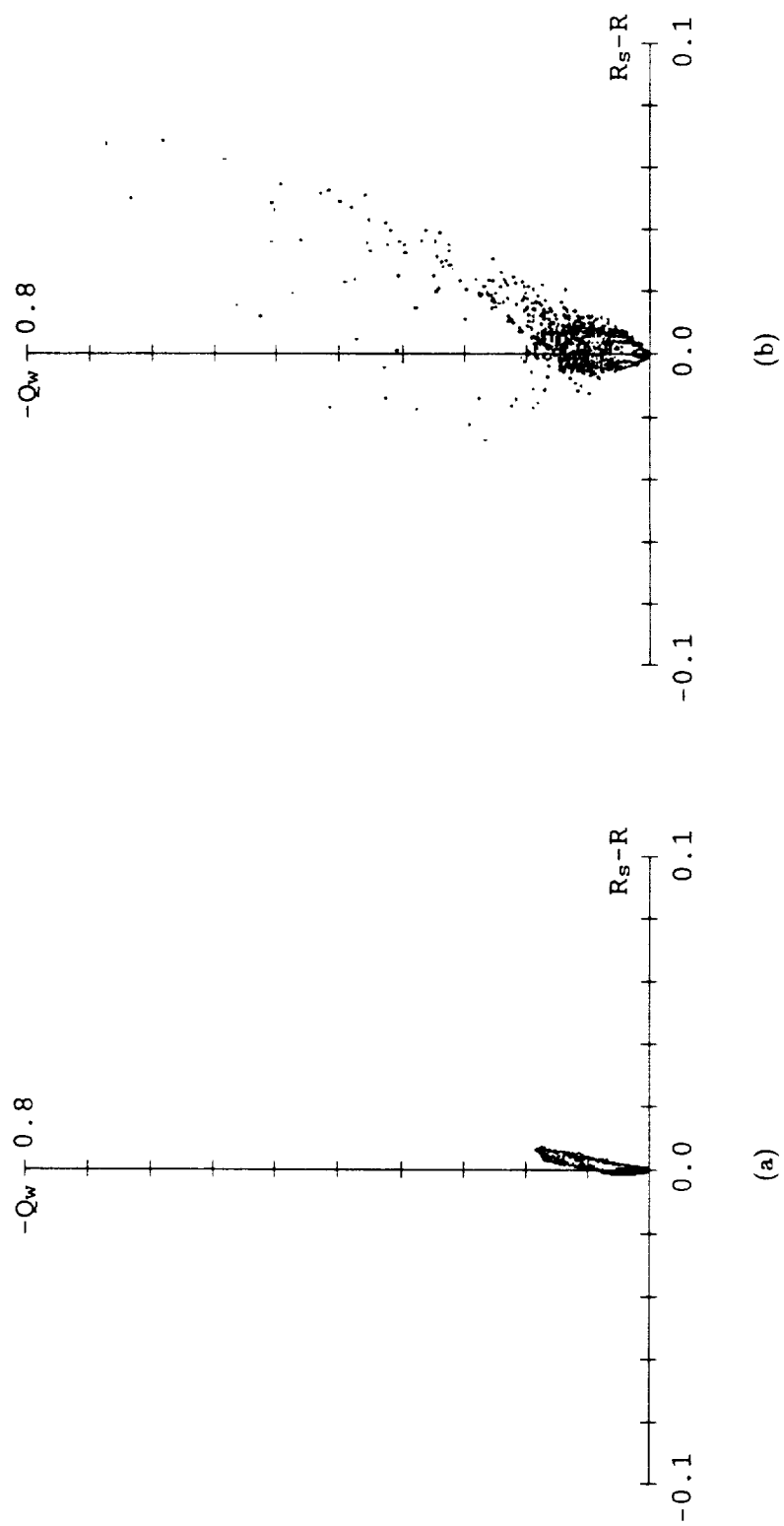


Figure E.12: See caption page 249.

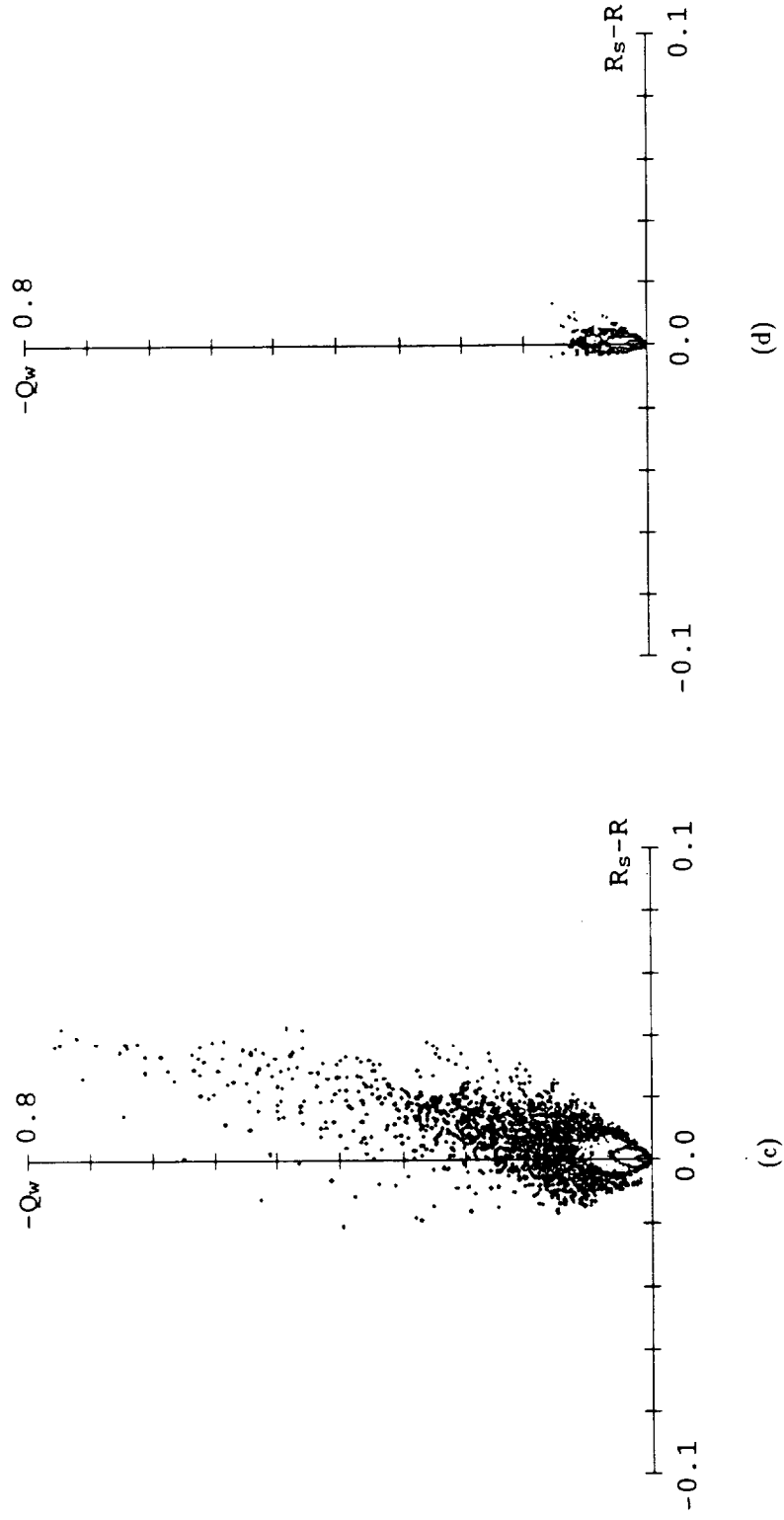


Figure E.12: Time evolution of contour plots of joint pdf of  $Q_w$  vs.  $R_s - R$  for 346(60)<sub>0xz</sub> wake (two-dimensional fundamental plus three-dimensional subharmonic). (a)  $t = 22.8$ . (b)  $t = 52.8$ . (c)  $t = 102.7$ . (d)  $t = 204.8$ .

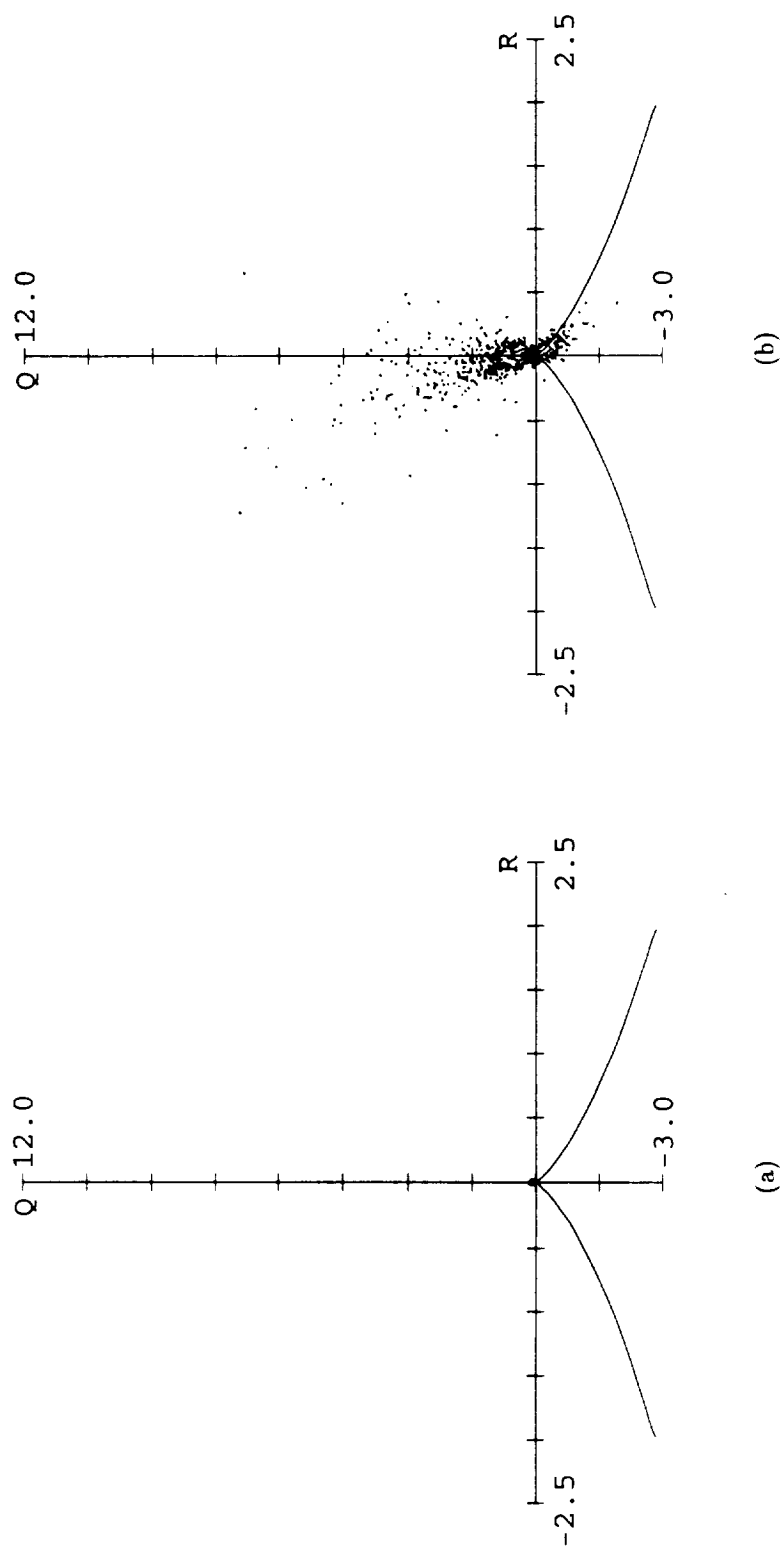


Figure E.13: See caption page 251.

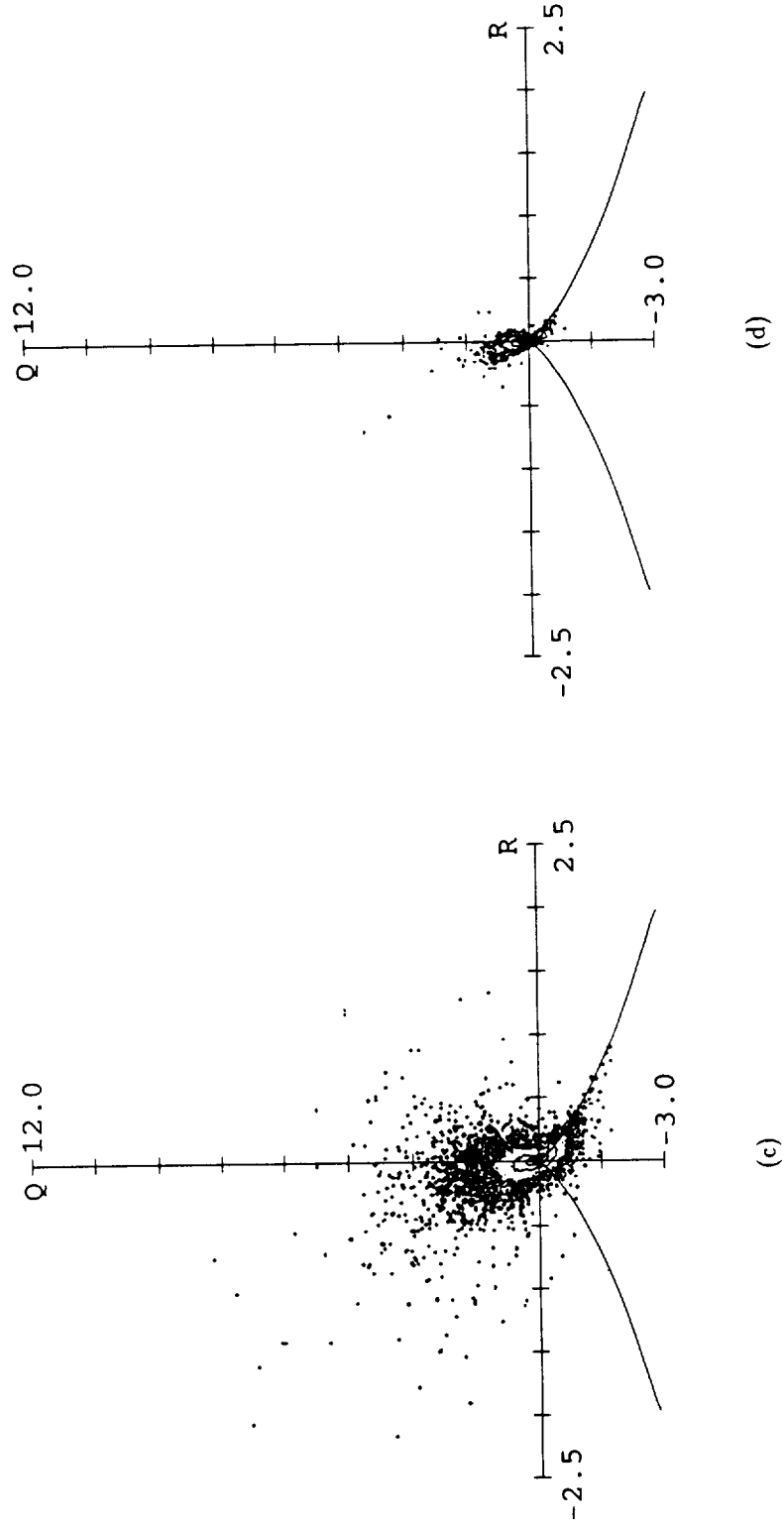


Figure E.13: Time evolution of contour plots of joint pdf of  $Q$  vs.  $R$  for  $1384(60)_{0xx}^{x0x}$  wake (two-dimensional fundamental plus three-dimensional subharmonic). (a)  $t = 28.4$ . (b)  $t = 51.1$ . (c)  $t = 101.5$ . (d)  $t = 199.3$ .

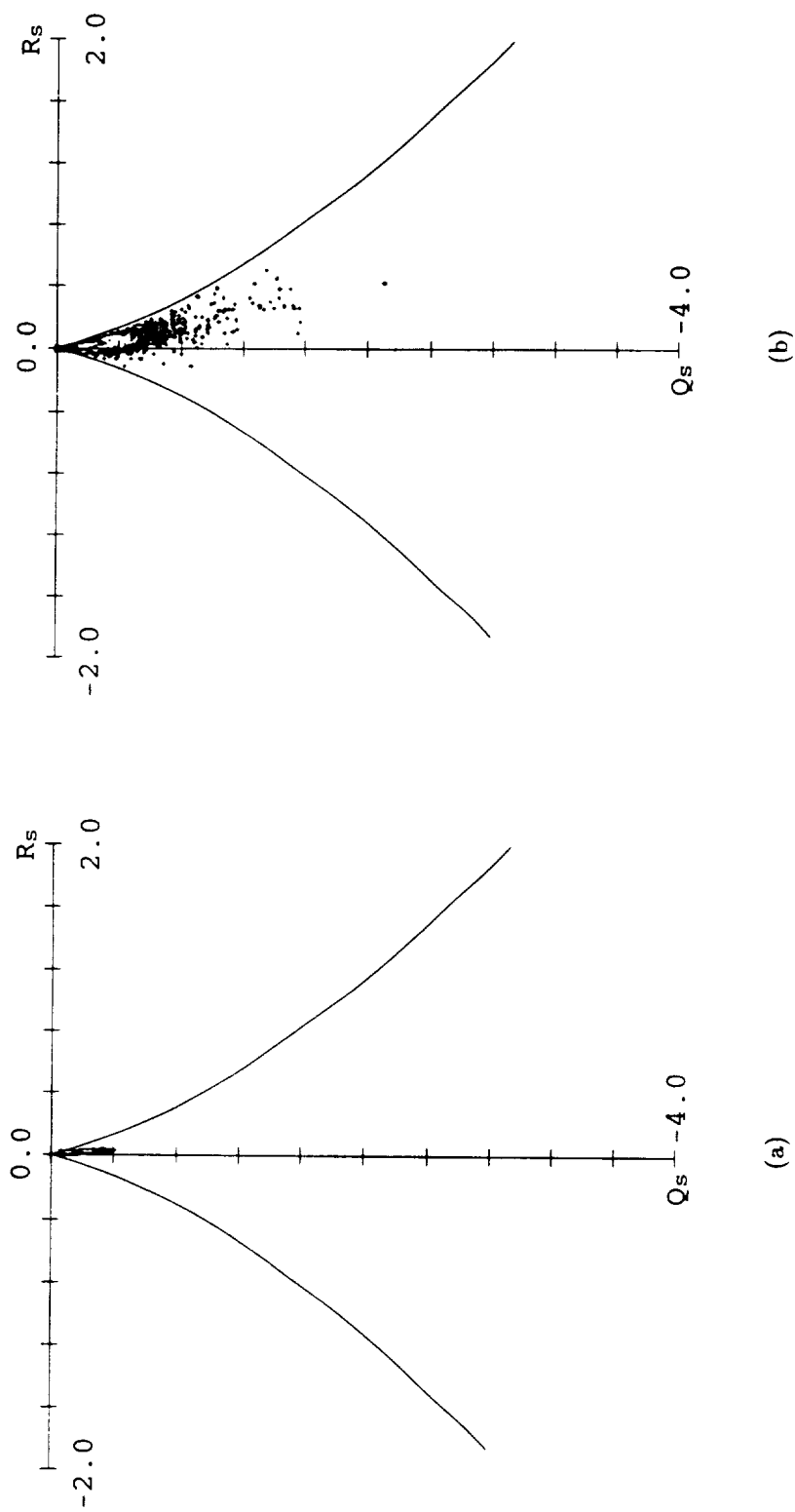


Figure E.14: See caption page 253.



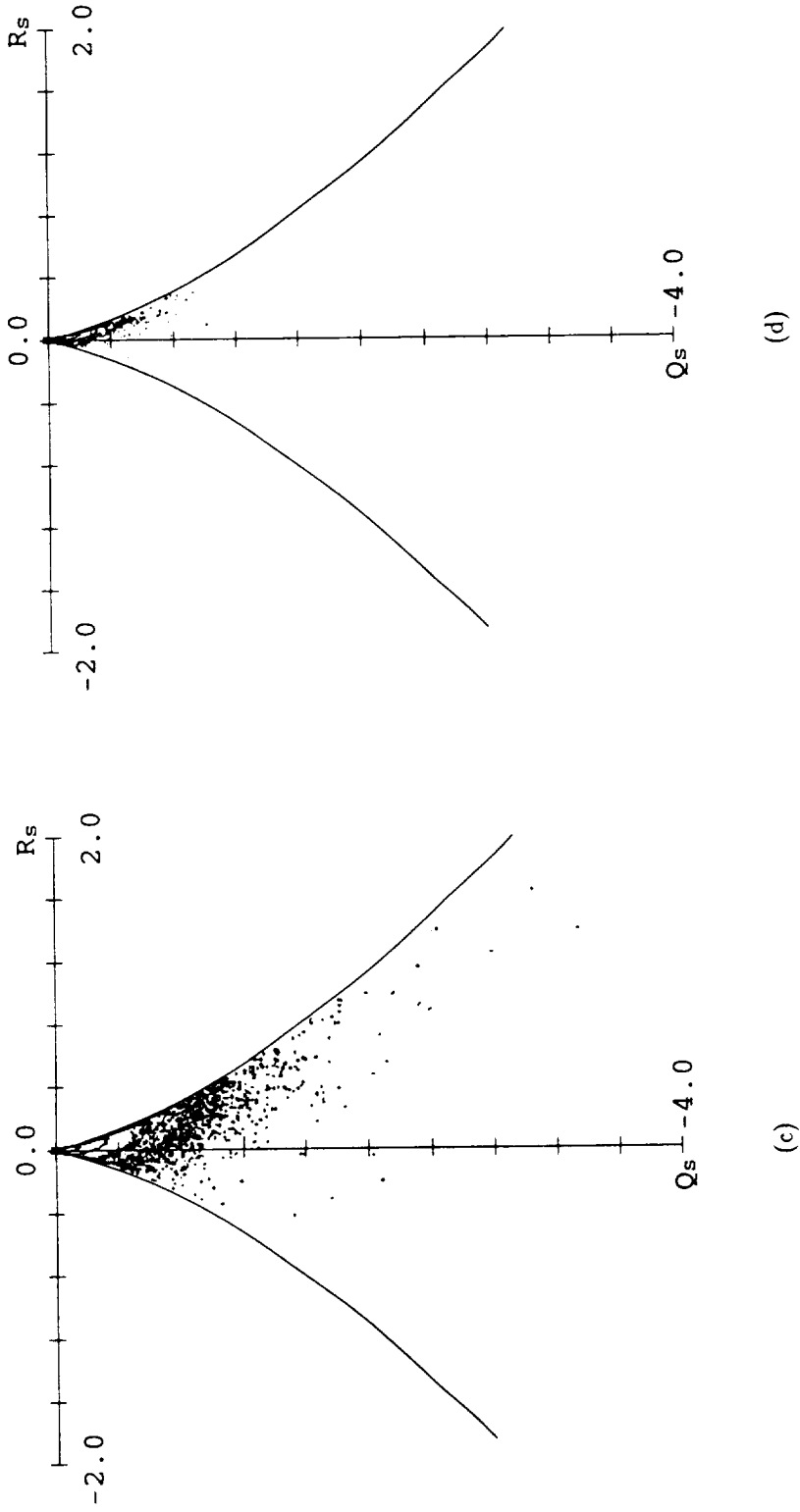


Figure E.14: Time evolution of contour plots of joint pdf of  $Q_s$  vs.  $R_s$  for 1384(60) $_{0xz}$  wake (two-dimensional fundamental plus three-dimensional subharmonic). (a)  $t = 28.4$ . (b)  $t = 51.1$ . (c)  $t = 101.5$ . (d)  $t = 199.3$ .

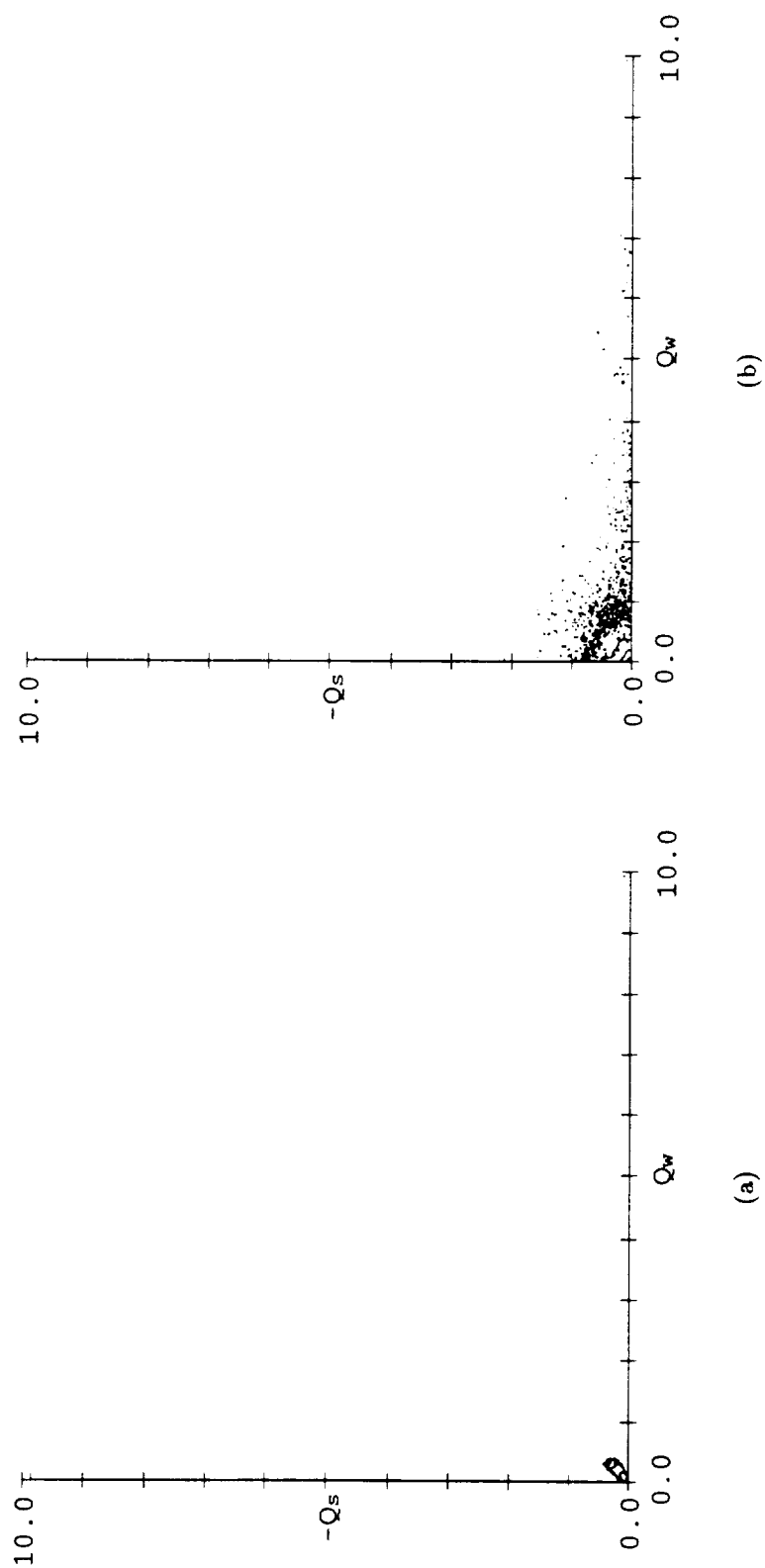


Figure E.15: See caption page 255.

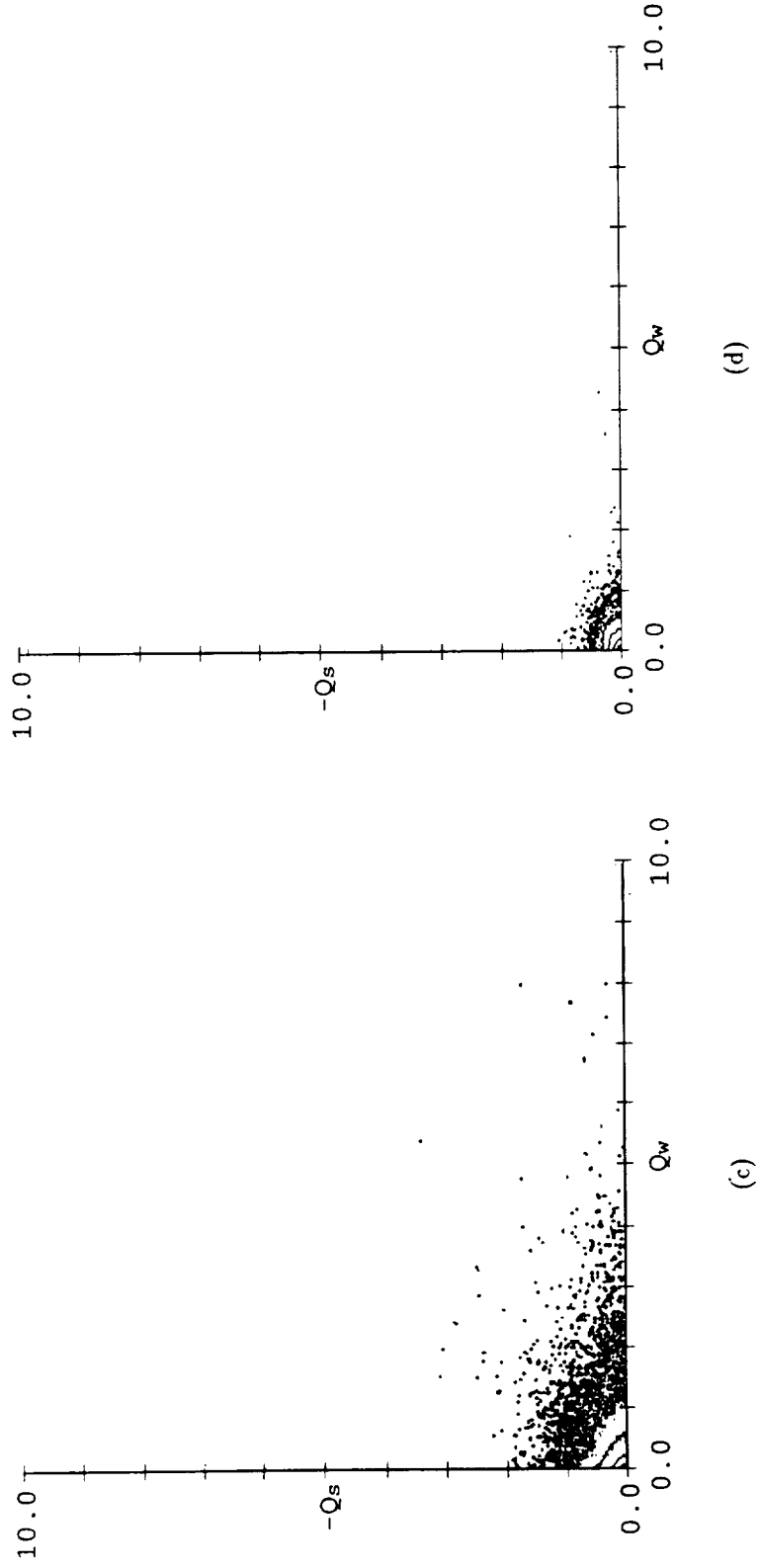


Figure E.15: Time evolution of contour plots of joint pdf of  $-Q_s$  vs.  $Q_w$  for 1384(60) $^{x0x}$  wake (two-dimensional fundamental plus three-dimensional subharmonic). (a)  $t = 28.4$ . (b)  $t = 51.1$ . (c)  $t = 101.5$ . (d)  $t = 199.3$ .

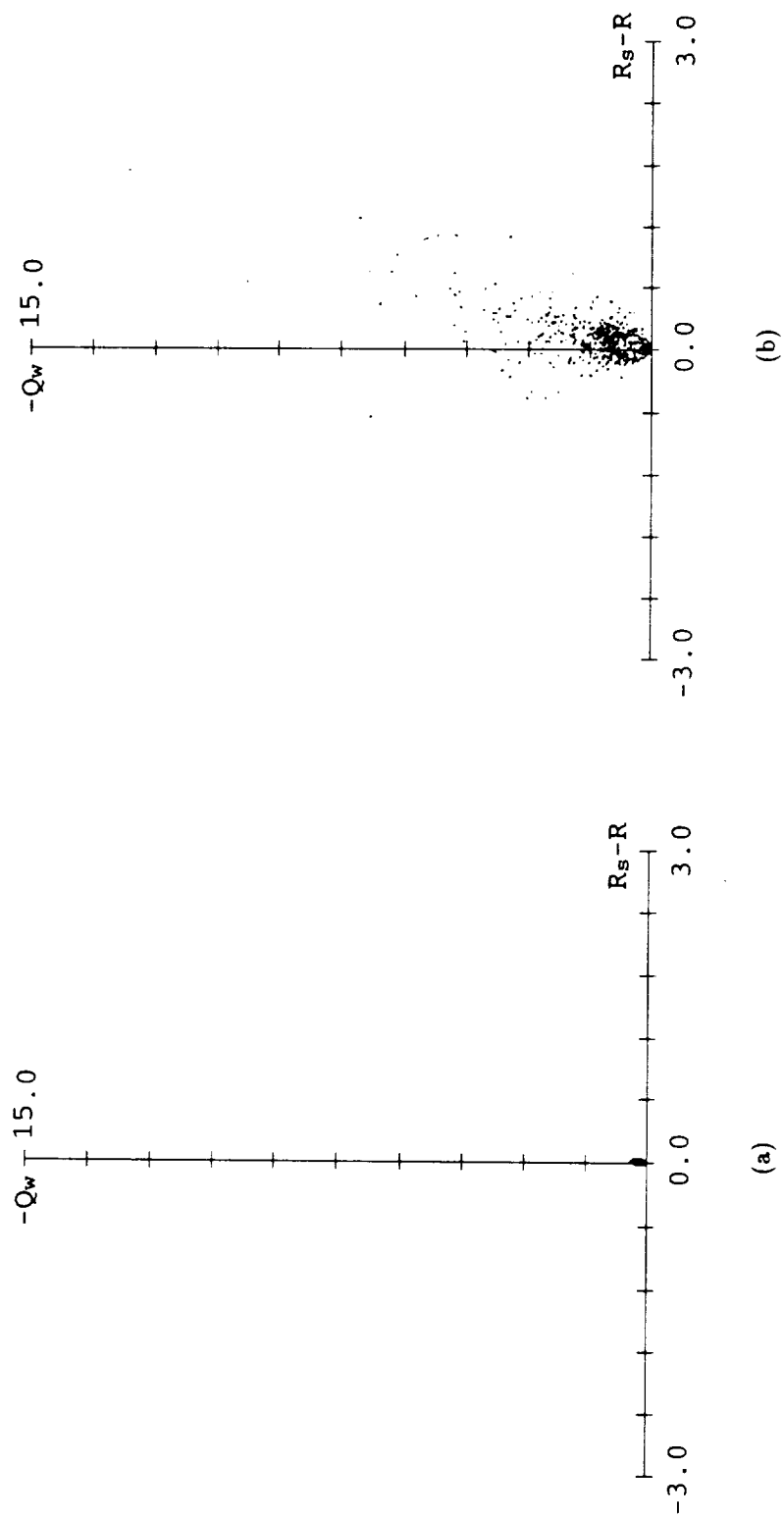


Figure E.16: See caption page 257.

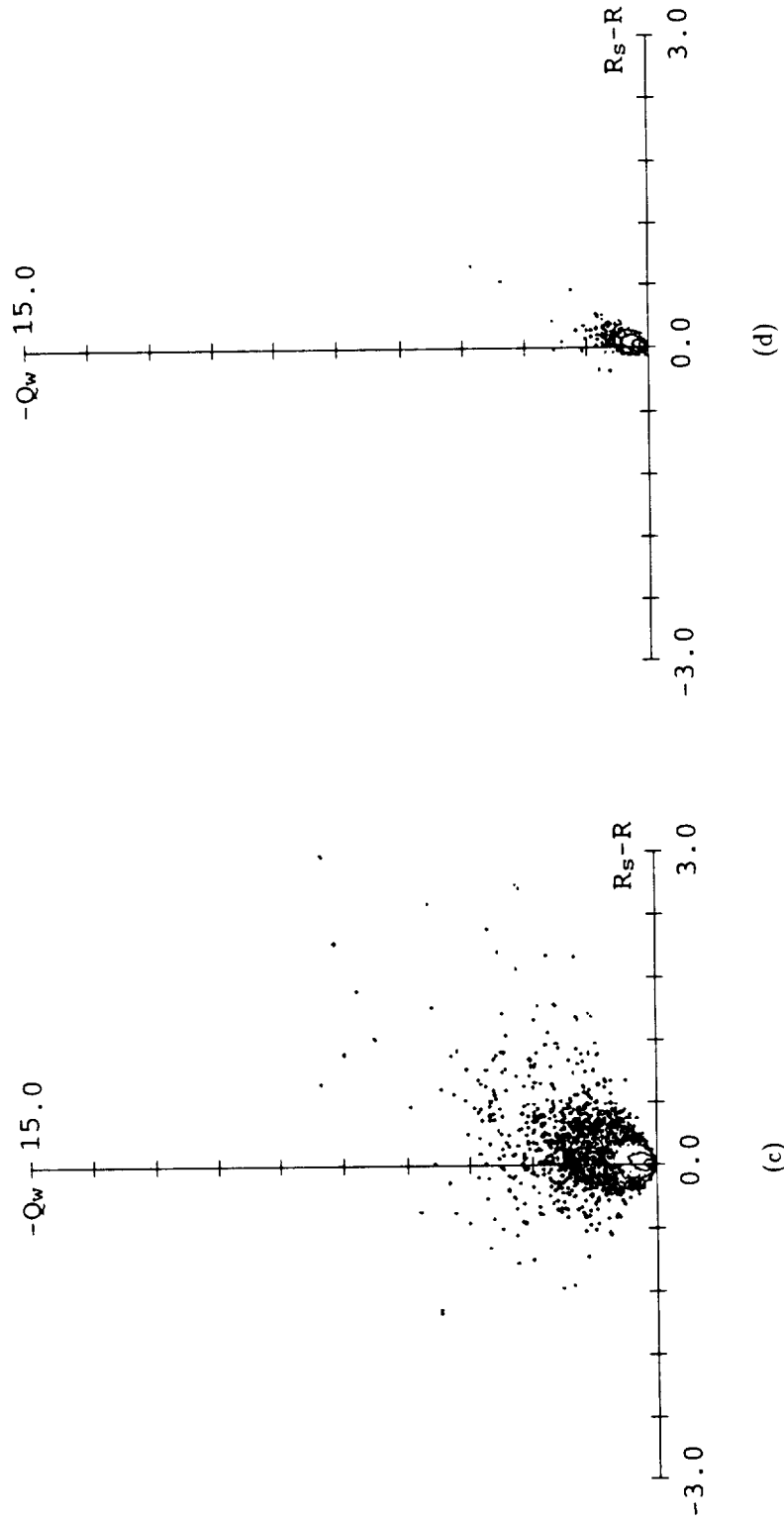


Figure E.16: Time evolution of contour plots of joint pdf of  $Q_w$  vs.  $R_s - R$  for  $1384(60)_{\text{Hz}}^{\text{wz}}$  wake (two-dimensional fundamental plus three-dimensional subharmonic). (a)  $t = 28.4$ . (b)  $t = 51.1$ . (c)  $t = 101.5$ . (d)  $t = 199.3$ .

## Appendix F

### Turbulence Statistics for Selected Datasets

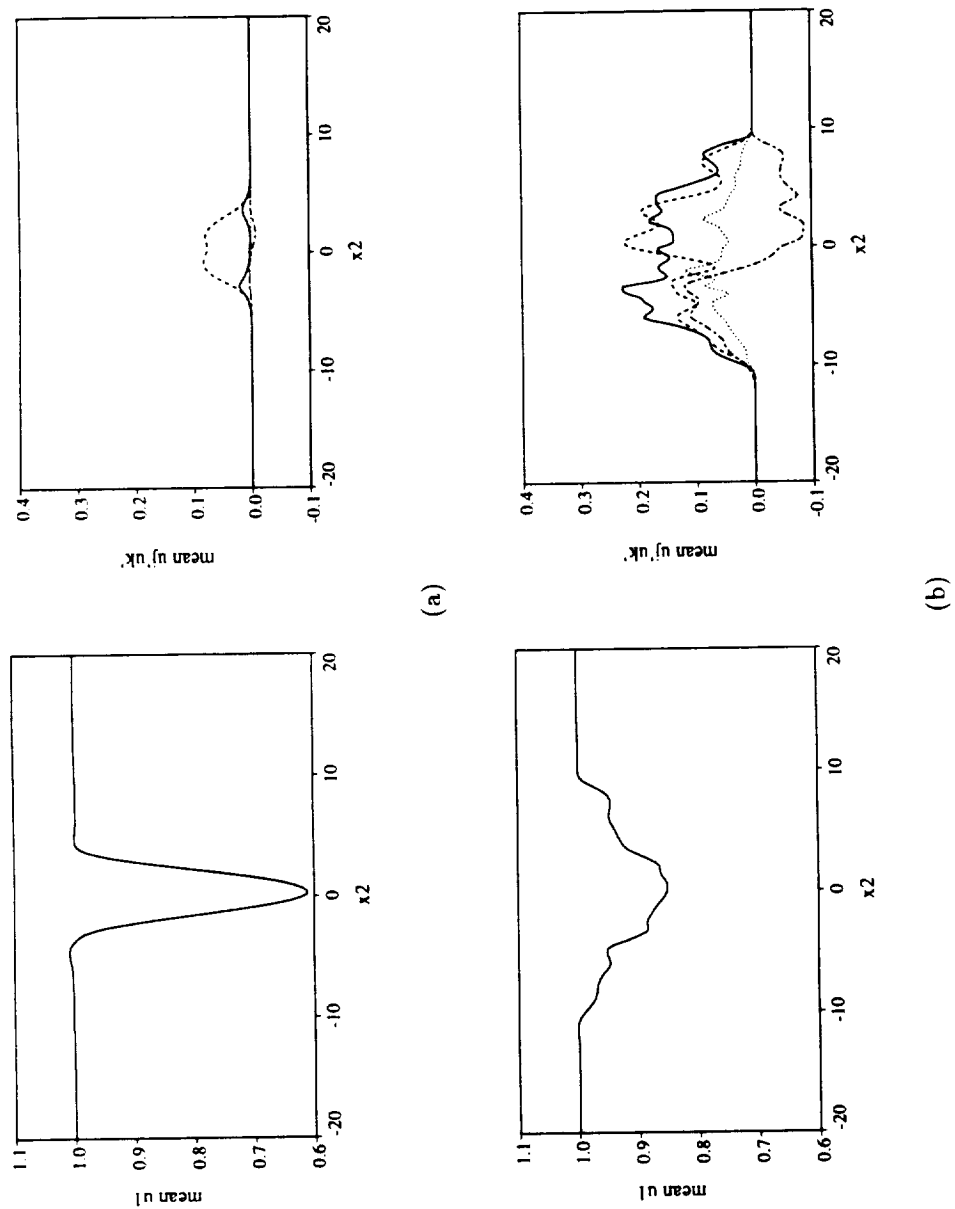
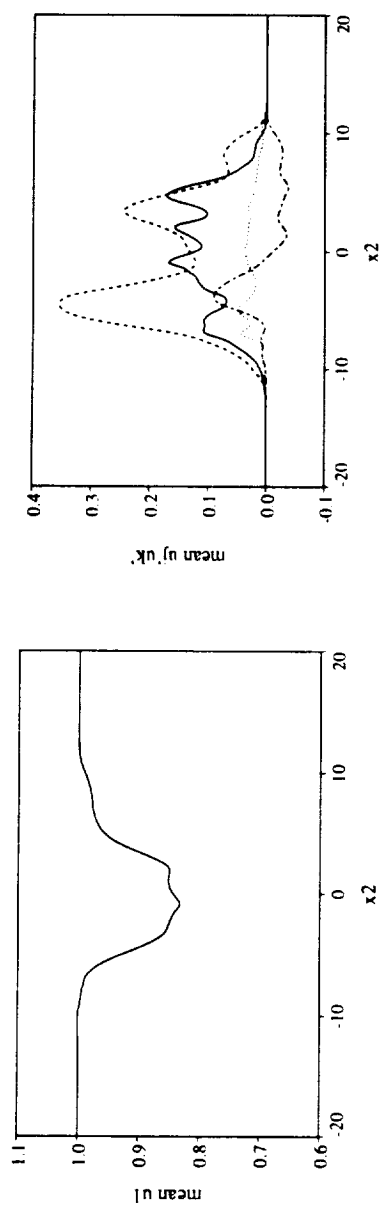
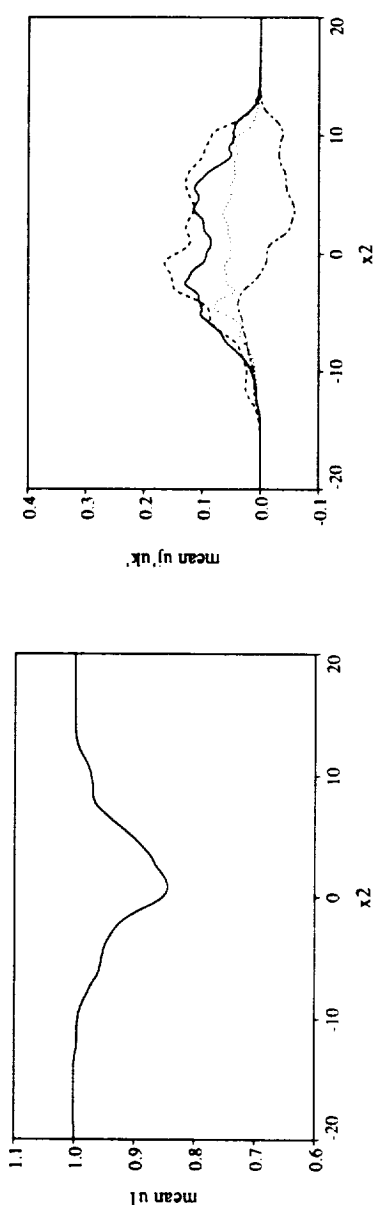


Figure F.1: See caption page 261.



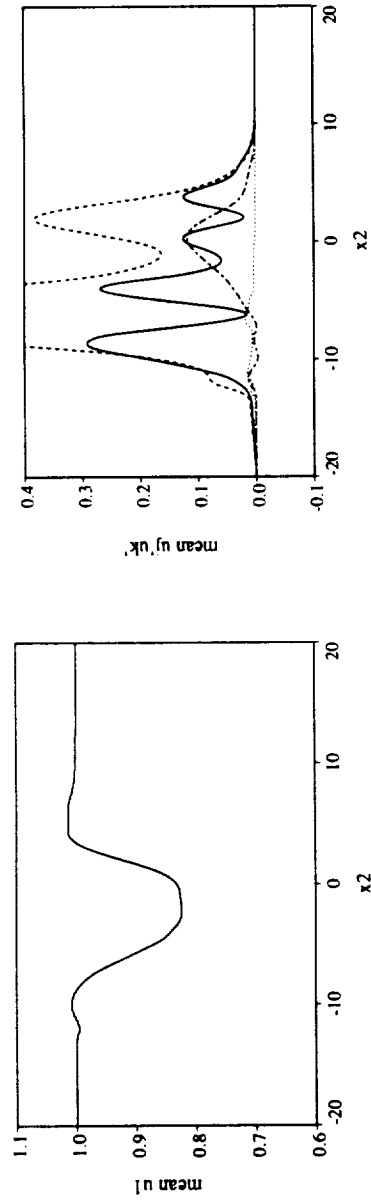
(c)



(d)

Figure F.1: See caption page 261.





(e)

Figure F.1: Mean velocity profiles and second order turbulence profiles for  $Re_b = 346$  wakes with various initial disturbance wavelengths. (a)  $346(60)_{0xx}^{0xx}$ ,  $t = 196.9$ . (b)  $346(60)_{0xx}^{0xx}$ ,  $t = 204.8$ . (c)  $346(60)_{00x}^{x0x}$ ,  $t = 181.1$ . (d)  $346(60)_{000}^{x00}$ ,  $t = 197.0$ . (e)  $346(60)_{00x}^{0xx}$ ,  $t = 202.8$ .

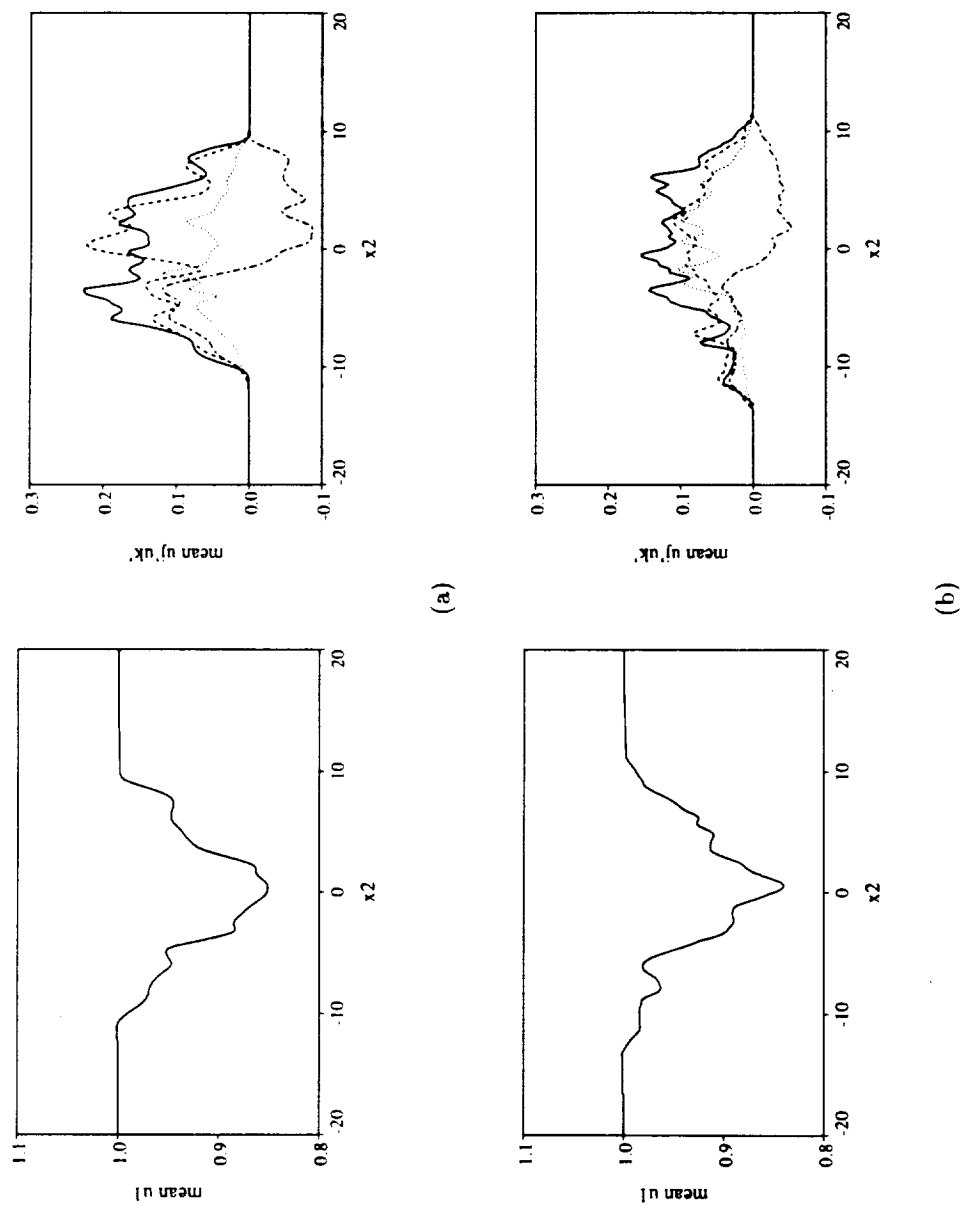
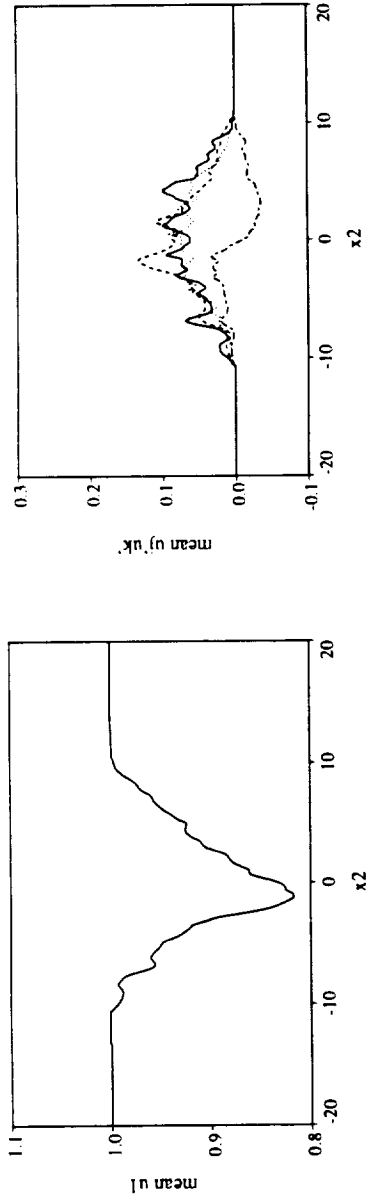
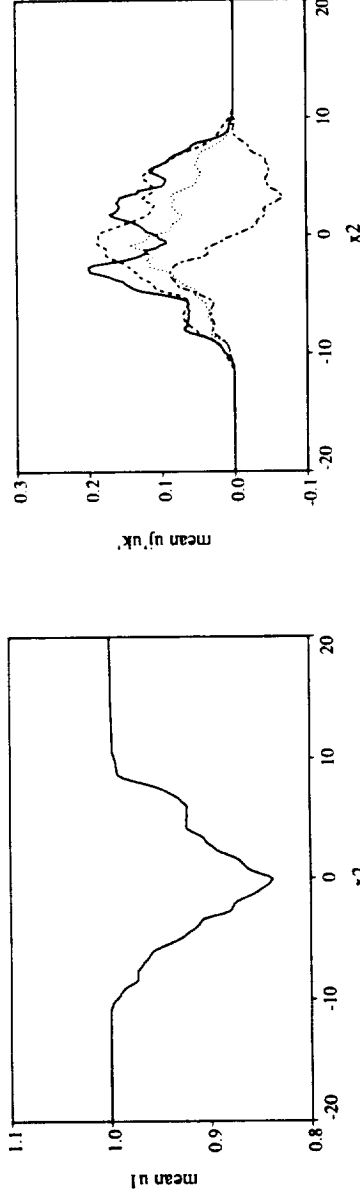


Figure F.2: See caption page 263.



(c)



(d)

Figure F.2: Mean velocity profiles and second order turbulence profiles for  $\langle ? \rangle (60)^{x0x}$  wakes (two-dimensional fundamental plus three-dimensional subharmonic with various Reynolds numbers). (a)  $Re_b = 204.8$ . (b)  $Re_b = 692$ ,  $t = 201.9$ . (c)  $Re_b = 1384$ ,  $t = 199.3$ . (d)  $Re_b = 2768$ ,  $t = 194.6$ .

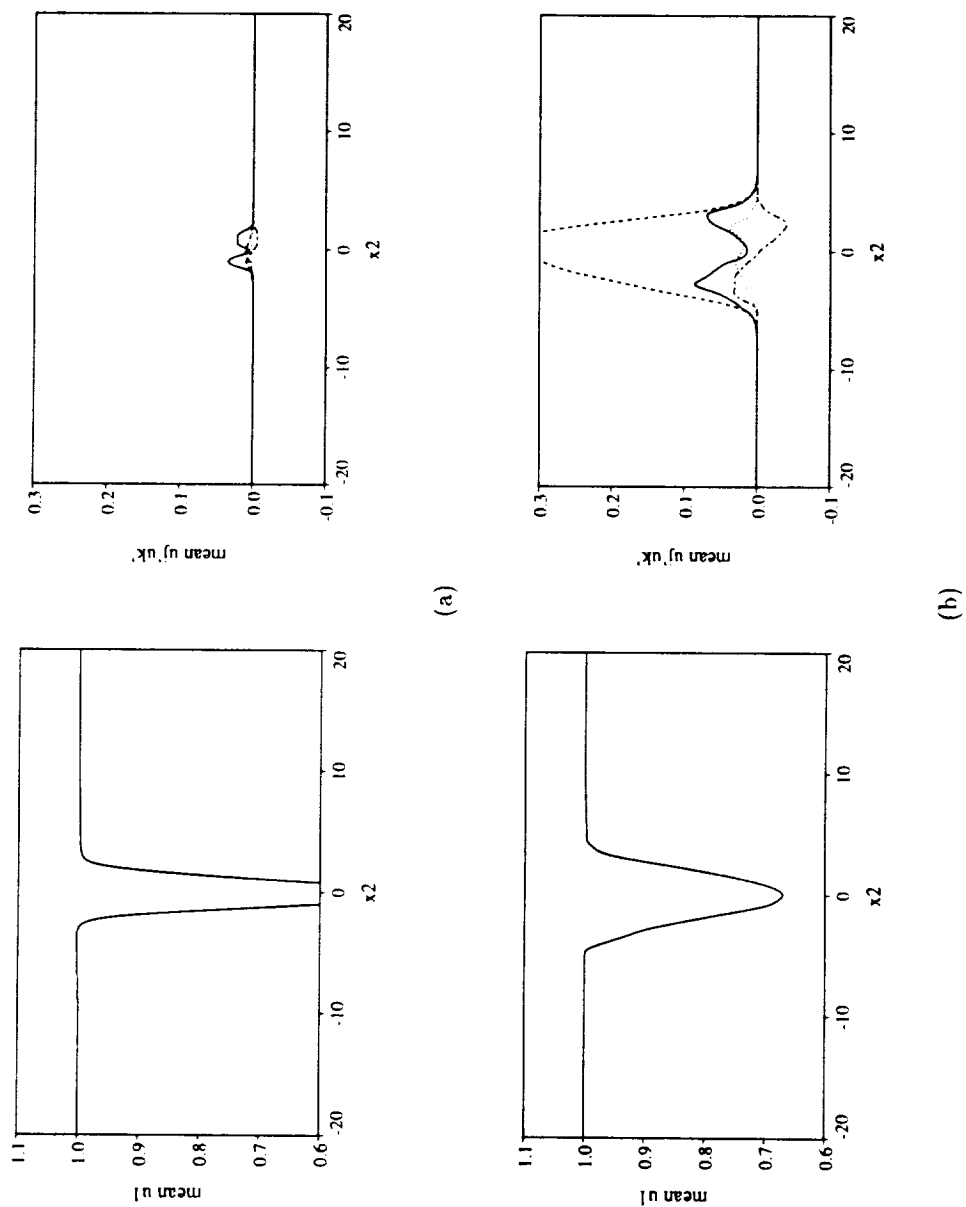
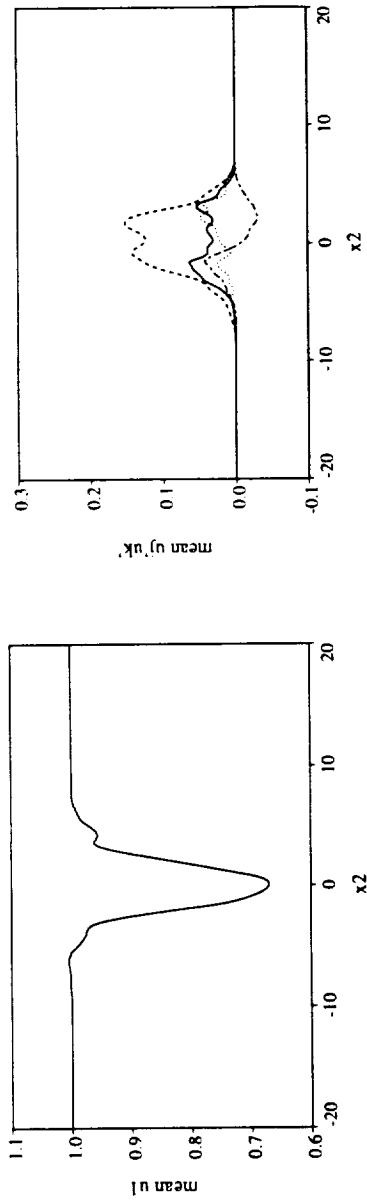
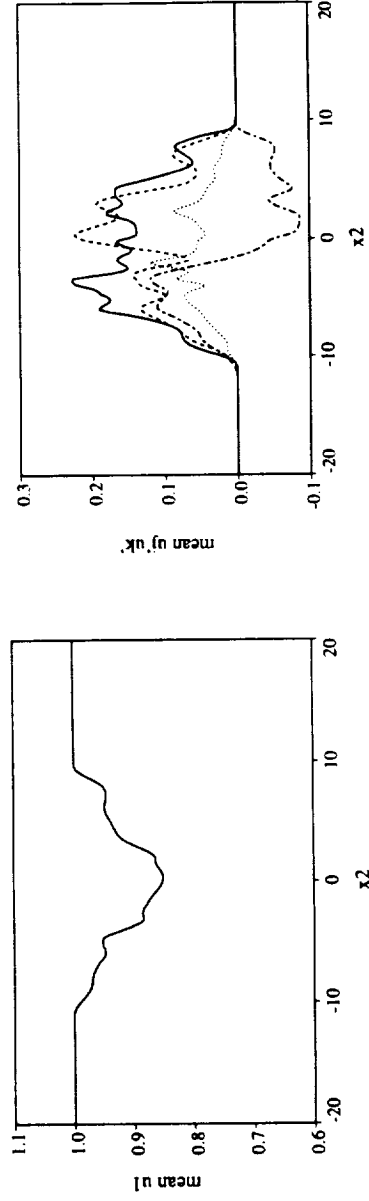


Figure F.3: See caption page 265.



(c)



(d)

Figure F.3: Mean velocity profiles and second order turbulence profiles for 346(60) $_{0xx}^{x0x}$  wake (two-dimensional fundamental plus three-dimensional subharmonic). (a)  $t = 22.8$ . (b)  $t = 52.8$ . (c)  $t = 102.7$ . (d)  $t = 204.8$ .

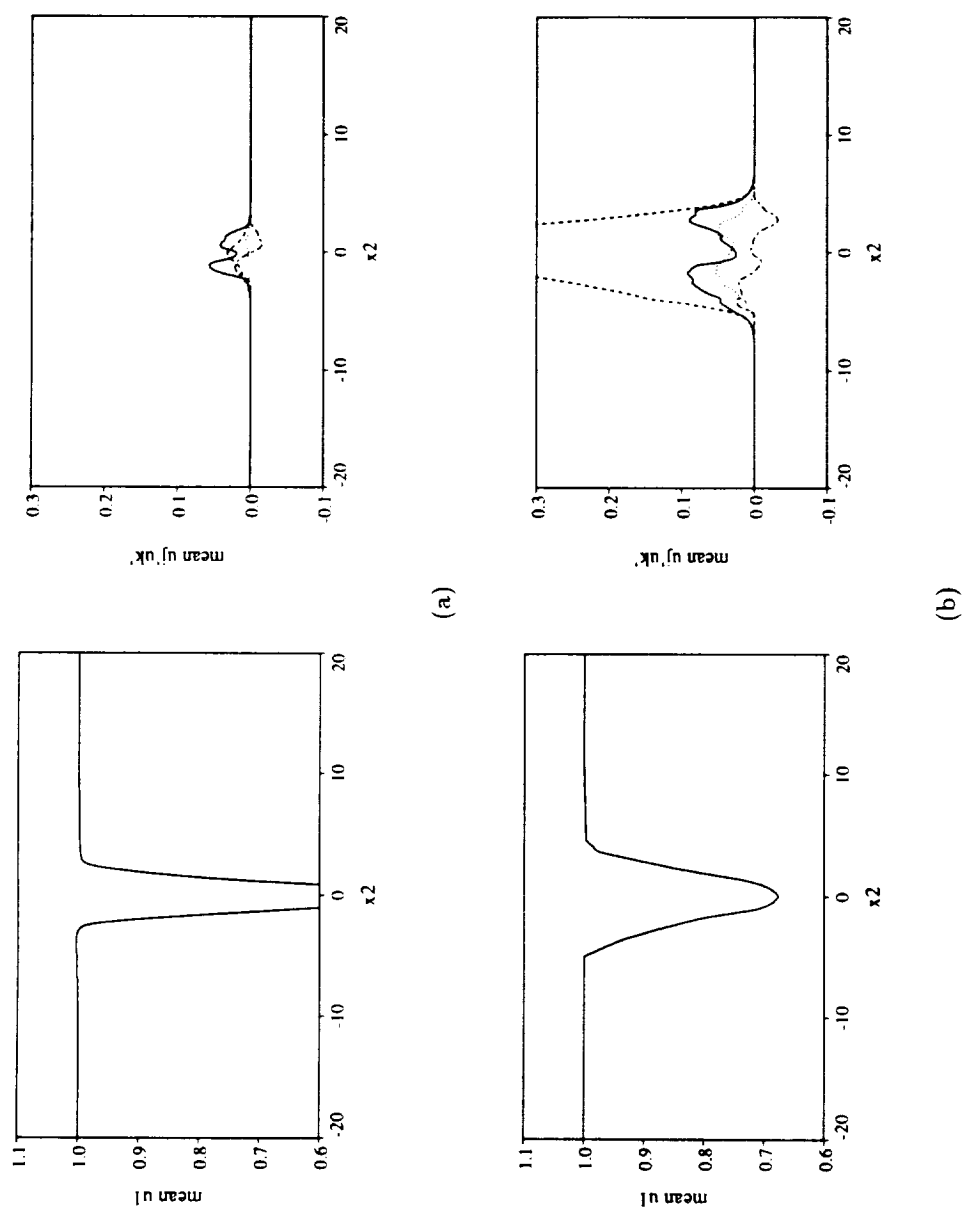


Figure F.4: See caption page 267.

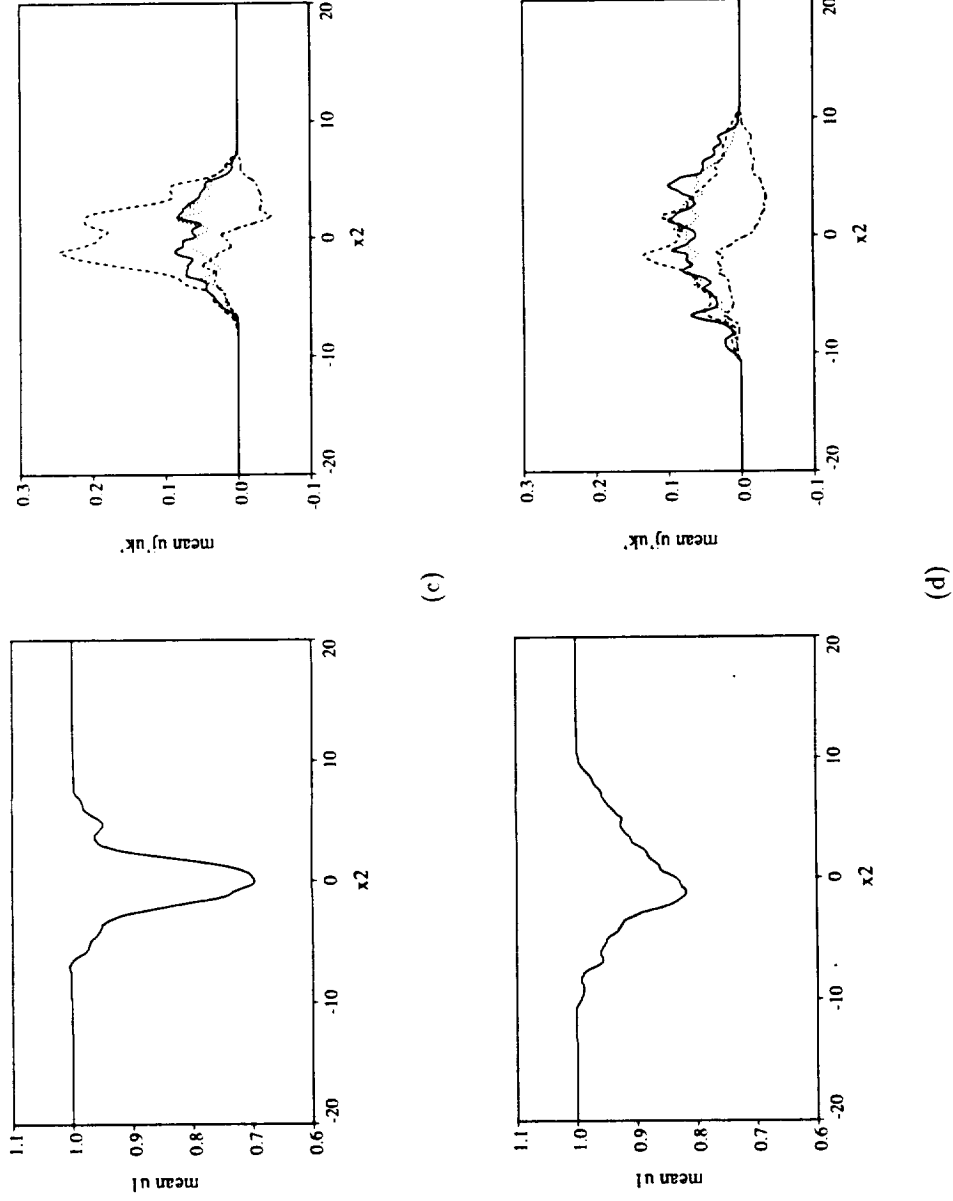


Figure F.4: Mean velocity profiles and second order turbulence profiles for 1384(60) $_{0xx}^{x0x}$  wake (two-dimensional fundamental plus three-dimensional subharmonic). (a)  $t = 28.4$ . (b)  $t = 51.1$ . (c)  $t = 101.5$ . (d)  $t = 199.3$ .

## Appendix G

### Wakes with an Oblique Fundamental

As discussed in the introduction, Williamson [52] and Williamson & Prasad [53, 54, 55] suggested an alternate to the mechanism examined in the bulk of this study for the development of strong three-dimensional motions in the plane wake. Their experiments indicated that strong, highly oblique coherent structures could be produced by an interaction between fundamental wavelength disturbances shed at a small oblique angle from the wake generator (as is common for the wakes behind bluff bodies such as cylinders) and long wavelength two-dimensional waves which grow due to the hydrodynamic instability of the far wake.

In order to verify that this proposed mechanism is indeed a legitimate path for the development of three-dimensional structures, a small set of simulations were run to examine the behavior of such wakes. The simulations were initiated with the same initial mean profile as used in the earlier simulations (see section 2.7 on page 36). Fundamental disturbances at angles of between  $5^\circ$  and  $30^\circ$  with respect to the spanwise direction ( $0^\circ$  being the non-oblique two-dimensional fundamental used in the earlier simulations) and two-dimensional ( $0^\circ$ ) subharmonic disturbances were superimposed on the mean. In each case, the width of the computational domain was chosen such that the fundamental disturbance was periodic in both the streamwise and spanwise directions. Note that because the fundamental disturbance is oblique,



there is no relevant measure of phase between the fundamental and the subharmonic. The phase, as defined for the two-dimensional wakes in chapter 3, effectively varies from 0 to  $2\pi$  along the span of the simulations.

Figures G.1, G.2, and G.3 show oblique views of an iso-entropy density contour for wakes initiated with the oblique fundamental at  $5^\circ$ ,  $15^\circ$ , and  $30^\circ$  respectively. The Reynolds number of these wakes,  $Re_b = 180$ , was chosen to approximately match the experiments of Williamson *et al.* The times (all approximately  $t \sim 100$ ) match the times for the wakes in figure 4.13 in section 4.3.2 on page 111. The viewing angle is also the same as for the earlier simulations.

The interaction of the oblique fundamental and the two-dimensional subharmonic causes the rollers of the (oblique) Kármán vortex street which initially forms from the oblique fundamental disturbance to wrap around one another. This reorients some of the spanwise vorticity from the Kármán vortex street into the streamwise direction. At low angles this wrapping is a result of the essentially two-dimensional interaction of the fundamental and the subharmonic. Each spanwise location sees a different phase between the fundamental and the subharmonic, thus each spanwise section pairs in a slightly different way as per the discussion in section 3.3.2. This is illustrated by the cuts through the vorticity field of the  $5^\circ$  wake which are shown in figure G.4. Eventually the rollers become sufficiently entwined for the three-dimensionality of the flow to become significant. At higher angles, the same basic process occurs, but the three-dimensionality of the flow begins to effect the dynamics at an earlier time.

As Williamson *et al.* suggest, this mechanism is a likely candidate for the cell pattern seen in the far of the plane wake by Cimbala, Nagib, & Roshko [13]. Figure G.5 is a top view of the  $30^\circ$  oblique wake in figure G.3 (the free stream flow is from left to right). The cell pattern here roughly matches the pattern seen in figure 19 of Cimbala *et al.*

The higher the angle of the oblique fundamental, the more quickly the rollers of the Kármán vortex street become distorted, and the more quickly streamwise vorticity is produced. Only at the highest angle shown,  $30^\circ$ , does the wake begin to develop streamwise structures similar in intensity to the wakes initiated with pairs of oblique

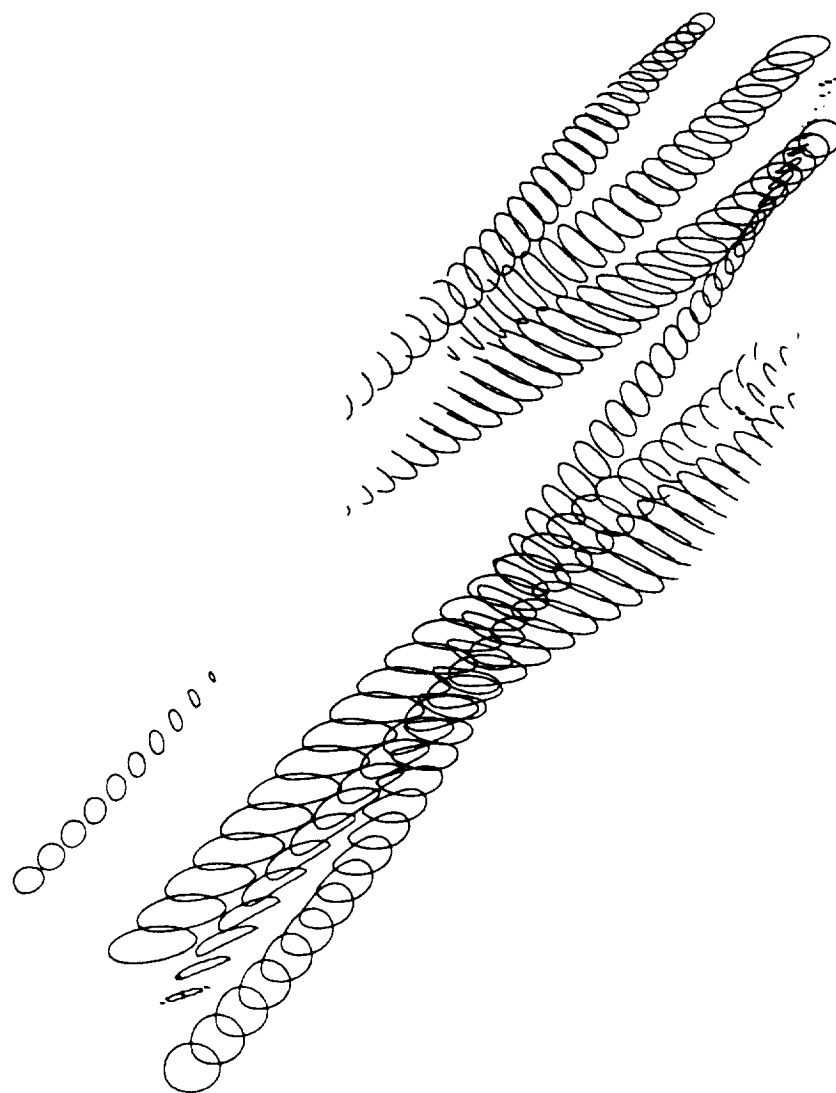


Figure G.1: Iso-entropy density contour for  $5^\circ$  oblique fundamental plus two-dimensional subharmonic.  $Re_b = 180$ .  $|\omega| = 0.2$ .  $t = 106.6$ .

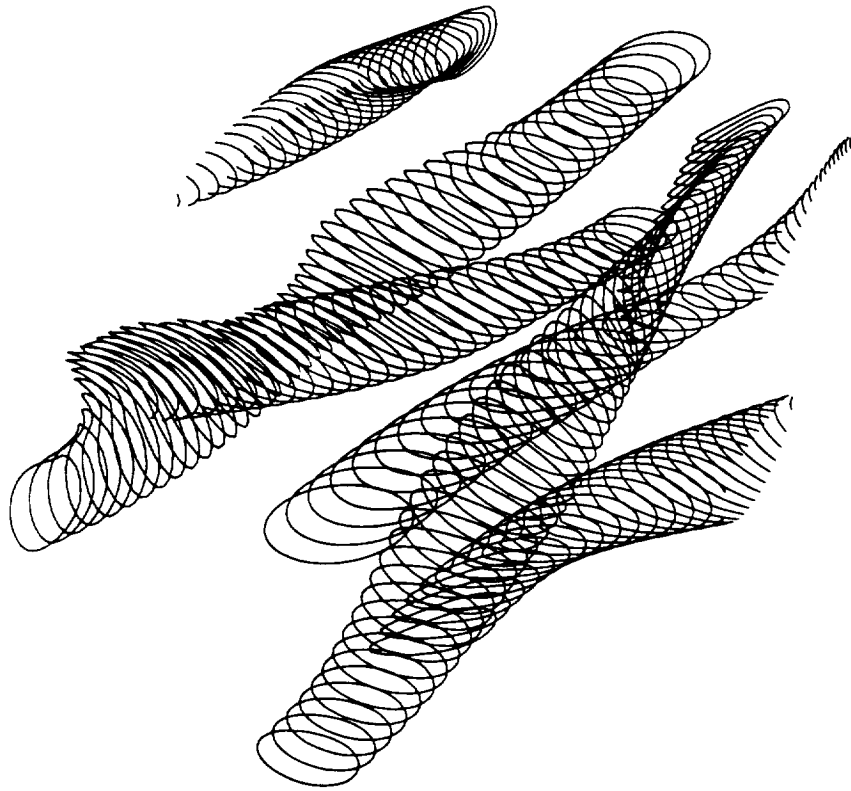


Figure G.2: Iso-entropy density contour for  $15^\circ$  oblique fundamental plus two-dimensional subharmonic.  $Re_b = 180$ .  $|\omega| = 0.2$ .  $t = 95.2$ .

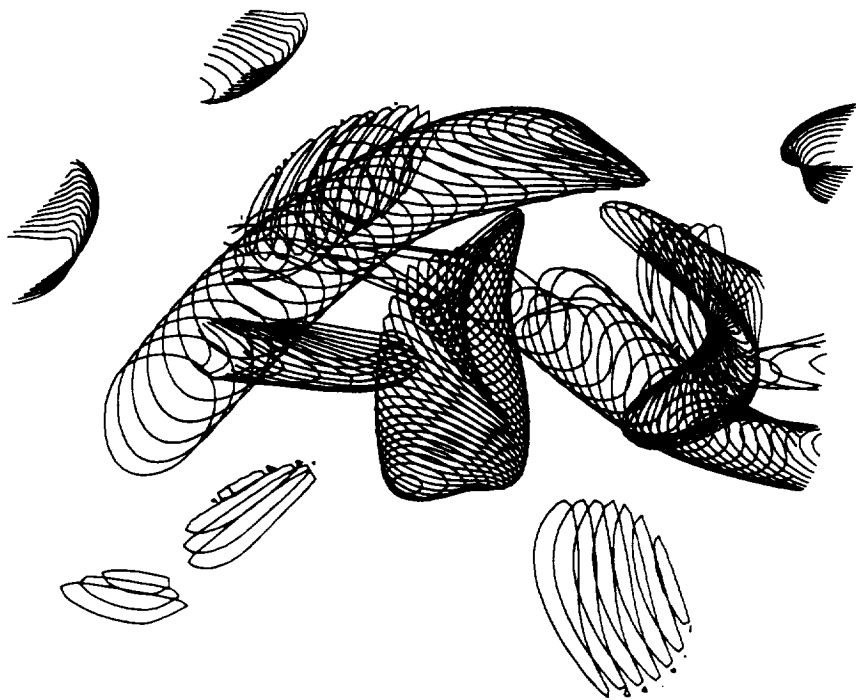


Figure G.3: Iso-entropy density contour for  $30^\circ$  oblique fundamental plus two-dimensional subharmonic.  $Re_b = 180$ .  $|\omega| = 0.2$ .  $t = 110.5$ .

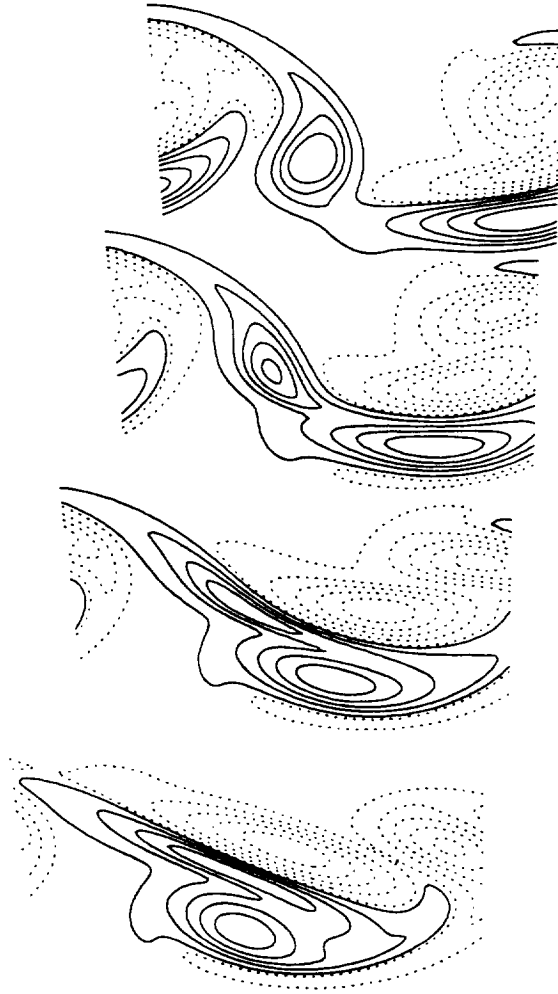


Figure G.4: Spanwise vorticity at various spanwise locations for  $5^\circ$  oblique fundamental plus two-dimensional subharmonic.  $Re_b = 180$ .  $t = 106.6$ . Contours are  $0.01 \leq |\omega_3| \leq 0.4$  in increments of 0.05.

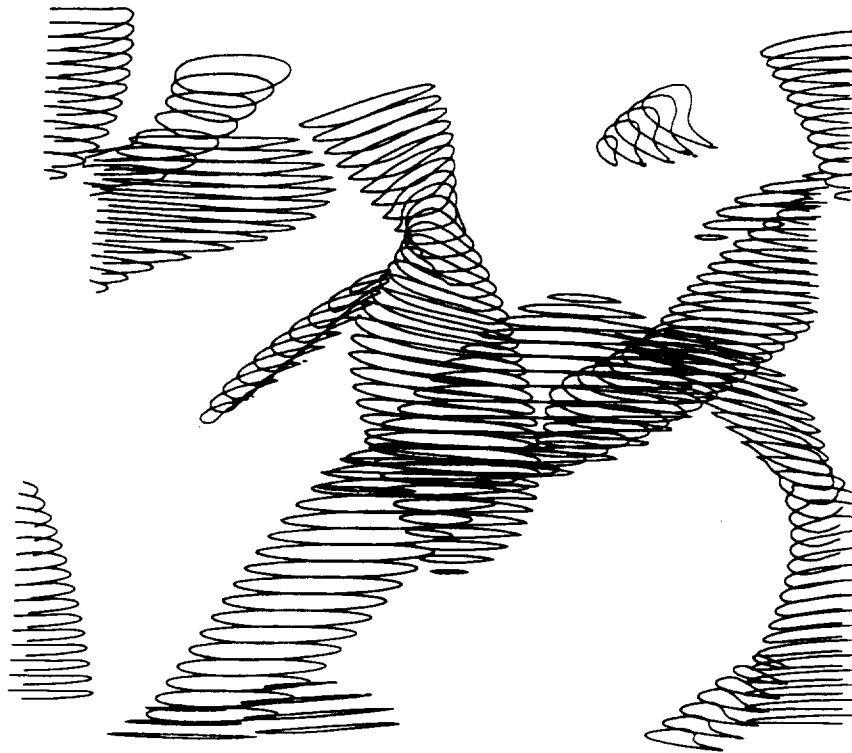


Figure G.5: Top view of iso-entropy density contour for  $30^\circ$  oblique fundamental plus two-dimensional subharmonic.  $Re_b = 180$ .  $|\omega| = 0.2$ .  $t = 110.5$ .

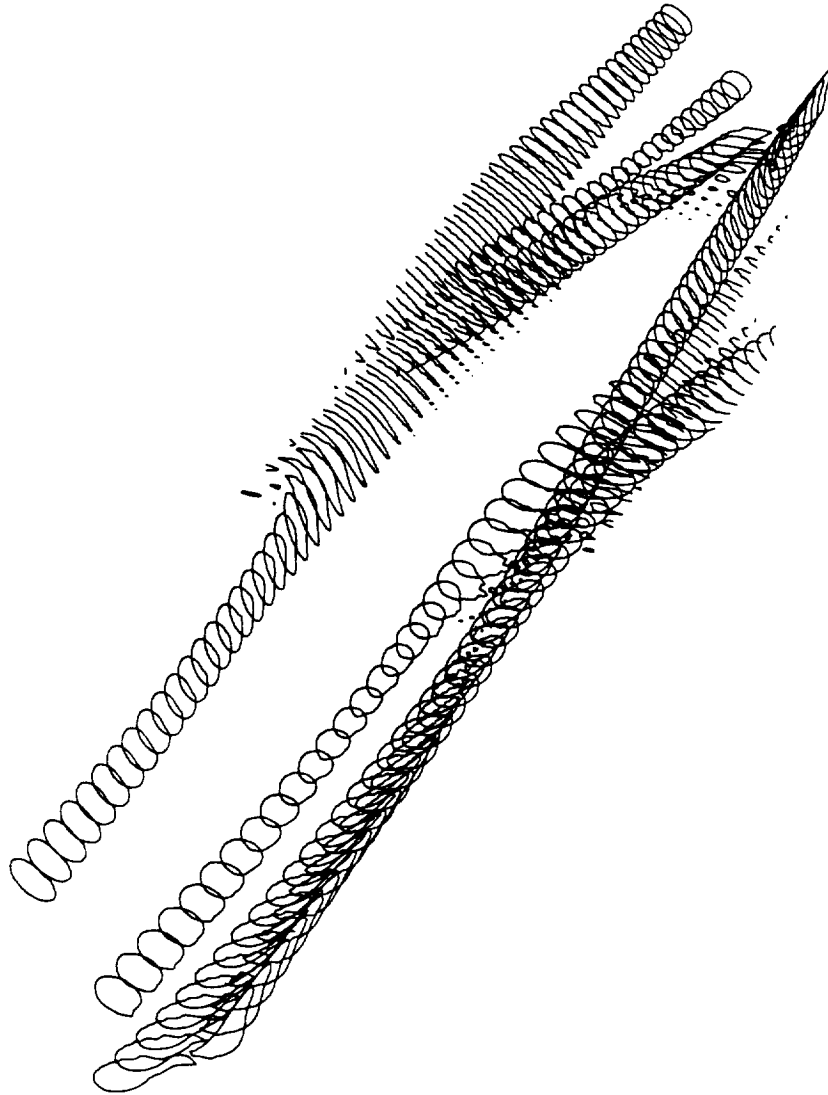


Figure G.6: Iso-entrophy density contour for  $5^\circ$  oblique fundamental plus two-dimensional subharmonic.  $Re_b = 1800$ .  $|\omega| = 0.2$ .  $t = 99.9$ .



Figure G.7: Iso-entropy density contour for  $30^\circ$  oblique fundamental plus two-dimensional subharmonic.  $Re_\delta = 1800$ .  $|\omega| = 0.8$ .  $t = 101.9$ .



subharmonic waves at the same development time (compare the wake in figures G.1, G.2, and G.3 to the the  $Re_b = 119$  wake in figure 4.13a in section 4.3.2 on page 109).

This result is consistent with the stability analysis of Flemming [16], which predicts strong growth of subharmonic disturbances at angles between approximately  $45^\circ$  and  $70^\circ$ . The  $5^\circ$  oblique fundamental case produces oblique subharmonic disturbances at angles well below  $45^\circ$ , and thus the three-dimensional structures do not grow in strength. At an oblique shedding angle of  $30^\circ$  however, the resulting oblique subharmonic disturbances are over  $45^\circ$  (see figure G.5) and thus grow in strength.

This is very significant to the development of fine scale motions at higher Reynolds numbers. Figures G.6 and G.7 show iso-entrophy density contours for the  $5^\circ$  and  $30^\circ$  oblique fundamental wakes, respectively, but this time at a Reynolds number of  $Re_b = 1800$ . This gives a Reynolds number and development time roughly equivalent to the wake in figure 4.13d in section 4.3.2 on page 110. At the time shown, the  $5^\circ$  wake, which does not produce significant streamwise structures, has developed no detectable fine scale motions even at this rather high Reynolds number. The only effect of increasing the Reynolds number has been to slow the diffusion of the vorticity in the spanwise rollers. In contrast, the  $30^\circ$  wake, which does produce strong coherent streamwise structures, develops strong fine scale motions. This is in line with the earlier simulations, and reinforces the result that the tertiary transition in the incompressible plane wake requires the presence of strong long wavelength coherent streamwise structures. These results indicate that the source and symmetry of those structures are not significant, so long as they are present.

# Appendix H

## Summary of Simulations

Table H.1: Summary of Two-dimensional Simulations

Tag Filename	$Re_b$ Max Time $N_1 \times N_2 \times N_3$	$\varepsilon_{100}$	$\varepsilon_{010}$ $\phi_{010}$	$\varepsilon_{001}$ $\phi_{001}$	$\varepsilon^{100}$ $\phi^{100}$	$\varepsilon^{010}$ $\phi^{010}$	$\varepsilon^{001}$ $\phi^{001}$
$m50(0)_{xxx}^{xxx}$ mixdiff	50 <sup>1</sup> 1102.9 $8 \times 128 \times 4$	–	–	–	–	–	–
$35(0)_{xxx}^{xxx}$ wkdiff	35 283.4 $8 \times 128 \times 4$	–	–	–	–	–	–
$346(0)_{0xx}^{xxx}$ wk2d_1	346 285.8 $128 \times 128 \times 4$	0.02	–	–	–	–	–
$69(0)_{0xx}^{xxx}$ wk2d_2	69 504.2 $128 \times 128 \times 4$	0.02	–	–	–	–	–

Table H.1: Summary of Two-dimensional Simulations  
(Cont.)

Tag Filename	$Re_b$ Max Time $N_1 \times N_2 \times N_3$	$\varepsilon_{100}$	$\varepsilon_{010}$ $\phi_{010}$	$\varepsilon_{001}$ $\phi_{001}$	$\varepsilon^{100}$ $\phi^{100}$	$\varepsilon^{010}$ $\phi^{010}$	$\varepsilon^{001}$ $\phi^{001}$
119(0) $_{0xx}^{xxx}$ wk2d_3	119 361.0 $128 \times 128 \times 4$	0.02	–	–	–	–	–
692(0) $_{0xx}^{xxx}$ wk2d_4	692 337.8 $128 \times 192 \times 4$	0.02	–	–	–	–	–
1384(0) $_{0xx}^{xxx}$ wk2d_5	1384 303.9 $192 \times 256 \times 4$	0.02	–	–	–	–	–
2768(0) $_{0xx}^{xxx}$ wk2d_6	2768 291.0 $192 \times 256 \times 4$	0.02	–	–	–	–	–
346(0) $_{00x}^{xxx}$ wk2d_7	346 311.4 $192 \times 192 \times 4$	0.02	0.02 0	–	–	–	–
346(0) $_{0\frac{\pi}{4}x}^{xxx}$ wk2d_8	346 251.5 $192 \times 192 \times 4$	0.02	0.02 $\pi/4$	–	–	–	–
346(0) $_{0\frac{\pi}{2}x}^{xxx}$ wk2d_9	346 312.4 $192 \times 192 \times 4$	0.02	0.02 $\pi/2$	–	–	–	–
119(0) $_{00x}^{xxx}$ wk2d_10	119 297.9 $128 \times 128 \times 4$	0.02	0.02 0	–	–	–	–

Table H.1: Summary of Two-dimensional Simulations  
(Cont.)

Tag Filename	$Re_b$ Max Time $N_1 \times N_2 \times N_3$	$\varepsilon_{100}$	$\varepsilon_{010}$ $\phi_{010}$	$\varepsilon_{001}$ $\phi_{001}$	$\varepsilon^{100}$ $\phi^{100}$	$\varepsilon^{010}$ $\phi^{010}$	$\varepsilon^{001}$ $\phi^{001}$
692(0) $_{00x}^{xxx}$ wk2d.11	692 265.7 $192 \times 192 \times 4$	0.02	0.02 0	—	—	—	—
1384(0) $_{00x}^{xxx}$ wk2d.12	1384 254.6 $192 \times 192 \times 4$	0.02	0.02 0	—	—	—	—
119(0) $_{0\frac{\pi}{4}x}^{xxx}$ wk2d.13	119 315.1 $128 \times 128 \times 4$	0.02	0.02 $\pi/4$	—	—	—	—
692(0) $_{0\frac{\pi}{4}x}^{xxx}$ wk2d.14	692 298.1 $192 \times 192 \times 4$	0.02	0.02 $\pi/4$	—	—	—	—
1384(0) $_{0\frac{\pi}{4}x}^{xxx}$ wk2d.15	1384 305.1 $192 \times 192 \times 4$	0.02	0.02 $\pi/4$	—	—	—	—
119(0) $_{0\frac{\pi}{2}x}^{xxx}$ wk2d.16	119 340.8 $128 \times 128 \times 4$	0.02	0.02 $\pi/2$	—	—	—	—
692(0) $_{0\frac{\pi}{2}x}^{xxx}$ wk2d.17	692 313.5 $192 \times 192 \times 4$	0.02	0.02 $\pi/2$	—	—	—	—
1384(0) $_{0\frac{\pi}{2}x}^{xxx}$ wk2d.18	1384 313.7 $192 \times 192 \times 4$	0.02	0.02 $\pi/2$	—	—	—	—

Table H.1: Summary of Two-dimensional Simulations  
(Cont.)

Tag Filename	$Re_b$ Max Time $N_1 \times N_2 \times N_3$	$\varepsilon_{100}$	$\varepsilon_{010}$ $\phi_{010}$	$\varepsilon_{001}$ $\phi_{001}$	$\varepsilon^{100}$ $\phi^{100}$	$\varepsilon^{010}$ $\phi^{010}$	$\varepsilon^{001}$ $\phi^{001}$
346(0) $_{000}^{xxx}$ wk2d_25	346 248.1 $256 \times 192 \times 4$	0.02	0.02 0	0.02 0	—	—	—
69(0) $_{000}^{xxx}$ wk2d_27	69 336.1 $128 \times 128 \times 4$	0.02	0.02 0	0.02 0	—	—	—

Table H.2: Summary of Three-dimensional Simulations

Tag Filename	$Re_b$ Max Time $N_1 \times N_2 \times N_3$	$\varepsilon_{100}$	$\varepsilon_{010}$ $\phi_{010}$	$\varepsilon_{001}$ $\phi_{001}$	$\varepsilon^{100}$ $\phi^{100}$	$\varepsilon^{010}$ $\phi^{010}$	$\varepsilon^{001}$ $\phi^{001}$
346(60) $_{0xx}^{0xx}$ wk3d_1	346 340.0 $192 \times 128 \times 64$	0.02	—	—	0.02 0	—	—
346(60) $_{0xx}^{\frac{\pi}{4}xx}$ wk3d_2	346 303.0 $128 \times 128 \times 64$	0.02	—	—	0.02 $\pi/4$	—	—
346(60) $_{0xx}^{\frac{\pi}{2}xx}$ wk3d_3	346 218.2 $96 \times 128 \times 64$	0.02	—	—	0.02 $\pi/2$	—	—
346(60) $_{0xx}^{x0x}$ wk3d_4	346 478.1 $192 \times 128 \times 64$	0.02	—	—	—	0.02 0	—

Table H.2: Summary of Three-dimensional Simulations  
(Cont.)

Tag Filename	$Re_b$ Max Time $N_1 \times N_2 \times N_3$	$\varepsilon_{100}$	$\varepsilon_{010}$ $\phi_{010}$	$\varepsilon_{001}$ $\phi_{001}$	$\varepsilon^{100}$ $\phi^{100}$	$\varepsilon^{010}$ $\phi^{010}$	$\varepsilon^{001}$ $\phi^{001}$
$346(60)_{0xx}^{\pi/4 x}$ wk3d_5	346 292.1 $192 \times 192 \times 64$	0.02	–	–	–	0.02 $\pi/4$	–
$346(60)_{0xx}^{\pi/2 x}$ wk3d_6	346 293.7 $192 \times 192 \times 64$	0.02	–	–	–	0.02 $\pi/2$	–
$346(60)_{00x}^{0xx}$ wk3d_7	346 318.4 $192 \times 192 \times 64$	0.02	0.02 0	–	0.02 0	–	–
$346(60)_{0\pi/4 x}^{0xx}$ wk3d_8	346 321.0 $192 \times 192 \times 64$	0.02	0.02 $\pi/4$	–	0.02 0	–	–
$346(60)_{0\pi/2 x}^{0xx}$ wk3d_9	346 232.0 $96 \times 128 \times 48$	0.02	0.02 $\pi/2$	–	0.02 0	–	–
$346(60)_{00x}^{\pi/4 xx}$ wk3d_10	346 200.3 $96 \times 128 \times 48$	0.02	0.02 0	–	0.02 $\pi/4$	–	–
$346(60)_{0\pi/4 x}^{\pi/4 xx}$ wk3d_11	346 321.6 $96 \times 128 \times 48$	0.02	0.02 $\pi/4$	–	0.02 $\pi/4$	–	–
$346(60)_{0\pi/2 x}^{\pi/4 xx}$ wk3d_12	346 417.0 $96 \times 128 \times 48$	0.02	0.02 $\pi/2$	–	0.02 $\pi/4$	–	–

Table H.2: Summary of Three-dimensional Simulations  
(Cont.)

Tag Filename	$Re_b$ Max Time $N_1 \times N_2 \times N_3$	$\varepsilon_{100}$	$\varepsilon_{010}$ $\phi_{010}$	$\varepsilon_{001}$ $\phi_{001}$	$\varepsilon^{100}$ $\phi^{100}$	$\varepsilon^{010}$ $\phi^{010}$	$\varepsilon^{001}$ $\phi^{001}$
$346(60)_{00x}^{\frac{\pi}{2}xx}$ wk3d_13	346 249.8 $96 \times 128 \times 48$	0.02	0.02 0	—	0.02 $\pi/2$	—	—
$346(60)_{0\frac{\pi}{4}x}^{\frac{\pi}{2}xx}$ wk3d_14	346 272.3 $96 \times 128 \times 48$	0.02	0.02 $\pi/4$	—	0.02 $\pi/2$	—	—
$346(60)_{0\frac{\pi}{2}x}^{\frac{\pi}{2}xx}$ wk3d_15	346 340.8 $96 \times 128 \times 48$	0.02	0.02 $\pi/2$	—	0.02 $\pi/2$	—	—
$346(60)_{00x}^{x0x}$ wk3d_16	346 321.1 $128 \times 128 \times 64$	0.02	0.02 0	—	—	0.02 0	—
$346(60)_{0\frac{\pi}{4}x}^{x\frac{\pi}{4}x}$ wk3d_17	346 282.4 $128 \times 128 \times 64$	0.02	0.02 $\pi/4$	—	—	0.02 0	—
$346(60)_{0\frac{\pi}{2}x}^{x0x}$ wk3d_18	346 293.6 $128 \times 128 \times 64$	0.02	0.02 $\pi/2$	—	—	0.02 0	—
$346(60)_{00x}^{x\frac{\pi}{4}x}$ wk3d_19	346 268.7 $96 \times 128 \times 48$	0.02	0.02 0	—	0.02 $\pi/4$	—	—
$346(60)_{0\frac{\pi}{4}x}^{x\frac{\pi}{4}x}$ wk3d_20	346 329.2 $96 \times 128 \times 48$	0.02	0.02 $\pi/4$	—	—	0.02 $\pi/4$	—

Table H.2: Summary of Three-dimensional Simulations  
(Cont.)

Tag Filename	$Re_b$ Max Time $N_1 \times N_2 \times N_3$	$\varepsilon_{100}$	$\varepsilon_{010}$ $\phi_{010}$	$\varepsilon_{001}$ $\phi_{001}$	$\varepsilon^{100}$ $\phi^{100}$	$\varepsilon^{010}$ $\phi^{010}$	$\varepsilon^{001}$ $\phi^{001}$
$346(60)_{0\frac{\pi}{4}x}^{\frac{\pi}{2}x}$ wk3d_21	346 302.9 $96 \times 128 \times 48$	0.02	0.02 $\pi/2$	–	–	0.02 $\pi/4$	–
$346(60)_{00x}^{\frac{\pi}{2}x}$ wk3d_22	346 288.2 $96 \times 128 \times 48$	0.02	0.02 0	–	–	0.02 $\pi/2$	–
$346(60)_{0\frac{\pi}{4}x}^{\frac{\pi}{2}x}$ wk3d_23	346 317.4 $96 \times 128 \times 48$	0.02	0.02 $\pi/4$	–	–	0.02 $\pi/2$	–
$346(60)_{0\frac{\pi}{2}x}^{\frac{\pi}{2}x}$ wk3d_24	346 210.5 $96 \times 128 \times 48$	0.02	0.02 $\pi/2$	–	–	0.02 $\pi/2$	–
$346(60)_{000}^{x00}$ wk3d_25	346 200.1 $256 \times 192 \times 64$	0.02	0.02 0	0.02 0	–	0.02 0	0.02 0
$2768(60)_{0xx}^{x0x}$ wk3d_26	2768 328.7 $256 \times 256 \times 192$	0.02	–	–	–	0.02 0	–
$69(60)_{0xx}^{x0x}$ wk3d_27	69 336.1 $128 \times 128 \times 32$	0.02	–	–	–	0.02 0	–
$1384(60)_{0xx}^{x0x}$ wk3d_28	1384 342.4 $192 \times 256 \times 128$	0.02	–	–	–	0.02 0	–



Table H.2: Summary of Three-dimensional Simulations  
(Cont.)

Tag Filename	$R_{\text{max}}$ Max Time $N_1 \times N_2 \times N_3$	$\varepsilon_{100}$	$\varepsilon_{010}$ $\phi_{010}$	$\varepsilon_{001}$ $\phi_{001}$	$\varepsilon^{100}$ $\phi^{100}$	$\varepsilon^{010}$ $\phi^{010}$	$\varepsilon^{001}$ $\phi^{001}$
1384(60) $_{0xx}^{0xx}$ wk3d_29	1384 100.2 $192 \times 256 \times 128$	0.02	–	–	0.02 0	–	–
119(60) $_{0xx}^{x0x}$ wk3d_30	119 425.6 $96 \times 128 \times 48$	0.02	–	–	–	0.02 0	–
119(60) $_{0xx}^{x\frac{\pi}{4}x}$ wk3d_31	119 459.0 $96 \times 128 \times 48$	0.02	–	–	–	0.02 $\pi/4$	–
119(60) $_{0xx}^{x\frac{\pi}{2}x}$ wk3d_32	119 478.6 $96 \times 128 \times 48$	0.02	–	–	–	0.02 $\pi/2$	–
119(60) $_{0xx}^{0xx}$ wk3d_33	119 402.7 $96 \times 128 \times 48$	0.02	–	–	0.02 0	–	–
119(60) $_{000}^{x00}$ wk3d_34	119 352.6 $192 \times 128 \times 64$	0.02	0.02 0	0.02 0	–	0.02 0	0.02 0
2768(60) $_{0xx}^{x\frac{\pi}{2}x}$ wk3d_40	2768 319.8 $192 \times 256 \times 128$	0.02	–	–	–	0.02 $\pi/2$	–
692(60) $_{0xx}^{x0x}$ wk3d_41	692 222.2 $192 \times 192 \times 128$	0.02	–	–	–	0.02 0	–

Table H.2: Summary of Three-dimensional Simulations  
(Cont.)

Tag Filename	$Re_b$ Max Time $N_1 \times N_2 \times N_3$	$\varepsilon_{100}$	$\varepsilon_{010}$ $\phi_{010}$	$\varepsilon_{001}$ $\phi_{001}$	$\varepsilon^{100}$ $\phi^{100}$	$\varepsilon^{010}$ $\phi^{010}$	$\varepsilon^{001}$ $\phi^{001}$
$692(60)_{0xx}^{x\frac{\pi}{2}x}$ wk3d_42	90.0 $192 \times 192 \times 128$	0.02	—	—	—	0.02 $\pi/2$	—

# Bibliography

- [1] H. Aref and E. D. Siggia. Evolution and breakdown of a vortex street in two dimensions. *J. Fluid Mech.*, 100:435–463, 1981.
- [2] W. T. Ashurst, A. R. Kerstein, R. M. Kerr, and C. H. Gibson. Alignment of vorticity and scalar gradient with strain rate in simulated Navier-Stokes turbulence. *Phys. Fluids*, 30(8):2343–2353, 1987.
- [3] H. M. Blackburn, N. N. Mansour, and B. J. Cantwell. Topology of fine-scale motions in turbulent channel flow. Submitted to *J. Fluid Mech.*, 1994.
- [4] A. B. Cain, W. C. Reynolds, and J. H. Ferziger. A three dimensional simulation of transition and early turbulence in a time-developing mixing layer. Technical Report TF-14, HTTM, Stanford University, 1981.
- [5] B. J. Cantwell. Exact solution of a restricted Euler equation for the velocity gradient tensor. *Phys. Fluids A*, 4 (4):782–793, 1992.
- [6] B. J. Cantwell. On the behavior of velocity gradient tensor invariants in direct numerical simulations of turbulence. *Phys. Fluids*, 5(8):2008–2013, 1993.
- [7] B. J. Cantwell, J. H. Chen, and G. Lewis. Topology of three-dimensional variable density flows. *Proceedings of the Tenth Australasian Fluid Mechanics Conference*, 1989.
- [8] C. Canuto, M. Y. Hussaini, A. Quarteroni, and T. A. Zang. *Spectral Methods in Fluid Dynamics*. Springer-Verlag, 1988.

- [9] J. H. Chen, B. J. Cantwell, and N. N. Mansour. The topology and vorticity dynamics of a three-dimensional plane compressible wake. *Proceedings of the 10th Australasian Fluid Mechanics Conference, Melbourne*, 1989.
- [10] J. H. Chen, B. J. Cantwell, and N. N. Mansour. The effect of Mach number on the stability of a plane supersonic wake. *Phys. Fluids A*, 2(6):984–1004, 1990.
- [11] J. H. Chen, M. Chong, J. Soria, R. Sondergaard, A. E. Perry, M. M. Rogers, R. D. Moser, and B. J. Cantwell. A study of the topology of dissipating motions in direct numerical simulations of time-developing compressible and incompressible mixing layers. *Center for Turbulence Research Report CTR-S90*, 1990.
- [12] M. Chong, A. E. Perry, and B. J. Cantwell. A general classification of three-dimensional flow fields. *Phys. Fluids A*, 2(5):765–777, 1990.
- [13] J. M. Cimbalá, H. M. Nagib, and A. Roshko. Large structure in the far wakes of two-dimensional bluff bodies. *J. Fluid Mech.*, 190:265–298, 1988.
- [14] T. C. Corke, J. D. Krull, and M. Ghassemi. Three-dimensional-mode resonance in far wakes. *J. Fluid Mech.*, 239:99–132, 1992.
- [15] R. Corral and J. Jiménez. Fourier/Chebyshev methods for the incompressible Navier Stokes equations in infinite domains. *Comp. Fluid Dyn.*, 1:361–368, 1992.
- [16] M. F. Flemming. Secondary instability in the far wake. Master's thesis, Illinois Institute of Technology, 1987.
- [17] H. L. Grant. The large eddies in turbulent motion. *J. Fluid Mech.*, 4:149–190, 1958.
- [18] J. O. Hinze. *Turbulence*. McGraw-Hill, 1975.
- [19] J. Jiménez. Kinematic alignment effects in turbulent flows. *Phys. Fluids A*, 4(4):652–654, 1992.
- [20] G. E. Karniadakis and G. S. Triantafyllou. Frequency selection and asymptotic states in laminar wakes. *J. Fluid Mech.*, 199:441–469, 1989.

- [21] G. E. Karniadakis and G. S. Triantafyllou. Three-dimensional dynamics and transition to turbulence in the wake of bluff objects. *J. Fluid Mech.*, 238:1–30, 1992.
- [22] D. R.-S. Ko, T. Kubota, and L. Lees. Finite disturbance effect on the stability of a laminar incompressible wake behind a flat plate. *J. Fluid Mech.*, 40:315–341, 1970.
- [23] E. Laurien and L. Kleiser. Numerical simulation of boundary-layer transition and transition control. *J. Fluid Mech.*, 199:403–440, 1989.
- [24] H. Maekawa, N. N. Mansour, and J. C. Buell. Instability mode interactions in a spatially developing plane wake. *J. Fluid Mech.*, 235:223–254, 1992.
- [25] N. N. Mansour. *Large-Eddy Simulation of a Turbulent Mixing Layer*. PhD thesis, Dept. of Mech. Eng, Stanford University, 1978.
- [26] G. Mattingly and W. Criminale. The stability of an incompressible two-dimensional wake. *J. Fluid Mech.*, 51:233–272, 1972.
- [27] R. D. Moser and M. M. Rogers. The three-dimensional evolution of a plane mixing layer: Pairing and transition to turbulence. *J. Fluid Mech.*, 247:275–320, 1993.
- [28] R. D. Moser and M. M. Rogers. Direct simulation of a self-similar plane wake. *AGARD Symp. on App. of DNS and LES. Chania, Crete, Greece*, 1994.
- [29] J. C. Mumford. The structure of large eddies in fully developed turbulent shear flows. part 2. the plane wake. *J. Fluid Mech.*, 137:447–456, 1983.
- [30] S. A. Orszag and Y.-H. Pao. Numerical computation of turbulent shear flows. *Advances in Geophysics, International Symposium on Turbulent Diffusion in Environmental Pollution*, 18A:225–236, 1974.
- [31] G. S. Patterson and S. A. Orszag. Spectral calculations of isotropic turbulence: Efficient removal of aliasing interactions. *Phys. Fluids*, 14:2538–2541, 1971.

- [32] R. Pierrehumbert and S. Widnall. The two- and three-dimensional instabilities of a spatially periodic shear layer. *J. Fluid Mech.*, 114:59–82, 1982.
- [33] J. Riley, P. Mourad, R. D. Moser, and M. M. Rogers. *Proceedings of the Summer Program, Center for Turbulence Research*, pages 91–116, 1990.
- [34] R. S. Rogallo. Numerical experiments in homogeneous turbulence. *NASA Technical Memorandum 81315*, 1981.
- [35] M. M. Rogers and R. D. Moser. The three-dimensional evolution of a plane mixing layer: The Kelvin-Helmholtz rollup. *J. Fluid Mech.*, 243:183–226, 1992.
- [36] M. M. Rogers and R. D. Moser. Spanwise scale selection in plane mixing layers. *J. Fluid Mech.*, 247:321–337, 1993.
- [37] A. Roshko. Structure of turbulent shear flows: A new look. *AIAA J.*, 14:1349–1357, 1976.
- [38] G. R. Ruetsch and M. R. Maxey. Small-scale features of vorticity and passive scalar fields in homogeneous isotropic turbulence. *Private Communication*, 1993.
- [39] H. Sato and K. Kuriki. The mechanism of transition in the wake of a thin flat plate placed parallel to a uniform flow. *J. Fluid Mech.*, 11:321–352, 1961.
- [40] H. Sato and H. Saito. Artificial control of the laminar-turbulent transition of a two-dimensional wake by external sound. *J. Fluid Mech.*, 84:657–672, 1978.
- [41] R. Sondergaard, J. Soria, J. H. Chen, and B. J. Cantwell. Local topology of small scale motions in turbulent shear flows. *Eighth Symposium on Turbulent Shear Flows*, 1991.
- [42] J. Soria, R. Sondergaard, B. J. Cantwell, M. S. Chong, and A. E. Perry. A study of the fine scale motions of incompressible time-developing mixing layers. *Phys. Fluids*, 6(2):871–884, 1994.
- [43] P. R. Spalart. Direct simulation of a turbulent boundary layer up to  $Re_\theta = 1410$ . *J. Fluid Mech.*, 187:61–98, 1988.

- [44] P. R. Spalart, R. D. Moser, and M. M. Rogers. Spectral methods for the Navier Stokes equations with one infinite and two periodic directions. *J. Comput. Phys.*, 96:297–324, 1990.
- [45] A. A. Townsend. *The Structure of Turbulent Shear Flow*. Cambridge University Press, 1956.
- [46] A. A. Townsend. Entrainment and the structure of turbulent flow. *J. Fluid Mech.*, 41:13–46, 1970.
- [47] A. Tsinober, E. Kit, and T. Dracos. Experimental investigation of the field of velocity gradients in turbulent flows. *J. Fluid Mech.*, 242:169–192, 1992.
- [48] P. Vieillefosse. Local interaction between vorticity and shear in a perfect incompressible fluid. *J. Physique*, 43:837–842, 1982.
- [49] P. Vieillefosse. Internal motion of a small element of fluid in an inviscid flow. *Physica*, 125A:150–162, 1984.
- [50] A. Vincent and M. Meneguzzi. The spatial and statistical properties of homogeneous turbulence. *J. Fluid Mech.*, 225:1–20, 1991.
- [51] A. Vincent and M. Meneguzzi. The dynamics of vorticity tubes in homogeneous turbulence. *J. Fluid Mech.*, 258:245–254, 1994.
- [52] C. H. K. Williamson. The natural and forced formation of spot-like ‘vortex dislocations’ in the transition of a wake. *J. Fluid Mech.*, 243:393–441, 1992.
- [53] C. H. K. Williamson and A. Prasad. Acoustic forcing of oblique wave resonance in the far wake. *J. Fluid Mech.*, 256:315–341, 1993.
- [54] C. H. K. Williamson and A. Prasad. A mechanism for oblique wave resonance in the far wake. *Proc. of IUTAM Symp. on Nonlin. Instab. of Nonpar. Flows*, 1993.
- [55] C. H. K. Williamson and A. Prasad. A new mechanism for oblique wave resonance in the ‘natural’ far wake. *J. Fluid Mech.*, 256:269–313, 1993.

- [56] C. H. K. Williamson and A. Roshko. Vortex formation in the wake of an oscillating cylinder. *J. Fluids and Struct.*, 2:355–381, 1988.
- [57] A. Wray. A manual of the VECTORAL language. *Private Communication*, 1989.
- [58] I. Wygnanski, F. Champagne, and B. Marasli. On the large scale structures in two dimensional, small deficit, turbulent wakes. *J. Fluid Mech.*, 168:31–71, 1986.
- [59] M. M. Zdravkovitch. Smoke observations of the formation of a Kármán vortex street. *J. Fluid Mech.*, 37:491–496, 1969.